ENGINEERING MATERIALS

Ali Rostami
Hamed Baghban
Reza Maram

Nanostructure Semiconductor Optical Amplifiers

Building Blocks for All-Optical Processing

Springer

Engineering Materials

For further volumes:
http://www.springer.com/series/4288

Ali Rostami · Hamed Baghban · Reza Maram

Nanostructure Semiconductor Optical Amplifiers

Building Blocks for All-Optical Processing

Springer

Prof. Ali Rostami
Nanophotonics School of Engineering-
Emerging Technology
University of Tabriz
Bolv. 29, Bahman
51666 Tabriz, Iran
e-mail: rostami@tabrizu.ac.ir

Reza Maram
Faculty of Electrical and
Computer Engineering
University of Tabriz
Bolv. 29, Bahman
51666 Tabriz, Iran
e-mail: r.maram.q@gmail.com

Hamed Baghban
Faculty of Electrical and
Computer Engineering
University of Tabriz
Emam Khomeini Bolv. 29, Bahman
51666 Tabriz, Iran
e-mail: h-baghban@tabrizu.ac.ir

ISSN 1612-1317 e-ISSN 1868-1212

ISBN 978-3-642-14924-5 e-ISBN 978-3-642-14925-2

DOI 10.1007/978-3-642-14925-2

Springer Heidelberg Dordrecht London New York

Library of Congress Control Number: 2010937667

Cover design: deblik, Berlin

Printed on acid-free paper

Springer is part of Springer Science+Business Media (www.springer.com)

Preface

The importance of semiconductor optical amplifiers (SOAs) as key components in optical communications and integrated optics, covering a wide range of applications for the 1550- and 1300-nm optical windows, has grown in recent years. All-optical signal processing, including wavelength conversion, optical logic gates and signal regeneration, etc, is one of the most important enabling technologies to realize optical switching, including optical circuit switching, optical burst switching and optical packet switching and SOAs are very promising in all-optical signal processing since they are compact, easy to manufacture and power efficient.

The need for all-optical elements for increasing the capacity of current and future communication networks and optimizing the operation of optical switching networks has been one of the main motivations for considering SOAs as essential elements in all-optical switching scenarios in recent years. The present book tries to mark a small portion of the SOAs and specially quantum-dot SOAs (QD-SOAs) capabilities in the mentioned topics.

In Chap. 1 of this book authors have tried to introduce different aspects of a SOA specially a QD-SOA including structural, optical and electrical specifications of a QDSOA. Different definitions in the field of a SOA such gain-related mechanisms, SOA polarization characteristics, effect of impurity doping in the active region and fabrication requirements are presented in this chapter.

Chapter 2 presents a general overview for different simulation methods of QD-SOAs. One of the most accurate ways of modeling a SOA is to solve the Semiconductor Bloch Equation (SBE). However, this method is extremely time-consuming. The computation time is not acceptable for the system applications of SOA-based devices, where many optical pulses have to be transmitted through the SOA to evaluate the system performance. Simplified approaches including certain physical processes phenomenologically, as it is done in rate-equation models, have much faster calculation speeds and are quite successful in explaining the experimental results. Although the accuracy for sub-picosecond pulses is not as good as the SBE calculation. Numerical modeling is always necessary to understand the working principle of the devices and to optimize their performance. Physical modeling of complex devices including SOA, such as all-active MZIs, is necessary

in order to understand their potential and limitations. In this chapter three different methods for investigation of the QD-SOA performances based on rate-equation model i.e. numerical methods, equivalent circuit-modeling methods and analytical methods is briefly described.

Chapter 3 of the book covers different techniques toward utilizing the high-speed operation capabilities of SOAs for high-bit-rate signal processing. This chapter reviews the most recent techniques in the field of bulk, quantum well and also quantum dot-based SOAs and gives an insight for possible future optimization methods for increasing the response of SOA-based devices for high-speed operations.

Chapter 4 covers the applications of SOAs in all-optical logic gates and subsystems which seem to be essential elements in all-optical signal processing scenarios. In this chapter it has been tried to introduce different techniques for realization of SOA-based optical units and hence, it hasn't suffice to QD-SOA based structures. This diversity of introduced structures may provide inspiration for novel ideas in eager readers. Authors believe that investigation of QD-SOA specifications in the beginning chapters and presentation of practical methods based on different types of SOAs provides this ability for researchers who are interested in the topics.

Finally, in Chap. 5 of the present book, recent progresses in all-optical signal processing and switching with considering SOAs as one of the main elements in the proposed structures are presented. Although these applications are not the whole SOA based architectures for optical switching and signal processing, a small part of recent development in this field is has been reviewed in this chapter.

Iran, October 2010 Ali Rostami

Contents

Chapter 1
Quantum-Dot Semiconductor Optical Amplifiers, Basic Principles, Design Methods, and Optical Characterizations

1.1 Introduction

The development of semiconductor optical amplifiers (SOAs) happened soon after the invention of the semiconductor laser. A SOA is very similar to a semiconductor laser without (or with negligible) optical facet feedback. An incoming signal injected into the SOA propagates along its optical waveguide and is amplified by stimulated emission. The optical gain is achieved by inverting the carrier population in the active region via electrical pumping. During the 1990s due to the development of the erbium doped optical amplifier (EDFA) the popularity of the SOA as a linear amplifier declined as the EDFAs provided higher gain without the detrimental nonlinearities associated with an SOA.

During the development of SOAs, there were three main challenges related to SOAs performance making them acceptable for practical applications: polarisation sensitivity reduction, optical feedback reduction, and decreasing the noise level of SOAs. However, attentions turned to SOAs in the late 1990s as SOA design techniques developed, and thus its possibilities for integration and cost effectiveness led the SOA to become a competitive component in comparison to the EDFA. The design of SOAs developed in two directions: as a linear amplifier, it is needed to reduce optical nonlinearities of SOA and as a nonlinear medium; the nonlinear effects should be exploited for use in variety of applications such as all-optical signal processing. The advantages of SOAs are their versatility and possibility of monolithic integration with other optical components like passive waveguides and couplers to perform more complex functions. They are compact, electrically pumped and have a large optical bandwidth. Moreover, they allow a wide flexibility in the choice of the gain peak wavelength. In linear operation such as a power booster, as an inline amplifier and as a preamplifier EDFAs are the dominant amplifiers specially in long-haul systems as they have lower noise levels and much better crosstalk properties for multi-channel amplification in comparison to SOAs. However, the SOA offers a cost competitive alternative to the EDFA

A. Rostami et al., *Nanostructure Semiconductor Optical Amplifiers*,
Engineering Materials, DOI: 10.1007/978-3-642-14925-2_1,

when used as an inline amplifier in metro networks, as a power booster and as a preamplifier. Also, in nonlinear operation they can perform all-optical signal processing due to their strong nonlinearities and their fast dynamics.

Advent of new SOA generation in the last decade (i.e. quantum well-SOAs and quantum dot-SOAs) has promised enormous improvements over traditional bulk-SOAs. SOAs with quantum wells or dots in their active region have presented higher output power, lower threshold current, good temperature stability, lower noise characteristics and interesting nonlinear properties compared with bulk SOAs. Quantum-dot SOAs (QD-SOAs) specially have attracted great interest recently due to interesting specifications of quantum dots and have developed along with quantum dot lasers in recent years. Low-threshold current, high output saturation power, fast gain dynamics and low noise level of QD-SOAs have been proved and it has emphasized that these elements can be utilized as building blocks of all-optical systems. Multi-channel operation capability of QD-SOAs such as multi-channel amplification and wavelength conversion provides a great chance for development of WDM network as well as demonstration of all-optical networks.

In this chapter, a brief overview of the operation principles of SOAs will be given and to prevent presentation of redundant subjects in the field of SOAs that have previously discussed in other valuable and outstanding books, specifications of QD-SOAs will be introduced as the main roadmap of this chapter. Optical properties of QD-SOAs, fabrication methods, polarisation-sensitivity, and properties of doped QD-SOAs are the main subjects that will be covered during the next pages.

1.2 Operation Principles

The operation principle of the SOA lies in the creation of an inversion in the carrier population used to amplify the input optical signal via stimulated emission. The population inversion is achieved by electric current injection into the SOA. Figure 1.1 shows the simplified band structure of a direct-gap semiconductor. The conduction band and the valence band are separated by the band-gap energy E_g. The current injection leads to free electron–hole pair generation in the conduction band and valence band, respectively. In quasi-equilibrium the relaxation times for transitions within either of the bands are much shorter than the relaxation time between the two bands. So, the carrier distribution within each band can be described by two quasi-Fermi levels denoted by E_{fc} and E_{fv}. The position of the quasi-Fermi levels is determined by the current injection. If the current injection is sufficiently large the separation between the quasi-Fermi levels exceeds the band-gap energy ($E_{fc} - E_{fv} > E_g$) and the semiconductor acts as an amplifier for optical frequencies (ν) with $E_g < h\nu < E_{fc} - E_{fv}$. The absorption process dominates over stimulated emission for photon energies larger than $\Delta E_f = E_{fc} - E_{fv}$ ($h\nu > \Delta E_f$) and the material acts as an attenuator [1].

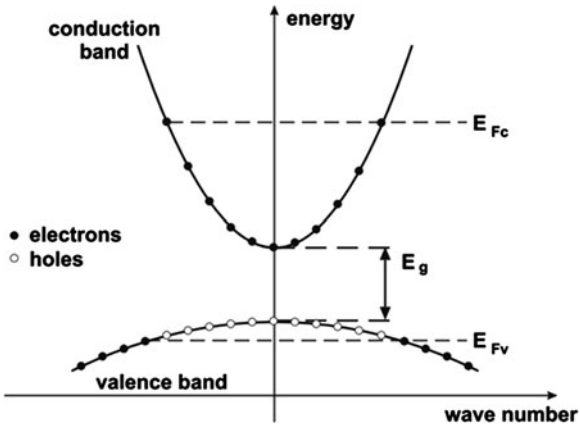

Fig. 1.1 Simplified band structure of a direct band-gap semiconductor in quasi-equilibrium [1]

In a QD-SOA, an optical signal pulse with a wavelength resonant to the GS can be amplified due to stimulated recombination of the GS excitons which lead to GS carrier depletion and consequently the empty states are refilled by fast carrier relaxation from the ES.

This fast relaxation from ES to GS is a result of two features: the large energy splitting between the dot levels which ensure slow thermal excitation of carriers, and a high WL carrier density resulting in fast Auger-assisted relaxation. Thus, the ultrafast gain recovery is achieved by the ES level, which acts as a nearby carrier reservoir for the GS level. This recovery time can occur in very short time scale (e.g. 140 fs) [2, 3].

The next optical pulse can only be amplified if the gain has recovered after the first optical excitation. The ultrafast gain recovery following a single pulse excitation is promising for QD-SOA-based ultrafast all-optical signal processing in the Tb/s range. However, since the carrier capture process from the WL into the dot is slower than intradot relaxation, the ES level recovers on a longer time-scale ($\sim$picoseconds). The refilling rate of the WL is much longer and is essentially determined by the injection current and the spontaneous recombination rate of the WL and occurs in $\sim$nanosecond time scale. A schematic of QD-SOA structure including the waveguide structure based on GaAs substrate, p-doped and n-doped cladding layers and QD stacks as active region is illustrated in Fig. 1.2. Also, the energy band diagram of a sample QD in Fig. 1.2 illustrates the amplification mechanism in a QD amplifier.

1.3 SOA Gain

The gain of the SOA results from transitions between the conduction and valence bands which depend on the carrier density and distribution in both bands.

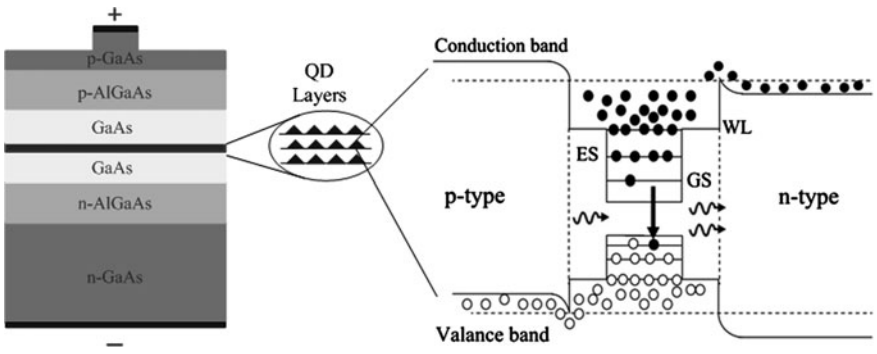

Fig. 1.2 GaAs-based waveguide structure of a QD-SOA including n and p cladding layers and multi-layer QD active region. Energy band diagram of a sample QD is also sketched

There dynamical processes that determine the gain variation after propagating an optical pulse through the SOA can be categorized into interband and intraband classes and the gain coefficient may be described as a combination of these processes

$$g = \underbrace{g_{CDP}(N)}_{interband} + \underbrace{g_{CH}(N,T) + g_{SHB}(N,T)}_{intraband} \tag{1}$$

where g_{CDP} (carrier density pulsation) is due to interband processes (e.g. spontaneous emission, stimulated emissions and absorption) depended on the carrier density whereas g_{CH} and g_{SHB} are because of the intraband processes (e.g. carrier heating and spectral hole burning). The interband dynamic refers to the exchange of carriers between the conduction band and the valence band which affects the carrier density and the interband energy gap determines the recovery of the carrier density (N) which is a slow process with a time constant in the range of several tenths of picoseconds. This time constant depends on the SOA geometry and the operating conditions. Interband mechanism dominates the SOA dynamics when long optical pulses are used.

On the other hand, when the SOA is operated using pulses shorter than few picoseconds, intraband effects become important. They change the electron distribution within the conduction band and the hole within the valence band. When a short optical pulse arrives to the SOA, it interacts with only a certain part of the carrier distribution, depended on the photon energy and the spectral width of the pulse. The pulse causes a reduction (hole) in the carrier distribution at the particular photon energy (a deviation from the Fermi distribution). This effect is called the spectral hole burning (SHB). The time τ_{SHB}, which is the time needed to restore the Fermi distribution by scattering processes (mainly carrier-carrier scattering), is typically several tens of femtoseconds. Carrier heating process (CH) tends to increase the temperature of the carrier distribution above the lattice temperature. The distribution cools down to the lattice temperature through phonon emission. The CH recovery time τ_{CH} is several hundreds of femtoseconds to a

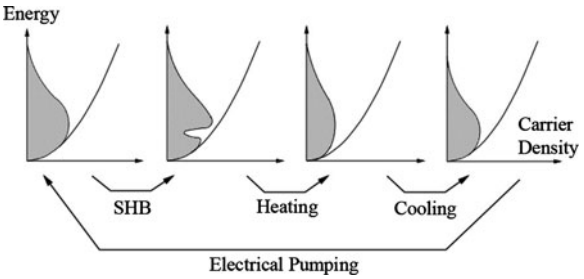

Fig. 1.3 Temporal evolution of conduction band free carrier density distribution after exciting by a picosecond optical pulse

few picoseconds. The evolution processes of conduction band free carrier distribution after exciting by a picosecond pulse are schematically illustrated in Fig. 1.3. As it was justified, the average temperature of carriers increase when the optical pulse leaves the SOA, meanwhile the carrier cooling process with a time constant of τ_{CH} redistribute the Fermi distribution to the initial condition and the electrical current injection refills the empty states of the lost carrier.

The gain of an amplifier (bulk, QW, or QD-SOA) can be generally defined as

$$G = \frac{P_{out}}{P_{in}} \tag{2}$$

where the input and output optical powers of the amplifier are denoted by $P_{in} = P$ $(z = 0)$ and $P_{out} = P$ $(z = L)$. The amplifier length in the growth direction (z) is given by L. The propagation of light power along the z-axis in an amplifying medium can be described by

$$\frac{dP}{dz} = gP \tag{3}$$

The solution of the above equation for a constant gain g is in the form of $P(z) = P_{in} \exp(gz)$ which results in the amplifier Gain by extracting output power at $z = L$ as

$$G = \exp(gL) \tag{4}$$

Since the optical gain depends on the input signal intensity and frequency, it is common to model the frequency-dependant gain coefficient with a homogeneously broadened two-level system

$$g(\omega) = \frac{g_0}{1 + (\omega - \omega_0)^2 T^2 + P/P_S} \tag{5}$$

where g_0 is the maximum value of the gain, ω is the optical angular frequency of the incident signal, ω_0 is the atomic transition angular frequency, T is the dipole relaxation time (typically ~ 0.1 ps in bulk semiconductors), P the optical power of the incident signal and P_S is the saturation power of the gain medium. Thus, the

frequency-dependant relation between the amplifier gain G and the optical gain g can be written as $G(\omega) = \exp(g(\omega)L)$. For input signal powers much smaller than the saturation power ($P \ll P_S$), the gain coefficient reduces to

$$g(\omega) = \frac{g_0}{1 + (\omega - \omega_0)^2 T^2} \tag{6}$$

which describes a Lorentzian-shape gain spectrum with maximum at $\omega = \omega_0$. The optical gain bandwidth is defined as the full-width-at-half-maximum (FWHM) of the gain spectrum given by $\Delta v_g = \Delta\omega_g/2\pi = 1/\pi T$. Hence, the amplifier bandwidth (FWHM of $G(\omega)$) can be obtained through Eq. 4

$$\Delta v_a = \Delta v_g \left(\frac{Ln\,2}{g_0 L - Ln\,2} \right) \tag{7}$$

It is clear from the above equation that the amplifier bandwidth is smaller than the optical gain bandwidth due to the exponential dependence of the amplifier gain to the optical gain. Also, this simplistic model of a homogeneously broadened two-level system cannot be applied to QD-SOAs with inhomogeneously broadened gain spectrum.

1.3.1 Gain Saturation

Increasing the input signal power to the amplifier will result in depletion of the carriers in the active region and consequently decreasing the amplifier gain. This fact is referred as gain saturation which is common between amplifiers and lasers and leads to signal distortion. A typical SOA gain versus output signal power characteristic is displayed in Fig. 1.4 where the 3 dB saturation power is defined as the amplifier output power at which the amplifier gain is half the small-signal gain. Combining Eqs. 3 and 5 at the maximum gain frequency, $\omega = \omega_0$, yields

$$\frac{dP}{dz} = \frac{g_0 P}{1 + P/P_S} \tag{8}$$

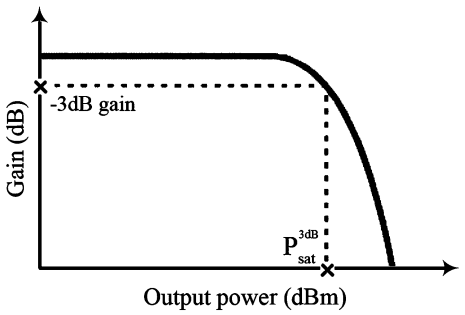

Fig. 1.4 SOA gain characteristic versus output signal power

The solution of the above equation when P is comparable to P_S, (large signal) will result in the amplifier gain given by

$$G = G_0 \exp\left(-\frac{G-1}{G}\frac{P_{out}}{P_S}\right) \tag{9}$$

where $G_0 = \exp(g_0 L)$ is unsaturated gain at small input powers. According to the definition presented above for 3 dB saturation power, $G(P_{sat}^{3dB}) = G_0/2$, one can obtain

$$P_{sat}^{3dB} = \frac{G_0 Ln2}{G_0 - 2} P_S \tag{10}$$

In bulk and QW amplifiers the peak gain depends linearly on first order carrier density given by

$$g = (\Gamma a/V)(N - N_0) \tag{11}$$

where Γ is the confinement factor, V is the volume of the active region, N_0 is the transparency carrier density and a is the differential gain coefficient (a = dg/dN). The carrier density rate equation can then described by

$$\frac{dN}{dt} = \frac{I}{q} - \frac{N}{\tau_e} - \frac{a(N - N_0)}{\sigma_m h v} P \tag{12}$$

where I, P, τ_e, σ_m and v are injection current, input signal power, carrier lifetime, effective cross section of the waveguide node and input signal frequency, respectively. For $t \gg \tau_e$ (CW operation), Eq. 12 may find stationary solution ($dN/dt = 0$). By substituting the obtained carrier density in Eq. 11, the gain saturation and saturation power in bulk and QW amplifiers, g and P_S, can relate to each other through

$$\begin{aligned} g &= \frac{g_0}{1 + P/P_S}, \quad g_0 = (\Gamma a/V)(I\tau_e/q - N_0) \\ P_S &= \frac{h v \sigma_m}{a}\frac{1}{\tau_e} \end{aligned} \tag{13}$$

Using a 2-level rate equation model for QDs in CW operation mode, the saturation power in the limit of high-inversion condition under high current density where the QD states and the WL band edge are completely filled, can be expressed by [4]

$$P_S^{HI} = \frac{h v \sigma_m}{a}\left(\frac{1}{\tau_C} - \frac{1}{\tau_G}\right) \tag{14}$$

where τ_C and τ_G are the characteristic capture time and spontaneous recombination lifetime of the GS which are typically $\sim$2 ps and $\sim$1 ns respectively. Thus, SHB of the WL (capture time into dot states) determines the saturation power. In the

above approximation the WL band edge is assumed to be completely filled while this condition is not fulfilled due to thermal degradation or lasing. It can be concluded by comparing Eqs. 13 and 14 for bulk, QW, and QD amplifiers that a much larger saturation power is expected for QD-SOAs since the carrier capture time is much smaller than the carrier lifetime.

It might be worthy to note that the dominant gain saturation mechanism in QD-SOAs can be either SHB or total carrier density depletion (TCDD) depending on the injection current density and input signal power [5]. In small injection currents compared with the signal power the QD states are mostly empty due to amplification process and the gain recovery is achieved through injection current after several carrier capture and escape processes via the common carrier reservoir of the QW-like capping layer since the carrier relaxation processes are incoherent. This gain saturation process is known as TCDD and occurs in bilk or QW-SOAs with a typical recovery time of ~ 0.1–1 ns [6]. In high injection currents compared with the signal power, the QD states are relatively full and the removed carriers through stimulated recombination are replaced from the ES or the WL states. Therefore, the gain saturation in the signal wavelength is attributed to SHB which recovers in less than a few picoseconds [7].

1.3.2 Confinement Factor

Since the optical mode inside an amplifier overlaps partly with the active region, a parameter is defined to determine the fraction of the overlapped mode which is known as confinement factor, Γ, and is different for bulk, QW, and QD active regions. For a QD array the confinement factor can be separated to in-plane and vertical parts given by

$$\Gamma = \overbrace{\frac{N_A N_D}{\mathrm{A}}}^{in-plane} \times \overbrace{\frac{1}{\mathrm{A}} \frac{\int \int_A \int_{dot} |E(z)|^2 dz}{\int_{-\infty}^{+\infty} E(z)|^2 dz}}^{vertical} \tag{15}$$

where N_D is the number of QDs in one layer with an average in-plane size of A_D in an area of A. The vertical overlap of the QDs and optical mode (optical field E) along the vertical direction z determines the vertical part of the confinement factor. The reported values for confinement factors in QD arrays are $\sim 10^{-3}$–10^{-4} while this value can be much larger in bulk materials.

The confinement factor is an important parameter in SOAs which relates the material gain of QDs, g_{mat}, to easily measurable modal gain, g_{mod}, via $g_{mod} = \Gamma g_{mat}$. Due to lower confinement factor and larger spectral width, the modal gain in QDs is about one order of magnitude smaller than QWs. Also, the optical gain for the transverse electric (TE) and transverse magnetic (TM) modes differs because the TE and TM modes have different confinement factors and therefore, SOAs generally exhibits a polarization dependence of gain.

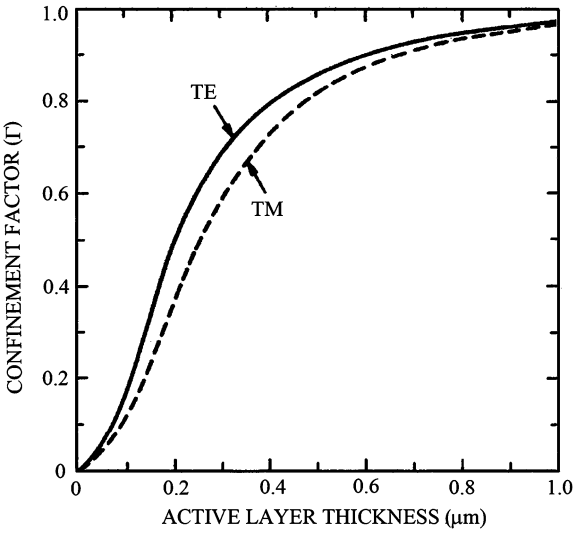

Fig. 1.5 Confinement factor of the fundamental TE and TM modes versus active layer thickness for a bulk InGaAsP waveguide with InP cladding layers at $\lambda = 1.3$ μm [8]

Figure 1.5 presents typical Γ values as a function of active layer thickness for the $\lambda = 1.3$ μm InGaAsP double heterostructure with p-InP and n-InP cladding layers for TE and TM modes.

1.4 Refractive Index

Refractive index and specially its dynamics provides a suitable tool to study the population variations of states involved in optical transitions non-resonant to the exciting optical pulses and therefore gives complementary information about gain dynamics in QD-SOAs. Because of the applications and opportunities for SOAs in nonlinear operations, a deep understanding of refractive index dynamics would be beneficial especially for high-speed applications such as all-optical signal processing. One can divide recent nonlinear applications of QD-SOAs into two main categories: gain nonlinearity-based applications such as cross-gain modulation and refractive index nonlinearity-based applications like cross-phase modulation. Interferometer-based QD-SOA structures are good examples to demonstrate ultrafast cross-phase modulation with low patterning effect [9]. This feature have became possible because of a decoupling of gain and refractive index modulation mechanisms occurring under high electrical injection which would allow a phase change experienced by a probe beam (e.g. in pump-probe experiment) being dominated by non-resonant transitions in the excited state and wetting layer without a change of the SOA gain by a control pulse.

The refractive index dynamics can be obtained from the phase change, ΔΦ, of an input signal injected to SOA through

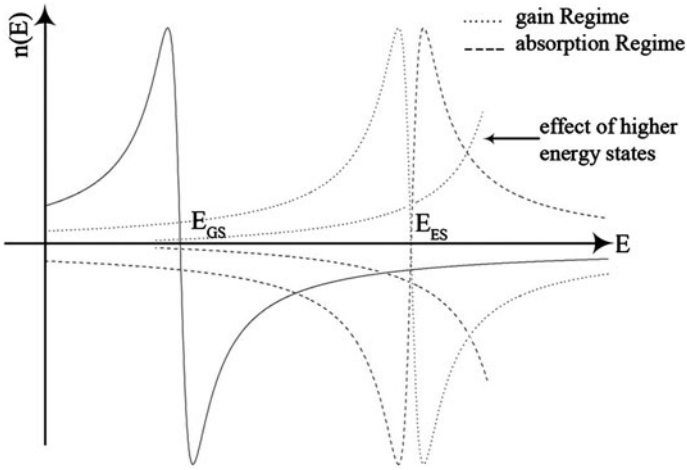

Fig. 1.6 Refractive index alteration due to the GS (*solid curve*), ES and higher energy states transitions (*dashed curve* for absorption regime and *dotted curve* for gain regime)

$$\Delta n = \frac{\lambda}{2\pi L}\Delta\Phi \tag{16}$$

where L is the amplifier length and λ is the signal wavelength. Figure 1.6 depicts the role of different transitions to the refractive index. A non-resonant transition from the GS to the ES gives a negative contribution to the refractive index.

When the GS is empty, a pump beam can promote carriers in the GS (absorption regime) and thus thermal excitation of carriers to the ES lead to an increase in the ES population seen by a probe beam which corresponds to a negative refractive index change or a negative change in the probe phase. Contrary, depletion of the GS carriers by a pump beam followed by carrier relaxation from the ES to the GS (gain regime) will cause a reduction in the ES population and hence gives a positive contribution to refractive index (a positive probe phase change). For the transitions between the GS and the WL, the refractive index changes with smaller amplitude because of higher energy distance as schematically depicted in Fig. 1.6.

1.5 Linewidth Enhancement Factor

An important parameter for the performance of semiconductor optical amplifiers and lasers is the linewidth enhancement factor (LEF), also called α-parameter (α_H). It is defined as the ratio between the change of the refractive index and gain (real and imaginary parts of the susceptibility), induced by the carrier-density (N) change. This parameter not only affects the linewidth of a semiconductor amplifier

and laser but also directly connects to the chirp, i.e. the change of emission wavelength during a change of the carrier density. The physical origin of this shift is related to the coupling of the real and imaginary parts of the complex susceptibility in the gain medium. A variation of gain due to a change of carrier density N leads to a variation of the refractive index that modifies the phase of the optical mode in the laser cavity. The coupling strength is defined by the linewidth enhancement factor via the expression [10]

$$\alpha_H = -\frac{4\pi}{\lambda}\frac{dn}{dN}\Big/\frac{dg}{dN} = -\frac{4\pi}{\lambda}\frac{\Delta n}{\Delta\Gamma g} \tag{17}$$

where Δn and ΔΓg are the density-induced variations of the modal refractive index and of the modal gain, λ is the light wavelength and g is the material gain respectively. A high value of α_H leads to self-focusing and therefore to filamentation, which limits the performance of high-power semiconductor lasers. In SOAs, the LEF has become a powerful tool for predicting the nonlinear phase shift observed in connection with gain nonlinearities.

In the ideal case of a perfect Gaussian energy distribution the gain spectrum is perfectly symmetric around the peak gain energy and $\alpha = 0$, i.e. chirp-free. Yet, due to the influence of the carrier density and thermal effects due to heating, the linewidth enhancement factors is neither constant nor zero. Values between 0 and 10, and even negative values have been reported depending on the measurement method and the operating condition.

Quantum dot based amplifiers in principle offer the potential to achieve zero LEF due to their atom-like density of states which results in a symmetric gain spectrum. Recent measurements of the LEF in InGaAs/GaAs QD lasers and amplifiers have indicated values of α_H below 1, however only at low injection currents near/below transparency or at low temperatures [11, 12]. A smaller LEF at photon energies above the GS, eventually reaching even negative values above the ES, was also observed [11]. The role of p doping on the α_H parameter of QD lasers was investigated recently [13]. It was predicted that p doping would result in a lower LEF near threshold.

Measuring the amplitude and phase of a probe pulse transmitted through the amplifier in the pump-probe differential transmission experiment allows the calculation of the LEF according to the definition in Eq. 17. In this experiment a pump pulse induces carrier density change in the active region of the amplifier and a delayed weak probe pulse experiences these changes. By measuring the transmitted amplitude (phase) of the probe pulse in the presence and without pump pulse respectively denoted by $T(\Phi)$ and $T_0(\Phi_0)$, the differential gain, ΔG, and phase, ΔΦ, can be expressed as

$$\begin{aligned} \Delta G\ (\mathrm{dB}) &= 10.\log_{10}\left(\frac{T}{T_0}\right), \\ \Delta\Phi\ (\mathrm{rad}) &= \Phi - \Phi_0 \end{aligned} \tag{18}$$

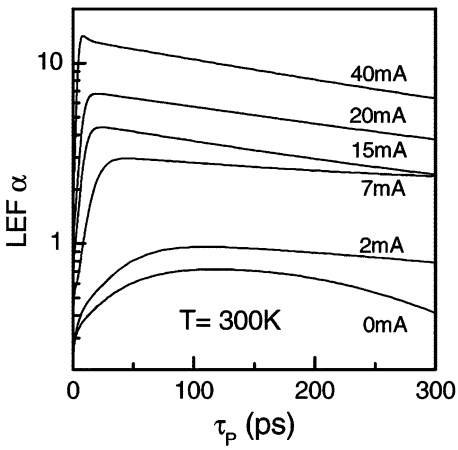

Fig. 1.7 LEF at the ground state transition of InGaAs QD amplifier as a function of pump-probe relative delay for different bias currents [11]

where $T/T_0 = \exp(\Delta g_{\text{mod}} \text{ L})$ and the LEF can then be calculated through [11]

$$\alpha = -20 \cdot \log_{10}(e) \frac{\Delta\Phi\,(\text{rad})}{\Delta G\,(\text{dB})} \tag{19}$$

Since increasing the amplifier bias current leads to increase in carrier density, it is expected that higher injection current result in enhanced LEF. Typical LEF curves as a function of temporal delay between pump and probe pulses (τ_P) in differential pump-probe experiment for an InGaAs QD amplifier [11] is depicted in Fig. 1.7 which proves the effect of increased bias current.

In this experiment the probe signal is in resonant with GS transition of the amplifier. For law injection currents, the LEF of the QD ground state interband transition is between 0.4 and 1, and increases with carrier density as illustrated. The resonantly modified carrier density due the presence of the pump pulse redistributes toward equilibrium carrier density and this phenomenon leads to transient dynamics of LEF as it is obvious. Also, the initial fast and final slow dynamics of the curves are attributed to thermalization inside QDs (which fastens with carrier density due to enhanced Auger processes) and thermalization among the QDs and with the WL, respectively.

1.6 Comparison of Operating Characteristics

In order to investigate the optical characteristics of QD-SOAs and compare different parameters with bulk and QW-SOAs, here a discussion based on the framework of Berg and Mørk [14] will be presented. Figure 1.8 shows a schematic of QD-SOA structure consisted of a ridge waveguide and an active region with characteristic sizes of L, W, H representing the length, the width and the height of the device. The active region includes N_{lay} number of QD layers which are grown

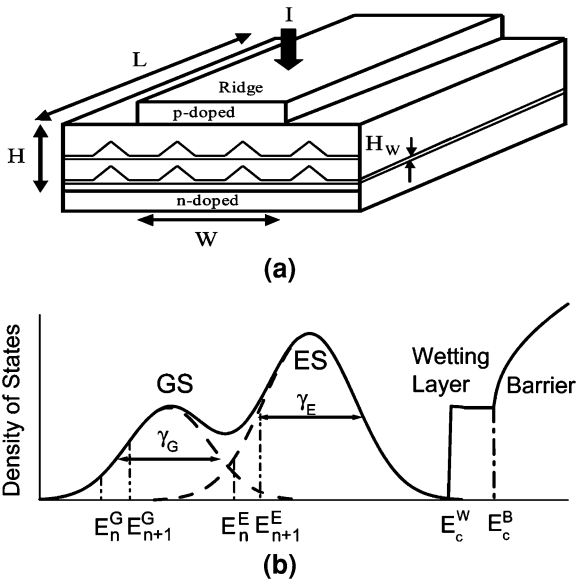

Fig. 1.8 **a** Schematic of a QD-SOA structure, **b** conduction band density of states [14]

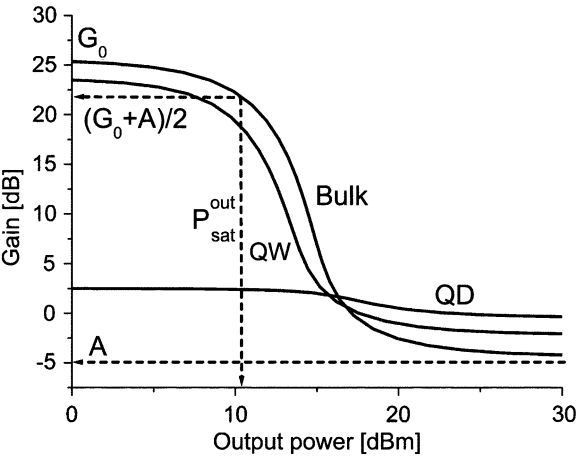

Fig. 1.9 Gain versus output power curves of bulk, QW and QD-SOA for injection current densities of 10 kA/cm^2 (bulk SOA), 4 kA/cm^2 (QW-SOA) and 2 kA/cm^2 (QD-SOA). Device lengths are 0.5 mm [14]

on a narrow WL (a quantum well with width of H_W and volume of V_W) and the coupling between the layers are neglected due to separation barrier. Each QD has a spin-degenerate GS and a fourfold degenerate ES with FWHM inhomogeneous broadenings of γ_G and γ_E, respectively. The conduction band density of states (DOS) for dot states, QW-like WL and bulk-like barrier is also depicted in Fig. 1.8b.

According to the presented model, a bulk SOA and a QW-SOA can be modeled by barrier material and WL plus barrier model of the QD case. A comparison of small signal gain for different SOA types is presented in Fig. 1.9 where the bulk

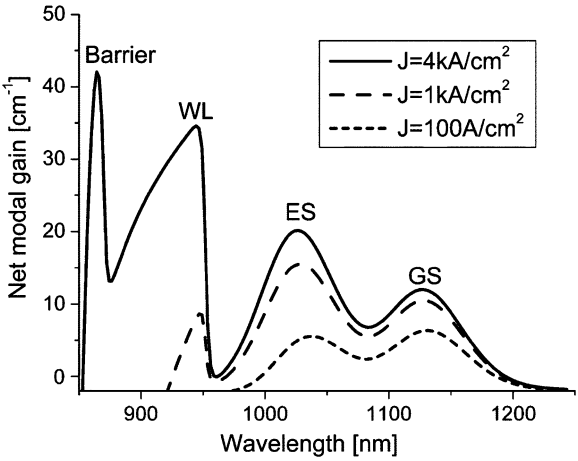

Fig. 1.10 Gain spectrum of QD-SOA at three different injection current densities [14]

SOA exhibits larger small signal gain compared to the other types. However, due to smaller carrier masses (meaning that there are fewer states in QW compared with bulk material) and the step-like DOS, QW device has higher inversion at much lower currents compared with the bulk device. Thus, the gain of QW-SOA is just slightly smaller than bulk SOA. For the case of QD-SOA, fewer states than QW lead to easier conversion while the maximum modal gain of QD limits the small signal gain. This is due to lower confinement factor and larger spectral width of QDs as discussed before. The modal gain spectrum of the QD-SOA presented in Fig. 1.10 proves this fact as the higher modal gain of the WL is obvious compared with the GS.

By increasing the input signal power, the amplifier gain saturates and in the gain transparency region the device gain is determined by the waveguide loss, $A = \exp(-\alpha L)$. The saturation output power (SOP) can be obtained from the gain-output power curve of Fig. 1.9 as it was discussed before. However, since the small signal gain of the QD-SOA is smaller than 3 dB, a new definition instead of the former definition i.e. $G(P_{sat}^{3dB}) = G_0/2$ should be used. Therefore, a more general gain saturation definition is defined by $G(P_{sat}^{3dB}) = (G_0 + A)/2$. Figure 1.11 provides a better understanding of the SOP of three different SOAs as the injection current increases. Increasing the injection current in the case of QD-SOA provides increased degree of band filling of the ES, WL and barriers and hence, inversion occurs more efficiently. In this case the saturating mechanism is the finite capture time of carriers from the WL to the ES which is typically ~ 2 ps.

Although the SOP determines the peak or average signal power which saturates the amplifier, but the operation of different amplifiers in the high-current saturation region differ. In the case of QD-SOA working in saturation region under high injection current, a high power signal may deplete the gain however it will recover in a short capture limited timescale which ensures that the input signal pattern won't affect the output signal (pattern-effect free operation). Thus, for input data rates below the inverse of capture time the output will be distorted a little. On the

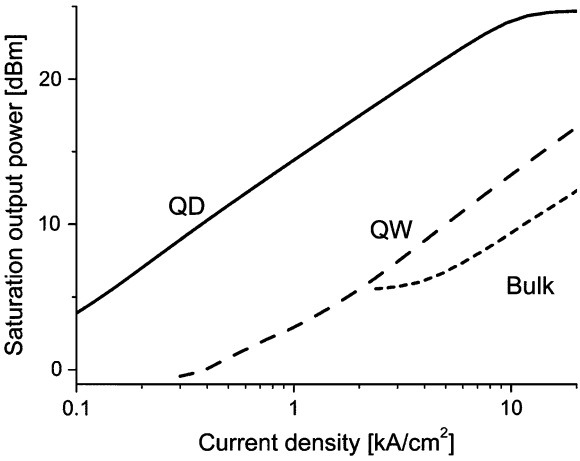

Fig. 1.11 Saturation output power as a function of injection current density for bulk, QW and QD-SOA (device length is 0.25 mm) [14]

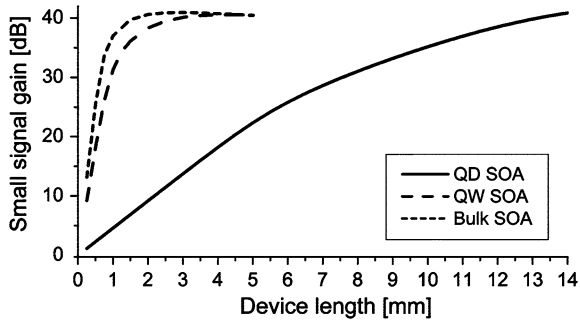

Fig. 1.12 Small signal gain versus device length curves of bulk, QW, and QD-SOAs at injection currents of 1 kA/cm^2 (QD-SOA), 2 kA/cm^2 (QW-SOA) and 10 kA/cm^2 (bulk SOA) [14]

other hand, the gain recovery in bulk and QW-SOAs is limited due to carrier lifetime (hundred of picoseconds) and increasing the injection current enhance the SOP which is still much lower than the SOP of QD-SOA as depicted in Fig. 1.11.

Unlike significantly high saturation power of QD-SOA compared with the other types, the small signal gain of this amplifier is one of the main challenges as presented in Fig. 1.9. Increasing the device length may compensate this deficiency and provide much larger gain. Due to nature of band filling in QDs, the optimum signal wavelength is nearly independent of device length. In spite of this, smaller modal gain of QD-SOAs leads to slow increase of device gain with length. This feature is depicted in Fig. 1.12 where for devices longer than a specific length, the gain saturation occurs just similar to bulk and QW-SOAs. Increasing the QD layers can also enhance the modal gain, but a higher bias current is required to provide the same level of inversion and therefore, the same SOP. However, it should be considered that by achieving to higher modal gain through increasing the QD layers, the device length can be shortened to reach the same device gain leading to unchanged bias current density.

1.6.1 Amplified Spontaneous Emission

Amplified spontaneous emission (ASE) is one of detrimental parameters for operation of SOAs which is caused by spontaneously emitted photons (without applying any input signal to the amplifier) travelling along the amplifier active region and being amplified. The ASE spectrum is a good measure of the position of the gain peak, FWHM of the gain curve and the gain ripple caused by the residual reflectivity of the facets. ASE is usually considered as noise, which degrades the SOA performance. If the spontaneous emission photons happen to be emitted close to the direction of travel of the signal photons, they will interact with the signal photons, causing both amplitude and phase fluctuations. Thus, the measured power of the amplifier output consists of both amplified signal power and the ASE power as noise which degrades the output signal-to-noise ratio (SNR). Also, ASE depletes carriers in the active region and hence, limits the maximum achievable device small signal gain and increases the stimulated recombination rate.

However, the ASE can also be useful as an intense and broadband optical source. Experimentally the ASE is the easiest optical SOA characteristic to be measured. This aspect makes the ASE interesting for testing purposes. In measuring SOA characteristics through ASE spectra no external signal has to be used and the access to only one chip facet is required. Moreover, the ASE simplifies considerably the procedures to adjust the optics to couple in and out the light from the SOA chip.

ASE plays an important rule specially in long amplifiers where more ASE is generated and the inversion is depleted. Thus, in long amplifiers the ASE saturates the device gain and cause the noise figure enhancement. Also, ASE increases the SOP with increasing the device gain. A comparison between the SOP of three SOAs as a function of device length and injection current as a parameter is shown in Fig. 1.13. The increase of the SOP with device length in bulk and QW-SOAs is

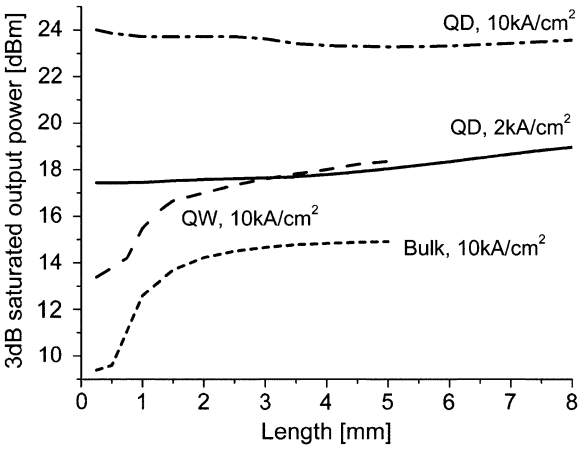

Fig. 1.13 3 dB saturation output power as a function of device length for bulk, QW and QD-SOA [14]

attributed to increased ASE and hence, decreased stimulated recombination time which results in increased SOP as described above. For QD-SOA, however, two different behaviors are observed. At lower bias current, the effective carrier lifetime decrease with device length whereas at higher current, the SOP is limited by the capture time instead of the carrier lifetime. Therefore, in the latter case the SOP not only does not increase further with device length but also decrease slightly due to highlighted waveguide losses when the ASE reduces the modal gain toward the end of the device in long QD amplifier. This behavior for QD-SOA at two different bias current levels is depicted in Fig. 1.13.

Strong ASE intensity leads to gain saturation in long amplifiers in the absence of input signal. It can be proved that the ASE power at each wavelength is proportional to the gain at that wavelength and hence, when the ASE power becomes comparable to the saturation power in long devices the gain tends to saturates.

1.6.2 Noise Figure

The noise added to the signal during the amplification is one of the important characteristics of optical amplifiers that can be quantified using a parameter called noise figure (NF). The NF is defined as the ratio of the input SNR to the output SNR in logarithmic units, $NF = 10 \log_{10} (SNR_{in}/SNR_{out})$, measured using an ideal receiver (i.e. with unity quantum efficiency) and a shot-noise limited input signal [15]. The term (SNR_{in}/SNR_{out}) is also called noise factor represented by F. $\mathrm{SNR_{in}}$ is defined as $SNR_{in} = P_{in}/2\hbar\omega$ where $\hbar$ is the Planck's constant, ω is the input signal frequency and P_{in} stands for shot-noise limited input signal. The added noise on the output signal can be categorized into shot noise, signal-spontaneous beat noise, spontaneous–spontaneous beat noise, and multipath interference noise (MPI). Sometimes additional noise sources are considered, such as noise caused by signal polarisation fluctuations especially in polarisation gain dependent amplifiers, and noise originating from the electrical pumping mechanism. The shot noise itself can be divided into the shot noise from the signal and from the ASE which can be expressed in terms of amplifier gain at input wavelength, G, and output ASE power, P_{ASE}, given by

$$F_{shot,sig} = \frac{1}{G} \tag{20}$$

$$F_{shot,ASE} = \frac{P_{ASE}}{G^2 P_{in}} \tag{21}$$

The beating between the signal and the ASE spectral components and among the ASE components themselves, which degrade the output SNR, is considered as the beat noise in optical amplifiers. The beat noise is attributed to fluctuations in the stimulated emission [16] in quantum theory or the noise appeared at detector's

output due to dependency of photocurrent to the square of the optical field in classical theory both given by

$$F_{sig.-sp.} = \frac{2\rho_{ASE}^{\parallel}}{\hbar\omega G} \tag{22}$$

$$F_{sp.-sp.} = \frac{1}{2\hbar\omega G^2 P_{in}} \int (\rho_{ASE,TE}^2 + \rho_{ASE,TM}^2)\, dv \tag{23}$$

where $\rho_{ASE}^{\parallel}$ is the ASE power spectral density (in W/Hz) and, $\rho_{ASE,TE}$ and $\rho_{ASE,TM}$ are the ASE power spectral densities in the TE and TM polarisation respectively.

The MPI noise is the other important noise which arises from multiple reflections in the signal path mainly due to residual facet reflectivity of SOA. Thus, if a small fraction of the emitted ASE is reflected back into the active region and is amplified, the total emitted ASE intensity will increases. For SOAs with low facet reflectivities the MPI can be neglected. Summation of each of the mentioned noise components will result the total F as

$$F = F_{shot,sig} + F_{shot,ASE} + F_{sig.-sp.} + F_{sp.-sp.} + F_{MPI} \tag{24}$$

The first term of above definition corresponds to the amplified input noise while the other terms represent the noise added by the amplifier. By filtering the ASE around the signal before detection, the second and the fourth terms of Eq. 24 can also be neglected and the expression reduces to

$$F = \frac{1}{G} + \frac{2\rho_{ASE}^{\parallel}}{\hbar\omega G} \tag{25}$$

In practical applications the second term (signal-spontaneous beat noise) is often dominant when the device gain is above a few decibels.

A comparison of NF behavior of three different SOAs as a function of device length is presented in Fig. 1.14 which corresponds to the small signal gain curves depicted in Fig. 1.12. Since the gain of QD-SOA at short devices is very low (see Fig. 1.12) hence, the corresponding NF is low too. However, for the longer devices the NF still remains low with a slight increase. This feature of QD-SOA relates to nearly complete inversion of active states of QDs.

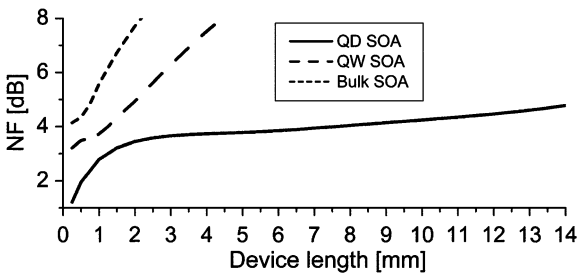

Fig. 1.14 Noise figure versus device length curves of bulk, QW, and QD-SOAs at injection currents of 1 kA/cm^2 (QD-SOA), 2 kA/cm^2 (QW-SOA) and 10 kA/cm^2 (bulk SOA) [14]

On the other hand, in bulk and QW-SOA due to the higher gain at shorter lengths, ASE saturates the device faster and the NF increase faster than QD-SOA.

1.7 Polarization Properties

One of the main challenges in designing state of the art QD-SOAs is the optical gain sensitivity to polarization of light, i.e. QD-based SOAs exhibit optical gain only for TE-polarized light but no for TM-polarized light. This is a common feature for quantum dots grown by Stranski–Krastanov (S–K) method attributed to half-oval shape of dots and bi-axial compressive strain imposed in this method. This sensitivity to light polarization limits application of QD-based devices grown by S–K method considering the fact that the polarization of optical signals is generally random in fiber communication. Polarization-insensitive operation in data transmission systems (as booster and in-line or pre-amplifiers) has been one of the technologically demanded features of SOAs with bulk, quantum-well or quantum dot active regions. The difference of the confinement factor for the TE and TM-modes in the waveguide and different amplification of the two polarizations in the gain region (active region), are main reasons of polarization-sensitivity of SOAs.

As a general rule, QDs with smaller transition energies between electrons and light holes than transition energies between electrons and heavy holes are more sensitive to TM-mode light than TE-mode light. In the other words, heavy-hole band to conduction band transitions respond only to an electric field with in-plane polarization due to transition selection rules. In comparison, degeneracy of HH and LH bands in bulk material, results in a polarization-insensitive material gain while in QW SOAs different quantization levels lead to polarization-sensitive gain. Reducing the difference in the confinement factor between TE and TM polarizations by thickening the active layer in bulk SOAs and introducing an anisotropic gain coefficient of the active layer in QW SOAs may lead to polarization-insensitive operation. Since the hydrostatic strain, the material, and the size of the QDs change the energy gap between the conduction and valence bands and also the deformational strain determines the extent of splitting between heavy- and light-hole bands, adjustment of the strain profile affects the light-polarization-sensitivity in QD structures as well as QD-based devices. It is known that the hydrostatic strain and biaxial strain components result in deformation in crystal unit cells which can be associated with volume change in the case of hydrostatic strain and change of the axial ratio in the presence of biaxial strain. The biaxial strain also determines the relative HH- and LH-bands energy. Defining these strains with $\varepsilon_{hydrostatic}$ and $\varepsilon_{biaxial}$, the HH and LH energy levels can describe by $E_{HH}(r) = a_v\ \varepsilon_{hydrostatic}(r) + b/2\ \varepsilon_{biaxial}(r)$ and $E_{LH}(r) = a_v\ \varepsilon_{hydrostatic}(r) - b/2\ \varepsilon_{biaxial}(r)$, with r being the radial vector and a_v and b as hydrostatic and biaxial potential of valence band. Introducing the biaxial strain by $\varepsilon_{biaxial}\ (r) = \varepsilon_{xx}(r) + \varepsilon_{yy}(r) - 2\varepsilon_{zz}(r)$, in terms of strain along the crystal directions, one can infer that the energy position of

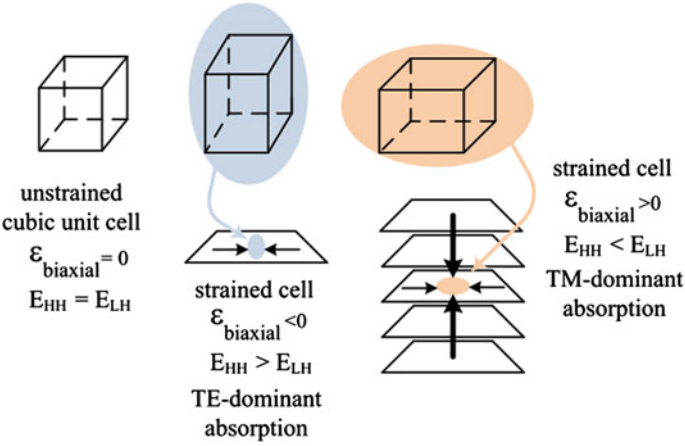

Fig. 1.15 Cubic cell deformation in single layer QD (*middle picture*) and multi-stack QDs (*right picture*) due to biaxial strain

HH and LH bands may changed when $\varepsilon_{\text{biaxial}}$ (r) becomes negative or positive ($\varepsilon_{xx}(r) + \varepsilon_{yy}(r) < 2\varepsilon_{zz}(r)$ or $\varepsilon_{xx}(r) + \varepsilon_{yy}(r) > 2\varepsilon_{zz}(r)$). This fact is schematically illustrated in Fig. 1.15 where the effect of strain is justified in terms of cubic unit cells. As it is illustrated in this figure, the biaxial strain within the QDs can change its sign in closely stacked QDs resulting in TM-dominant absorption while in the case of a single QD, the interband transition is TE-dominant.

Demonstration of TM-mode-sensitive QD-SOAs can lead to appearance of polarization-insensitive QD-SOAs with alternatively stacking TE-mode and TM-mode-sensitive SOAs at the first glance. For example, TM-mode-sensitive optical transition at 1.5 μm bands has obtainable by proper adjustment of QD strains [17].

Calculation for different In contents in $In_xGa_{1-x}As$ ternary QDs on InP substrate reveal the effect of strain on transition energies and thus the capability of polarization mode selection. Assuming box-shaped quantum dot for simplicity of calculation and using a six-band Hamiltonian, the energy levels of conduction band, heavy-hole and light-hole band in the presence of strain can be calculated as [17]

$$E_c^{dot} = E_c^{w.o.strain} + a_c(\varepsilon_{xx} + \varepsilon_{yy} + \varepsilon_{zz}) + \frac{\hbar^2}{2m_0}\left(\frac{K_{x-n}^2 + K_{y-n}^2 + K_{z-n}^2}{m_e}\right) \tag{26}$$

$$E_{v-HH}^{dot} = E_{v-uppermost}^{w.o.strain} + a_v(\varepsilon_{xx} + \varepsilon_{yy} + \varepsilon_{zz}) - \frac{1}{2}\delta E - \frac{\hbar^2}{2m_0}[(\gamma_1 + \gamma_2)(K_{x-n}^2 + K_{y-n}^2) + (\gamma_1 - 2\gamma_2)K_{z-n}^2] \tag{27}$$

$$E_{v-LH}^{dot} = E_{v-uppermost}^{w.o.strain} + a_v(\varepsilon_{xx} + \varepsilon_{yy} + \varepsilon_{zz}) - \frac{1}{2}\Delta_0 + \frac{1}{4}\delta E + \frac{1}{2}\sqrt{\Delta_0^2 + \Delta_0\delta E + \frac{9}{4}\delta E^2} - \frac{\hbar^2}{2m_0}[(\gamma_1 - \gamma_2)(K_{x-n}^2 + K_{y-n}^2) + (\gamma_1 + 2\gamma_2)K_{z-n}^2] \quad (28)$$

In above calculations the strain components ε_{xy}, ε_{yz}, and ε_{zx} are considered to be zero. Also, a_c and a_v are hydrostatic potentials of conduction and valence bands, Δ_0 is spin–orbit splitting, b is the deformation potential, γ_1 and γ_2 are Luttinger parameters, K_{j-n} are wave numbers and $\delta E = 2a[\varepsilon_{zz} - 0.5(\varepsilon_{xx} + \varepsilon_{yy})]$. The calculated values for light-hole transition energy (E_{LH}) and heavy-hole transition energy (E_{HH}) for GaAs (x = 0) and InAs (x = 1) QDs with 3.8% smaller and 3.1% larger lattices respectively than InP, are presented in Figs. 1.16 and 1.17

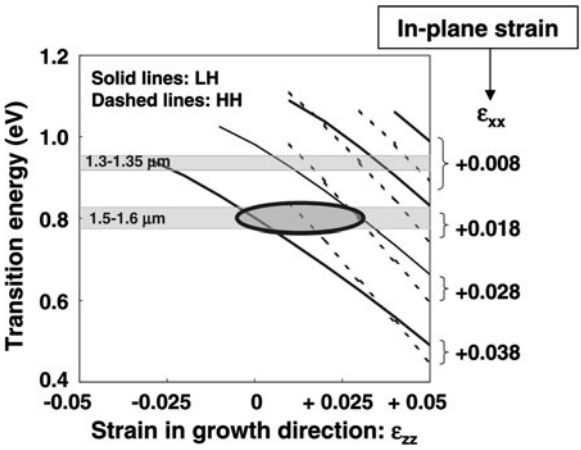

Fig. 1.16 Electron-light hole and electron-heavy hole transition energies (E_{LH}, E_{HH}) as functions of in-plane and in growth direction strains in GaAs QDs. The ellipse indicates the TM-mode-sensitive region [17]

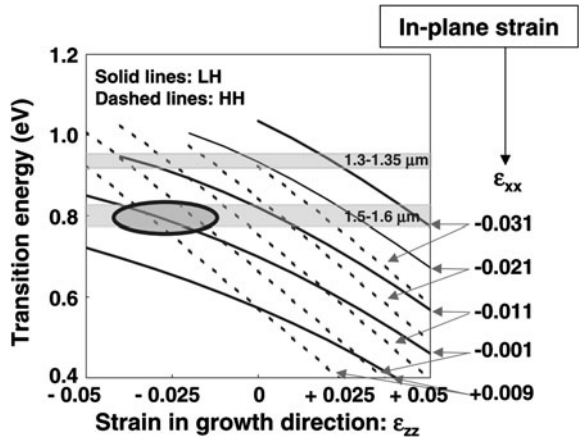

Fig. 1.17 Electron-light hole and electron-heavy hole transition energies (E_{LH}, E_{HH}) as functions of in-plane and in growth direction strains in InAs QDs. The *ellipse* indicates the TM-mode-sensitive region [17]

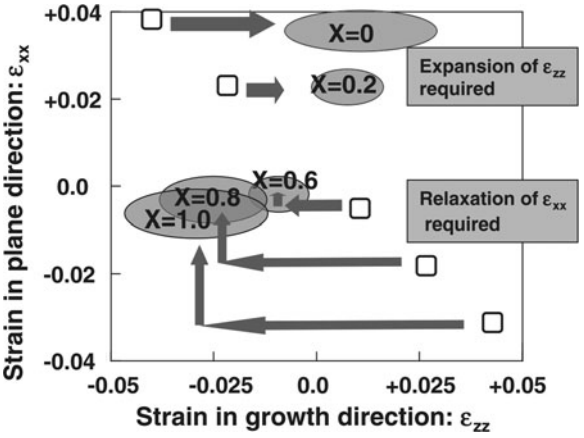

Fig. 1.18 Strain of $In_xGa_{1-x}As$ QDs where the open squares show the strain of free-standing $In_xGa_{1-x}As$ epilayers lattice matched to InP and *arrows* illustrate variations needed to achieve TM-mode-sensitive QDs depicted by ellipses [17]

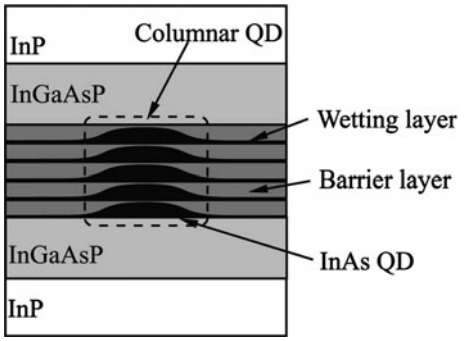

Fig. 1.19 Columnar QDs composed of stacking InAs QDs and InGaAsP barrier layers [19]

respectively. The solid and dashed lines consist for E_{LH} and E_{HH} with the fixed in-plane strain ε_{xx} (= ε_{yy}) and varied strains in the growth direction, ε_{zz}. The regions where $E_{LH} < E_{HH}$ corresponds to TM-mode-sensitive conditions where $E_{LH} =$ 0.78–0.83 eV (wave-lengths: 1.5–1.6 μm).

One can summarize the strain of $In_xGa_{1-x}As$ QDs sensitive to TM-mode around 1.5 μm according to material composition as it is depicted in Fig. 1.18.

Changing the strain from the strain value for free-standing $In_xGa_{1-x}As$ epilayers (lattice-matched to InP substrate) by expanding the lattice in the growth direction for $x < 0.4$ (in this case the lattice constant of the QD is smaller than the substrate) and also compressing the lattice in the growth direction and relaxing the strain in the plane direction for $x > 0.6$ (in this case the lattice constant of the QD is larger than the substrate), contributes to TM-mode sensitive QDs around 1.5 μm.

To achieve this goal, one should control the in-plane (ε_{xx} and ε_{yy}) and in-growth direction (ε_{zz}) strains independently. Two types of barriers can meet the challenge of controlling the strain components in different directions. One type indicated by (A) in Fig. 1.19 (above and below the QD) can control ε_{xx} and ε_{yy} components and the other type indicated by (B) can control ε_{zz}. Barrier (B) with smaller lattices and

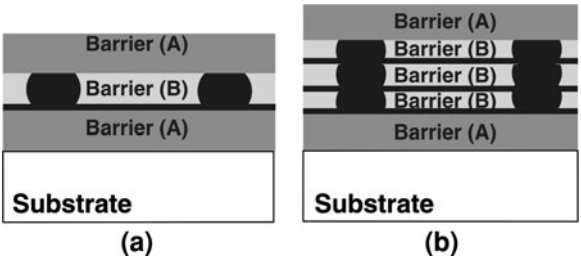

Fig. 1.20 Schematics of **a** a single layer QD and **b** stacked QDs to control the strain components via two type of barriers (barrier A and barrier B) [17]

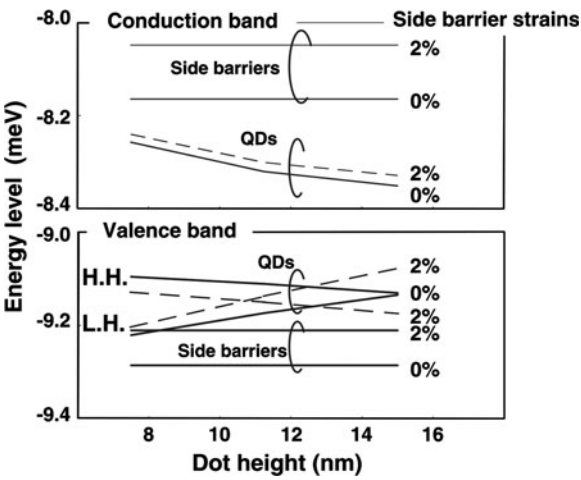

Fig. 1.21 Energy levels of conduction and valence bands for InAs QDs With a 15 nm base size. *Solid and dashed lines* indicate 0 and 2%-strained side barriers respectively [17]

barrier (A) with larger lattices are requirements for TM-mode-sensitive InAs QDs as an instance.

Owing to the point that stacking QDs relaxes the in-plane strain [18], stacked structures are of other candidates for controlling the strain components. Stacked or columnar QDs consist of several stacked QD layers with thin inter-layers and can be considered as a QD system with a high aspect ratio (QD height/QD base size). Figure 1.19 presents a schematic of columnar QDs fabricated by stacking InAs QDs and InGaAsP barriers.

The idea of utilizing stacked QDs is also schematically depicted in Fig. 1.20b with the mentioned barrier types.

Calculating the energy levels as a function of dot height by considering the strain components affected by the two mentioned barrier types reveal the possibility of realizing TM-mode-sensitive InAs QDs. InAs QDs with surrounding side barriers with 2% smaller lattice constants than substrate meet the strain requirements. Figure 1.21 shows the calculated energy levels for conduction and valence bands with different content of strain in side barriers where the efficiency of 2%-strained side barriers is obvious in the heavy hole and light hole energy difference.

The above theoretical discussions may interpret as a technique to symmetries the strain of the QD structure which suffers from the properties of the S–K growth method. QDs with symmetric shape and strain have discussed to be polarization insensitive that is favorable for practical applications. However, these structures are still far from practical point of view. Thus, controlling both strain and shape of QD structures such as height of coupled QDs using the stacking number and controlling the strain within QDs using the thickness of barriers in columnar QDs may lead to polarization-insensitive QD-system [19].

Alternative stacking of QD layers with specified deposition amount of InGaAsP tensile-strained barriers (like the schematically showed structure in Fig. 1.19) can cancel out the biaxial compressive strain in InAs QDs. An experimental structure (similar to the schematic of Fig. 1.19) [19] for this purpose grown by metal organic vapor-phase epitaxy (MOVPE) consists of two monolayers (ML) of $In_{0.17}Ga_{0.83}As_{0.60}P_{0.40}$ barriers with a tensile strain 3.7% compared with InP substrate, 50 nm-thick unstrained $In_{0.85}Ga_{0.15}As_{0.33}P_{0.67}$ capping layers and 3 μm-thick InP layer which form a waveguide like structure and provides optical confinement.

With a QD sheet density of about 7.5×10^{10} and QDs and wetting layer as high as 1.2 and 0.6 nm respectively in each layer, polarized PL spectra has been obtained for 7, 13, 22 and 25-fold samples at room temperature.

For samples with lower QD layers, the PL spectrum is similar to results expected from QDs grown by S–K method and the TE-mode is dominant as it is depicted in Fig. 1.22 for sevenfold sample. Increasing the number of layers decrease the polarization dependency since increasing the stack number increase the effective height of coupled QDs.

In the whole samples with 2-ML tensile-strained barriers, the TE mode is dominant even in 22-fold sample considering the point that the height of QD structure is longer than the lateral size in this case. However, the dominancy of TE mode intensity implies that most quantized axis has not changed from the growth direction to the in-plane direction to make the TM-mode to have higher intensity. This is because of the remaining compressive strain due to existence of wetting layer. Highly tensile-strained barriers by changing the deposition amount of barrier layers from 2 ML to 2.5 ML or 3 ML symmetries the QD structure to have TM-dominant polarization mode or to be polarization independent. Figure 1.23 presents the experimentally obtained results for a 22-fold sample with different barrier thickness.

Longer peak wavelength for TM-dominant condition compared with the TE peak wavelength implies the fact that the transition occurs between conduction band and LH band instead of HH band. This objective is final strain engineering aim to achieve to TM-mode-sensitive regions ($E_{LH} < E_{HH}$) as it described before.

Although effective QD strain and height engineering have done successfully for columnar QDs, realization of a real QD-SOA requires several considerations beside the controllable mode sensitivity. As an instant, the confinement factor of TM-mode light is smaller than TE-mode in standard waveguides that should take into account during the device fabrication.

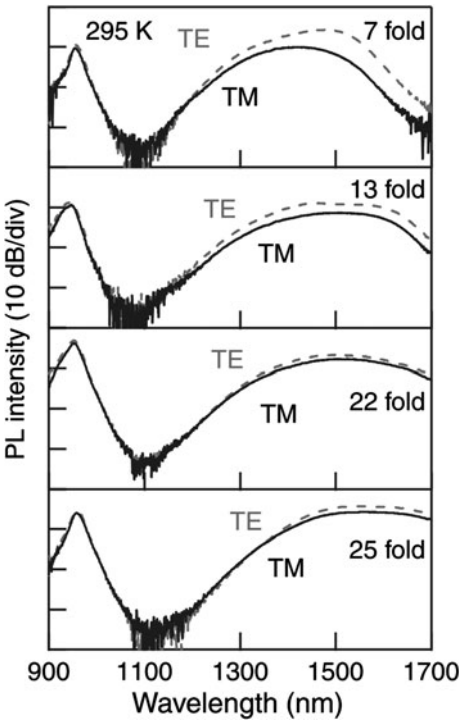

Fig. 1.22 PL spectra of 7, 13, 22 and 25-fold columnar QD structures with a 2 ML deposition amount of strained barriers [19]

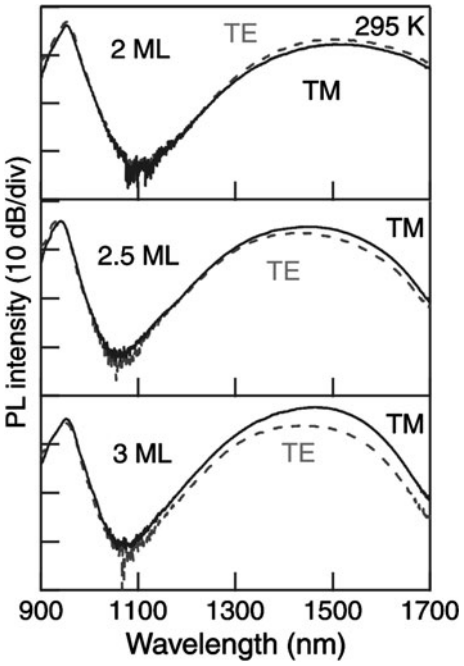

Fig. 1.23 PL spectra of a 22-fold columnar QD structure with 2 ML, 2.5 ML and 3 ML deposition amounts of strained barriers [19]

Experimental TE-/TM-gain dominant and polarization-insensitive QD-SOAs have been demonstrated recently by controlling the optical polarization in columnar QDs [20–22].

Measurements for chip gain spectra of TE and TM polarizations at wavelength range from 1350 to 1610 nm have reported in [20] for a QD-SOA with a active region similar to the schematically illustrated structure in Fig. 1.19 with columnar quantum dots of height 11 nm and 1% tensile strain barriers. The waveguide of the device have designed to have less than 20% difference in confinement factor for TE and TM polarizations and the waveguide has tilted 8° off angle. To reduce the facet reflections, antireflection coating has applied. The whole SOA chip length is 1000 μm and is biased with 300 mA input current. TE-dominant gain has obtained with the noted QD height and barrier strain. However, for the SOA with 22 nm high columnar QDs and 3.7% tensile-strained barriers the results indicate TM-dominant gain spectra. The TM and TE gains in the latter case are 17.3 and 11.1 dB at 1.55 μm. The measured chip gains for both of the TE and TM-dominant samples are depicted in Fig. 1.24a, b respectively. This experiment proves the possibility of controlling the polarization mode gain dominancy by controlling the dot heights and strain.

Polarization-insensitive QD-SOAs at 1.55 μm has also fabricated using 13 stacked QD layers and 3.2% tensile-strained InGaAsP barriers [21].

The waveguide structure mesa has formed dry etching and then has buried by current blocking layers. Also, the waveguide has designed such that the polarization difference in the waveguide confinement factor is less than 10%. Figure 1.25 display the waveguide structure schematically.

With a device length of 6 mm and bias current of 1200 mA the gain characteristics with a CW signal at 1.55 μm reveals unsaturated gains of 8 dB and 7.6 dB for TE and TM lights respectively. Also, a 3 dB saturation output power of 18.5 dB has obtained for both of TE and TM lights. The chip gain curves versus output power have plotted in Fig. 1.26 for both of the polarization modes.

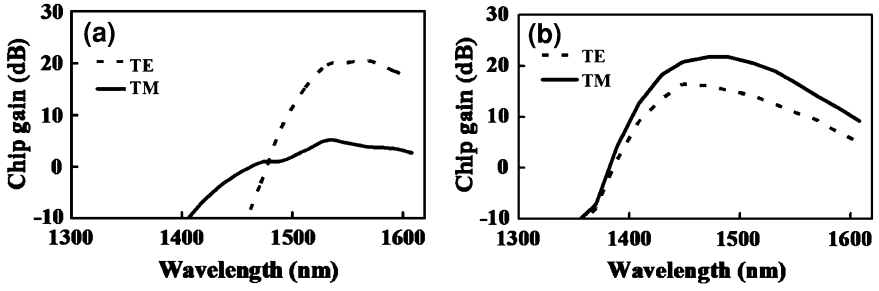

Fig. 1.24 Chip gain spectra for two QD-SOAs with **a** 11 nm high Columnar QDs and 1% tensile-strained barrier and **b** 22 nm high columnar QDs and 3.7% tensile-strained barrier [20]

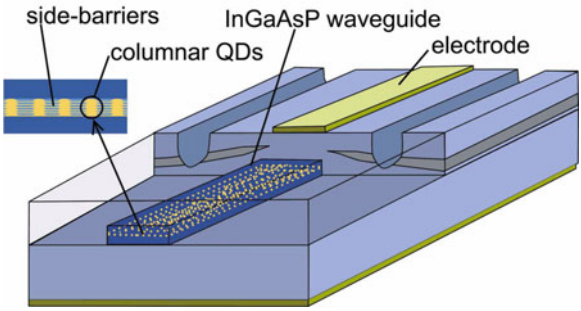

Fig. 1.25 Structure of polarization-insensitive QD-SOA [21]

1.8 Doped QD-SOAs

Semiconductor quantum dot amplifiers based on self-assembled InGaAs/GaAs materials are among the most widely investigated and most advanced systems owing to continuous improvements in their fabrication and their emission in the optical telecommunication 1.3–1.55 μm wavelength range. However, the electronic structure of these quantum dots leads to some limitations in the operation of the opto-electronic devices designed and fabricated based on these elements. The large density of states in the wetting layer with respect to the quantum dots causes tendency of remaining in the wetting layer for electrons rather than the dot states and this challenge limits the operation bandwidth. On the other hand, small level-spacing of hole states limits the performance of the InGaAs/GaAs based QD-SOAs and QD Lasers. At room temperature, a depopulation of the ground state hole level occurs because of the thermal promotion of holes into the closely spaced excited states and wetting layer. Due to large hole effective mass and strong band mixing, the energy band of a QD exhibits large number of closely spaced ($\sim$10 meV) hole states and a few electron states. Thus, to maintain enough carriers in the quantum dots and provide acceptable level of optical gain in the active region, *p* type doping of the active region have been proposed in quantum dot laser and amplifiers.

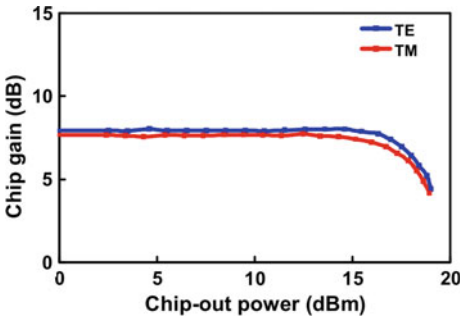

Fig. 1.26 Gain saturation curves for TE and TM-polarized lights at 1.55 μm [21]

Recently, InGaAs QD lasers incorporating *p* type modulation doping have demonstrated temperature insensitive threshold current [23], increased peak modal gain [24–26] and high modulation bandwidth [27]. Time-resolved photoluminescence experiments have shown faster carrier capture and relaxation from the GaAs barrier to the QD ground state in doped QDs as compared to undoped ones, both at low and room temperature [28, 29]. These findings suggest that doped QDs can exhibit interesting properties for high-speed lasers and amplifiers, faster gain recovery in QD-SOAs and higher optical gain in both QD-SOAs and lasers.

In this section a detailed overview of doping effect (*p* and *n* type) on the optical characteristics of QD-SOAs will be presented by introducing the experimental and theoretically reported results in recent years.

1.8.1 p-Doped QD-SOAs

Experimental demonstrations of p-doped QD-SOAs also indicate that p-doping enhance the amplifier gain and leads to lower noise figure and increased temperature stability [30]. Comparison between a 10-stack, 2 mm long, p-doped InGaAs/GaAs QD-SOA with peak wavelength at 1310 nm and nominal doping level of 5×10^{17} cm^{-3} and a 3 mm long undoped one with peak wavelength at 1290 nm reveals that the p-doped and undoped samples exhibit 22 and 23.5 dB chip gain, 9 and 10 dB noise figure and saturation output power of 12 and 15 dBm respectively at a same current density. Over a specific current level, the emission intensity of ground and excited state of the undoped sample saturates due to thermal heating of the device whereas the p-doped sample exhibit no saturation behavior at that current. These results describe improvement of gain, noise figure and temperature stability in p-doped structure. Figure 1.27 shows the amplified spontaneous emission spectra for different current densities in both p-doped and undoped SOAs.

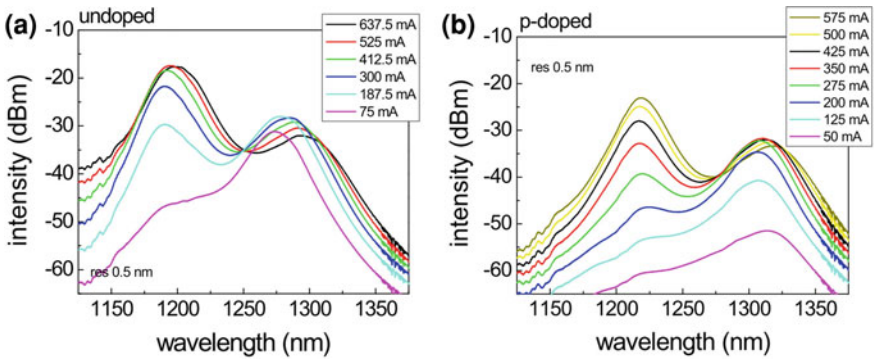

Fig. 1.27 Amplified spontaneous emission spectra of **a** undoped and **b** p-doped QD-SOAs at different bias currents [30]

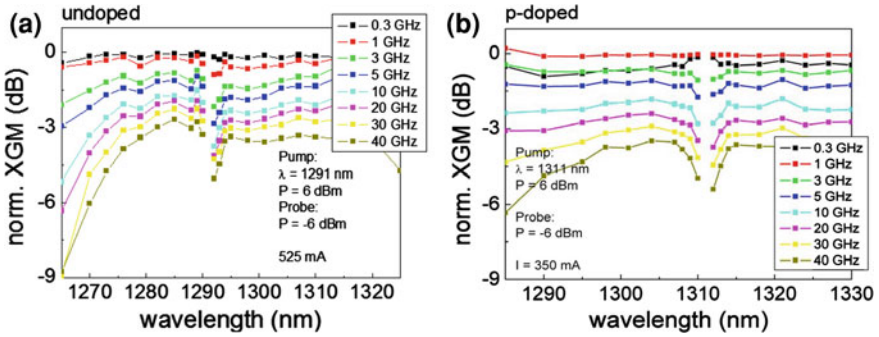

Fig. 1.28 Comparison of the XGM at different frequencies dependent on the detuning for **a** undoped QD-SOA with pump wavelength centered at 1291 nm and **b** p-doped QD-SOAs with pump frequency centered at 1311 nm [30]

Small signal cross gain modulation (XGM) experiments for both undoped and p-doped structures shows a XGM bandwidth beyond 40 GHz for undoped sample but a bandwidth of 25 to 30 GHz for p-doped sample due to lower population of the excited state and wetting layer reservoirs. A comparison of the XGM for p-doped and undoped samples is presented in Fig. 1.28. Since carriers are relaxed faster into QDs in p-doped sample, slow dynamic of carriers in the wetting layer cannot track the fast carrier depletion. This deficiency of p-doped devices may compensate by higher current density due to better temperature stability of p-doped QD structures.

Investigation of the temporal gain and phase dynamics with differential transmission spectroscopy (DTS) experiment can determine the carrier dynamics in the undoped and p-doped amplifiers [31]. The pump intensity in the DTS experiment is usually chosen to induce a linear change in the gain of the device while the probe intensity has to be low enough to minimize the modification of the transmittivity of the device. Figure 1.29 shows a scheme of the pump-probe differential transmission (DT) technique in heterodyne detection. In this configuration, $\sim$100 fs Fourier-limited laser pulses at 76-MHz repetition rate are divided into pump, probe and reference beams where pump and probe beams are coupled into the transverse electric waveguide mode with a relative delay time τ_p (positive for pump leading). The transmitted probe is detected using a heterodyne technique which is capable of monitoring both the amplitude and phase dynamics induced by pump beam [32].

In the presence or without the pump field, the probe field amplitude at the end of the device (after propagation) may denoted by $E_{off}(L)$ or $E(L)$ respectively where the probe amplitude obeys the Beers low given by

$$E_{off}(L) = E_0 \exp(\Gamma g L/2) \tag{29}$$

$$E(L) = E_0 \exp((\Gamma g + \Delta\Gamma g)L/2) \tag{30}$$

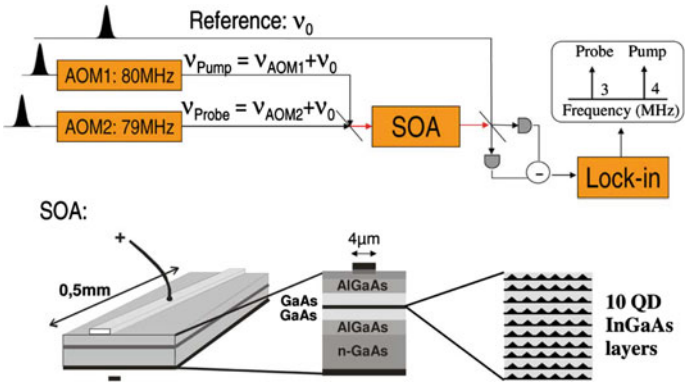

Fig. 1.29 Schematics of heterodyne pump-probe detection method and the QD-SOA structure as the sample [32]

where E_0 is the incident probe field amplitude, Γg is the device modal gain per unit length, $\Delta\Gamma g$ is the modal gain change induced by the pump, and L is the device length. Therefore, the differential transmission signal can be described by

$$\frac{E(L)}{E_{off}(L)} = \exp\left(\Delta\Gamma g L/2\right) \tag{31}$$

Thus, the gain changes can be expressed as

$$\Delta G = 20 \times \log_{10}\left(\frac{E(L)}{E_{off}(L)}\right) \tag{32}$$

The absorption ($\Gamma g < 0$) and gain ($\Gamma g > 0$) regimes can thus be determined according to the mentioned equations. Figure 1.30 presents the measured gain and phase change imposed on the probe beam as a function of delay between the pump and the probe beams denoted by τ_p for three different samples of quantum dot amplifiers. The first sample is an undoped InAs/GaAs quantum dot structure while the other samples are p-doped by incorporating a 10 nm-thick layer of carbon-doped GaAs in the spacer layer, ending 9 nm below each dot-in-well layer in the device structure [31]. These two samples contain different amount of dopant atoms against quantum dots and are defined by p (doping level of ~ 8) and p+ (doping level of ~ 15) respectively. As it is clear in Fig. 1.30, depending on injection current, the pump beam can be absorbed or amplified during the propagation in the active region. The pump intensity average along the amplifier can be described as

$$\bar{I}_P = \frac{I_P(0)}{L}\int_0^L \exp\left((\Gamma g + \Delta\Gamma g)z\right) dz \tag{33}$$

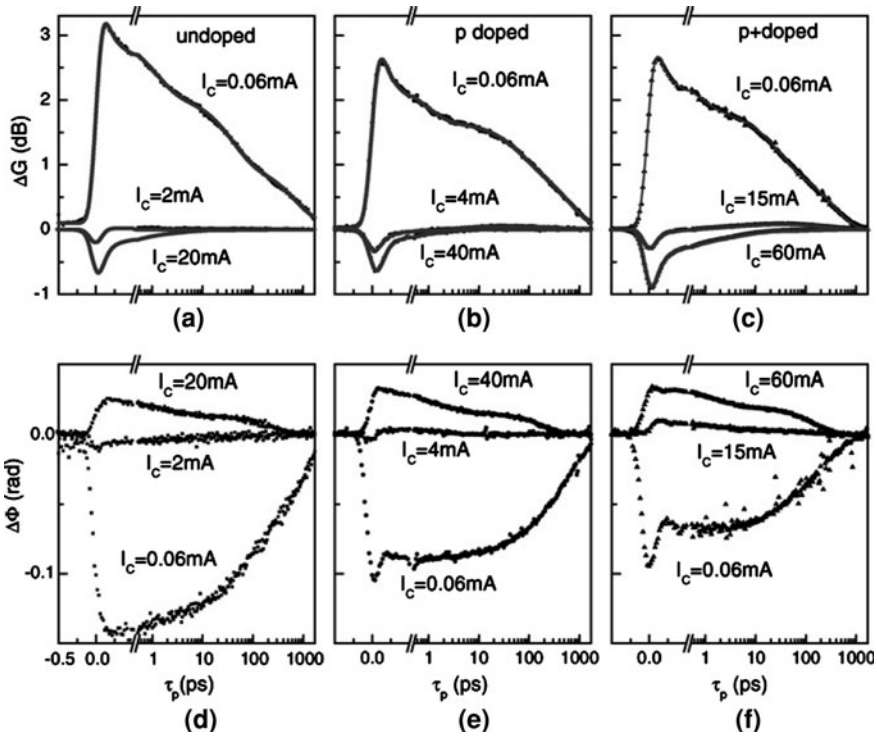

Fig. 1.30 Pump-induced gain and phase variations of the GS for **a**, **d** undoped sample, **b**, **e** p-doped sample and **c**, **f** p+doped sample as a function of pump-probe delay time and at same incident pump intensity (~ 1 pJ). The gain regime ($\Delta G < 0$, $\Delta\Phi > 0$) and the absorption regime ($\Delta G > 0$, $\Delta\Phi < 0$) are both considered [31]

where L is the length of the amplifier and $\Delta\Gamma g$ is the average gain change by the pump at zero time delay. Then, the measured gain changes have normalized to $\bar{I}_P/I_P(0)$. At low bias currents, the amplifier operates at the absorption regime where for $\tau_p \geq 0$ an absorption bleach occurs due to Pauli blocking. Increasing the injection current would change the operation regime to gain regime with $\Delta G < 0$ and $\Delta\Phi > 0$.

The gain change for three different time delay between the pump and the probe beams has measured as a function of small signal modal gain Γg. Two distinct features of gain change can be observed in absorption and gain regions in undoped and p-doped samples. Due to excess holes created by p-doping inside QDs, the carrier-carrier scattering mediated dynamics such as hole-hole scattering processes within excited state and wetting layer are accelerated which lead to faster absorption bleach in the doped samples (smaller gain change in doped samples rather than undoped one). Also, in the gain regime the undoped device exhibits the smallest gain change as presented in Fig. 1.31.

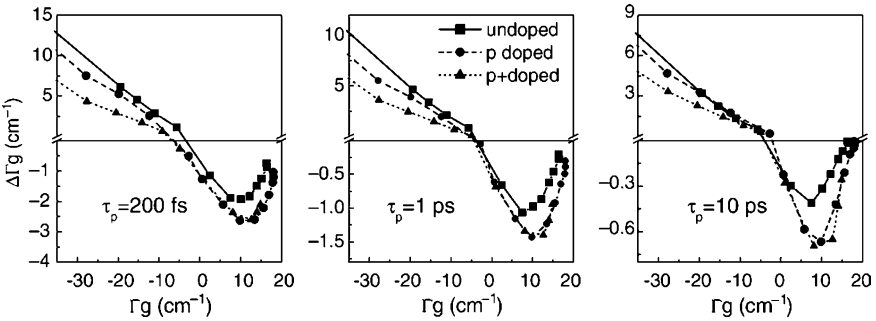

Fig. 1.31 Pump-induced modal gain variation at 200 fs, 1 ps, and 10 ps pump-probe delay versus small signal gain [31]

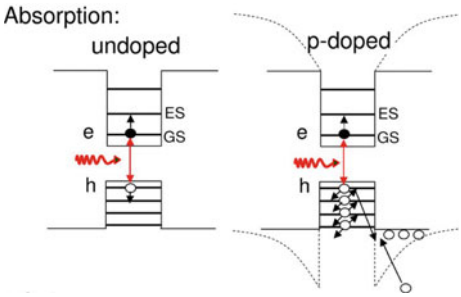

Fig. 1.32 Scheme of the carrier transition processes to explain gain and refractive index variations in the absorption regime [32]

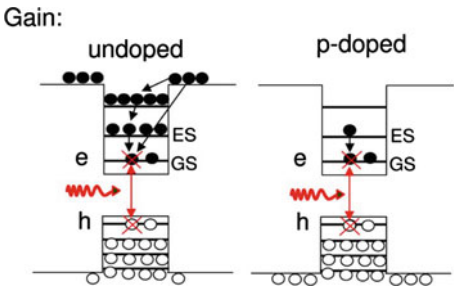

Fig. 1.33 Scheme of the carrier transition processes to explain gain and refractive index variations in the gain regime [32]

Refractive index dynamics can also be altered by doping the SOA through doping-induced variations in carrier densities of quantum dots. It was previously discussed in Sect. 1.4 that a transition from the ES to the GS induces a positive contribution to refractive index while a reverse transition decrease the refractive index as schematically displayed in Fig. 1.32. These phenomena can be justified through considering the carrier transitions between the GS and the ES in both absorption and gain regimes for undoped and p-doped structures as shown in Figs. 1.32 and 1.33 for absorption and gain situations respectively.

In the absorption regime, the refractive index variation in the case of p-doped samples is smaller than un-doped structure which can be attributed to hole-hole

scattering. Due to this effect, the optically injected hole removes from the GS and hence the hole occupation at higher energy states (most probably in the wetting layer rather than the ES) has small influence on the refractive index [32]. The scheme presented in Fig. 1.32 can give an imagination of this status. A similar scheme in Fig. 1.33 indicates the intraband transitions in the gain regime for undoped and p-doped structures. In this regime, a pump photon stimulates the recombination of an electron–hole pair and consequently carriers relax form the ES to GS which gives a positive contribution to the refractive index probed at the GS.

Due to existence of a large electron reservoir in the ES and the wetting layer of undoped structure, a small variation of higher energy states is probed after the pump pulse whereas in the case of p-doped structure, carrier distribution change substantially in the ES and a large refractive index change is probed at the GS. Figure 1.34 displays the measured pump-induced refractive index change in the gain and absorption regimes for an undoped and two p-doped QD amplifiers which contain different levels of dopant concentrations.

It is important to note that the refractive index change occurs with time scale of carrier–carrier scattering which is about several femtoseconds whereas the gain variation of a QD-SOA occurs within the input pulse duration. Also, the refractive index variations decay with carrier lifetime which is ~ 1 ns while the gain variations decay with carrier-carrier scattering. In the wide time span between the carrier–carrier scattering time scale and carrier lifetime a decoupling of the pump-induced gain and refractive index variations occurs (i.e. only the refractive index variations remains). This interesting feature can be exploited for demonstration of cross-phase modulation-based architectures [9].

The effect of p-doping on optical characteristics of QD-SOAs has also investigated theoretically by solving the rate equations [33]. In the doped QD system the charge neutrality is ensured by $N_A + n = p$ where N_A is the acceptor

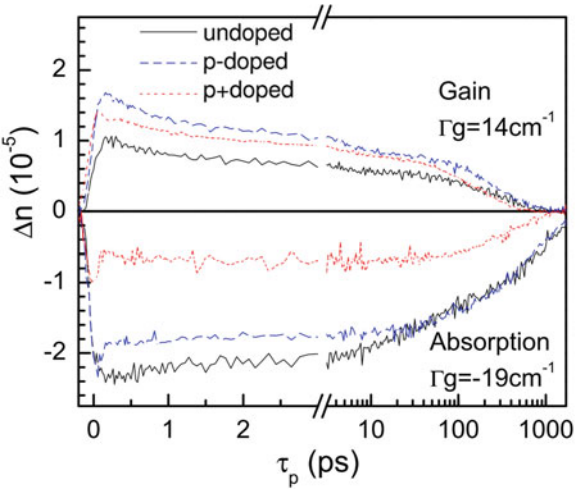

Fig. 1.34 Pump-induced refractive index variation as a function of pump-probe delay for undoped (*solid curves*), p-doped (*dashed curves*), and p+doped (*dotted curves*) QD amplifiers including both gain and absorption regimes with small signal gains of 14 and -19 cm^{-1} respectively [32]

concentration, and n and p are the electron and the hole concentrations respectively. Also, the waveguide loss increases with p-doping due to inter valence band absorption and enhanced nonradiative Auger recombination and can be expressed by $\alpha = \alpha_0 + \alpha_A\, p$ where α_0 is waveguide loss for undoped QDs and α_A is the loss parameter for p-doping [34].

The energy separation of electron and hole states in the conduction and the valence bands are considered to be 60 and 10 meV respectively. Therefore, the input photon energy may define as $\hbar\omega = \hbar\omega_0^{\max} + \Delta\Omega$ where $\hbar\omega_0^{\max}$ stands for the ground state gain peak and $\Delta\Omega$ refers to energy detuning ($\Delta\Omega = 0$ and $\Delta\Omega = 70$ meV refer to ground and first excited states gain peaks respectively). If the applied current is relatively larger than the transparency current, increasing the doping concentration enhances the optical gain. This fact is illustrated in Fig. 1.35 where the for the case of normalized bias current of $J = 1$, the optical gain decreases with doping concentration due to increased waveguide loss which becomes comparable with the gain at lower bias currents.

The inset of Fig. 1.35, i.e. $U_{in} = 0.05$, describes the normalized photon density with respect to quantum dot volume density and ground state modal. It should be noted that the transparency current increases in p-doped SOAs compared to undoped structures. Considering the fact that increasing the acceptor concentration in the active layer increase the occupation probability of the hole states, higher state population leads to higher stimulated emission rate and hence the device saturates at lower input powers. Figure 1.36 illustrates the doping effect on evolution of normalized 3 dB saturated density ($S_{3\mathrm{dB}}^{in}$) for different energy detuning. Because of higher differential gain of excited state ($\Delta\Omega = 60$ meV) than the ground state, saturation density is lower for excited state compared with the ground state.

P-doping not only modifies the gain and saturation characteristics of QD-SOAs, but also influences the carrier relaxation in QDs through altering the carrier-carrier

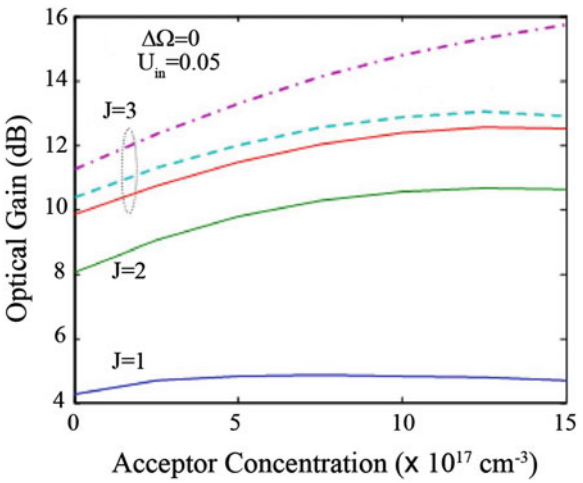

Fig. 1.35 Optical gain of the p-doped QD-SOA versus acceptor concentration for different bias currents and with $\Delta\Omega = 0$ [33]

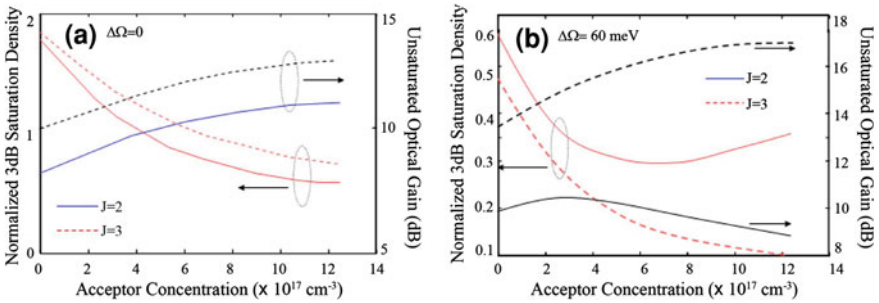

Fig. 1.36 Normalized 3 dB saturated density and unsaturated optical gain versus acceptor concentration and in different bias currents for **a** $\Delta\Omega = 0$ and **b** $\Delta\Omega = 60$ meV [33]

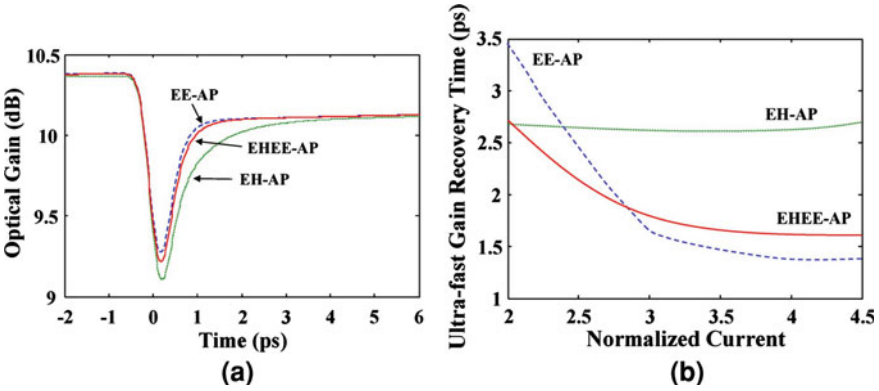

Fig. 1.37 Optical gain dynamics for normalized bias current of J = 4 **a** and ultrafast gain recovery time as a function of injected current **b** for an undoped QD-SOA [36]

interactions or the well-known Auger processes. At high doping concentrations or high injection currents, Auger-type carrier–carrier scatterings increase and carriers can relax to lower energy states. This process influences the ultrafast gain recovery and gain compression in QD-SOAs [35]. Because of ultra-fast characteristic time scale related to carrier–carrier scattering in QDs ($\sim$100 fs) and dense hole states in the valence band of QDs, the effect of p-doping on electron–hole scattering can be very important.

The effect of doping concentration on the gain recovery time and gain compression can be studied by considering the dynamics of the electron–electron Auger-assisted process (EE-AP) and the electron–hole Auger-assisted process (EH-AP) separately and finally both of the electron–hole, electron–electron Auger-assisted processes (EHEE-AP) [36].

In an undoped QD-SOA, the EH-AP produces larger gain compression rather than the EE-AP, as it is evident in Fig. 1.37a. Also, the gain recovery time due to

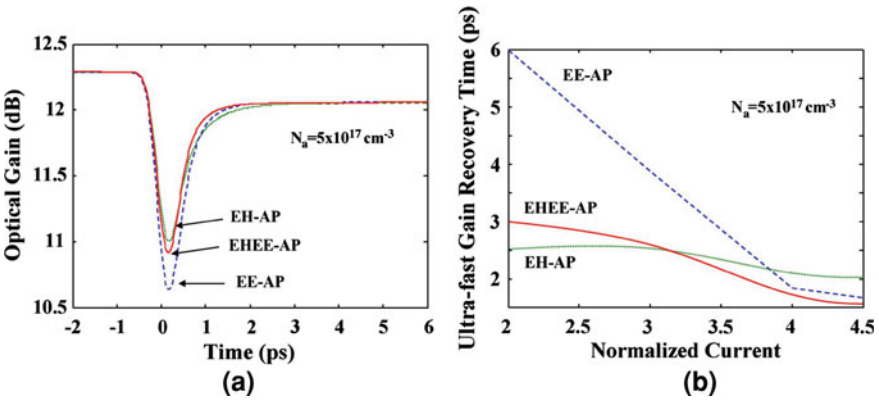

Fig. 1.38 Optical gain dynamics for normalized bias current of J = 4 **a** and ultrafast gain recovery time as a function of injected current **b** for a p-doped QD-SOA ($N_A = 5 \times 10^{17}$ cm^{-3}) [36]

EE-AP is faster than the EH-AP in a defined bias current. Increasing the applied injection current increases the electron concentration in the wetting layer and consequently the EE-AP increases which leads to a decrease in gain recovery time. This phenomenon is illustrated in Fig. 1.38b. Since the EH-AP is almost independent of bias current, the total gain recovery time decreases with bias current in undoped QD-SOA. It can be shown that operation at high bias currents doesn't enhance the gain compression.

The optical gain dynamics and the gain recovery time at different injection currents are presented in Fig. 1.38 for a p-doped amplifier where a doping concentration of $N_A = 5 \times 10^{17}$ cm^{-3} has considered. Due to high electron concentration in the wetting layer at high bias currents, the EE-AP determines the ultrafast gain recovery whereas the EH-AP is dominant at low bias currents because of small electron concentration.

Considering both of the processes (EHEE-AP), the gain recovery happens slower in p-doped amplifier compared with undoped one at low bias currents and remains approximately unchanged at higher bias currents. According to the previous discussions on the effect of p-doping on gain enhancement, it is predictable to have higher gain compression in the presence of EHEE-AP compared with undoped device. It is shown in [36] that the value of gain compression can increase to more than 80% at high bias currents in a p-doped amplifier.

In order to investigate the effect of higher acceptor concentration level on the ultrafast gain recovery time and gain compression, evolution of different Auger-assisted relaxation processes are plotted at different doping concentrations in Fig. 1.39. The ultrafast gain recovery time as presented in Fig. 1.39a is governed with the lowest gain recovery time and slightly increases with doping concentration.

The gain compression is also governed by the process with lowest gain compression as it is depicted in Fig. 1.39b.

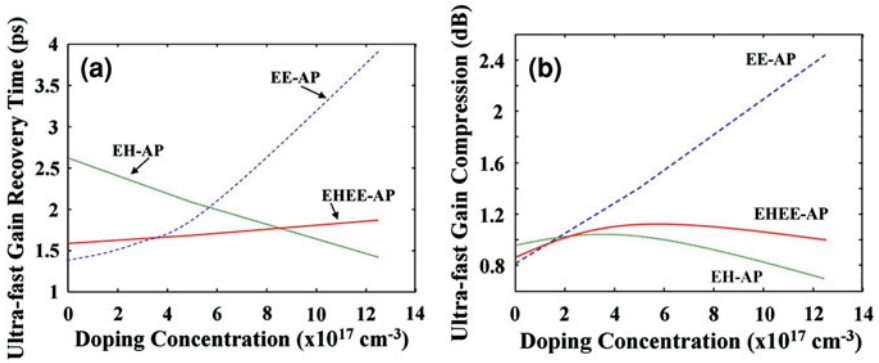

Fig. 1.39 Ultrafast gain recovery time **a** and gain compression **b** as a function of acceptor concentration and at a normalized bias current of J = 4 [36]

1.8.2 n-Doped QD-SOAs

Excess to thermal broadening of the hole states in undoped QD-SOAs, large signal crosstalk in multichannel WDM systems is another issue for QD-SOAs in multi-wavelength operations which stem from gain saturation effects between different wavelength channels [37]. n-Type doping of the QD-SOA active region has proposed to improve the linearity of the amplifier and increase the saturation density to reduce the crosstalk [33]. In this kind of doping saturation of hole states determines the device saturation properties rather than occupied electron states.

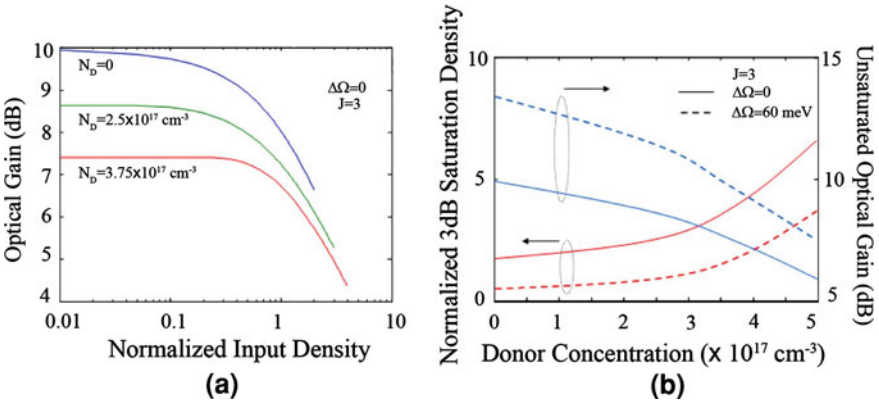

Fig. 1.40 **a** Optical gain versus normalized input density for three different donor concentrations and **b** normalized 3 dB saturated density and unsaturated optical gain versus donor concentration. Both of the plots are for $\Delta\Omega = 0$ and $\Delta\Omega = 60$ meV [33]

Figure 1.40 presents the evolution of optical gain and normalized 3 dB saturation density for a n-doped QD-SOA at a normalized bias current of $J = 3$. The effect of n-doping can be summarized in two facts; decreasing the optical gain as it is obvious in Fig. 1.40a, and considerable increasing of the saturation density as it can be seen clearly in Fig. 1.40b and also it can be understood to somewhat from part (a) of this figure.

As it was discussed earlier, electron–hole scattering plays a crucial role in bipolar QD-SOAs (both of the electron and hole dynamics should be taken into account). It is proved through experiments that the intradot relaxation processes are dominated by electron–hole scattering in bipolar QD-based devices which has a similar time scale to the carrier capture. Thus, only one time scale is obtained for ground state recovery time [38–40]. However, in unipolar (n-doped) QD structures the intradot relaxation process is slower than initial capture of electrons into QDs through continuum states. In the other words, in the n-doped QD structures the carrier capture and intradot relaxations are dominated by Auger-type electron–electron scattering with time constant of 10 and 100 ps respectively which are both longer relaxation processes in bipolar devices due to faster electron–hole scattering [41]. The intradot relaxation time scale can be $\sim$150 fs for an almost same electron density as in an n-doped sample. It is reported in [41] that the intradot relaxations in an n-doped QD-based structure happen about three orders of magnitude slower rather than bipolar devices which electron–hole scattering occurs. Therefore, n-doping a QD structure can determine inter-level relaxation through increasing electron density.

1.9 Fabrication Process

1.9.1 Quantum-Dot Growth

Several techniques have been used in the past decade to growth and realize quantum dots. Epitaxial growth is of widely investigated methods for fabrication of quantum dots based on commonly used In(Ga)As/GaAs and (Si)Ge/Si semiconductor materials. Considering various growth methods for fabrication of quantum dots, conventional and most commonly used molecular beam epitaxy (MBE) and metal organic vapor phase epitaxy (MOVPE) techniques have mostly employed for growth of quantum dots. Self-assembled growth of QDs by the Stranski–Krastanow (SK) method [42] has yielded quite homogeneous size dispersion and also defect-free growth of QDs. Also, accurately controlling and monitoring the growth conditions is one of the advantages of MBE method to the other vastly used growth techniques such as metal organic chemical vapor deposition (MOCVD). The growth process in MBE can be controlled through controlling the substrate temperature and molecular flow. In situ monitoring of the growth process by exposure of electron beams known as reflection high-energy electron diffraction (RHEED) is another feature of MBE.

Self-assembled In(Ga)As/GaAs QDs obtained from the SK growth method are the most investigated semiconductor QDs nowadays and several applications have been proposed according to these materials. Therefore, the fabrication process of a QD-SOA is described here based on such QDs. In the SK method the QDs are grown on a substrate due to lattice mismatch of the dot and the substrate materials. Normally, after growth of one or more complete monolayers (MLs) of dot material, three dimensional islands appear on the grown thin film. This layer is called wetting layer or quantum well depending on the thickness of the dot material and involves the QDs. This configuration of QDs is referred as dot-in-well (DWELL) structure. A high-band gap material that can serve as barrier is overgrown on dot material and a capping layer may be grown to embed the QDs into a GaAs matrix for most of applications. These processes are schematically illustrated in Fig. 1.41 where in the second stage (i.e. part b) strain-driven surface migration of some indium atoms decomposed from the InGaAs alloy enrich the QDs with In and leads to a red shift in the emission wavelength.

Figure 1.42 shows a scanning tunneling microscope (STM) image of InAs/GaAs QDs at room temperature where the QDs have obtained by depositing 1.8 MLs of InAs on GaAs (001) substrate at a substrate temperature of 500°C. The gray scale below the figure denotes the magnitude of local surface which small (large) slop areas are animated in light (dark) gray.

Two distinct types of QDs can be observed in the figure where the smaller dots are bound by shallow facets (pyramids) and larger ones are bound by steeper facets (domes). The overgrowth process of InGaAs layer (quantum well) has proposed to shift the emission wavelength of plain InAs QDs from 1200 to 1250–1300 nm and close to telecommunication O-band [45].

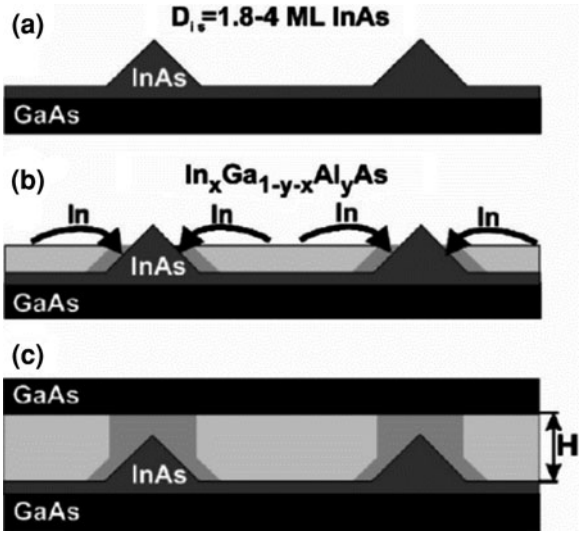

Fig. 1.41 Schematics of growth processes for InAs quantum dots. **a** Initial form of QDs after deposition of 1.8–4 MLs of InAs on GaAs substrate, **b** InGaAs layer overgrowth, **c** growth of GaAs capping layer [43]

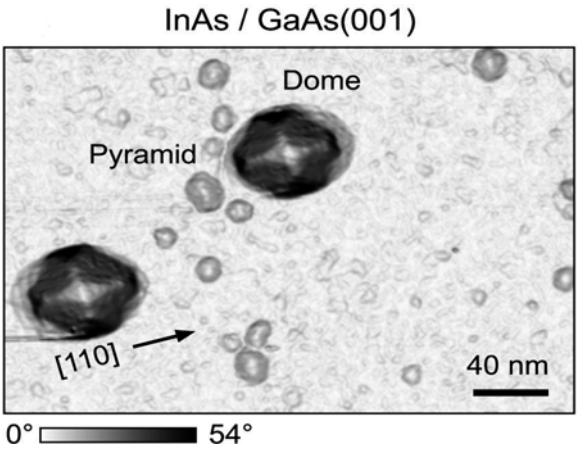

Fig. 1.42 STM image of InAs/GaAs QDs [44]

1.9.2 Epitaxial Structure of QD-SOA

QD-SOAs consist of an epitaxial structure similar to lasers with a separate optical confinement heterostructure (SCH). A typical structure like the structure fabricated in [45, 46] consists of substrate, cladding active region and contact layers as illustrated in Fig. 1.43. An oxide layer is deposited on a n-doped GaAs substrate and then a 300 nm GaAs buffer layer is grown on the oxide layer at 600°C to provide the surface smoothness. A 15 nm thick layer with graded Al content is then grown before the 1.5 μm Si-doped $Al_{0.35}Ga_{0.65}As$ layer as the lower cladding layer. The substrate temperature is then lowered to ∼480°C to make suitable situation for deposition of QD active region. The upper cladding layer consisting of 1.5 μm C-doped $Al_{0.35}Ga_{0.65}As$ layer should be grown at a substrate temperature of again 600°C on the waveguide layer following by a 15 nm thick graded layer. Finally, a 200 nm thick p-doped GaAs layer is grown which serves as contact layer. The whole grown layers organize a p–i–n structure. The active region may consist of 10 or 15 QD layers with 33 nm thick GaAs capping or

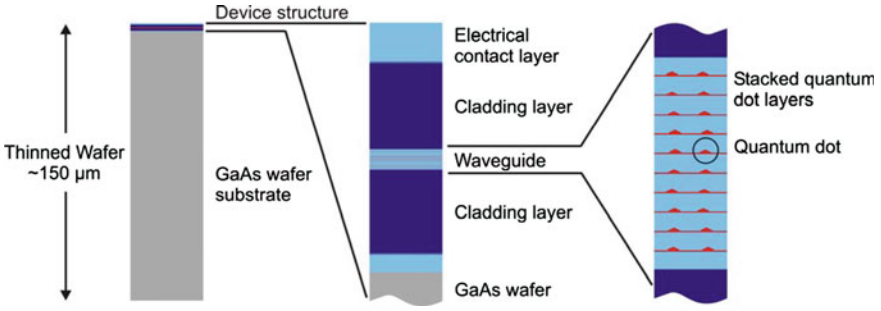

Fig. 1.43 Epitaxial structure of a QD-SOA

spacer layers. Effectively thick spacer layers can release the accumulated strain of each QD layer to avoid undesirable effects such as QD site correlation and electronic state intermixing between adjacent QD layers.

The thickness of the cladding layer should be chosen to hold the optical mode mainly inside the active region and avoid its leakage to adjacent layers. Also, the Al content of the cladding layers provide the necessary broadening of the optical mode to overlap with outer QD layer. Hence, there is a close relationship between the spacer layer thickness, cladding layer composition and the modal gain of the structure.

On the other hand, the optical mode must be guided in the transverse direction of the device to obtain single transverse mode operation and the current should be confined to the gain region in lateral direction for efficient carrier injection. Therefore, an appropriate waveguide structure should be employed to achieve these requirements. Index guided laser and optical amplifier structures are characterized by optical confinement in both lateral and transversal direction. The transversal confinement is a result of the electrical and optical properties of double heterostructures as shown in Fig. 1.44 for a GaAs-based epitaxial structure as an example. These structures consist of an active layer formed by a e.g. GaAs-layer between two A1GaAs-layers with a larger energy gap than GaAs. This configuration forms potential barriers on both sides of the active region causing confinement of carriers which in turn results in high carrier densities, allowing a low current to satisfy population inversion conditions.

Similar to transverse direction, the light has to be confined along lateral axis. In this case there is no possibility to exploit the epitaxial growth to provide optical confinement. Thus, if a single lateral mode operation of a device is required, special post-growth methods are to be used for this purpose. Example is overgrowth of deep etched mesa structures (or buried heterostructures) by another semiconductor material with smaller refractive index. Deep mesa means that the etching profile passes the active region. This type of structure is mostly used in

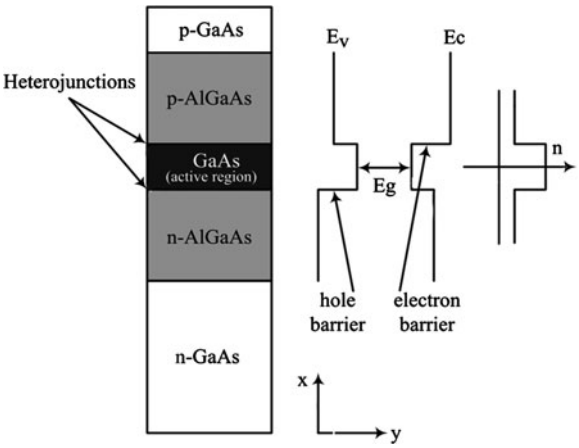

Fig. 1.44 Double heterostructure configuration, related energy band-edges and transversal confinement (x-direction) profile of an epitaxial GaAs-based waveguide structure

Al-free material systems like InGaAsP since Al-containing material suffer from interface recombination being exposed to air and subjected to overgrowth.

If overgrowth by semiconductor material is applied, the necessary width of mesa for single mode operation must be roughly the same as in the transverse direction; i.e. $\sim$1–2 μm which requires a sophisticated etching technique to guarantee uniformity of mesa width. Ridge waveguides are more simplified structures where the mesa depth is much shallower than buried heterostructures and the etching profile penetrates partially into upper cladding layer and because the active region remains unperturbed, various dielectric materials can be deposited around the mesa to provide the lateral confinement by forming a step-like refractive index. To achieve sufficient lateral optical confinement, the difference in thickness between ridge and the areas next to it must be large enough to cause reflection of light in this ridge. Due to effectively smaller step in ridge waveguides compared with buried heterostructures, a main challenges should be considered during waveguide design process of lasers and semiconductor optical amplifiers: The necessary width of single-mode ridge waveguide will be significantly broader than buried heterostructures and also in sufficiently wide waveguides, the lateral field pattern will be multimode. Figure 1.45 represents a structural schematic of a ridge waveguide and a buried heterostructure. Optically, the lateral confinement results in an effective index distribution as illustrated in Fig. 1.46a. By oxidizing the region outside the ridge and then metalizing the whole surface, a current distribution similar to that of oxide stripe structures can be obtained as presented in Fig. 1.46b. The current confinement causes gain guiding, the intensity distribution (Fig. 1.46c) however, is mainly a result of the index profile. Therefore ridge waveguide structures are in general of the index guiding type.

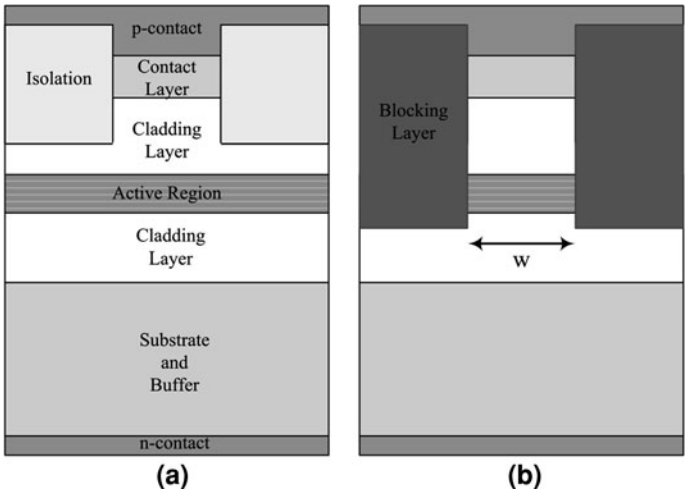

Fig. 1.45 Structural schematic of **a** ridge waveguide and **b** buried heterostructure

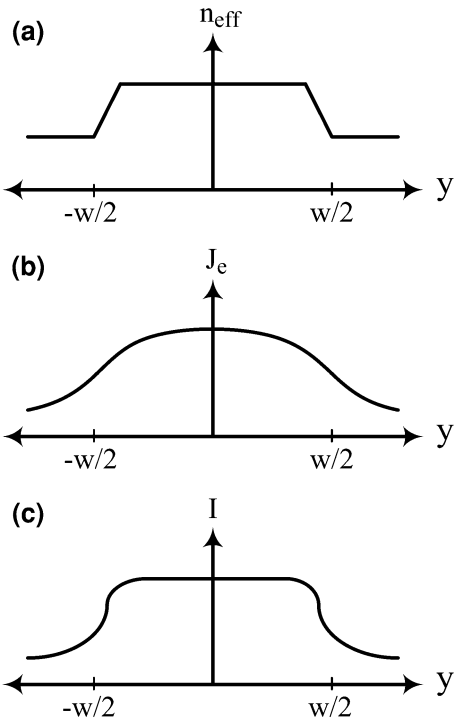

Fig. 1.46 **a** Lateral confinement (*y*-direction), **b** current distribution, and **c** intensity profile of a ridge waveguide structure

1.9.3 Waveguide Requirements of QD-SOA

1.9.3.1 Far-Field Pattern

Far-field characteristics of the output beam such as far-field divergence angle is an important design factors during fabrication and processing of semiconductor lasers and amplifiers. Based on different confinements in lateral and transverse directions due to different levels of confinement in various waveguide fabrication methods, the weaker confined transverse (or lateral) modes with their relative intensity determine the shape of far-field pattern of optoelectronic devices. Considering a first order mode intensity with two-dimensional Gaussian shape, the far-field shape of a QD-SOA may described as

$$I(X,Y) = |E_0|^2 e^{-2\left(\left(\frac{X}{w_X}\right)+\left(\frac{Y}{w_Y}\right)\right)^2} \tag{34}$$

where w_x and w_y are the beam waist diameters of the mode in vertical and lateral directions. The far-field divergence angles can be obtained accordingly based on the waist diameters as

$$\Theta_X = \frac{\lambda}{\pi w_X}, \quad \Theta_Y = \frac{\lambda}{\pi w_Y} \tag{35}$$

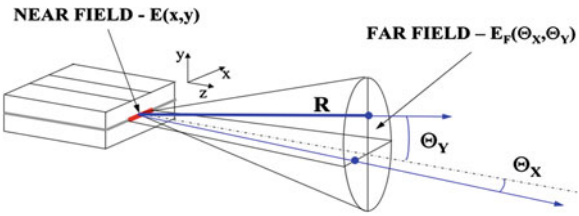

Fig. 1.47 Far-field and near-field emission patterns in lateral and transverse directions

Figure 1.47 illustrates the far and near field emission patterns with the angle distribution of the optical field far from the device.

Since most fiber coupling optics have numerical apertures below 0.5 (corresponding to a full acceptance angle of 50°), the far-filed divergence angle determines the efficient coupling condition. This means that a mode with larger far-field divergence than the numerical aperture will experience large coupling loss. The far-filed divergence angle can be lowered by increasing the active waveguide thickness. Although this method may lead to multimode operation of the waveguide but various techniques such as tilted cavities can be applied to the waveguide to support only the first order mode.

Computer aided design (CAD) programs such as BPM (beam propagation method) and WAVEGUIDE can be utilized to obtain the modal distribution, effective refractive index, near-field and far-field characterizations of ridge waveguide and buried heterostructures based on beam propagation and transfer matrix methods respectively. However, in order to utilize these programs in designing waveguides with QD active region, one should approximate the QD layers with an average refractive index since the CAD programs have been designed for epitaxial structures.

1.9.3.2 Facet Reflectivity Reduction

To create a traveling wave amplifier, the reflectivity of the semiconductor device facets, which prepare a Fabry–Perot cavity, must be reduced. These reflections at the facets of a SOA cause gain ripple. A reflection coefficient below −40 dB over the 3 dB gain bandwidth of the SOA is required for most of the applications. In practice, even antireflection coated facets will exhibit some residual reflectivity and form an optical cavity. Thus, the SOA transmission characteristic contains resonant peaks (ripple) whose absolute wavelength and spacing depends on the cavity dimensions. Increasing the amplifier gain, increases the gain ripple consequently and therefore any external parameter (e.g. input current) capable of increasing the amplifier gain, increases the gain ripple. This fact is illustrated in Fig. 1.48.

Assuming that the period of the input signal's maximum frequency component is much greater than the cavity round trip time, the intensity amplitude gain is defined as [47]

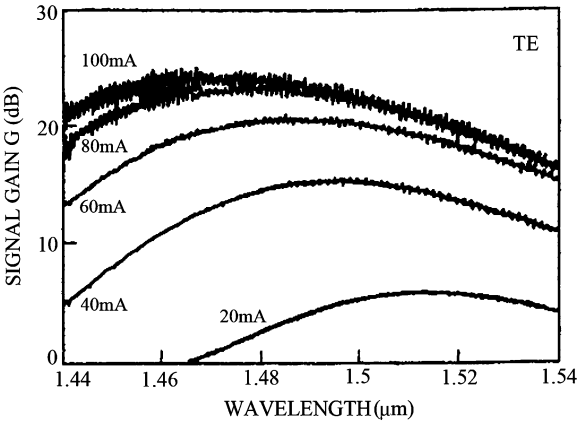

Fig. 1.48 Gain spectrum of a travelling wave SOA at different injection currents [8]

$$G = \frac{(1-R_1)(1-R_2)G_s}{(1+\sqrt{R_1R_2}G_s)^2 + 4\sqrt{R_1R_2}G_s \sin^2\phi} \tag{36}$$

where R_1 and R_2 are the residual facet reflectivity of two facets and G_s is the single pass gain given by

$$G_s = \exp(gL) = \exp\left[\left(\frac{\Gamma g_0}{1+P/P_s} - \alpha\right)L\right] \tag{37}$$

and ϕ is the phase shift defined as

$$\phi = \phi_0 + \frac{g_0 L\alpha}{2}\left(\frac{P}{P+P_s}\right) \tag{38}$$

In above equations g is net gain per unit length, L is the amplifier length, g_0 is unsaturated material gain coefficient, P and P_s are the internal optical power and the saturation power respectively, α is the linewidth enhancement factor, $\phi_0 = 2\pi$ Ln/λ is the nominal phase shift with n being the effective refractive index of the amplifier and Γ is the optical confinement factor. In most of practical cases R_1 and $R_2 < 10^{-3}$. Three approaches are commonly used to reduce the facet reflectivity: using an anti-reflection (AR) coating with a very low reflexivity, orienting the cavity at an angle with respect to the output fiber (tilting), or introducing transparent window regions at each face of the device.

1.9.3.3 Anti-Reflection Coating

Semiconductor optical amplifiers fabricated using an AR coating with a reflexivity of less than 10^{-2} can be classified as resonant or traveling-wave TW devices. As the reflexivity decreases the gain saturation decreases and the bandwidth capacity increases. Travelling wave devices with an AR coating with reflexivity less than

10^{-4} have a gain saturation of a few dB and a bandwidth capacity of more than 5 THz, for instance [48]. As a result of high bandwidth capacity, most telecommunications applications of SOAs require a travelling wave device design. Using titanium oxide/silicon oxide (TiO_2/SiO_2) for AR coating, reflectivity on the order of 10^{-5} has been achieved [48]. Also, by combining an AR coating with tilted facets at an angle of around 7°, devices with very small gain saturations can be created. AR coating can results in R = 0 theoretically using one dielectric layer with a coating thickness of $d = \lambda/4$ and refractive index of $n_{AR}=\sqrt{n_1 n_3}$ for the semiconductor–air interface (n_1 and $n_3 = 1$ are refractive indexes of semiconductor and air respectively) however, the resulting n_{AR} ($n_{AR} = 1.8$–1.9 for $n_1 = 3.2$–3.8) is not always achievable. Also, this reflectivity changes with wavelength variation. In turn, multi-layer AR coating provides more design flexibility for material and wavelength selection. Dielectric materials such as SiO_2, SiN and SiO_2–Si_3N_4 can be used as AR coatings and can be applied to an SOA by evaporation or sputtering techniques. Figure 1.49 shows a model of multilayer AR coating deposited on a SOA waveguide with effective active and cladding layer refractive indexes of n_a and n_c.

In order to determine the propagation of a plane monochromatic wave through a homogeneous dielectric medium one can use the characteristic matrix approach of the medium defined by [50]

$$M(z) = \begin{pmatrix} \cos(k_0 n_j h_j \cos\theta_j) & -\frac{i}{p_j}\sin(k_0 n_j h_j \cos\theta_j) \\ -i\, p_j \sin(k_0 n_j h_j \cos\theta_j) & \cos(k_0 n_j h_j \cos\theta_j) \end{pmatrix} \tag{39}$$

where $p_j = \sqrt{\varepsilon/\mu}\cos\theta_j$ for TE wave and for a TM wave the matrix hold with p replaced by $q_j = \sqrt{\mu/\varepsilon}\cos\theta_j$. In the case of a homogeneous dielectric film ε, μ and $n = \sqrt{\varepsilon\mu}$ are constants and for non-magnetic case the refractive ($\mu = 1$) index reduces to $n = \sqrt{\varepsilon}$. In the above characteristic matrix θ is the angle between the incident beam and the normal vector to the facet (z-axis) defined by $\theta_j = \sin^{-1}(n_i/n_j)\sin\theta_i$, h denotes the layer height, and i, j are the numbers of successive

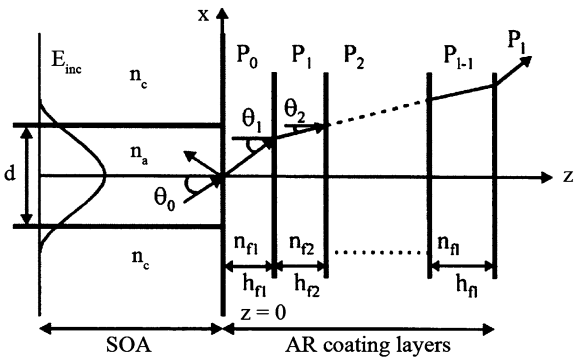

Fig. 1.49 Model of multi-layer AR coating (z > 0) deposited on SOA waveguide (z < 0) [49]

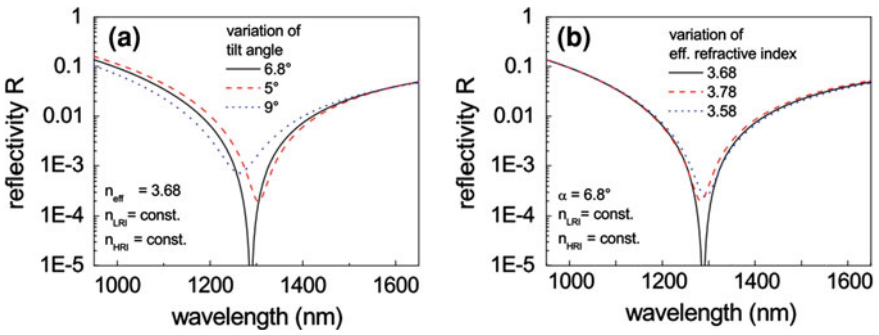

Fig. 1.50 Reflectivity of a two-layer AR coating for different **a** tilted waveguide angles and **b** effective refractive indexes, for TE light. *Courtesy*: M. Laemmlin (Institut für Festkörperphysik TU, Berlin)

layers. Introducing m_{11}, m_{12}, m_{21}, and m_{22} as the elements of the characteristic matrix, propagation through a multilayer structure can be obtained by multiplication of the characteristic matrix of each layer which results in reflection coefficient of the structure as

$$r = \frac{(m_{11} + m_{12}p_l)p_0 - (m_{21} + m_{22}p_l)}{(m_{11} + m_{12}p_l)p_0 + (m_{21} + m_{22}p_l)} \tag{40}$$

where p_0 and p_l stand for the first and last layers respectively and the reflexivity of the structure can be obtained via $R = |r|^2$. Although this method is not fully accurate for modal nature of light but provides a good insight for investigating the effect of multilayer AR coating. In Fig. 1.50, the reflectivity of a two-layer AR coating with constant low and high refractive indexes (LRI and HRI) for TE polarization have presented. The minimum reflectivity wavelength and also depth is completely dependent on the effective refractive index and tiled angle of the waveguide which demonstrate the importance of accurate coating process. It should be considered that in tilted waveguides, the reflectivity is strongly dependant to the light polarization.

1.9.3.4 Buried Facet (Window Structure)

Low facet reflectivity can also be achieved by window structures or buried facets for which the active waveguide is terminated in semiconductor material with a matching refractive index [51, 52]. Only a small part of the light coupled through the window sections will be reflected back into the waveguide and a gain ripple of 1.5 dB for a gain of 26 dB has been reported which corresponds to residual reflectivity of $\sim 10^{-4}$ [53]. Polarization independent reduction of the mode reflectivity is the main advantages of buried facet structures compared with

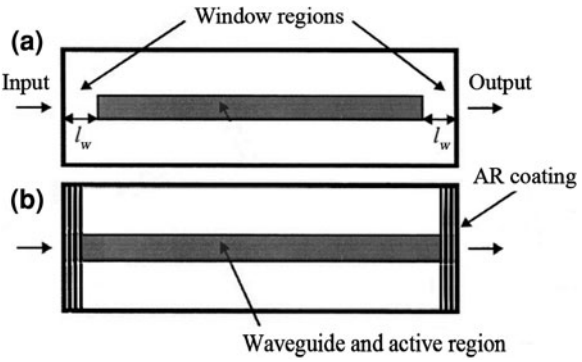

Fig. 1.51 Top view of **a** window structure **b** AR-coated SOAs

AR-coated devices. Window structures are composed a transparent region between the active region and end facets of which has an energy bandgap greater than the signal photon energy. Therefore, the propagating signal undergoes loss due to intrinsic material absorption and also deflects due to diffraction. Finally, the partially reflected signal from the end facet continues to broaden in space and only a small part of signal couples back into the active region. Therefore, extending the beam waist of the fundamental mode after the waveguide is the main purpose of window structures. Top structural view of a window structure and a AR-coated SOA has presented in Fig. 1.51 in order to compare the two reflectivity reduction methods.

The effective reflectivity of such a structure can be calculated using a Gaussian beam approximation for the propagating optical mode. Considering a distance dependant Gaussian beam waist from the spot size of the beam waist, w_0, with

$$w(z)^2 = w_0^2\left(1 + \left(\frac{\lambda z}{\pi w_0^2}\right)^2\right) \tag{41}$$

the reflectivity R reduces to

$$R_{eff} = \frac{R}{1 + (2d/kw^2)^2} \tag{42}$$

where d is the length of the buried facet region and λ is the optical wavelength ($k = 2\pi/\lambda$). It is possible to decrease the effective reflectivity with increasing the length of window region denoted by l_w in Fig. 1.51. However, this will happen at the hands of degrading the coupling efficiency from the SOA to an optical fiber.

Although the residual reflection may cause deficiencies in optical characteristics of SOAs, an optimal design for facet reflections can accelerate gain recovery and improve cross-gain modulation (XGM) and cross-phase modulation (XPM) related dynamic characteristics of SOAs. A half reflective semiconductor optical amplifier (HR-SOA) with a cleaved rear facet and an AR-coated front facet can be

considered to investigate the effect of different reflectivities on dynamic characteristics of SOA [54].

1.9.3.5 Tilted Waveguide/Facet

The main idea in an angled facet SOA is decreasing the effective reflectivity of the tilted facet relative to a normally cleaved facet. Considering a Gaussian waveguide mode filed given by $E_y = A_y \exp(-x^2/w^2)$ with w as the half width of the mode at 1/e, reflectivity of a tilted waveguide can be obtained as [55]

$$R = R_f(\theta)\left[-\left(\frac{2\pi n_2 w\theta}{\lambda}\right)^2\right] \tag{43}$$

where R_f is the Fresnel reflection of a plane wave reflected from a tilted interface between the amplifier facet and air. Considering n_1 and n_2 as the effective refractive indices of the active and cladding regions, R_f for a TE wave can be described by [50]

$$R_f(\theta) = \left(\frac{n_{air}\cos\theta - n_1\sqrt{1-(n_1^2/n_{air}^2)\sin^2\theta}}{n_{air}\cos\theta + n_1\sqrt{1-(n_1^2/n_{air}^2)\sin^2\theta}}\right)^2, \quad (n_{air}=1) \tag{44}$$

where θ is the tilt angle. It should be noted that increasing the tilt angle degrades the coupling efficiency between the amplifier and optical fiber due to far-field asymmetry. Figure 1.52 shows a schematic of a tilted facet SOA with related reflectivity simulations. Typical facet angles between 7° and 10° are usually used in order to reduce the facet reflectivity.

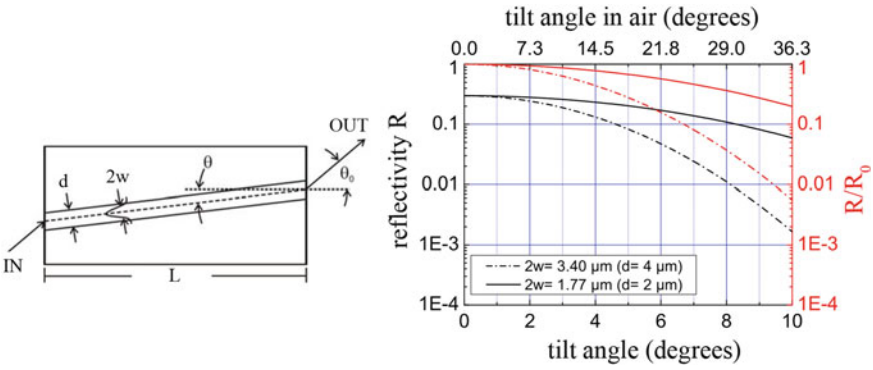

Fig. 1.52 Schematic of a tilted facet SOA and related reflectivity (*left axis data*) and relative loss (*right axis data*) as a function of waveguide tilt angle. *Courtesy*: M. Laemmlin (Institut für Festkörperphysik TU, Berlin)

References

1. Schubert, C., Ludwig, R., Weber, H.-G.: High-speed optical signal processing using semiconductor optical amplifiers. J. Opt. Fiber Commun. Rep. **2**, 171–208 (2004)
2. Borri, P., Langbein, W., Hvam, J.M., Heinrichsdorff, F., Mao, H.M., Bimberg, D.: Spectral hole-burning and carrier-heating dynamics in InGaAs quantum-dot amplifiers. IEEE J. Sel. Topics Quantum Electron. **6**, 544–551 (2000)
3. Borri, P., Schneider, S., Langbein, W., Woggon, U., Zhukov, A.E., Ustinov, V.M., Ledentsov, N.N., Alferov, Z.I., Ouyang, D., Bimberg, D.: Ultrafast carrier dynamics and dephasing in InAs quantum-dot amplifiers emitting near 1.3 μm-wavelength at room temperature. Appl. Phys. Lett. **79**, 2633–2635 (2001)
4. Berg, T.W.: Quantum dot semiconductor optical amplifiers—Physics and application. In: Department of Communications, Optics & Materials (COM). 2004, Technical University of Denmark, Lyngby
5. Kim, J., Laemmlin, M., Meuer, C., Bimberg, D., Eisenstein, G.: Small-signal cross-gain modulation of quantum-dot semiconductor optical amplifiers. IEEE J. Quantum Electron. **45**, 240–248 (2009)
6. Mork, J., Nielsen, M.L., Berg, T.W.: The dynamics of semiconductor optical amplifiers: modeling and applications. Opt. Photon. News **14**, 42–48 (2003)
7. Dommers, S., Temnov, V.V., Woggon, U., Gomis, J., Pastor, J.M., Laemmlin, M., Bimberg, D.: Complete ground state gain recovery after ultrashort double pulses in quantum dot based semiconductor optical amplifier. Appl. Phys. Lett. **90**, 033508–033510 (2007)
8. Dutta, N.K., Wang, Q.: Semiconductor Optical Amplifiers. World Scientific, New Jersey (2006)
9. Uskov, A., O'Reilly, E., Manning, R., Webb, R., Cotter, D., Laemmlin, M., Ledentsov, N., Bimberg, D.: On ultrafast optical switching based on quantum-dot semiconductor optical amplifiers in nonlinear interferometers. IEEE Photon. Technol. Lett. **16**, 1265–1267 (2004)
10. Henry, C.: Theory of the linewidth of semiconductor lasers. IEEE J. Quantum Electron. **18**, 259–264 (1982)
11. Schneider, S., Borri, P., Langbein, W., Woggon, U., Sellin, R., Ouyang, D., Bimberg, D.: Linewidth enhancement factor in InGaAs quantum-dot amplifiers. IEEE J. Quantum Electron. **40**, 1423–1429 (2004)
12. Van der Poel, M., Gehrig, E., Hess, O., Birkedal, J., Hvam, D.: Ultrafast gain dynamics in quantum-dot amplifiers: theoretical analysis and experimental investigations. IEEE J. Quantum Electron. **41**, 1115–1123 (2005)
13. Kim, J., Su, H., Minin, S., Chuang, S.L.: Comparison of linewidth enhancement factor between p-doped and undoped quantum-dot lasers. IEEE Photon. Technol. Lett. **18**, 1022–1024 (2006)
14. Berg, T.W., Mørk, J.: Saturation and noise properties of quantum-dot optical amplifiers. IEEE J. Quantum Electron. **40**, 1527–1539 (2004)
15. Baney, D.M., Gallion, P., Tucker, R.S.: Theory and measurement techniques for the noise figure of optical amplifiers. Opt. Fiber Technol. **6**, 122–154 (2000)
16. Desurvire, E., Desthieux, B.: Fundamental limitations of EDFAs in amplified transmission systems. In: Proceedings of the OFC '99, Tutorial Session, Paper ThL, pp. 123–140 (1999)
17. Ebe, H., Uetake, A., Akiyama, T., Kawaguchi, K., Ekawa, M., Kuramata, A., Nakata, Y., Sugawara, M., Arakawa, Y.: Internal strain of self-assembled $In_xGa_{1-x}As$ quantum dots calculated to realize transverse-magnetic-mode-sensitive interband optical transition at wavelengths of 1.5 μm bands. Jpn. J. Appl. Phys. **44**, 6312–6316 (2005)
18. Saito, T., Nakaoka, T., Kakitsuka, T., Yoshikuni, Y., Arakawa, Y.: International Symposium on Quantum Dots and Photonic Crystals (QDPC2003), P-20 (2003)
19. Kawaguchi, K., Yasuoka, N., Ekawa, M., Ebe, H., Akiyama, T., Sugawara, M., Arakawa, Y.: Controlling polarization of 1.55 μm columnar InAs quantum dots with highly tensile-strained InGaAsP barriers on InP(001). Jpn. J. Appl. Phys. **45**, L1244–L1246 (2006)

20. Yasuoka, N., Kawaguchi, K., Ebe, H., Akiyama, T., Ekawa, M., Tanaka, S., Morito, K., Uetake, A., Sugawara, M., Arakawa, Y.: Demonstration of transverse-magnetic dominant gain in quantum dot semiconductor optical amplifiers. Appl. Phys. Lett. **92**, 101108 (2008)
21. Yasuoka, N., Kawaguchi, K., Ebe, H., Akiyama, T., Ekawa, M., Morito, K., Sugawara, M., Arakawa, Y.: 1.55 μm polarization-insensitive quantum dot semiconductor optical amplifier. ECOC 2008, vol. 4, pp. 17–18, Brussels, Belgium, 2008
22. Yasuoka, N., Kawaguchi, K., Ebe, H., Akiyama, T., Ekawa, M., Morito, K., Sugawara, M., Arakawa, Y.: Quantum-dot semiconductor optical amplifiers with polarization-independent gains in 1.5 μm wavelength bands. IEEE Photon. Technol. Lett. **20**, 1908–1910 (2008)
23. Sandall, I.C., Smowton, P.M., Thomson, J.D., Badcock, T., Mowbray, D.J., Liu, H.Y., Hopkinson, M.: Temperature dependence of threshold current in p-doped quantum dot lasers. Appl. Phys. Lett. **89**, 15–17 (2006)
24. Rossetti, M., Li, L., Fiore, A., Occhi, L., Velez, C., Mikhrin, S., Kovsh, A.: High-power quantum-dot superluminescent diodes with p-doped active region. IEEE Photon. Technol. Lett. **18**, 1946–1948 (2006)
25. Deppe, D.G., Freisem, S., Huang, H., Lipson, S.: Electron transport due to inhomogeneous broadening and its potential impact on modulation speed in p-doped quantum dot lasers. J. Phys. D **38**, 2119–2125 (2005)
26. Sandall, I.C., Smowton, P.M., Walker, C.L., Badcock, T., Mowbray, D.J., Liu, H.Y., Hopkinson, M.: The effect of *p* doping in InAs quantum dot lasers. Appl. Phys. Lett. **88**, 111113-1-3 (2006)
27. Fathpour, S., Mi, Z., Bhattacharya, P.: High-speed quantum dot lasers. J. Phys. D **38**, 2103–2111 (2005)
28. Ğundogdu, K., Hall, KC., Boggess, T.F., Deppe, D.G., Shchekin, O.B.: Ultrafast electron capture into *p*-modulation-doped quantum dots. Appl. Phys. Lett. **85**, 4570-1-3 (2004)
29. Sun, K.W., Kechiantz, A., Lee, B.C., Lee, C.P.: Ultrafast carrier capture and relaxation in modulation-doped InAs quantum dots. Appl. Phys. Lett. **88**, 163117-1-3 (2006)
30. Bimberg, D., Meuer, C., Fiol, G., Schmeckebier, H., Arsenijevic, D., Eisenstein, G.: Influence of p-doping in quantum dot semiconductor optical amplifiers at 1.3 μm. ICTON (2009)
31. Cesari, V., Langbein, W., Borri, P., Rossetti, M., Fiore, A., Mikhrin, S., Krestikov, I., Kovsh, A.: Ultrafast carrier dynamics in p-doped InAs/GaAs quantum-dot amplifiers. IET Optoelectron. **1**, 298–302 (2007)
32. Cesari, V., Borri, P., Rossetti, M., Fiore, A., Langbein, W.: Refractive index dynamics and linewidth enhancement factor in p-doped InAs–GaAs quantum-dot amplifiers. IEEE J. Quantum Electron. **45**, 579–585 (2009)
33. Qasaimeh, O.: Effect of doping on the optical characteristics of quantum-dot semiconductor optical amplifiers. J. Lightw. Technol. **27**, 1978–1984 (2009)
34. Asasa, M., Kameyama, A., Suematsu, Y.: Gain and intervalence band absorption in quantum-well lasers. IEEE J. Quantum Electron. **20**, 745–753 (1984)
35. Berg, T.W., Bischoff, S., Magnusdottir, I., Mørk, J.: Ultrafast gain recovery and modulation limitations in self-assembled quantum-dot devices. IEEE Photon. Technol. Lett. **13**, 541–543 (2001)
36. Qasaimeh, O.: Ultra-fast gain recovery and compression due to Auger-assisted relaxation in quantum dot semiconductor optical amplifiers. J. Lightw. Technol. **27**, 2530–2536 (2009)
37. Qasaimeh, O.: Characteristics of cross-gain wavelength conversion in quantum dot semiconductor optical amplifiers. IEEE Photon. Technol. Lett. **16**, 542–544 (2004)
38. Ohnesorge, B., Albrecht, M., Oshinowo, J., Forchel, A., Arakawa, Y.: Rapid carrier relaxation in self-assembled InGaAs-GaAs quantum dots. Phys. Rev. B **54**, 11532–11538 (1996)
39. Morris, D., Perret, N., Fafard, S.: Carrier energy relaxation by means of Auger processes in InAs/GaAs self-assembled quantum dots. Appl. Phys. Lett. **75**, 3593–3595 (1999)
40. Giorgi, M.D., Lingk, C., Plessen, G.V., Feldmann, J., Rinaldis, S.D., Passaseo, A., Vittorio, M.D., Cingolani, R., Lomascolo, M.: Capture and thermal re-emission of carriers in long-wavelength InGaAs/GaAs quantum dots. Appl. Phys. Lett. **79**, 3968–3970 (2001)

41. Wu, Z., Choi, H., Su, X., Chakrabarti, S., Bhattacharya, P., Norris, T.B.: Ultrafast electronic dynamics in unipolar n-doped InGaAs–GaAs self-assembled quantum dots. IEEE J. Quantum Electron. **43**, 486–496 (2007)
42. Stranski, I.N., Krastanow, L.: Sitz. Ber., Oesterr. Akad. Wiss., Math.-Nat.wiss.Kl.II **146**, 797 (1938)
43. Maximov, M.V., Tsatsul'nikov, B.V., Volovik, B.V., Sizov, D.S., Shernyakov, Y.M., Kaiander, I.N., et al.: Tuning quantum dot properties by activated phase separation of an InGa(Al)As alloy grown on InAs stressors. Phys. Rev. B **62**, 16671–16680 (2000)
44. Costantini, G., Rastelli, A., Manzano, C., Songmuang, R., Schmidt, O.G., Kern, K., von Känel, H.: Universal shapes of self-organized semiconductor quantum dots: striking similarities between InAs/GaAs(001) and Ge/Si(001). Appl. Phys. Lett. **85**, 5673–5675 (2004)
45. Kovsh, A.R., Maleev, N.A., Zhukov, A.E., Mikhrin, S.S., Vasil'ev, A.P., Semenova, E.A., Shernyakov, Y.M., Maximov, M.V., Livshits, D.A., Ustinov, V.M., Ledentsov, N.N., Bimberg, D., Alferov, Z.I.: InAs/InGaAs/GaAs quantum dot lasers of 1.3 μm range with enhanced optical gain. J. Cryst. Growth **251**, 729–736 (2003)
46. Laemmlin, M., Bimberg, D., Uskov, A.V., Kovsh, A.R., Ustinov, V.M.: Semiconductor optical amplifiers near 1.3 μm based on InGaAs/GaAs quantum dots. CThB6, 96, Conference on Lasers and Electro-Optics (CLEO). Optical Society of America, San Francisco, (2004)
47. O'Mahony, M.: Semiconductor laser optical amplifiers for use in future fiber systems. J. Lightw. Technol. **6**, 531–544 (1988)
48. Bernard, J., Renaud, M.: Semiconductor optical amplifiers. SPIE's OE Mag. **1**, 36–38 (2001)
49. Saitoh, T., Mukai, T., Mikame, O.: Theoretical analysis and fabrication of antireflection coatings on laser-diode facets. J. Lightw. Technol. **3**, 288–293 (1985)
50. Born, M., Wolf, E.: Principles of Optics, 6th edn. Pergamon Press, Oxford (1993)
51. Olsson, N.A., Kazarinov, R.F., Nordland, W.A., Henry, C.H., Oberg, M.G., White, H.G., Garbinski, P.A., Savage, A.: Polarisation-independent optical amplifier with buried facets. Electron. Lett. **25**, 1048–1049 (1989)
52. Dutta, N.K., Lin, M.S., Piccirilli, A.B., Brown, R.L., Wynn, J., Coblentz, D., Twu, Y., Chakrabarti, U.K.: Fabrication and performance characteristics of buried-facet optical amplifiers. J. Appl. Phys. **67**, 3943–3947 (1990)
53. Cha, I., Kitamura, M., Honmou, H., Mito, I.: 1.5 μm band travelling-wave semiconductor optical amplifier with window facet structure. Electron. Lett. **25**, 1241–1242 (1989)
54. Zhou, E., Zhang, X., Huang, D.: Analysis on dynamic characteristics of semiconductor optical amplifiers with certain facet reflection based on detailed wideband model. Opt. Express **15**, 9096–9106 (2007)
55. Marcuse, D.: Reflection loss of laser mode from tilted end mirror. J. Lightw. Technol. **7**, 336–339 (1989)

Chapter 2
Simulation Methods of Quantum-Dot Semiconductor Optical Amplifiers

2.1 Introduction

In modeling a semiconductor optical amplifier, one would first consider how the carrier dynamics are modeled. Secondly, one would be concerned about how to model the optical field propagation. There exist many SOA models of different accuracies. The most accurate way of modeling an SOA is to solve the semiconductor bloch equation (SBE) but this is extremely time-consuming. The computation time is not acceptable for the system applications of SOA-based devices, where many optical pulses have to be transmitted through the SOA to evaluate the system performance. A simplified approach is to include certain physical processes phenomenologically, as it is done in rate-equation models. These models enjoy the much faster calculation speeds. Although the accuracy for sub-picosecond pulses is not as good as the SBE calculations, the rate equation models are quite successful in explaining the experimental results for both laser diodes and SOAs. In early 1990s, Mørk et al. introduced the concept of the local carrier density in the SOA modeling and by doing so, intra-band carrier dynamics such as spectral hole burning, carrier heating and free carrier absorption can be modeled with great success to explain the pump-probe experimental results.

Numerical modeling is always necessary to understand the working principle of the devices and to optimize their performance. It is also useful to verify a novel idea before implementing it in the lab. It also allows the applications engineer to predict how an SOA or cascade of SOAs behaves in a particular application. It means, physical modeling of complex devices including SOA, such as all-active MZIs, is necessary in order to understand their potential and limitations. In addition, a reliable physical model may be used to investigate new configurations leading to superior ways of operating devices, or possibly to development of entirely new device structures.

The main purpose of modeling a SOA is to relate the internal variables of the amplifier to measurable external variables such as the output signal power,

A. Rostami et al., *Nanostructure Semiconductor Optical Amplifiers*,
Engineering Materials, DOI: 10.1007/978-3-642-14925-2_2,

saturation output power and amplified spontaneous emission (ASE) spectrum. This aids the design and optimization of SOA for a given application. As the SOA model equations contain coupled derivatives of time and space, thus they have rarely analytical solutions. However, analytical solutions of SOA equations can give a deep understanding on how internal variables of the device vary by external conditions such as injection current, input pump, temperature, etc. Also, an analytical solution may exactly exhibit the limitation of the operation since it contains the influence of physical phenomena explicitly. Due to the mentioned difficulties of obtaining an analytical solution, a numerical solution is required in most of applications.

Numerical techniques are usually more complex but make fewer assumptions and are often applicable over a wide range of operating regimes. With the advent of fast personal computers, numerical techniques are beginning to supersede analytical techniques.

In spite of intensive research on numerical modeling of QD-SOAs, both theoretically and experimentally, there still remains an unexplored area. This involves the development of equivalent circuit models for QD-SOAs suitable for circuit simulation by using standard packages like SPICE. Considering the fact that numerical techniques as the solution of the rate equations require long and tedious computational time, analysis of equivalent circuit models with circuit programs reduces the computational time several orders.

In this chapter, we bring examples of modeling QD-SOAs by well-known numerical, analytical and equivalent circuits.

2.2 Numerical Methods

A comprehensive model should include the effect of several factors on QD-SOA performance. Most of modeling methods consider quantum dots grown by the Stranski–Krastanov mode as active region for QD-SOAs and thus some presumptions are considered. In this manner, performance of QD-SOAs is primarily dominated by the dynamics of carriers and photons, like carrier relaxation, capture, re-excitation rate into quantum dots, radiative and non-radiative recombination rates of carriers, inhomogeneous broadening of dot resonant energy due to size fluctuation of dots, homogeneous broadening of optical gain due to polarization dephasing rate, coulomb effects between electrons and holes and optical nonlinearities.

The most popular and useful way to deal with carrier and photon dynamics in opto-electronic devices is to solve rate equations for carriers and photons. In the modeling process described in this section, quantum dots are considered to be spatially isolated and each quantum dot exchange carries with the wetting layer. Quantum dots are grouped by their resonant energy so that the model can justify the inhomogeneously broadened gain spectra due to dot size fluctuation and the homogeneous broadening of dots which originates from carrier-LO phonon and carrier-carrier scatterings, has inserted into the rate equations. The homogeneous

broadening plays a crucial rule in processing applications and determines the channel spacing in multi-wavelength operations [1]. Also, an interesting phenomenon happens in quantum dot lasers due to homogeneous broadening where homogeneous broadening of optical gain connects spatially isolated and energetically different quantum dots by bringing the carriers into the central lasing mode by stimulated emission and thus lasing emission with a narrower linewidth takes place even compared with negligible homogeneous broadening case [2].

The schematic of inhomogeneously broadened quantum dot ensemble grouped by the resonant energy of dots and the related photon distribution is illustrated in Fig. 2.1.

Different approaches have been introduced to treat electron and hole dynamics. In a vastly used model, one may consider an electron and a hole as an exciton and use a common time constant for various processes [2, 3]. Separate consideration of electron and hole dynamics is another approach used in the researches [4].

By separate considering the electron and hole dynamics, one can develop a generalized set of equations to consider the effect of different physical phenomena such as carrier doping [5]. So, this section introduces this approach by considering separate time constant for the processes associated with electrons and holes in a quantum dot structure.

Band diagram of a quantum dot group consisting discrete ground and excited energy levels, continuum like upper state (ensemble of dense energy states in each dot which merge into the two-dimensional energy states of the wetting layer) and quantum well-type wetting layer is displayed in Fig. 2.2 where ground states, excited states and upper states are considered to be two-spin degenerate, fourfold degenerate and many-fold degenerate respectively. Finally, quantum dots and photon modes are divided into M ($j = 1, \ldots, M$) and N ($k = 1, \ldots, N$) groups, respectively.

The linear optical gain of ground or excited state of jth quantum dot group to kth photon mode can be expressed as

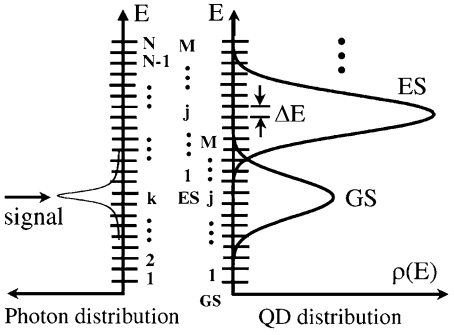

Fig. 2.1 Grouping of inhomogeneously broadened quantum dot ensemble and the related photon mode distribution [5]

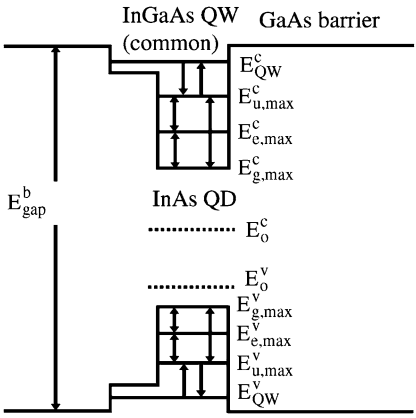

Fig. 2.2 Band diagram of a quantum dot group with maximally allowable energy states defined by $E_{i,max}$ [5]

$$g_{jk}^{g(e)} = \frac{\pi q^2}{n_b c \varepsilon_0 m_0^2 \omega_k} |p_{cv}|^2 D_{g(e)} N_D G_j^s \times \frac{\Gamma_h/(2\pi)}{\left(E^c_{g(e),j} - E^v_{g(e),j} - \hbar\omega_k\right)^2 + (\Gamma_h/2)^2} \tag{1}$$

where p_{cv} is the transition matrix element, c is the velocity of light, q is the electron charge, m_0 is the free electron mass, n_b is the background refractive index, ε_0 is the permittivity of vacuum, N_D is quantum dot volume density, G_j^s is the fraction of the radiative electron–hole recombination from the *j*th quantum dot group which has the Gaussian distribution with the FWHM of $\Gamma_s = \Gamma_c + \Gamma_v = 50$ meV. The degeneracy of ground and excited states denoted by $D_{g(e)}$ are $D_g = 2$ and $D_e = 4$ and their related energy in *j*th group are described by $E^c_{g(e),j}$, for conduction band and $E^v_{g(e),j}$ for valence band. Γ_h is the FWHM of homogeneous broadening ranging from 16 to 19 meV in quantum dot lasers [2] and about 10 meV in quantum dot amplifiers [6]. As it is obvious in (1), a Lorentzian line shape function is used for the homogeneous broadening.

The transition matrix element (neglecting the optical-field polarization dependence) is expressed as

$$|p_{cv}|^2 = |I_{c,v}|^2 \cdot M^2 \tag{2}$$

where $I_{c,v}$ is the overlap integral between the envelope functions of an electron and a hole given by

$$M^2 = \frac{m_0^2}{12 m_e^*} \frac{E_g(E + \Delta)}{E_g + 2\Delta/3} \tag{3}$$

Here, E_g is the band gap, Δ is the spin–orbit splitting energy and m_e^* is the electron effective mass.

The propagation of optical signal and the ASE along the QD-SOA can be expressed by

$$\frac{\partial P(\omega_k, z)}{\partial z} = [\Gamma g(\omega_k, z) - \alpha_i] P(\omega_k, z) \tag{4}$$

$$\frac{\partial P_{sp}(\omega_k, z)}{\partial z} = [\Gamma g(\omega_k, z) - \alpha_i] P_{sp}(\omega_k, z) + \Gamma g_{sp}(\omega_k, z) P_{vac}(\omega_k). \tag{5}$$

P, P_{sp}, α_i, Γ, g_{sp} and P_{vac} are optical signal power, ASE power, intrinsic loss, confinement factor, optical gain for spontaneous emission and the optical power of the vacuum field between the frequency ω_k and $\omega_k + \Delta\omega$ [7].

In self-assembled quantum dots, carriers are injected into the wetting layer and then they are captured by upper states following with relaxation to excited and ground states. Then, the carrier population dynamics of the wetting layer $n_w^{c(v)}$, the upper state $n_{u,j}^{c(v)}$, the excited state $n_{e,j}^{c(v)}$ and the ground state $n_{g,j}^{c(v)}$ of the jth group with corresponding occupation probabilities of $f_w^{c(v)}$, $f_{u,j}^{c(v)}$, $f_{e,j}^{c(v)}$ and $f_{g,j}^{c(v)}$ is described by the following rate equations [5]

$$\begin{aligned} \frac{dn_w^{c(v)}}{dt} &= \frac{J.A}{q} + \sum_j \frac{n_{u,j}^{c(v)}}{\tau_{uw,j}^{c(v)}} \left(1 - f_w^{c(v)}\right) \\ &\quad - \sum_j \frac{n_w^{c(v)}}{\tau_{wu}^{c(v)}} G_j^{c(v)} \left(1 - f_{u,j}^{c(v)}\right) - \frac{\sqrt{n_w^c n_w^v}}{\tau_{wr}} \end{aligned} \tag{6}$$

$$\begin{aligned} \frac{dn_{u,j}^{c(v)}}{dt} &= \frac{n_w^{c(v)}}{\tau_{wu}^{c(v)}} G_j^{c(v)} \left(1 - f_{u,j}^{c(v)}\right) - \frac{n_{u,j}^{c(v)}}{\tau_{uw}^{c(v)}} \left(1 - f_w^{c(v)}\right) \\ &\quad + \frac{n_{e,j}^{c(v)}}{\tau_{eu}^{c(v)}} \left(1 - f_{u,j}^{c(v)}\right) - \frac{n_{u,j}^{c(v)}}{\tau_{ue}^{c(v)}} \left(1 - f_{e,j}^{c(v)}\right) + \frac{n_{g,j}^{c(v)}}{\tau_{gu}^{c(v)}} \left(1 - f_{u,j}^{c(v)}\right) \\ &\quad - \frac{n_{u,j}^{c(v)}}{\tau_{ug}^{c(v)}} \left(1 - f_{g,j}^{c(v)}\right) - \frac{\sqrt{n_{u,j}^c n_{u,j}^v}}{\tau_{dr}} \end{aligned} \tag{7}$$

$$\begin{aligned} \frac{dn_{e,j}^{c(v)}}{dt} &= \frac{n_{u,j}^{c(v)}}{\tau_{ue}^{c(v)}} \left(1 - f_{e,j}^{c(v)}\right) - \frac{n_{e,j}^{c(v)}}{\tau_{eu}^{c(v)}} \left(1 - f_{u,j}^{c(v)}\right) \\ &\quad + \frac{n_{g,j}^{c(v)}}{\tau_{ge}^{c(v)}} \left(1 - f_{e,j}^{c(v)}\right) - \frac{n_{e,j}^{c(v)}}{\tau_{eg}^{c(v)}} \left(1 - f_{g,j}^{c(v)}\right) \\ &\quad - \frac{\sqrt{n_{e,j}^c n_{e,j}^v}}{\tau_{dr}} - \Gamma L \sum_k g_{jk}^e \frac{P_k}{\hbar \omega_k} \left(f_{e,j}^c + f_{e,j}^v - 1\right) \end{aligned} \tag{8}$$

$$\begin{aligned}\frac{dn_{g,j}^{c(v)}}{dt} &= \frac{n_{u,j}^{c(v)}}{\tau_{ug}^{c(v)}}\left(1-f_{g,j}^{c(v)}\right)-\frac{n_{g,j}^{c(v)}}{\tau_{gu}^{c(v)}}\left(1-f_{u,j}^{c(v)}\right)\\ &+\frac{n_{e,j}^{c(v)}}{\tau_{eg}^{c(v)}}\left(1-f_{g,j}^{c(v)}\right)-\frac{n_{g,j}^{c(v)}}{\tau_{ge}^{c(v)}}\left(1-f_{e,j}^{c(v)}\right)\\ &-\frac{\sqrt{n_{g,j}^{c}n_{g,j}^{v}}}{\tau_{dr}}-\Gamma L\sum_{k}g_{jk}^{g}\frac{P_k}{\hbar\omega_k}\left(f_{g,j}^{c}+f_{g,j}^{v}-1\right).\end{aligned} \tag{9}$$

In above equations, J is the input injection current density and A is the cross section area. The transition time constants for carriers are denoted by $\tau_{xy}^{c(v)}$ where the superscript $c(v)$ stands for electron (hole) band and the subscript xy stands for transition from state x to state y $\tau_{eg}^{c(v)}$ determines the relaxation time from the excited state to the ground state for instant). τ_{dr} and τ_{wr} are the recombination time constants in dot and wetting layer, respectively. Typical value of parameters and time constants used in the rate equations can be summarized as, $\tau_{wr} = 0.2$ ns, $\tau_{dr} = 1$ ns, $\tau_{wu}^{c} = 3$ ps, $\tau_{ue}^{c} = \tau_{ug}^{c} = \tau_{eg}^{c} = 1$ ps, $\tau_{wu}^{v} = \tau_{ue}^{v} = \tau_{ug}^{v} = \tau_{eg}^{v} = 0.13$ ps, $D_g = 2$, $D_e = 4$, $D_u^{c(v)} = 10(20)$, $D_w^{c(v)} = 100(200)$, $\alpha_i = 5$ cm^{-1} and $\Gamma = 0.025$.

The value of time constants have obtained from the pump-probe experiments [8], [9] and carrier escape times can be evaluated from the reported relaxation time constants through the relation

$$\tau_{yx}^{c(v)} = \tau_{xy}^{c(v)}\frac{D_y}{D_x}\exp\left(\frac{\Delta E_{xy}^{c(v)}}{kT}\right) \tag{10}$$

where $\Delta E_{xy}^{c(v)}$ is the energy difference between the state y and the state x in the conduction (valence) band.

2.3 Equivalent Circuit Methods

In order to derive an equivalent circuit model of a QD-SOA one should first determine band structure of the active region and then the governing rate equation of the active region should be obtained.

It is assumed that the QDs and WL are surrounded by a barrier material which separates the QD layers to the extent that the dot layers do not couple directly. Furthermore, tunneling between dots within the same layer is neglected. The transition of conduction band ground state (CBGS) to valence band ground state (VBGS) is assumed to be the main stimulated transition by input signal.

Band energy diagram of a quantum dot with related energy levels and intraband relaxation processes considered for extraction of rate equations and subsequent circuit model is illustrated in Fig. 2.3. Here, the rate equations of the active region model are written. The photon propagation equation of input signal and the

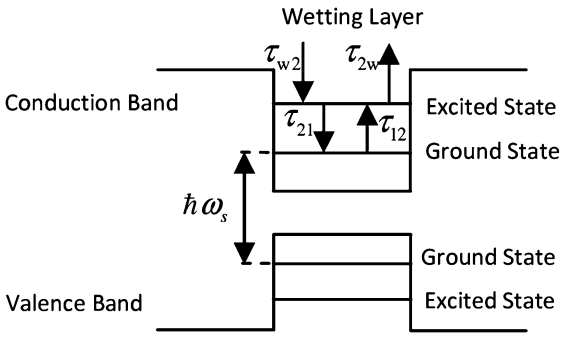

Fig. 2.3 Band energy diagram of a quantum dot with related energy levels and intraband relaxation processes [10]

population dynamics of the wetting layer, the excited state and the ground state can be written as [10]

$$\frac{\partial P_s(z,\tau)}{\partial z} = (g - \alpha_{\text{int}})P_s(z,\tau) \tag{11}$$

$$\frac{\partial N_w(z,\tau)}{\partial \tau} = \frac{I}{eV} - \frac{N_w(1-h)}{\tau_{w2}} + \frac{\tilde{N}_Q h}{\tau_{2w}} - \frac{N_w}{\tau_{wR}} \tag{12}$$

$$\frac{\partial \tilde{N}_Q h(z,\tau)}{\partial \tau} = \frac{N_w(1-h)}{\tau_{w2}} - \frac{\tilde{N}_Q h}{\tau_{2w}} - \frac{\tilde{N}_Q h(1-f)}{\tau_{21}} + \frac{\tilde{N}_Q f(1-h)}{\tau_{12}} \tag{13}$$

$$\frac{\partial \tilde{N}_Q f(z,\tau)}{\partial \tau} = \frac{\tilde{N}_Q h(1-f)}{\tau_{21}} - \frac{\tilde{N}_Q f(1-h)}{\tau_{12}} - \frac{\tilde{N}_Q f^2}{\tau_{1R}} - \frac{g}{\sigma\hbar\omega_s}P_s(z,\tau) \tag{14}$$

where P_s, g and α_{int} are the optical power of input signal, the modal gain, the absorption coefficient of material in signal wavelength, respectively and z is the distance in longitudinal direction, i.e. $z = 0$ and $z = L$ stand for input and output facets of the QD-SOA. $\hbar\omega$ is the photon energy. L_w, σ and V are the effective thickness of active layer, cross section of the quantum dots or active layer and total volume of the quantum dots, respectively. N_Q is the surface density of quantum dots where its typical value is $\sim 5\times10^{10}$ cm^{-2} and $\tilde{N}_Q = N_Q/L_w$ is the effective volume density of quantum dots. Due to the larger effective mass of holes compared to electrons and resulting smaller level spacing, holes are expected to relax faster than electrons [11] and hence, electrons are assumed to limit the carrier dynamics.

The pump term in (12) is given as I/eV, with I being the bias current and e the magnitude of the electronic charge. Current is assumed to be injected directly into the wetting layer and transport phenomena, such as drift or diffusion, are not explicitly included in the model. τ_{wR} is attributed to spontaneous recombination time, which contain contributions from nonradiative, radiative, and Auger recombination. τ_{w2} is the effective capture time and carrier capture is mediated by phonon and Auger processes. Phonon and Auger-assisted capture and relaxation can be taken into account phenomenologically through the relation

$\tau_i = 1/(A + CN_w)$, $i = w2, 21$ where $1/A$ is the phonon-assisted capture (relaxation) time and C is the coefficient determining the rate of Auger-assisted capture (relaxation) by scattering with carriers in the wetting layer. τ_{2w} is the characteristic escape time and τ_{21}, τ_{12} are electron relaxation time from the excited state to the ground state and escape time from the ground state to the excited state, respectively and $\tau_{12} = \tau_{21}$ exp $((E_S - E_G)/k_BT)$ where $E_{S,G}$ are the energies of the excited state and ground state. τ_{1R} is spontaneous radiation lifetime in quantum dots.

The gain expression is given by $g = g_{\max}(f_n + f_p - 1)$ where $g_{\max}$ is maximum modal gain [12] and can be defined as $g_{\max} = \Gamma l\tilde{N}_Q a^{-1} \sum_i \sigma_i(\omega_0)$ where Γ is the confinement factor, l is the number of quantum dot layers, a is the mean size of QD and $\sigma_i(\omega_0)$ is the effective cross section of the QDs at the signal frequency. $f_n(f_p)$ is the electron (hole) occupation probability in the GS. The term $(f_n + f_p - 1)$ is the effective population inversion in GSs where the expressions of f_n and f_p are given in [13]. For simplicity, $f_n = f_p = f$ is assumed [14, 15]. Also $h_n(h_p)$ is the electron (hole) occupation probability in the ES ($h_n = h_p = h$ is presumed).

In order to achieve an input/output model of QD-SOA, we integrate the gain over the length of the device [16]. Therefore, the charge carrier density is supposed to be constant over the SOA length, $N_w(z,\tau) = N_w(\tau), \tilde{N}_Q h(z,\tau) = \tilde{N}_Q h(\tau)$ and also$\tilde{N}_Q f(z,\tau) = \tilde{N}_Q f(\tau)$. Integration of the optical output relation reduces the SOA to a lumped element and averages the internal spatial information to single values, $N_w(\tau), \tilde{N}_Q h(\tau)$ and $\tilde{N}_Q f(\tau)$.

To relate the optical outputs at $z = L$ to the inputs at $z = 0$, one may separate variables of the propagation equation (11), integrate and normalize on $[0, z]$, and solve for the optical power at location z in terms of the input power

$$P_s(z,\tau) = P_s(0,\tau)\exp((g - \alpha_{\text{int}})z) \tag{15}$$

the optical output at the end of the device may describe as

$$P_{s\_out}(\tau) = P_{s\_in}(\tau)\exp((g - \alpha_{\text{int}})L) \tag{16}$$

where L is the SOA length and $P_{s\_in}(\tau) = P_s\ (0,\ \tau)$, $P_{s\_out}(\tau) = P_s\ (L,\ \tau)$. Integrating the ground state rate equation (14) on $z \in [0, L]$ and normalizing by $1/L$ yields

$$\frac{d\tilde{N}_Q f(\tau)}{d\tau} = \frac{\tilde{N}_Q h(1-f)}{\tau_{21}} - \frac{\tilde{N}_Q f(1-h)}{\tau_{12}} - \frac{\tilde{N}_Q f^2}{\tau_{1R}} - \frac{g}{\sigma\hbar\omega}\bar{P}_s(\tau) \tag{17}$$

where Leibnitz's rule has been employed to interchange the time derivative and the spatial definite integral in (17) [17]. It is also defined that

$$\bar{P}_s(\tau) \triangleq \frac{1}{L}\int_0^L P_s(z,\tau)\mathrm{d}z \tag{18}$$

and because f is assumed to be spatially invariant

$$\bar{f}(\tau) \triangleq \frac{1}{L}\int_0^L f(\tau)\mathrm{d}z \tag{19}$$

is simply given by $f(\tau)$ and the over script bar has omitted $\bar{f}(\tau) = f(\tau)$. Substituting (15) into (18) gives

$$\bar{P}_s(\tau) = \frac{P_s(0,\tau)[\exp((g-\alpha_{\text{int}})L) - 1]}{(g-\alpha_{\text{int}})L} \tag{20}$$

So, by substituting (20) into the rate equation (17)

$$\begin{aligned}\frac{\mathrm{d}\tilde{N}_Q f(\tau)}{d\tau} = \frac{\tilde{N}_Q h(1-f)}{\tau_{21}} - \frac{\tilde{N}_Q f(1-h)}{\tau_{12}} - \frac{\tilde{N}_Q f^2}{\tau_{1R}} \\ - \frac{gP_{s\_in}(\tau)[\exp((g-\alpha_{\text{int}})L) - 1]}{V\hbar\omega(g-\alpha_{\text{int}})}\end{aligned} \tag{21}$$

It is possible to rewrite the equations (12) and (13) in a similar manner described above.

Simple algebraic manipulation of new rate equations along with (15) yields equivalent circuit equations as

$$I = C_1\frac{\mathrm{d}v_1}{dt} + \frac{v_1}{R_4} - k_1 v_1 v_2 - k_2 v_2 \tag{22}$$

$$k_3 v_1 + k_4 v_3 + k_5 v_2 v_3 = C_2\frac{\mathrm{d}v_2}{dt} + \frac{v_2}{R_5} + k_6 v_1 v_2 \tag{23}$$

$$k_7 v_2 + k_8 v_2 v_3 = C_3\frac{\mathrm{d}v_3}{dt} + \frac{v_3}{R_3} + k_9 v_3^2 + \zeta v_{s\_in}[\exp(\beta(v_3 - v_{trf})) - 1] \tag{24}$$

$$v_{s\_out} = v_{s\_in}\exp(\beta(v_3 - v_{trf})) \tag{25}$$

where the related parameters are listed below [18]

$$\begin{aligned}i_1 = \frac{eVN_w}{\tau_{w2}} = \frac{v_1}{R_1}, i_2 = \frac{eV\tilde{N}_Q h}{\tau_{21}} = \frac{v_2}{R_2}, i_3 = \frac{eV\tilde{N}_Q f}{\tau_{12}} = \frac{v_3}{R_3}, i_4 = \frac{eVN_w}{\tau_{wR}} = \frac{\tau_{w2}}{\tau_{wR}}i_1, i_5 \\ = \frac{eV\tilde{N}_Q h}{\tau_{2w}} = \frac{\tau_{21}}{\tau_{2w}}i_2, i_6 = \frac{eV\tilde{N}_Q f}{\tau_{1R}} = \frac{\tau_{12}}{\tau_{1R}}i_3,\end{aligned}$$

with $R_1 = R_2 = R_3 = 1\Omega$ and $R_4 = R_1/(1+\tau_{w2}/\tau_{wR}), R_5 = R_2/(1+\tau_{21}/\tau_{2w})$, $C_1 = \tau_{w2}/R_1, C_2 = \tau_{21}/R_2, C_3 = \tau_{12}/R_3, k_1 = k_6 = \tau_{21}/eV\tilde{N}_Q R_1 R_2, k_2 = \tau_{21}/\tau_{2w}$ $R_2, k_3 = 1/R_1$, $R_5 = R_2/(1 + \tau_{21}/\tau_{2w})$, $C_1 = \tau_{w2}/R_1$, $C_2 = \tau_{21}/R_2, C_3 = \tau_{12}/R_3$, $k_1 = k_6 = \tau_{21}/eV\tilde{N}_Q R_1 R_2$, $k_2 = \tau_{21}/\tau_{2w}R_2, k_3 = 1/R_1, k_4 = 1/R_3, k_5 = (\tau_{12} - \tau_{21})/$ $eV\tilde{N}_Q R_2 R_3$, $k_7 = 1/R_2$, $k_8 = (\tau_{21} - \tau_{12})/eV\tilde{N}_Q R_2 R_3$, $k_9 = \tau_{12}^2/\tau_{1R}eV\tilde{N}_Q R_3^2$, $\zeta = e^2/\tau_p\hbar\omega_s$, $\beta = 2g_{\max}\tau_{12}L/eV\tilde{N}_Q R_3, v_{trf} = eV\tilde{N}_Q R_3/\ 2\tau_{12}$, $v_{s\_out} = \tau_p P_{s\_out}/e$, $v_{s\_in} = \tau_p P_{s\_in}/e$ with $\tau_p = 1.6 \times 10^{-19}$ s.

It is clear from above definitions that v_1, v_2 and v_3 circuit voltages are proportional to N_w, h and f, respectively. Equations 22–25 can be employed to develop the SPICE circuit model of the QD-SOA as shown in Fig. 2.4a–d with $E1 = v_{s\_in} \exp(\beta(v_3 - v_{trf}))$, $G1 = k_1 v_1 v_2$, $G2 = k_2 v_2$, $G3 = k_3 v_1$, $G4 = k_4 v_3$, $G5 = k_5 v_2 v_3$, $G6 = k_6 v_1 v_2$, $G7 = k_7 v_2$, $G8 = k_8 v_2 v_3$, $G9 = k_9 v_3^2$, $G10 = \zeta v_{s\_in}[\exp(\beta(v_3 - v_{trf})) - 1]$.

The resistors R_{is} and R_{os} are arbitrary. Equations 22–24 are employed to construct equivalent circuit models shown in Fig. 2.4b–d. Considering v_1 as the node voltage in Eq. 22, the four right-hand terms of Eq. 22 are proportional to currents of a capacitor, resistor and voltage-dependant current sources (dependant on node voltages v_1 and v_2) with k_1 and k_2 coefficients, respectively and form the circuit model of Fig. 2.4b for instance. Equation 25 is used to form an equivalent sub-circuit model for V_{s_out} (related to the optical output power of QD-SOA) which is drawn in Fig. 2.4a. These four sub-circuits are coupled to each other to determine the gain saturation characteristics, output power, carrier dynamics and chirp of QD-SOA.

The current source I in Fig. 2.4b is proportional to the SOA bias current in (12), G_1 dependant current source is dependent on v_1 and v_2 variables or N_w and h, respectively and is proportional to the $N_w h/\tau_{w2}$ in (12). The dependant current source G_2 is related to v_2 variable which is proportional to $\tilde{N}_Q h/\tau_{2w}$term and C_1 (capacitance) is the coefficient of wetting layer population variation (τ_{w2}/R_1). All of the parameters can be obtained from other rate equations in a similar manner.

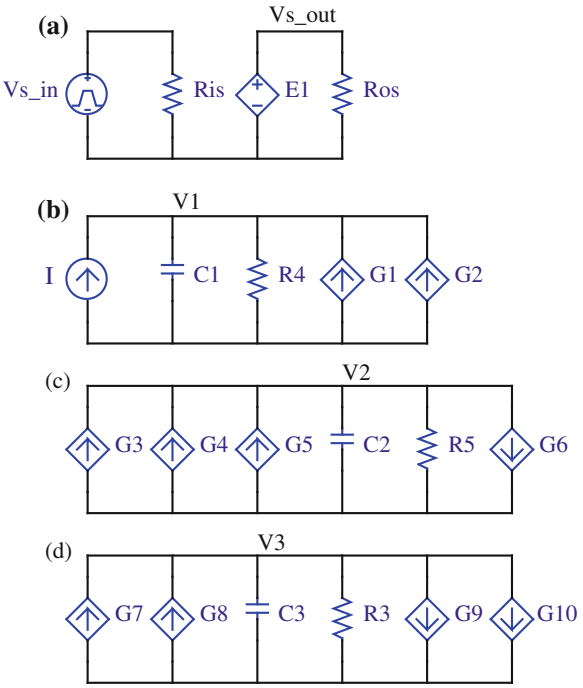

Fig. 2.4 (a) SPICE sub-circuit model to determine the optical output power. (b)–(d) Equivalent sub-circuits to measure V_1, V_2 and V_3, respectively, due to the bias current and V_{s_in} [10]

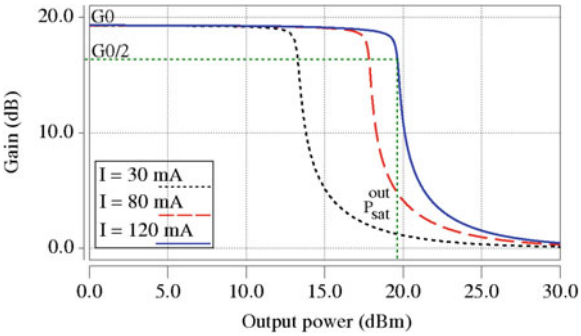

Fig. 2.5 Gain saturation characteristics of a QD-SOA for CW beam amplification, with the SOA gain plotted as a function of the output power, *Pout*, for different pump current *I* in the SOA [10]

To investigate the accuracy of the equivalent circuit model, the gain saturation characteristics, the output pulse shape, the state occupation probabilities and the frequency chirping of the QD-SOA have obtained using SPICE package using the typical parameters given in [19, 20].

The saturation properties with the considered parameters for different bias currents are illustrated in Fig. 2.5. The gain approaches its unsaturated value, G_0, for small optical powers; in present case $G_0 \approx 19$ dB. As the input power (and consequently the output power) is increased, the gain starts to saturate and eventually the amplifier is forced toward transparency.

The output power at which the gain decrease by 3 dB, i.e., at $G_{sat} = G_0/2$ is considered as output saturated power.

Beside the saturation properties, the temporal shape of amplified pulse and the gain dynamic have great importance in QD-SOA operation. As the pulse is amplified inside the SOA, the pulse shape becomes asymmetric due to variation in electronic level population and the leading edge becomes sharper compared with the trailing edge. Sharpening of the leading edge is a common feature of all amplifiers and occurs because the leading edge experiences larger gain than trailing edge [21]. This fact is clear in Fig. 2.6 where the output pulse shape of an input Gaussian pulse is plotted.

Fast gain dynamic is the other issue that should be addressed. The explanation for the fast gain recovery can be seen in Fig. 2.7, which shows the variations of the carrier densities of the three different levels during the amplification of the strong input pulse. As carriers of ground state are removed through stimulated emission the excited state acts as a nearby carrier reservoir and enables ultrafast gain recovery. Since the process of carrier capture is slower than intra-dot relaxation, the excited state recovers on a longer time-scale of several picoseconds which is the upper limit for fast gain recovery time. The long recovery time of the wetting layer is depicted in the inset of Fig. 2.7 which is in several hundred picoseconds timescale.

Since the gain change of SOAs gives rise to changes in the refractive index, a signal that has been amplified or processed with an SOA has a large frequency

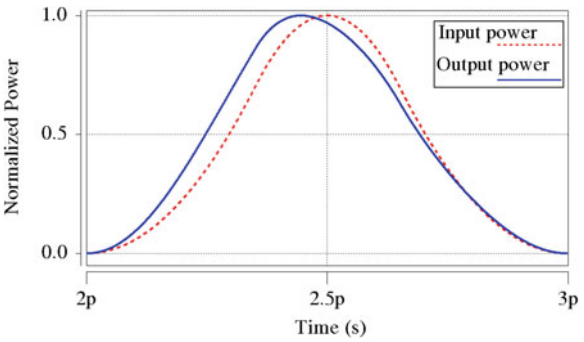

Fig. 2.6 Output pulse shape of a QD-SOA when a Gaussian pulse passes through the amplifier [10]

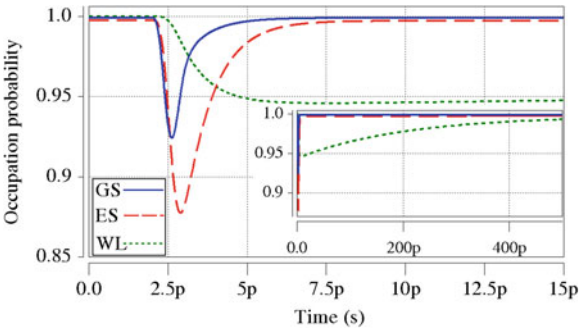

Fig. 2.7 Simulated evolution of occupation probability for the ground state, the excited state and the wetting layer of the QD-SOA. The inset shows the slow dynamics of the wetting layer [10]

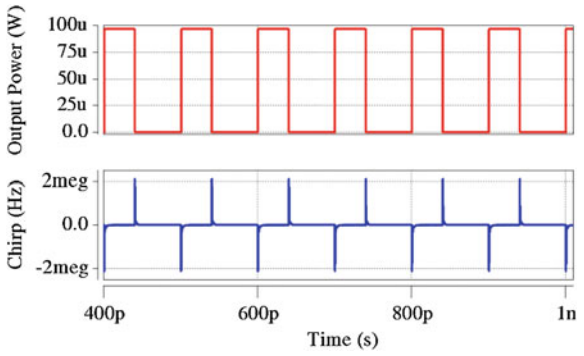

Fig. 2.8 Output power (pulse pattern) and chirp of a pulse train passing through the QD-SOA operating in its linear gain regime, $P_{s\_in} = 10$ μW [10]

chirp at the leading and trailing edges of the signal pulse. Figures 2.8 and 2.9 show the frequency chirp of the amplified pulses for two input pulse trains at linear ($P_{s\_in} = 10$ μW (peak value)) and nonlinear ($P_{s_in} = 10$mW) operation regions of the QD-SOA. The obtained results for frequency chirp, saturation power and gain recovery process agree well with reported results in mentioned reports (The negligible mismatch is due to $\alpha_{int} = 0$ assumption).

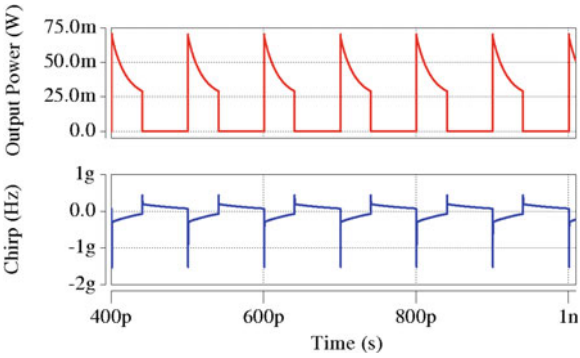

Fig. 2.9 Output power (pulse pattern) and chirp of a pulse train passing through the QD-SOA operating in its nonlinear gain regime, $P_{s\_in} = 10$ mW [10]

2.4 Analytical Methods

Most of the successful models in predicting the optical properties of QD-SOAs treat quantum dots as three-state systems and describe the SOA dynamics based on transitions between the ground state, the excited state and the wetting layer. Therefore, a comprehensive analytical solution for explanation of the operation characteristics of QD-SOAs should take into account the carrier transitions between these three states. The quantum dot model for active region of QD-SOA in this section comprises two nondegenerate energy states (ground and excited states) similar to the model introduced in the previous section. Signal propagation equation through the SOA length and also the rate equations for state occupation probabilities may describe as [22]

$$\frac{\partial S}{\partial z} = [g_{GS}(\hbar\omega)(2f-1) + g_{ES}(\hbar\omega)(2h-1) - \alpha]S \tag{26}$$

$$\frac{\partial f}{\partial t} = \left(\frac{(1-f)h}{\tau_{10}} - \frac{f(1-h)}{\tau_{01}}\right)(a_{10} + c_{10}w) - \frac{f^2}{\tau_{0R}} - \frac{v_g g_{GS}(\hbar\omega)(2f-1)S}{N_Q} \tag{27}$$

$$\frac{\partial h}{\partial t} = \left(\frac{(1-h)w}{\tau_{21}} - \frac{h(1-w)}{\tau_{12}}\right)(a_{21} + c_{21}w) - \left(\frac{(1-f)h}{\tau_{10}} - \frac{f(1-h)}{\tau_{01}}\right)(a_{10} + c_{10}w) - \frac{h^2}{\tau_{1R}} - \frac{v_g g_{ES}(\hbar\omega)(2h-1)S}{N_Q} \tag{28}$$

$$\frac{\partial w}{\partial t} = \frac{J}{\tau_{0R}} - \left(\frac{(1-h)w}{\tau_{21}} - \frac{h(1-w)}{\tau_{12}}\right)(a_{21} + c_{21}w) - \frac{w}{\tau_{wR}}(a_w + b_w w + c_w w^2) \tag{29}$$

The occupation probabilities of the ground state, the excited state and the wetting layer at the band edge are expressed by f, h and w respectively, S is the photon density, α is the waveguide loss, g_{GS} and g_{ES} are the modal gain of the ground and excited states. The phonon-assisted and Auger-assisted processes are included in the rate equations via a_{10}, a_{21}, a_{w} and c_{10}, c_{21}, c_{w} coefficients. Carrier relaxation and excitation processes are denoted by τ_{01}, τ_{10}, τ_{21}, τ_{12}, $\tau_{0\mathrm{R}}$, $\tau_{1\mathrm{R}}$ and τ_{wR} as scape time from the GS to the ES, relaxation time from the ES to the GS, relaxation time from the WL to the ES, escape time from the ES to the WL, spontaneous radiative lifetimes in the GS, ES and WL respectively. N_Q is the quantum dot volume density and J is normalized injection current density ($J = (I \times \tau_{0R})/\, qV_aN_{WL}$ where V_a is the volume and N_{WL} is the carrier density of the WL).

Figure 2.10 describes the variation of the GS occupation probability and photon intensity during SOA length at specified points. When a signal is injected to the SOA at $z = 0$, it experiences unsaturated gain. During the propagation of the signal inside the SOA, the material gain will be decreased and for $z > L_m$ this gain will be equal to material loss. Thus, for $z > L_m$ SOA will be transparent. Meanwhile, the photon intensity increases during the pulse propagation due to stimulated emission and reaches to its maximum value for $z > L_m$.

Therefore, the maximum output density of the devices is expected when the total gain equals with the material loss or $g_{tot} = \alpha$. Since the values of the GS occupation probability and the photon intensity at $z = 0$, z_{ref}, L_m and L will be used to obtain output and threshold characteristics of the SOA, It is useful to define $f\,(z = L_m) = f_m$, $h\,(z = L_m) = h_m$, and $S\,(z = L_m) = S_m$. Considering the photon energy given by $\hbar\omega_0$ and defining $g_{GS}(\hbar\omega_0) = g_0$ and $g_{ES}(\hbar\omega_0) = g_1$ and finding the roots of equation (27) - (29) for $S = 0$, one may obtain the unsaturated occupation probabilities of the GS, ES and WL. It should be noted that this method is valid at steady state and for CW condition where the time derivatives of the carrier rate equations can be set to zero. After evaluating the unsaturated occupation probabilities as f_{us}, h_{us} and W_{us}, the total unsaturated material gain and optical gain of the amplifier may rewrite as

$$g_{tot}^{us} = g_0(2f_{us} - 1) + g_1(2h_{us} - 1) - \alpha \tag{30}$$

$$G_{us} = \exp(g_{tot}^{us} L) \tag{31}$$

and at the $z = L_m$

$$f_m = \frac{1}{2}\left(1 + \frac{\alpha}{g_0}\right) - \frac{g_1(2h_m - 1)}{2g_0}. \tag{32}$$

By replacing the above expression for f_m in (28) and (29), h_m and w_m can be extracted and the maximum output density at $z = L_m$ can be extracted from (27) as (by finding the equivalent value for the expression between parentheses of (29) and replacing in (28) and doing so for (28) and (27)

$$S_m = \frac{g_m}{\alpha} S_{sat} \tag{33}$$

where

$$g_m = g_0\tau_{0R}\left(\frac{J}{\tau_{0R}} - \frac{f_m^2}{\tau_{0R}} - \frac{h_m^2}{\tau_{1R}} - \frac{w_m}{\tau_{wR}}(a_w + b_w w_m + c_w w_m^2)\right) \tag{34}$$

and

$$S_{sat} = \frac{N_Q}{v_g g_0 \tau_{0R}} \tag{35}$$

By introducing the point $z = z_{ref}$ as obvious in Fig. 2.10 with the property $f(z_{ref}) = f_r = (f_{us} + f_m)/2$, the photon density at this point may be evaluated as

$$S_{ref} = \frac{S_{sat}\tau_{0R}}{2f_r - 1}\left(\frac{(1-f_r)h_r}{\tau_{10}} - \frac{f_r(1-h_r)}{\tau_{01}} - \frac{f_r^2}{\tau_{0R}}\right) \tag{36}$$

where h_r can be obtained from f_r similar to h_m and f_m. After a few mathematical manipulation [22] the optical gain of the QD-SOA can be obtained in a closed-form model as

$$\frac{S_{out}}{S_{in}} = e^{g_{tot}^{us}L}\left(\frac{S_m - S_{out}}{S_m - S_{in}}\right)^{\left(1+\frac{S_m}{S_Y}\right)} \approx e^{g_{tot}^{us}L}\left(\frac{S_m - S_{out}}{S_m - S_{in}}\right)^{\left(\frac{S_m}{S_{ref}}-1\right)} \tag{37}$$

where $S_{in} = S(z = 0)$ is the input density, $S_{out} = S(z = L)$ and $S_Y^{-1} = S_X^{-1} - \varepsilon$ with

$$S_X = \frac{S_m}{2(1 - \varepsilon S_m)}\left(\frac{g_0(2f_m - 1) + g_1(2h_m - 1)}{g_0(f_{us} - f_m) + g_1(h_{us} - h_m)}\right) \tag{38}$$

with

$$\varepsilon = \frac{\frac{1}{S_m} - \frac{\rho}{S_{ref}}}{1 - \rho} \tag{39}$$

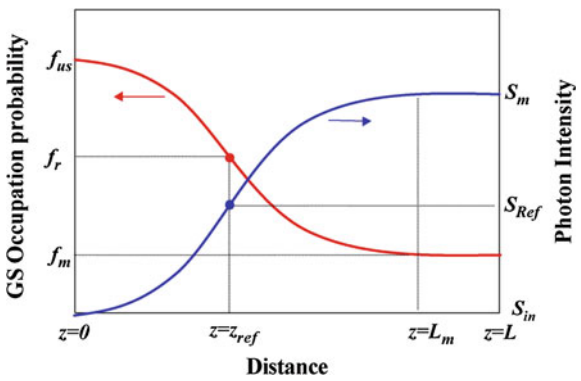

Fig. 2.10 GS occupation probability and photon density at different distances for $S_{in} << S_{sat}$ and $L > L_m$ [22]

and

$$\rho = \frac{[g_0(2f_m - 1) + g_1(2h_m - 1)][g_0(f_{us} - f_r) + g_1(h_{us} - h_r)]}{[g_0(2f_r - 1) + g_1(2h_r - 1)][g_0(f_{us} - f_m) + g_1(h_{us} - h_m)]}. \quad (40)$$

Therefore, the optical gain of the QD-SOA can be obtained analytically only if S_m, S_{ref} and the unsaturated optical gain are known. The output optical gain of the QD-SOA with analytically obtained solution and also with numerical solution of the rate equations using fourth-order Runge–Kutta method have plotted in Fig. 2.11 to compare the accuracy of the solutions.

The following parameters have been used in the simulation; $\tau_{0R} = \tau_{1R} = \tau_{wR} = 0.2$ ns, $\tau_{10} = 8$ ps, $\tau_{21} = 2$ ps, $\tau_{01} = 80$ ps, $\tau_{12} = 20$ ps, $\alpha = 3$ cm^{-1}, $a_{10} = a_{21} = a_w = 1$, $b_w = c_w = 0$, $c_{10} = c_{21} = 80$, $N_Q = 2.5 \times 10^{17}$ cm^3, $v_g = 8.45 \times 10^9$ cm/s, $g_0 = 14$ cm^{-1} and $g_1 = 14$ cm^{-1}. The photon intensity as a function of SOA length is also presented in Fig. 2.12 for both numerical and analytical methods.

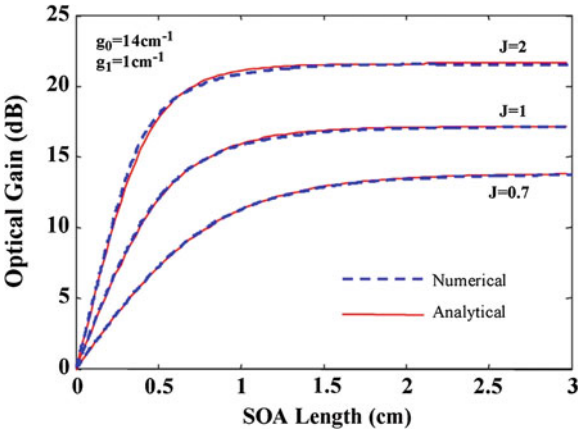

Fig. 2.11 Optical gain of the QD-SOA versus device length for three different applied current values. The Solid lines present the results of analytical method and dashed lines are for numerical method [22]

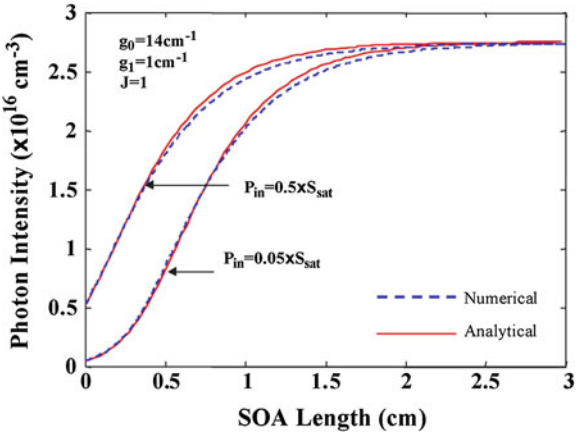

Fig. 2.12 Photon density versus SOA length for two different input signal intensities. The Solid lines present the results of analytical method and dashed lines are for numerical method [22]

By defining the maximum SOA length as the length when the maximum output is 3 dB less than S_m ($S_{out} = 0.5 \times S_m$), one can express an analytical formula for SOA length after which the device provided no gain. Hence, this criteria can be defined from (37) as

$$L < \frac{1}{g_{tot}^{us}} \ln \left(\frac{0.5 S_m}{S_{in}^{\max}} \left[\frac{S_m - S_{in}^{\max}}{S_m - 0.5 S_m} \right]^{\left(1 + \frac{S_m}{S_Y}\right)} \right) \tag{41}$$

As it is obvious from Fig. 2.11, this length is about 1 cm for the given device and for $z > 1$ cm the SOA will be transparent.

References

1. Sugawara, M., Hatori, N., Akiyama, T., Nakata, Y., Ishikawa, H.: Quantum-dot semiconductor optical amplifiers for high bit-rate signal processing over 40 Gbit/s. Jpn. J. Appl. Phys. **40**, L488–L491 (2001)
2. Sugawara, M., Mukai, K., Nakata, Y., Ishikawa, H.: Effect of homogeneous broadening of optical gain on lasing spectra in self-assembled $In_xGa_{1-x}As/GaAs$ quantum dot lasers. Phys. Rev. B **61**, 7595–7603 (2000)
3. Bilenca, A., Eisenstein, G.: On the noise properties of linear and nonlinear quantum-dot semiconductor optical amplifiers: The impact of inhomogeneously broadened gain and fast carrier dynamics. IEEE J. Quantum Electron **40**, 690–702 (2004)
4. van der Poel, M., Gehrig, E., Hess, O., Birkedal, D., Hvam, J.M.: Ultrafast gain dynamics in quantum-dot amplifiers: Theoretical analysis and experimental investigations. IEEE J. Quantum Electron **41**, 1115–1123 (2005)
5. Kim, J., Laemmlin, M., Meuer, C., Bimberg, D., Eisenstein, G.: Theoretical and experimental study of high-speed small-signal cross-gain modulation of quantum-dot semiconductor optical amplifiers. IEEE J. Quantum Electron **45**, 240–248 (2009)
6. Borri, P., Langbein, W., Schneider, S., Woggon, U., Sellin, R.L., Ouyang, D., Bimberg, D.: Exciton relaxation and dephasing in quantum-dot amplifiers from room-to cryogenic temperature. IEEE J. Sel. Topics Quantum Electron **8**, 984–991 (2002)
7. Sugawara, M., Ebe, H., Hatori, N., Ishida, M., Arakawa, Y., Akiyama, T., Otsubo, K., Nakata, Y.: Theory of optical signal amplification and processing by quantum-dot semiconductor optical amplifiers. Phys. Rev. B **69**, 235332-1-39 (2004)
8. Borri, P., Schneider, S., Langbein, W., Bimberg, D.: Ultrafast carrier dynamics in InGaAs quantum dot materials and devices. J. Opt. A **8**, S33–S46 (2006)
9. Dommers, S., Temnov, V.V., Woggon, U., Gomis, J., Martinez-Pastor, J., Laemmlin, M., Bimberg, D.: Complete ground state gain recovery after ultrashort double pulses in quantum dot based semiconductor optical amplifier. Appl. Phys. Lett. **90**, 033508 (2007)
10. Maram, R., Baghban, H., Rasooli, H., Ghorbani, R., Rostami, A.: Equivalent circuit model of quantum dot semiconductor optical amplifiers: dynamic behaviour and saturation properties. J. Opt. A **11**, 105205-1-8 (2009)
11. Sosnowski, T.S., Norris, T.B., Jiang, H., Singh, J., Kamath, K., Bhattacharya, P.: Rapid carrier relaxation in $In_{0.4}Ga_{0.6}As/GaAs$ quantum dots characterized by differential transmission spectroscopy. Phys. Rev. B **57**, R9423–R9426 (1998)
12. Steiner, T. (ed.): Semiconductor Nanostructures for Optoelectronic Applications. Artech House, London (2004)

13. Asryan, L.V., Suris, R.A.: Longitudinal spatial hole burning in a quantum-dot laser. IEEE J. Quantum Electron **36**, 1151–1160 (2000)
14. Qasaimeh, Q.: Characteristics of cross-gain (XG) wavelength conversion in quantum dot semiconductor optical amplifiers. IEEE Photon. Technol. Lett. **16**, 542-544 (2004)
15. Qasaimeh, O.: Optical gain and saturation characteristics of quantum-dot semiconductor optical amplifiers. IEEE J. Quantum Electron. **39**, 793–798 (2003)
16. Saleh, A.A.M.: Nonlinear models of travelling-wave optical amplifiers. Electron Lett. **24**, 835–837 (1988)
17. Kuntze, S.B., Pavel, L., Aitchison, J.S.: Controlling a semiconductor optical amplifier using a state-space model. IEEE J. Quantum Electron **43**, 123–129 (2007)
18. Biswas, A., Basu, P.K.: Equivalent circuit models of quantum cascade lasers for SPICE simulation of steady state and dynamic responses. J. Opt. A **9**, 26–32 (2007)
19. Li X., Li, G.: Comments on "theoretical analysis of gain-recovery time and chirp in QD-SOA". IEEE Photon. Technol. Lett. **18**, 2434–2435 (2006)
20. Ben-Ezra, Y., Haridim, M., Lembrikov, B.I.: Theoretical analysis of gain-recovery time and chirp in QD-SOA. IEEE Photon. Technol. Lett. **17**, 1803–1805 (2005)
21. Agrawal, G.P., Olsson, N.A.: Self-phase modulation and spectral broadening of optical pulses in semiconductor laser amplifiers. IEEE J. Quantum Electron **25**, 2297–2306 (1989)
22. Qasaimeh, O.: Novel closed-form model for multiple-state quantum-dot semiconductor optical amplifiers. IEEE J. Quantum Electron **44**, 652–657 (2008)

Chapter 3
Techniques Toward High Speed Operation of Semiconductor Optical Amplifiers

3.1 Introduction

In this section some theoretical and experimental techniques will be presented to increase the gain and phase recovery time and speed up the Semiconductor Optical Amplifier (SOA) operation. These methods include the regular bulk SOAs and also quantum dot SOAs (QD-SOAs). However one can generalize these techniques to quantum-well SOAs (QW-SOAs) either.

One of the simplest methods to speed up the gain recovery in SOAs is increasing the applied bias current. A high current provides a large carrier density and also a high amplified spontaneous emission power, both of which tend to shorten the carrier lifetime. Therefore, to obtain a fast gain recovery, a high current must be applied. Another way to enhance the gain recovery is by increasing the optical intensity in the active layer. This leads to a higher stimulated recombination rate, and therefore, to a shorter carrier lifetime. The optical intensity either can be generated inside the SOA, or injected into the SOA from an external laser. However applying higher bias currents decrease the optical bandwidth, increase the amount of amplified spontaneous emission, and increase the electrical consumption. Following discussion gives an insight to some methods to improve the recovery time without emphasizing the SOA bias current.

3.2 Gain Recovery Improvement Techniques in Bulk and QW-SOAs

3.2.1 Carrier Reservoir

It has been suggested that SOA with a carrier reservoir can have a short gain recovery time [1]. This carrier reservoir (CR) model described here is applicable to

A. Rostami et al., *Nanostructure Semiconductor Optical Amplifiers*,
Engineering Materials, DOI: 10.1007/978-3-642-14925-2_3,

bulk, QW, or QD SOA. In CR-SOA, the carrier reservoir (CR) region is grown in the vicinity of the active region. Under certain conditions, CR is significantly populated and it supplies the active region with carriers with nearly the same transition time as that for QD-SOA, i.e., 0.5–10 ps [2].

The CR layer has larger bandgap compared with active region (AR) layer. The schematic of band diagram of SOA with a CR is depicted in Fig. 3.1. Injection of electrons fills the states of CR and AR and carriers are relaxed from CR to AR to fill the depletion-induced unoccupied states due to stimulated emission in the presence of an optical signal. This refilling time is primarily determined by electron–phonon interaction time and has been indirectly measured to be in the ~0.5 to 5 ps range in GaAs [3].

Due to the larger effective mass of holes compared to electrons, and the resulting smaller level spacing (especially in low dimensional heterostructures), holes are expected to relax faster than electrons and therefore, electrons are assumed to limit the carrier dynamics [4, 5]. In other words, the electron relaxation time determines the SOA gain response. As an experimentally reported sample, the carrier relaxation time measurement in self-organized $In_{0.4}Ga_{0.6}As/GaAs$ quantum dots have been done in [6] by the means of differential transmission (DT) measurements and (it is observed that the interband optical-matrix element is strong only between electron and hole levels with the same quantum number, thus the absorption and PL spectra will be dominated by transitions at E_1H_1 and E_2H_2) it is reported that carrier relaxation time for n = 2 to n = 1 for holes is much smaller than for electrons.

Considering this fact, the dynamic model of the CR-SOA can be described by the nonlinear coupled equations:

$$\frac{\partial h_{active}}{\partial t} = \frac{I_1}{eV_{active}} + \frac{\Delta N}{\tau_t(1+\eta)} - gP(t,z) \tag{1}$$

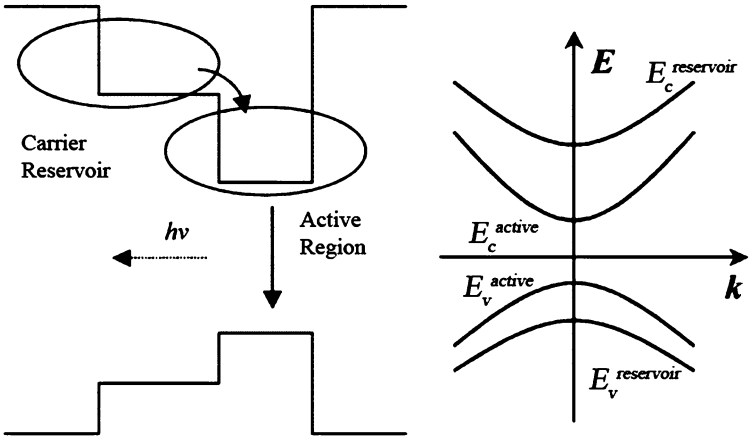

Fig. 3.1 Schematic of band diagram of SOA with carrier reservoir [1]

$$\frac{\partial h_{reservior}}{\partial t} = \frac{I_2}{eV_{reservior}} - \frac{N_{reservior}}{\tau_c} - \frac{\eta \Delta N}{\tau_t(1+\eta)} \tag{2}$$

$$\Delta N = N_{reservior} - N_{active} \tag{3}$$

where N, V, I, τ_c and τ_t ($\tau_t = 5$ ps is considered) are the carrier density in each region, volume, total injected current ($I = I_1 + I_2$), recombination lifetime in both the active and reservoir regions, and the transition time from the CR level to AR level, respectively. The quantity P(t,z) denotes the power in the optical pulse at a distance z from the input facet of SOA. The quantity η is the population inversion factor defined as the ratio of steady-state carrier densities in AR and CR (i.e., $\eta = N_{ar}/N_{cr}$). The last terms in (1) and (2) represent the transition process between the CR to the AR levels. The coupling factors are employed here since the transition rate is proportional to occupation of the destination states. Optical gain in the SOA can be linearly scaled to the carrier density in active region as in [7]. Therefore Eqs. 1–3 can be converted into the following:

$$g_l = a(N_d - N_{tr}) \tag{4}$$

$$\frac{\partial g_{ar}}{\partial t} = \frac{g_0^{ar} - g_{ar}}{\tau_c} - g_{ar}P(t,z) + \frac{g_{cr} - g_{ar}}{\tau_t(1+\eta)} \tag{5}$$

$$g_0^{ar} = \Gamma a N_{tr}(I_1 \tau_c / qV_1 N_{tr} - 1) \tag{6}$$

where a and N_{tr} are the differential gain and the transparent density in SOA, respectively. Carrier heating and spectral hole burning effects on the gain g are introduced using the procedure of a previous analysis [8]

$$\frac{\partial g_{SHB}}{\partial t} = -\frac{g_{SHB}}{\tau_{SHB}} - \frac{\varepsilon_{SHB}}{\tau_{SHB}} g_{total} P(t,z) - \left(\frac{\partial g_{CH}}{\partial t} + \frac{\partial g_l}{\partial t}\right) \tag{7}$$

$$\frac{\partial g_{CH}}{\partial t} = -\frac{g_{CH}}{\tau_{CH}} - \frac{\varepsilon_{CH}}{\tau_{CH}} g_{total} P(t,z) \tag{8}$$

g_{SHB} and g_{CH} are additional gains at the input optical wavelength due to spectral hole burning and carrier heating processes. $1/\tau_{SHB}$ is the carrier–carrier scattering rate while $1/\tau_{CH}$ is the temperature relaxation rate. ε_{SHB} and ε_{CH} are the nonlinear gain suppression factors due to carrier heating and spectral hole burning. The total gain is given by

$$g_{total} = g_l + g_{SHB} + g_{CH} \tag{9}$$

The optical gain as a function of time can be numerically solved from rate equations in temporal gain forms. For a regular SOA (no carrier reservoir)

$$\frac{dh_{active}}{dt} = -\left(e^{h_{total}-1}\right)P(t,0) + \frac{h_0}{\tau_c} - \frac{h_{active}}{\tau_c} \tag{10}$$

$$\frac{dh_{SHB}}{dt} = -\frac{h_{SHB}}{\tau_{SHB}} - \frac{\varepsilon_{SHB}}{\tau_{SHB}}(e^{h_{total}} - 1)P(t,0) - \frac{d(h_{active} + h_{CH})}{dt} \tag{11}$$

$$\frac{dh_{CH}}{dt} = -\frac{h_{CH}}{\tau_{CH}} - \frac{\varepsilon_{CH}}{\tau_{CH}}\left(e^{h_{total}} - 1\right)P(t,0) \tag{12}$$

$$h_{total} = h_{active} + h_{CH} + h_{SHB} \tag{13}$$

where the quantities h (h_{active}, h_{SHB} and h_{CH}) are defined as the total integrated gain as follows:

$$h_0 = \int g_0 dz' = \int_0^z \frac{\alpha I \tau_c}{eV} dz \tag{14}$$

The expression for phase change is given by

$$\phi(t) = -\frac{1}{2}[\alpha h_d(t) + \alpha_{CH} h_{CH}(t)] \tag{15}$$

where α is the usual linewidth enhancement factor (LEF) associated with the interband transitions and α_{CH} is the LEF for carrier heating. The LEF for spectral hole burning and carrier heating processes are $\alpha_{SHB} \sim 0$ and $\alpha_{CH} \sim 1$ [8, 9]. The input optical signal was set as a 10 Gb/s Gaussian pulse train (FWHM = 1 ps).

For a CR-SOA, (i.e. SOA with a carrier reservoir) temporal gain rate equations are derived from (1) to (4) as follows:

$$\frac{dh_{active}}{dt} = \frac{h_{reservior} - h_{active}}{\tau_t(1+\eta)} + \frac{\eta h_0}{\tau_c(1+\eta)} - \frac{h_{active}}{\tau_c} - \left(e^{h_{total}} - 1\right)P(t,0) \tag{16}$$

$$\frac{dh_{reservior}}{dt} = -\frac{\eta(h_{reservior} - h_{active})}{\tau_t(1+\eta)} + \frac{h_0 - h_{reservior}}{\tau_c(1+\eta)} - \frac{h_{reservior}}{\tau_c} \tag{17}$$

Equations 16 and 17 together with 11 and 12 form a complete set of CR-SOA temporal gain equations. The quantities for the parameters used in the equations are [8–10]: $\tau_C = 200$ ps, $\tau_t = 5$ ps, $\tau_{SHB} = 100$ fs, $\tau_{CH} = 300$ fs, $\varepsilon_{SHB} = \varepsilon_{CH} = 0.1$ and $\eta = 0.3$.

Figure 3.2 shows the comparison of gain recovery for a regular SOA (left) and a CR-SOA (right) for 100-Gb/s input optical signals. Although the short term recovery is considerably improved, the gain takes a long time to recover completely.

The faster response of SOA with carrier reservoir (CR-SOA) is based on a similar principle as that for the QD-SOA. In the QD-SOA, the wetting layers serve as a carrier reservoir while the QDs act as the active region.

The gain recovery by injection of second light (in some references called assist light or holding beam) is another way to speed up the gain recovery process. The externally injected SOA exhibits an exponential recovery without oscillations. Several research groups have reported theoretical and experimental results on

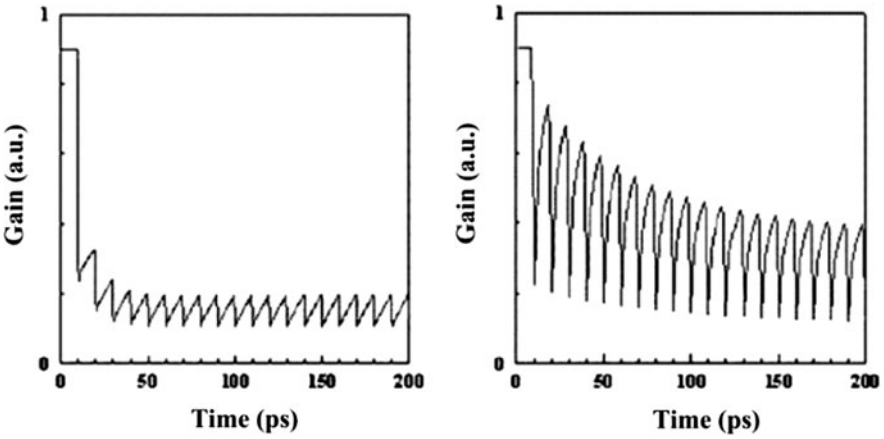

Fig. 3.2 Calculated gain recovery for (*left*) normal SOA and (*right*) CR-SOA for input 100-Gb/s Gaussian pulse train [1]

externally injected SOAs. It has been shown that the injected light accelerates the gain recovery [11–14], enhances the gain linearity [15], and increases the saturation output power [12], [15–17]. The injection wavelength is typically chosen in the gain region [17, 18], or toward the transparency wavelength, [12–16]. In the latter case, the required optical injection power will be high, but the available gain of the SOA will also remain high [12, 14, 16]. By using a wavelength around the gain maximum, the required acceleration can be obtained with small optical injection power, but the gain of the SOA is greatly reduced.

3.2.2 Optical Pulse Injection and Holding Beam

Acceleration of the gain recovery and also increasing the saturation power has been proved experimentally by optical injection near the transparency wavelength [19]. In this method, an important parameter for external pumping is the material transparency wavelength (λ_{tr}^{mat}) where the material gain is zero. This wavelength has been measured by injecting light from a tunable laser together with a weak continuous-wave (CW) signal at 1550 nm into the SOA. When the tunable laser reaches the material transparency wavelength, the cross-gain modulation induced on the 1550 nm signal will vanish. At two SOA bias currents of 150 mA and 450 mA, the values of this parameter are reported to be $\lambda_{tr}^{mat} = 1486$ nm and at $\lambda_{tr}^{mat} = 1454$ nm respectively.

The architecture depicted in Fig. 3.3 has been used to measure the gain recovery characterization of the SOA where an actively mode-locked fiber ring laser had been used to generate 3 ps pulses with a repetition rate of 2.5 Gb/s at

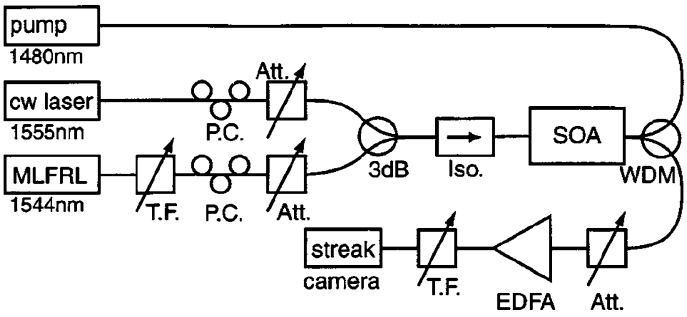

Fig. 3.3 Experimental setup used for the gain recovery characterization of the SOA with 1480 nm pump injection. *MLFRL* mode-locked fiber ring laser, *P.C.* polarization controller, *T.F.* tunable filter, *Att.* attenuator, *Iso.* isolator, *WDM* 1480/1550 coupler [19]

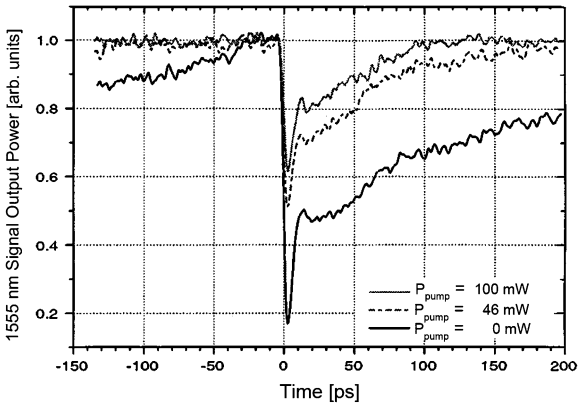

Fig. 3.4 Streak camera measurement of the gain recovery for a SOA current of 300 mA for different pump powers [19]

1544 nm. These pulses induce gain depletion in the SOA, and the recovery of this depletion is probed by a weak signal, generated by a tunable laser set at 1555 nm.

The 1480 nm pump power is injected in a counter-propagating scheme via a 1480/1550 WDM coupler. A filter at the output removes the 1544 nm pulses and a streak camera detects the 1555-nm probe signal. The estimated time resolution for the experiment was 8 ps. The gain recovery of the SOA in this experiment is shown in Fig. 3.4 for a bias current of 300 mA. In the absence of 1480 nm pump power, the signal has not yet reached its steady-state after a full period of 400 ps, as indicated by the increase of the signal output power for negative times.

The extracted gain recovery time is 207 ps without 1480 pump, and is reduced to 39 ps by injecting 100 mW of pump power. The fastest gain recovery (27 ps) was obtained at the highest SOA current at 450 mA of SOA current and injection of around 75 mW of pump power. Also it has been demonstrated that optical injection of 80 mW near the transparency point of SOA can improve the 3-dB saturation output power by 3 dB.

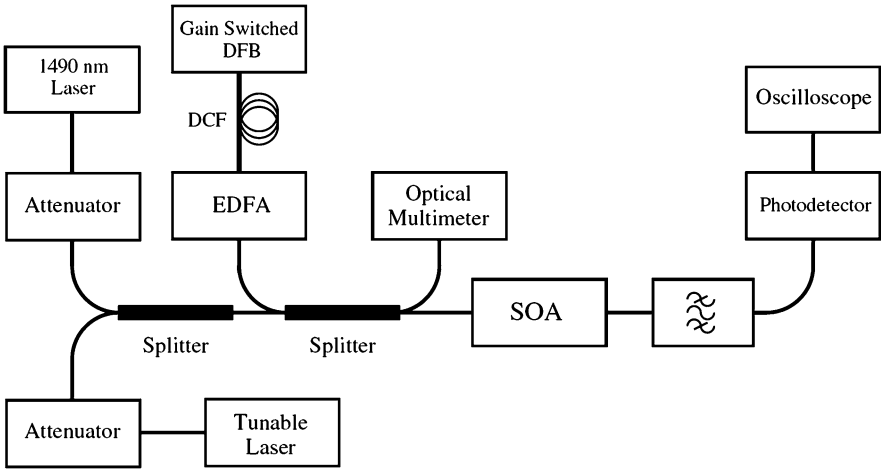

Fig. 3.5 Set-up used for the TWD gain recovery measurements in co-propagating configuration [20]

A similar experimental study on gain recovery has done for a semiconductor optical amplifier saturated by a holding beam at a wavelength near the gain transparency in co- and counter-propagating configurations [20]. It has investigated that the gain recovery in this three wavelength device (TWD) when the holding beam is propagating in the same direction as the saturating pulse (co-propagating) can be significantly different from the case when the holding beam is propagating in the opposite direction (counter-propagating).

Figure 3.5 shows the set-up used for the co-propagating configuration measurements. The saturating pulse is generated by a gain switched DFB, compressed by a length of dispersion compensating fiber (DCF) and amplified by an EDFA. The pulse energy was 86 fJ at a wavelength of 1550 nm and the pulse width at the input of the SOA was measured to be 19 ps FWHM using an APE pulse check autocorrelator assuming a Gaussian pulse shape. The SOA used in the experiment is a MQW polarization-insensitive device. The gain peak of the SOA is in the 1550 nm region and the transparency point is near 1490 nm at 300 mA bias current.

The tunable laser and the 1490 nm commercial laser are injected co-propagating with the pulse using a fiber splitter. The injected power is controlled using attenuators between lasers and splitter and it is measured using the optical multimeter. The gain recovery measurements as a function of wavelength are performed using the tunable laser to generate the holding beam and instead of injecting a third probe beam the gain recovery is measured on the holding beam to reduce the set-up complexity.

Also the set-up in Fig. 3.6 was used to characterize the gain recovery in a counter-propagating configuration. In this case the holding beam generated either by the tunable laser or by the 1490 nm laser, is injected in the opposite direction to

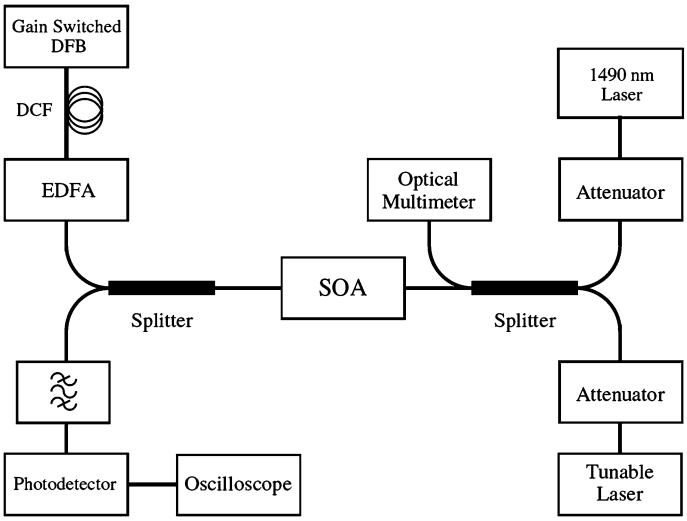

Fig. 3.6 Set-up used for the TWD gain recovery measurements in counter-propagating configuration [20]

that of the saturating pulse. The detection system, formed by oscilloscope, photodiode and optical filter, is also connected to the opposite port of the SOA.

In all the set-ups used the probe beam is propagating in the same direction as the holding beam and also the probe beam is either co- or counter-propagating with respect to the pulse.

The gain recovery had measured as an example using the tunable laser to generate the holding beam at a wavelength of 1530 nm with input power 0 dBm and for SOA bias current of 200 mA for co-propagating (solid line) and counter-propagating (dashed line) configurations. As it is clear in Fig. 3.7, an overshoot is present for the counter-propagating configuration, but it is absent in the co-propagating one thus causing a slower gain recovery.

The overshoot in the gain recovery is caused by saturation induced by pulse amplification which perturbs the carrier concentration distribution along the length of the amplifier. In simple terms, when the holding beam is not present, we can consider that most of the carrier saturation due the pulse amplification is occurring near the opposite facet with respect to the one where the pulse is injected. The temporary reduction of the carriers in this region causes a reduction of the ASE that is propagating in the opposite direction of the pulse. The reduction of the counter-propagating ASE reduces the stimulated recombination which increases the carrier concentration over the steady state value in the region close to where the pulse is injected. For high bias currents, and thus high ASE powers propagating in the SOA, this increase of the carrier concentration has the overall effect of increasing the device gain over the steady state value and thus of creating the gain overshoot.

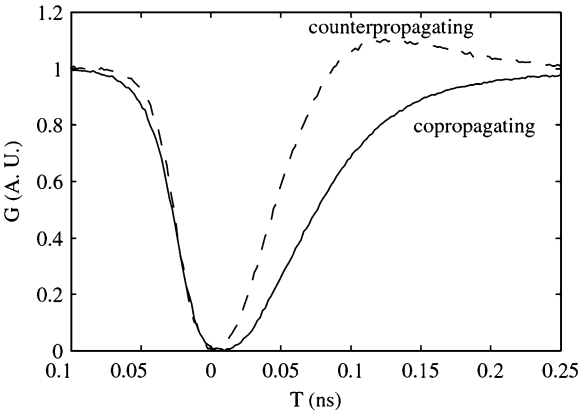

Fig. 3.7 Gain recovery evolution measured for the two directions of injection with a holding beam power of 0 dBm, wavelength of 1530 nm and bias current of 200 mA [20]

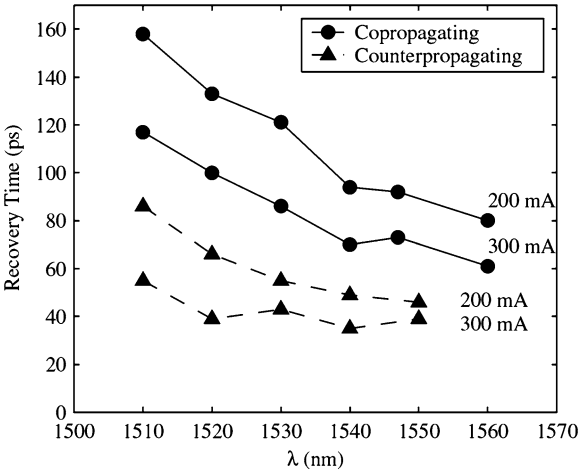

Fig. 3.8 Measured recovery time as a function of the injected wavelength in co-propagating and counter-propagating configurations for bias currents of 200 and 300 mA and injected power of 0 dBm [20]

The injection of a holding beam to the device has different effects when the beam is co- or counter-propagating. In the counter-propagating configuration the holding beam has the same effect as the counter-propagating ASE and it thus enhances the increase of the carrier concentration near the facet where the pulse is injected. For this reason, an increase in the power of the counter-propagating holding beam has the effect of increasing the gain overshoot. On the other hand, a co-propagating holding beam has the effect of saturating the region near the end of the device before the arrival of the pulse. The perturbation of the carrier concentration distribution induced by the pulse amplification is thus reduced. For this reason as the power of the co-propagating holding beam is increased the gain overshoot decreases and it eventually disappears completely as we can see in Fig. 3.7. Figure 3.8 shows the recovery time for holding beam wavelengths ranging from 1510 to 1560 nm, injected power of 0 dBm and SOA bias currents of

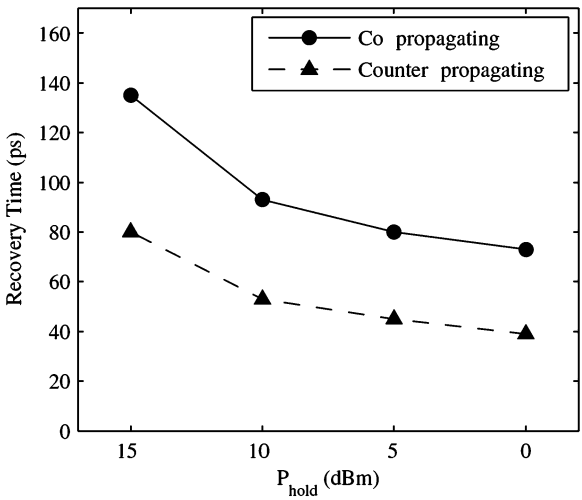

Fig. 3.9 Measured recovery time as a function of the injected power in co- and counter-propagating configurations for bias currents of 300 mA and injected wavelength of 1548 nm for the co-propagating configuration and 1550 nm for the counter-propagating one [20]

200 and 300 mA. For both currents the recovery time of the counter-propagating configuration is always shorter than that of the co-propagating one. This is caused by the absence of the overshoot in the co-propagating gain recovery due to the relatively high power of the holding beam. On the other hand, in the counter-propagating gain recovery the holding beam enhances the overshoot and thus reduces the recovery time. When the holding beam is in the gain region it also saturates the carrier concentration, with a net result of reducing the recovery time for both directions of propagation as the injected power increases due to the increased carrier saturation [21].

The recovery time measured as a function of the holding beam power for a bias current of 300 mA, injected wavelength of 1548 nm for the co-propagating configuration and 1550 nm for the counter-propagating one, is illustrated in Fig. 3.9. The reduction of the recovery time caused by the increase of the holding beam power can be clearly seen for both directions of holding beam propagation. Beside the acceleration of the recovery process, the measured times are relatively small still for the powers used in the experiments. This fact deduces from the strong ASE present in the device at high bias currents.

The effects holding beam on gain recovery characteristics in a bulk SOA can be investigated by considering the ASE on the gain recovery efficiently and precisely using effective parameters for the gain and the spontaneous emission coupling factor [21]. The numerical and experimental reports presented for the TWD show that in long SOAs, the ASE plays an important role in the gain recovery even when a holding beam is applied to the structure. The time evolution of carrier concentration in different sections into which the device is divided for a given bias current and pulse energy (Fig. 3.10) and a detailed scheme of the carrier concentration in the first and last section of the device (Fig. 3.11) give a deeper insight to this role.

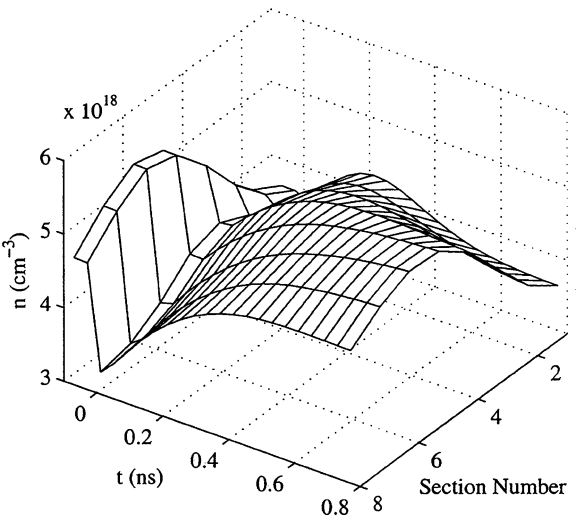

Fig. 3.10 Carrier concentration time evolution inside the device simulated with the model for bias current of 120 mA, probe power of −10 dBm, pulse energy of 1.2 pJ, and pulse width of 25 ps FWHM [21]

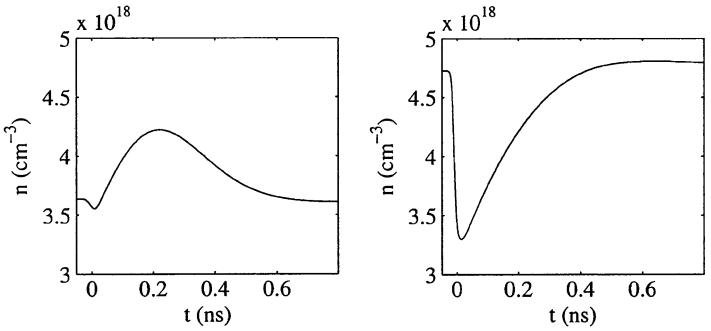

Fig. 3.11 Carrier concentration time evolution **a** for the first section of the device and **b** for the last section simulated with the model for bias current of 120 mA, probe power of −10 dBm, pulse energy of 1.2 pJ and pulse width of 25 ps FWHM [21]

The sections in the above figure are numbered starting from the side where the pulse starts to propagate. One can clearly notice the effect of the pulse that reduces the carrier concentration due to stimulated recombination and the subsequent recovery to the initial value. Also it is obvious that a small reduction of the carrier concentration due to pulse amplification followed by large increase in carrier concentration over the steady-state value as shown in Fig. 3.11a. This large increase is caused by reduction of the power of the backward-propagating ASE power, with reference to the pulse beam, due to the large reduction of carrier concentration in the last sections of the device (Fig. 3.11b) caused by the amplification of the pulse.

The effect of carrier concentration increase in the first sections of the device is an increase in the device gain that causes the overshoot in the gain recovery.

3.2.3 Optical Filtering

Optical filtering at output of semiconductor optical amplifiers is another interesting technique driven by the chirp properties of the SOAs. Fast frequency chirp dynamics allows pattern-independent and error-free high speed wavelength conversion at 160 Gb/s and higher [22]. Optical filtering of chirped wavelength-converted output light of an SOA has been utilized to achieve polarity-preserved wavelength conversion at 40 Gb/s [23–25]. It has been shown that the red-chirped component of the converted output light, filtered by an optical step filter (with a sharp frequency response), can be used to obtain non-inverted wavelength conversion [23]. Similarly, it has been demonstrated that filtering of the blue-chirped part of the converted output pulse can lead to non-inverted wavelength conversion [24]. The general behavior of such a system can be summarized in the following sentences: The injected pulses to the semiconductor optical amplifier contribute to the modulation of SOA gain as well as refractive index. The latter case results in chirp on the output signal which the leading edges of the converted signal pulses are red shifted, whereas the trailing edges are blue shifted [23–25].

If the central wavelength of the optical bandpass filter (OBF) placed at the output of the SOA is blue shifted with respect to the central wavelength of the considered beam (probe beam in this case) (Fig. 3.12b), the converted signal recovers much faster compared to the case that the central wavelengths of the filter and the probe beam coincide. The operation of the wavelength converter is schematically presented in Fig. 3.12c. The dotted and dashed lines in Fig. 3.12c are the SOA gain and chirp, respectively, and also shown in Fig. 3.12a.

When the pulse appears at point A, the SOA carriers deplete and the gain drops, reaching its minimum at point B. The SOA gain saturates during timeslot A–B. Furthermore, in timeslot A–B, the wavelength of the probe light moves to a longer wavelength (red chirp) and thus receives more attenuation by the filter. As a result, the transmittance of the probe light through the filter is reduced. At point B, the chirp becomes 0, and the SOA starts to recover. From this point onwards, the wavelength of the probe light is blue shifted, leading to an increased transmittance. If the OBF is properly selected (the slope of the OBF is especially essential), the enhancement of transmittance due to the blue chirp can compensate the gain saturation. Thus, the transmittance at point C is equal to the transmittance at point A. From points C to D, the wavelength of the probe light slowly moves back to the probe carrier wavelength, leading to a decreased transmittance.

Experimental results verify the successfulness of this method at 160 Gb/s wavelength conversion by setting up the measurement devices as illustrated in Fig. 3.13. It should be noted that the SOA used in the experiment has a recovery time of more than 90 ps and the center wavelength of the OBF is detuned 1.23 nm to the blue side with respect to the probe carrier wavelength. The inverted 160 Gb/s signal is subsequently injected into the delayed interferometer, where the polarity of converted signal is changed, i.e., the inverted signal is changed into a non-inverted signal. It is noted that differential operation in the delayed interferometer

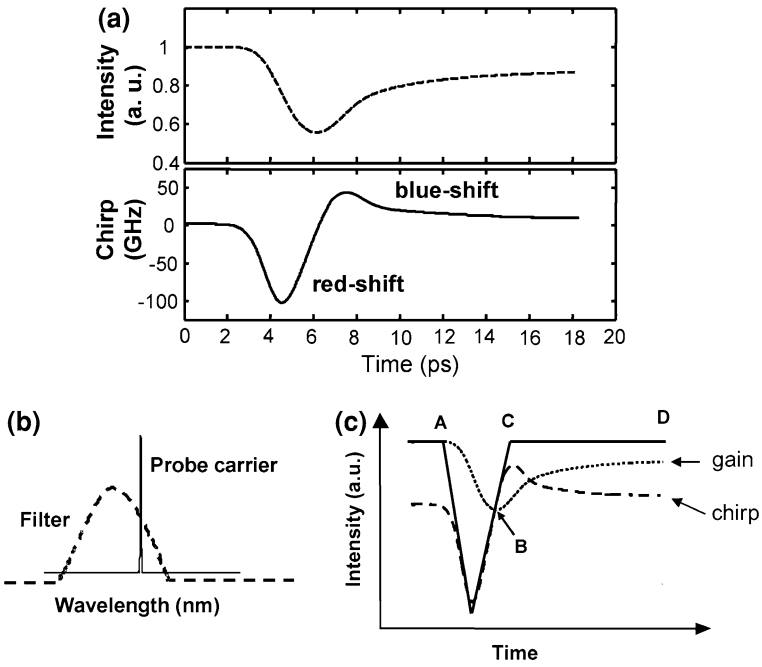

Fig. 3.12 Operation principle of the OBF-based wavelength converter. **a** SOA gain (*upper panel*) and chirp response (*lower panel*) as a function of time. **b** Schematic of the optical spectrum of the input probe light and the filter characteristic. **c** Transmittance through the OBF as a function of time. The *dotted* and *dashed lines* are the SOA gain and chirp, respectively, the same as the curves in **a** [22]

is not essential for realizing 160 Gb/s operation because the input (inverted) pulses have already been fully recovered within 3 ps.

The bit error rate (BER) measurements of the 160 Gb/s input signal (the 16 × 10-Gb/s tributaries in the input Multiplexer as it is depicted in Fig. 3.13) and the converted signal are presented in Fig. 3.14. It can be observed that the average sensitivity penalty for wavelength conversion at a BER = 10^{-9} is about 2.5 dB with respect to that of the original 160 Gb/s signal. The input dynamic range is about 6 dB to keep BER values under 10^{-9}. Moreover, it is visible that no error floor is observed, which indicates excellent performance of the proposed wavelength converter.

Simulations indicate that the fast component of the recovery is determined by the duration of the pulse, whereas the slow component is determined by the SOA carrier dynamics. This means that for pulses with duration as short as 1 ps, the recovery of the wavelength converter is limited by the pulse width and not by the carrier dynamics in the SOA. However, if the pulse width is decreased further (to about 200 fs), ultimately, the recovery of the wavelength converter is limited by ultrafast carrier dynamics in the SOA (carrier–carrier scattering and carrier–phonon interactions) [26, 27].

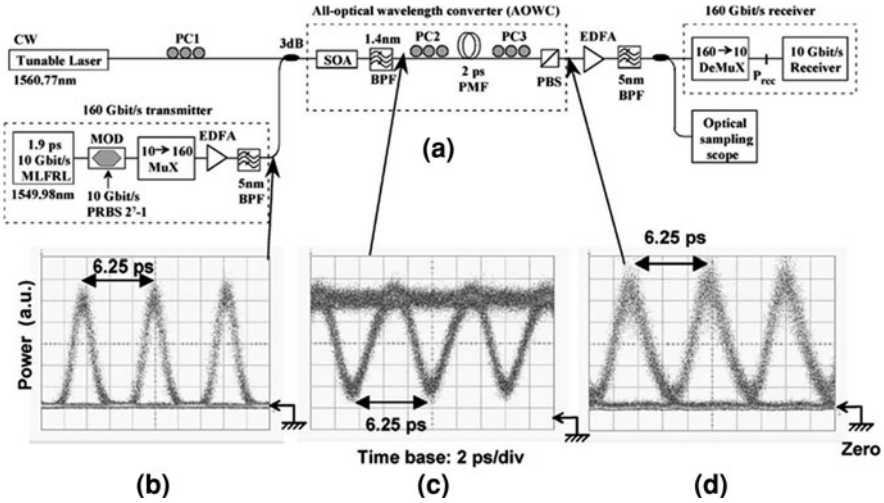

Fig. 3.13 **a** 160-Gb/s all-optical wavelength-conversion setup. Eye diagram of the **b** 160-Gb/s input pump signal, **c** converted light at the output of the bandpass filter, **d** converted light at the output of the delayed interferometer. *PC* polarization controller, *MLFRL* mode-locked fiber ring laser, *BPF* (optical) bandpass filter, *PBS* polarizing beam splitter, *PMF* polarization maintaining fiber, *EDFA* erbium-doped fiber amplifier [22]

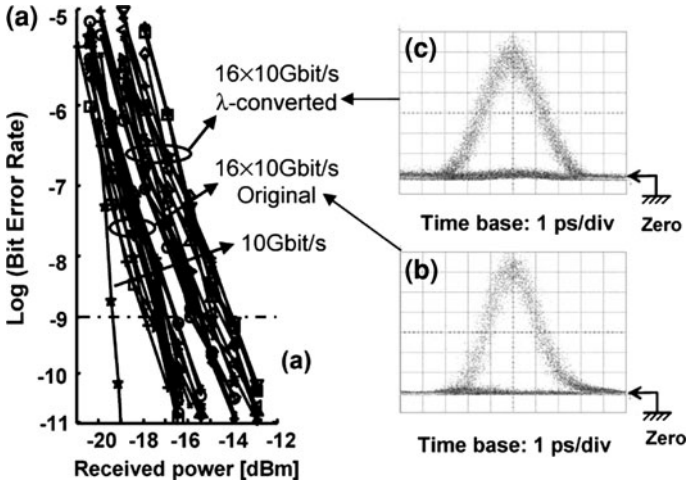

Fig. 3.14 **a** BER performance of 160-Gb/s wavelength conversion. **b**, **c** Eye diagrams of the demultiplexed 10-Gb/s input and wavelength-converted signals respectively [22]

The discussed arrangement in the previous lines has been used for wavelength conversion at bit rates as high as 320 Gb/s, albeit with a 10 dB penalty [28]. A drawback of this scheme is that the band-pass filter removes power due to suppression of part of the signal spectrum, resulting in reduced optical signal

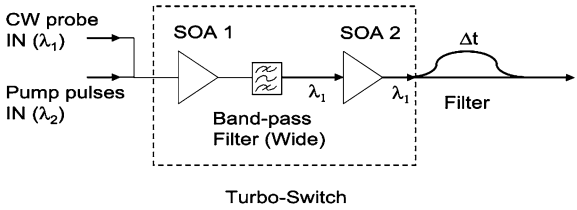

Fig. 3.15 Turbo-Switch scheme. A DISC filter is placed after the Turbo-Switch for wavelength conversion [31]

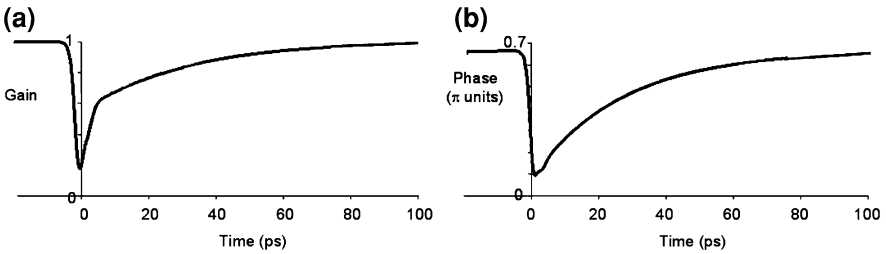

Fig. 3.16 Typical **a** gain and **b** phase response of a SOA to a ~2 ps optical pulse [31]

to noise ratio [29]. Other sophisticated linear filtering schemes which pass and recombine both red and blue shifted parts of the spectrum have also been reported [30], but with the drawback of a complex filter construction.

An alternative approach to improve the SOA's effective response speed is to use the Turbo-Switch arrangement, shown in Fig. 3.15 [31].

The CW probe has gain and phase modulation imposed upon it by the response of SOA1 (Fig. 3.16). The wide band-pass filter (~5 nm) used here blocks the pump, but is sufficiently wide to pass the entire modulated spectrum of the CW probe. The gain response of SOA2 is shown in Fig. 3.17a, and is now quite different to the response of SOA1.

It is this gain that acts upon the modulated CW beam (a self-gain response), and the effect is to act in opposition to the slow recovery component of the amplitude and phase modulation. The effect is to considerably enhance the high-speed response of the SOA combination (Fig. 3.17b).

The phase response is very similar to the gain response. Comparing this to the filtering technique which was discussed above, it may be seen once again that much of the ultrafast response of SOA1 has been preserved, whilst the effect of the slow response has been mostly suppressed. Experiments measuring the gain and phases responses of the Turbo-Switch have verified the predictions of Fig. 3.17b [32].

As already mentioned, patterning effects in SOA1 still occur. However Fig. 3.18a, which shows the power and phase of the output from the Turbo-Switch in response to an input data train, illustrates that the patterning of the power is in the opposite sense to that normally observed. Here the power minimum progressively increases with each successive pump pulse after the first. When this output is used in conjunction with a DISC (an asymmetric Mach–Zehnder interferometer

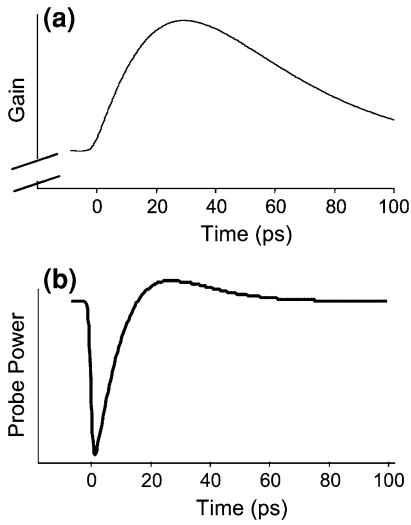

Fig. 3.17 **a** Gain response of SOA2 to the modulated CW input from SOA1. **b** Overall Turbo-Switch response [31]

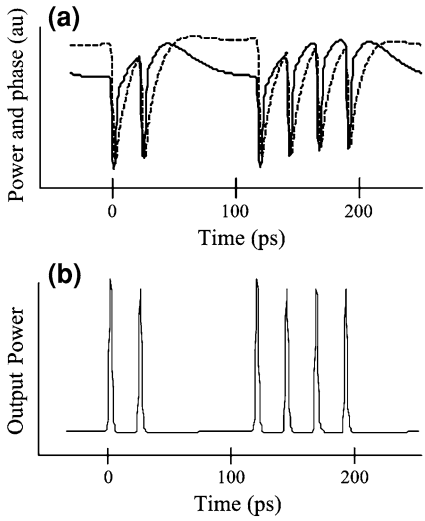

Fig. 3.18 **a** Power output (*solid line*) and phase (*dashed line*) from the Turbo switch. The reduction in phase change for successive pulses is compensated by larger optical power. **b** Power output from interferometer [31]

or delay-interferometer signal wavelength conversion, which may also be regarded as a filter in the frequency domain [29]), one may use the Turbo-switch for wavelength conversion. The phase differences between the two arms of the DISC interferometer lead to the formation of a patterned set of switching windows. However, the power acts now in the opposite way, tending to balance the effect of diminishing phase differences in a pulse sequence and giving a relatively unpatterned output [31].

A Turbo-Switch arrangement has been used for wavelength conversion at 170 Gbit/s with 3 dB penalty [31]. The DISC was made with birefringent polarization

maintaining (PM) fiber, giving different path lengths for the two orthogonal polarizations, and a polarizer, which forms the interferometer. In the case of [31], the PM fiber was placed between the two SOAs, and the polarizer, which completes the interferometer, was placed after the SOA2, hence distributing the DISC throughout the Turbo-Switch. This appears to further ameliorate patterning. It should be noted that the DISC filter itself removes power from the signal, as it necessarily translates the modulated CW signal into well shaped pulses of a few picoseconds in duration.

There is clearly a similarity between the two schemes presented in Figs. 3.12 and 3.15, both methods relying on a fortuitous balance of the gain and phase (or chirp) dynamics to give an output with low patterning [33].

3.2.4 Active Region Modification

The schemes that have described so far are ways of increasing the effective response bandwidth of the SOA, without actually changing the fundamental response of the SOA itself. An alternative approach is to increase the speed and hence bandwidth of the SOA by design of the active waveguide [34–36].

Here, the dependence of the recovery speed of semiconductor optical amplifiers on the active region dimensions will be investigated utilizing a picosecond pump-probe arrangement to experimentally measure the gain and phase dynamics of four SOAs with varying active region dimensions [37]. Pump-probe measurements of the gain and phase dynamics of the SOAs were carried out using the setup in Fig. 3.19.

Two tunable mode-locked lasers (TMLLs), driven by a 10.645 GHz RF synthesizer, provided the 3 ps pump (1544 nm) and probe (1560 nm) pulses. Using

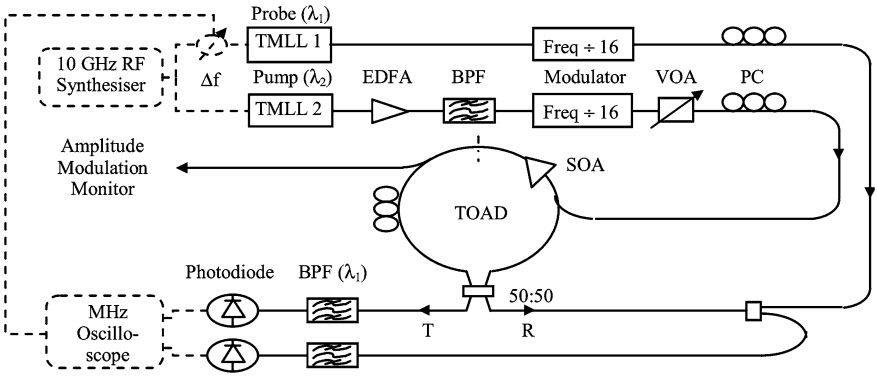

Fig. 3.19 Experimental pump-probe arrangement. *TMLL* tunable mode-locked laser, *EDFA* erbium doped fiber amplifier, *BPF* band pass filter, *VOA* variable optical attenuator, *PC* polarization controller, *R* reflected signal from the TOAD, *T* transmitted signal [37]

optical modulators, the repetition rates of these pulse trains were reduced to 665 MHz, which ensured that the SOA under test could recover fully between successive pulses. A small frequency shift, Δf, was applied to the RF drive to the probe laser so that the probe pulses could scan temporally through the gain response of the SOA to the pump pulse. The output from the pump laser was amplified with an EDFA to increase its power to roughly 25 dB greater than that of the probe. The probe beam was input to the 50:50 base coupler of a terahertz optical asymmetric demultiplexer (TOAD) [38], which consisted of a loop of fiber with an SOA offset from the loop centre by several nanoseconds. Here the probe pulses were divided into two counter-propagating components, one of which entered the SOA before the other (the counter-clockwise traveling component in Fig. 3.19).

The polarization of the TOAD loop was biased for full reflection of the probe in the absence of a pump pulse. A pump pulse incident on the SOA, and timed to arrive before the counter-clockwise probe, caused gain and phase modulation in this probe component. The SOA then recovered before the arrival of the clockwise traveling pulse and so net phase and amplitude differences existed between the probe components recombining at the base coupler. Due to the frequency shift between the input signals, the constantly changing delay between the pump and probe pulses lead to time dependent reflection (R) and transmission (T) coefficients that were detected on photodiodes and observed in real time on a MHz bandwidth electronic oscilloscope, triggered at the frequency Δf. Pump pulses and ASE exiting the TOAD from the base coupler were optically filtered out from the signal incident on the photodiodes.

The SOAs measured in this way were commercially available buried heterostructure bulk GaInAs devices from Kamelian™. They each had an active region of width 1 μm and the (length, depth) pairs were (1 mm, 0.1 μm), (1 mm, 0.2 μm), (1.9 mm, 0.1 μm) and (1.8 mm, 0.2 μm) respectively. The confinement factors for the 0.1 and 0.2 μm deep SOAs were ∼0.2 and ∼0.4 respectively. The 0.1 μm deep devices incorporated a separate confinement heterostructure (SCH) layer to increase the confinement to the value quoted here. Each SOA was operated at currents of between 100 and 400 mA and the dynamic curves recorded.

In the absence of a CW beam, it appears that ASE is the dominant contributor to the speed of the gain recovery. The ASE acts in a similar way to a holding beam [11]: reducing the equilibrium carrier density to which the device must recover and thus reducing the time constant of this recovery. Since the band filling by current injection provides the slow stage in the gain recovery process, the influence of ASE on gain recovery may be described by the dependence of band filling time constant on the ASE through

$$\frac{1}{\tau_{bf}} = \frac{1}{\tau_{Auger}} + \frac{1}{\tau_{ASE}} \tag{18}$$

where the Auger recombination lifetime and the ASE lifetime are denoted by τ_{Auger} and τ_{ASE} respectively [11]. The ASE lifetime is the dominant term here, and

its expansion is provided in Eq. 19, where P_{ASE} is the ASE power, E_{SAT} is the SOA saturation energy, Γ is the confinement factor, A is the cross sectional area of the active region, g is the material gain coefficient and hv is the photon energy [11].

$$\frac{1}{\tau_{ASE}} = \frac{P_{ASE}}{E_{SAT}} = \frac{\Gamma g P_{ASE}}{A \quad hv} \tag{19}$$

For an SOA of specified material composition, the ASE lifetime, and therefore τ_{bf}, is dependent on the ratio Γ/A (the inverse of the optical area) and clearly, this ratio should be maximized for fastest device recovery speeds. Although not considered here, optimization of the recovery speed by increasing the material gain coefficient is discussed in [39]. In assessing the length dependence of the speed of recovery of the SOA gain, it is important to note that the parameter to be fixed for comparison between devices of different length is the bias current and not the current density [40, 41], or transmission gain [42]. The Γ/A ratio is plotted as a function of active region width for a device of fixed depth (0.1 μm) in Fig. 3.20. This figure suggests that a width of approximately 0.6 μm will yield the maximum ratio of confinement factor to active region area. The proposal that this optimum width should correspond to the fastest gain recovery speed was tested using the numerical model [37] and are indicated in Fig. 3.21.

It is clear from Fig. 3.21 that an optimum width for fastest SOA recovery exists, and that it corresponds closely to that predicted from the simple theory. By reducing the active region width from 1 μm (which is the width of the real devices characterized) to 0.6 μm, a reduction of the recovery time constant by roughly 20% is possible.

Also evident from Fig. 3.21 is the close agreement between the recovery time variation predicted from the numerical model and the A/Γ ratio, which supports the argument that the ASE is indeed contributing greatly to the gain recovery mechanism. Further modeling of the SOA confinement factor for varying widths as well as depths was carried out to determine whether an overall optimum dimension set exists for fast recovery speeds. The Γ/A ratio for depths ranging between 0.05 and 0.5 μm, and for varying widths, are plotted in Fig. 3.22, with the dimensions of the active region for each curve indicated in the legend.

Figure 3.22 predicts a maximum Γ/A ratio for a square active region of side 0.3 μm. For an SOA with a 0.3 μm square active region cross-section, the

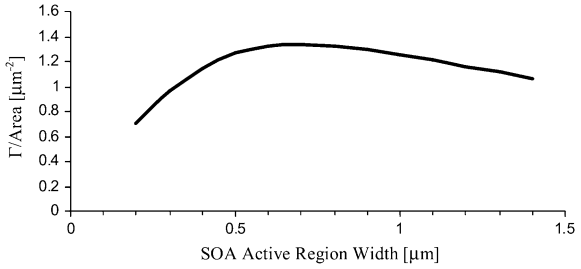

Fig. 3.20 Variation of the Γ/A ratio with active region width for a device of fixed depth [37]

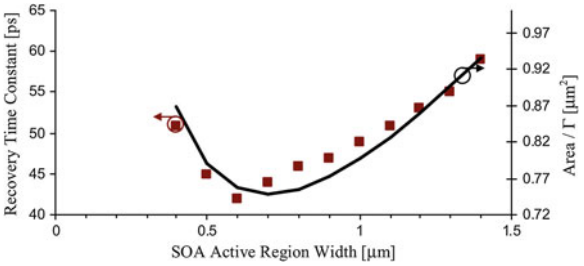

Fig. 3.21 Modeled recovery time constant as a function of active region width (*points*) and modeled area to confinement factor ratio (*solid line*) overlaid for comparison [37]

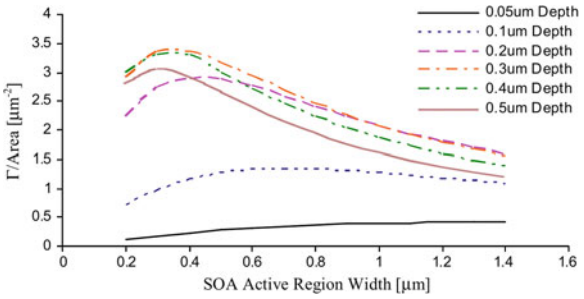

Fig. 3.22 Γ/A ratio as a function of active region width for SOAs of differing depths [37]

numerical model predicts a recovery time constant of less than 10 ps for an operating current of 200 mA, compared to the 50 ps measured for the real device. As well as the obvious advantage of the much faster recovery speeds offered by this optimum dimension set, the gain of the device should be polarization insensitive due to the square nature of its cross-section [43]. Such a design optimization of the active region would result in significant improvement in the speed response and performance of the SOA.

3.3 Gain Recovery Improvement Techniques in QD-SOAs

3.3.1 Two-Photon Absorption-Assisted Recovery

In spite of several techniques presented to reduce the recovery process in bulk SOAs, there are a few methods about which discuss QD-SOA in the literatures. However, many of the methods introduced for bulk or QW semiconductor optical amplifiers are applicable in QD-SOA case.

In the conventional models of a QD-SOA, the direct injection of carriers into WL is assumed. It can be shown that considering the effect of two-photon absorption (TPA) on carrier dynamics in the bulk region (TPA-induced carrier pumping) that constitutes the waveguide core of a QD SOA especially for sufficiently high pulse energies enhances the recovery speed [44]. Since the TPA pumping is quasi-synchronous in time and space with the gain bleaching along the

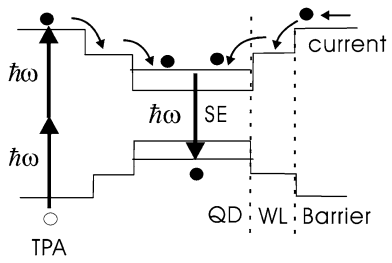

Fig. 3.23 A schematic of carrier dynamics with TPA in a QD-SOA. *SE* Stimulated emission [44]

pulse propagation through the QD SOA, it qualitatively leads to the change in carrier recovery dynamics in QDs.

TPA-induced carrier pumping is schematically illustrated in Fig. 3.23 where carriers are relaxed into wetting layer (WL). A similar process has been considered for carriers injected by current. Rate equation model is applied to investigate the dynamics of the system.

The modeling consists of InAs QDs embedded in the waveguide core that is composed of bulk material and uses a small-signal gain of 20 dB, given an amplifier length of 500 μm. For pulse propagation through the SOA, 120 fs optical pulse is injected with pulse energy of 10.5 and 2.3 pJ at the central wavelength of 1578 nm coinciding with the gain-peak wavelength. The coupled rate equations may be described as [44]:

$$\frac{\partial N_B}{\partial t} = \frac{J}{ed} - \frac{N_B V_W}{\tau_{rel} V_B}(1 - P_W) - \frac{N_B}{\tau_B} + \frac{N_W V_W D_B}{\tau_{ex} V_B D_W}(1 - P_B) + \frac{\kappa}{2\hbar\omega}\left[\frac{S(z,t)}{A}\right]^2 \tag{20}$$

$$\frac{\partial N_W}{\partial t} = \frac{N_B}{\tau_{rel}}(1 - p_W) - \frac{N_W D_B}{\tau_{ex} D_W}(1 - P_B) - \frac{N_W}{\tau_W} - \frac{N_W V_D}{\tau_{cap} V_W}(1 - P_G) + \frac{N_G V_D D_W}{\tau_{esc} V_W N_D}(1 - P_W) \tag{21}$$

$$\frac{\partial N_G}{\partial t} = \frac{N_W}{\tau_{cap}}(1 - p_G) - \frac{N_G D_W}{\tau_{esc} N_D}(1 - P_W) - \frac{N_G}{\tau_G} - \frac{2Lg(z,t)S(z,t)}{V_D \hbar\omega} \tag{22}$$

where N_B, N_W and N_G are the volume density of carriers in the barrier, WL and QDs that are normalized with respect to the volume of the barrier, WL and QDs interacting with the propagating photons, respectively.

$P_B \equiv N_B/(2D_B)$, $P_W \equiv N_W/(2D_W)$ and $P_G \equiv N_G/(2N_D)$ are defined as the occupation probabilities of the barrier, WL and QDs where D_B and D_W are the three-dimensional effective density-of-states (DOS) at the barrier and WL band-edges and N_D is the volume density of QDs. J is the current density of electronic charge e, and d is the thickness of the bulk region. The volumes of the barrier, WL, and QDs are denoted by V_B, V_W, and V_D, respectively. τ_B, τ_W, and τ_G are the

radiative spontaneous recombination lifetimes of carriers in the barrier, WL and QDs, respectively. τ_{rel} is the relaxation time from barrier to WL, τ_{ex} is the escape time of carriers from WL to barrier, τ_{cap} is the capture time of carriers from WL to QDs, and τ_{esc} is the escape time of carriers from QDs to WL. The last term of (20) describes the TPA-generated carriers where κ is the TPA coefficient, S(z, t) is the optical power with the single photon energy of $\hbar\omega$ corresponding to the QD ground state inter-band transition and A is the modal area. The modal gain g(z, t) used in (22) can be defined by

$$g(z,t) = \Gamma a[2P_G(z,t) - 1](2N_D) \tag{23}$$

where Γ is the QD confinement factor and a is the stimulated emission cross-section in the QDs. The optical power S(z, t) can be calculated by $S(z, t) \equiv |E(z, t)|^2$ where the E(z, t) is the optical field envelop given by

$$\frac{\partial E(z,t)}{\partial z} = \left[\frac{1}{2}(1+i\alpha)g(z,t) - \frac{1}{2}\gamma_{\text{int}} - \frac{1}{2}(1+i\alpha_{TPA})\kappa\frac{S(z,t)}{A}\right]E(z,t) \tag{24}$$

where α is the line-width enhancement factor, γ_{int} is the waveguide internal loss parameter, and α_{TPA} is the phase modulation parameter associated with TPA.

Just like the case of bulk amplifiers [27], the barrier supplies carriers to the WL on a relaxation timescale of $\sim$70 fs by ultrafast processes such as carrier-carrier scattering. In addition, the WL supplies carriers to the QDs on the timescale of $\sim$200 fs by Auger-assisted or multi-phonon-assisted capture. These fast processes for QD carrier filling drives ultrafast recovery of gain following gain bleaching. Thus, carrier capture rate becomes enhanced by these extra-carriers generated by TPA, compared to the case without TPA.

The simulated $P_G(z, t)$ for the case without and also with TPA is depicted in Fig. 3.24a and b, respectively. Figure 3.24c and d provides the magnified view of the ΔP_G, showing that the inclusion of TPA in the calculation flip the sign of the ΔP_G at the input facet and decrease the magnitude of ΔP_G at the output facet.

Also the P_G modulation depth continues to decrease along the propagation since TPA with the larger confinement factor than that of the QD active region attenuates the pulse intensity, leading to the decrease of the QD carrier depletion, as it is shown in Fig. 3.24b.

In order to investigate gain modulation dynamics, a train of periodic pulses is injected in the QD SOA at a repetition rate of 1 THz, using input pulse energy of 10.5 pJ. Figure 3.25a displays the simulation of optical gain modulation for the cases without TPA and with TPA (Fig. 3.25b). It is obvious that without the TPA effect, gain modulation is stabilized to be $\sim$1.5 dB following the rapid decrease of modulation depth. This is attributed to the fact that the QD carrier recovery is incomplete enough to give a strong transient effect on the gain modulation. Taking the TPA into account, nearly constant gain modulation of $\sim$8 dB, however, occur

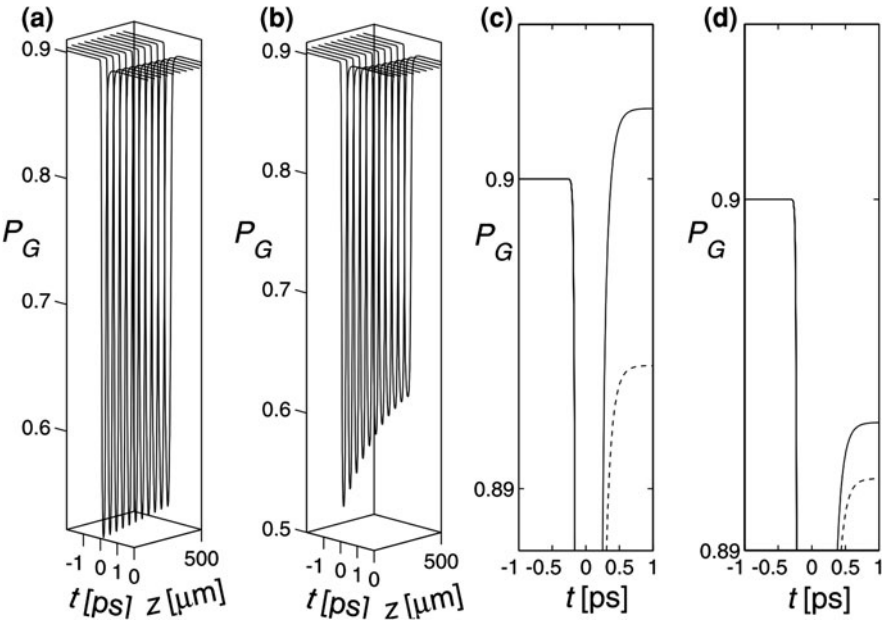

Fig. 3.24 **a** P_G without TPA, **b** P_G with TPA, **c**, **d** the magnified view of P_G at input and output facet, respectively, for the cases with TPA (*solid*) and without TPA (*dashed*). The input pulse energy is 10.5 pJ [44]

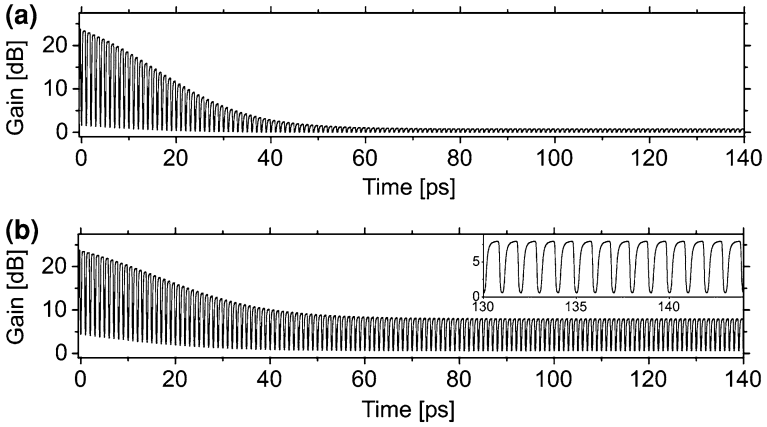

Fig. 3.25 Gain modulation as a 1 THz train of periodic pulses is injected **a** without TPA, **b** with TPA. The *inset* of **b** offers the magnified view from 130 to 145 ps. The input pulse energy is 10.5 pJ [44]

after the modulation depth decreases by a factor of only about two. For the qualitative investigation of pattern phenomena in the optical gain modulation, random bits of pulses are injected in the QD SOA at the repetition rate of 1 THz as

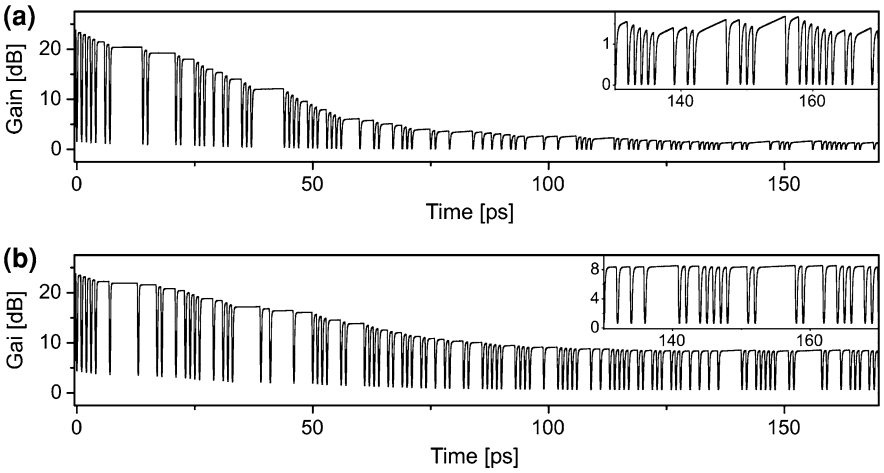

Fig. 3.26 Gain modulation as a 1 THz pulse train of random bits, using single pulse energy of 10.5 pJ. **a** Without TPA, **b** with TPA. The *insets* of **a** and **b** provide the magnified view from 130 to 170 ps [44]

illustrated in Fig. 3.26a and b for the case without TPA and the case with TPA taken into account, respectively. In the case without TPA, strong pattern effects are seen while, in the case with TPA, the substantially reduced pattern-effects are visible. Consequently, it is clear that TPA-induced carrier pumping which is quasi-synchronous in propagation time and distance with QD gain bleaching plays an important role in reducing the pattern effects for ultrafast optical gain modulation.

3.3.2 Control Pulse-Assisted Recovery

High speed operation of QD-SOA-based all-optical logic gates at Tb/s speeds is also predicted via applying a control pulse to accelerate the recovery process of QD-SOA [45]. The main advantage of QD-SOAs, compared to the bulk and quantum-well SOAs (QW-SOAs), as it discussed before, is based on the existence of the gap between the QD levels and wetting layer, and on the lower cross section of carrier-photon interaction which results, in particular, in shorter carrier relaxation times and lower gain saturation [46, 47]. The observed relaxation times in QD-SOAs, range from hundred of femtoseconds to tens of picoseconds which are significantly shorter than its value in QW-SOAs [48] and bulk SOAs [49]. However the main challenge in QD-based SOAs is still related to carrier relaxation from WL into ground or ES of QD because of the phonon bottleneck phenomenon peculiar to discrete energy levels [50, 51].

The QD-SOA-based logic gates operation capability at 250 Gb/s has been predicted [52] and it has been theoretically proved that high quality pattern-free

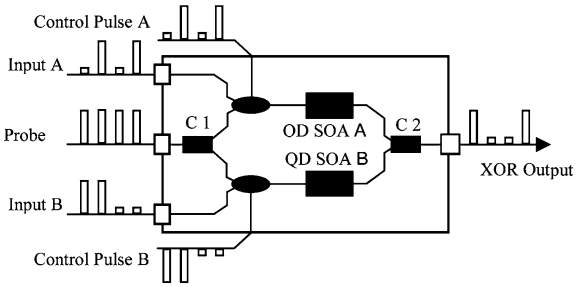

Fig. 3.27 Configuration of all-optical XOR gate using QD-SOA [45]

operation of XOR logic gate and also an all-optical processor is limited to 200 Gb/s at 50 mA bias current which is limited by electron relaxation time from WL to ES [53]. Thus an upper limit has been concluded for SOA-based logic gates and systems.

The operation principles of Tb/s gain recovery is described in a symmetric MZI-based-XOR-gate system [52, 53].

For the Boolean XOR operation A $\oplus$ B = C, the input logic signals, A and B at wavelength λ_S, enter the arms of MZI via two multiplexers, respectively as it is schematically illustrated in Fig. 3.27. A probe signal at wavelength λ_P enters to the structure and splits into two equal parts in coupler C1. The wavelength separation between λ_S and λ_P should be less than the homogeneous broadening of the single QD gain to ensure effective cross gain modulation. If the input signals A and B are identical, the QD-SOA-MZI is balanced and no signal emerges from XOR output. In contrast, if one of the input signals is zero while the other is one; a differential phase shift is introduced due to the cross-phase modulation (XPM) in the QD-SOA and the probe signal switches to the output consequently. The control pulses (CPs) at wavelength $\lambda_C$enter to each QD-SOA according the input signal patterns (A, B) via the multiplexers. The time delay between control pulses and input signals, which affects the QD-SOA performance and hence the XOR gate operation, will be discussed in the following. The XOR output intensity can be expressed as

$$P_{XOR} = P_{probe}\{k_1k_2G_A(t) + (1-k_1)(1-k_2)G_B(t) - 2\sqrt{k_1k_2(1-k_1)(1-k_2)G_A(t)G_B(t)}\cos[\phi_A(t) - \phi_B(t)]\} \quad (25)$$

where $G_A(t)$, $G_B(t)$ are the integral of QD-SOA gains and $\phi_A(t)$, $\phi_B(t)$ are nonlinear phase shifts. k_1 and k_2 are the ratios of couplers C1 and C2 which are equally set to 0.5 for simplicity.

The output power, gain and phase characteristics of the QD-SOA can be obtained by solving the rate equations of the structure. To describe the control-pulse-assisted QD-SOA model, the two band model of Fig. 3.28 is considered where the transition of conduction band ground state (CBGS) to valence band ground state (VBGS) is assumed to be the main stimulated transition by input signal and the transition of valence band ES (VBES) to conduction band ES (CBES) is assumed to populate the CBES via absorption of CP.

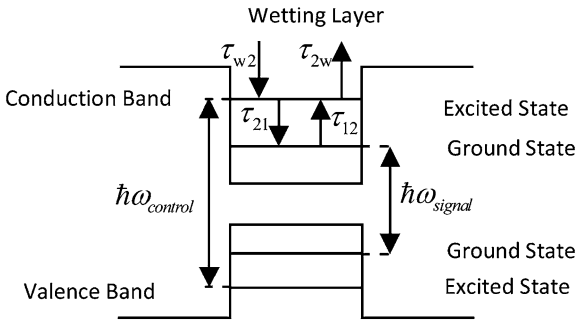

Fig. 3.28 Band diagram of the QD structure with related energy levels [45]

The photon rate equations for input signal, probe and CP are given as

$$\frac{\partial S_{signal,probe}(z,\tau)}{\partial z} = \left(g(\hbar\omega_{signal,probe}) - \alpha_{\text{int}}\right) S_{signal,probe} \tag{26}$$

$$\frac{\partial S_{control}(z,\tau)}{\partial z} = -\alpha_{abs} S_{control} \tag{27}$$

where τ is time transformed by $\tau = \text{t} - \text{v}_\text{g}^{-1}\text{z}$ with the group velocity v_g of the light pulse, S_{signal}, S_{probe} and $\text{S}_{\text{control}}$ are the photon densities of input signal, probe and CP respectively, $g(\hbar\omega)$is modal gain, α_{int} is the material absorption coefficient, $\alpha_{\text{int}}$is modal absorption coefficient of CP and z is the distance in longitudinal direction, i.e. $\text{z} = 0$ and $\text{z} = \text{L}$ stand for input and output facets of the QD-SOA. In terms of photon density, $S(z, \tau) = P(z, \tau)/(A_{eff} V_g h\nu)$, where A_{eff} is the effective cross-section of QD-SOA and hν declares the photon energy. The gain expression is given by $g(\hbar\omega_{signal,probe}) = g_{GS}(\hbar\omega_{signal,probe}) \times (f_n + f_p - 1)$ where $\text{g}_{\text{max}} = g_{GS}(\hbar\omega_{signal,probe})$is maximum modal gain [54] and $f_n(f_p)$is the electron (hole) occupation probability in the ground state (GS). The term $(f_n + f_p - 1)$ is the effective population inversion in GSs. The expressions of f_n and f_p are given in [55]. For simplicity, $f_n = f_p = f$is assumed [56, 57]. Equation 27 may primitively be written as $\partial S_{CP}/\partial z = [g(\hbar\omega_{control}) - \alpha_{\text{int}}]S_{CP}$ or in the other words,$\partial S_{CP}/\partial z = -[g_{ES}(\hbar\omega_{control})(1 - (h_n + h_p)) + \alpha_{\text{int}}]S_{CP}$ and finally it can be described in the form presented in (3). The modal absorption coefficient of the CP may be described as $\alpha_{abs} = \alpha_{\text{max}}(1 - (h_n + h_p)) + \alpha_{\text{int}}$ where $\alpha_{\text{max}} = g_{ES}(\hbar\omega_{control})$ is the maximum modal absorption coefficient and $h_n(h_p)$is the electron (hole) occupation probability in the ES.

QD-SOA dynamics relate to CP propagation equation through $1 - (h_n + h_p)$ term which describes the ES carrier dynamic, i.e. $(h_n + h_p) > 1$ and $(h_n + h_p) < 1$ stand for optical gain and absorption (in the proposed model), respectively ($h_n = h_p = h$ is presumed). The rate equations for the WL, ES and GS can be written as

$$\frac{\partial N_w(z,\tau)}{\partial \tau} = \frac{J}{eL_w} - \frac{N_w(1-h)}{\tau_{w2}} + \frac{N_w h}{\tau_{2w}} - \frac{N_w}{\tau_{wR}} \tag{28}$$

$$\frac{\partial h(z,\tau)}{\partial \tau} = \frac{N_w L_w (1-h)}{N_Q \tau_{w2}} - \frac{N_w L_w h}{N_Q \tau_{2w}} - \frac{(1-f)h}{\tau_{21}} + \frac{f(1-h)}{\tau_{12}} + \frac{\alpha_{\max} L}{N_Q}(1-2h) S_{control}(z,\tau)\frac{c}{\sqrt{\varepsilon_r}} \tag{29}$$

$$\frac{\partial f(z,\tau)}{\partial \tau} = \frac{(1-f)h}{\tau_{21}} - \frac{f(1-h)}{\tau_{12}} - \frac{f^2}{\tau_{1R}} - \frac{g_{\max,S} L}{N_Q}(2f-1) S_{signal}(z,\tau)\frac{c}{\sqrt{\varepsilon_r}} - \frac{g_{\max,P} L}{N_Q}(2f-1) S_{probe}(z,\tau)\frac{c}{\sqrt{\varepsilon_r}} \tag{30}$$

where e is electron charge and J is the injection current density. Also τ_{w2} is the electron relaxation time from the WL to the ES, τ_{2w} is the electron escape time from the ES to the WL, τ_{wR} is the spontaneous radiative lifetime in WL, τ_{21} is the electron relaxation time from the ES to the GS, τ_{12} is the electron escape time from the GS to the ES, τ_{1R} is the spontaneous radiative lifetime in the QD. N_Q is the surface density of QDs where its typical value is $\sim 5 \times 10^{10}$ cm^{-2}, N_w is the electron density in the WL, L_w is the effective thickness of active layer, ε_r is the SOA material permittivity and c is the velocity of light in free space. The last term in (5) and two last terms in (6) demonstrate the absorption of CP and stimulated emission in CBGS respectively. For simplicity, we presume an ideal facet reflectivity and neglect the amplified spontaneous emission. The time-dependence of the integral QD-SOA gain and pulse phase-shift can be expressed as $G(\tau) = \exp\left(\int_0^L g(z',\tau)\, dz\right)$ and $\phi(\tau) = -\alpha/2\left(\int_0^L g(z',\tau)\, dz\right)$ respectively where α is the LEF. It has been discussed in several articles that LEF may vary in a large interval from the experimentally measured value of 0.1 up to giant values of 60 in QDs [58, 59].

The wavelengths of signal, probe and CP are considered to be: $\lambda_S = 1.56$ μm, $\lambda_P = 1.53$ μm and $\lambda_C = 1.31$ μm. For the structure parameters $\alpha_{int} = 3$ cm^{-1}, $g_{max} = 11.5$ cm^{-1}, $\alpha_{max} = 10$ cm^{-1}, α(LEF) = 1, $\tau_{w2} = 3$ ps, $\tau_{2w} = 1$ ns, $\tau_{wR} = 0.2$ ns, $\tau_{1R} = 0.4$ ns, $\tau_{12} = 1.2$ ps, $\tau_{21} = 0.16$ ps, $L_w = 0.2$ μm, L = 1500 μm, W = 10 μm (the width of QD-SOA), $\Gamma \sim 3 \times 10^{-2}$ (the confinement factor), the state occupation probabilities of electrons in the presence and without CP for one of the QD-SOAs located on MZI arms, at 1 Tb/s and 2 Tb/s input bit sequences, 50 mA bias current, 200 μW input signal, 250 μW CP and 2 μW probe signal are displayed in Figs. 3.29 and 3.30 respectively.

At both bit rates of 1 Tb/s and 2 Tb/s the oscillation of ES and GS completely follow the input signal variation however at 2 Tb/s bit sequence, the population variation can not reach to the final population value but still varies with relatively high amplitude.

The high population of GS (f $\sim$ 0.75) and ES (h $\sim$ 0.35) is due to fast electron transition between ES and GS and absorption of the CP which compensates the relaxed population of ES to GS. The maximum value for state population

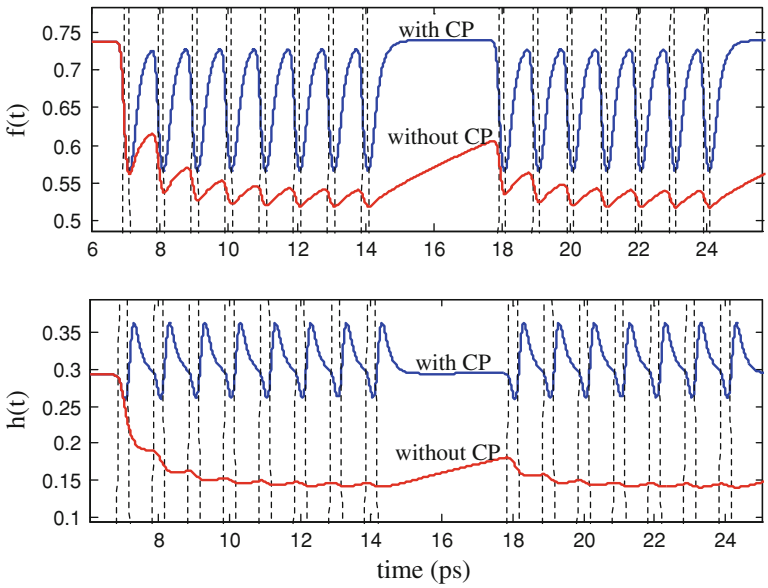

Fig. 3.29 Electron state occupation probabilities of GS, f(t), and ES, h(t), in the presence and without CP. The *dashed lines* correspond to input bit sequence at 1 Tb/s. The bias current is 50 mA, input signal, CP and probe signal powers are: 200, 250 and 2 μW respectively [45]

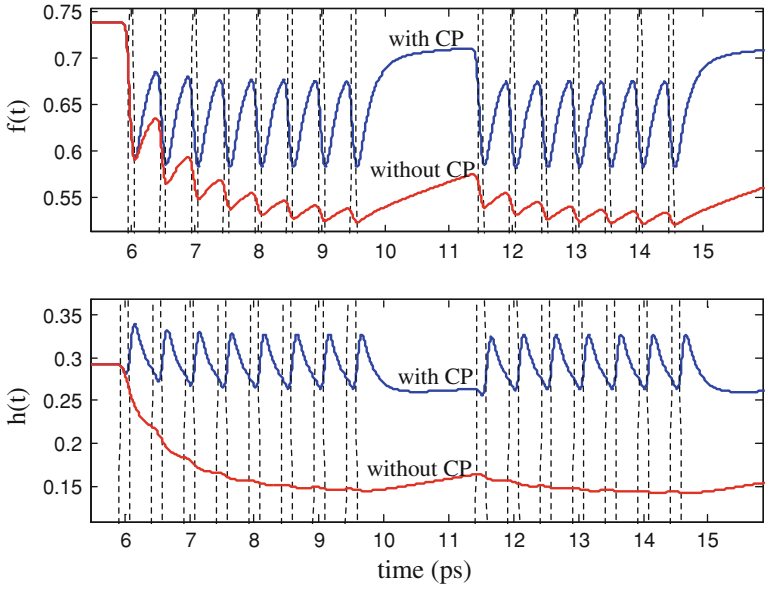

Fig. 3.30 Electron state occupation probabilities of GS, f(t), and ES, h(t), in the presence and without CP. The *dashed lines* correspond to input bit sequence at 2 Tb/s. The bias current is 50 mA, input signal, CP and probe signal powers are: 200, 250 and 2 μW respectively [45]

probability of ES, h, versus increasing the CP power and in enough large values of CP power will tend to 0.5.

This fact can be justified by considering the last term of (29). Whenever the h value tends to 0.5, the expression (1-2h) tends to zero and in this case, the effect of

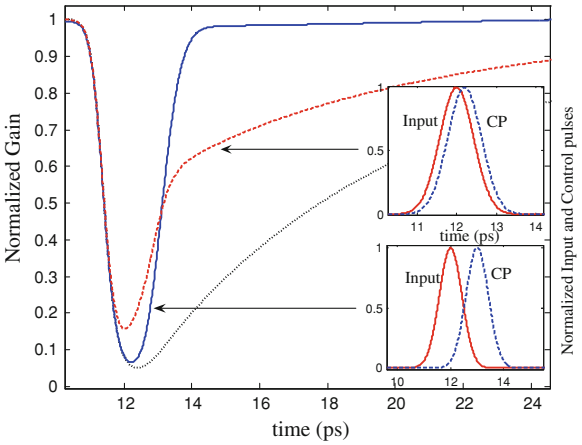

Fig. 3.31 Gain dynamics of QD-SOA following an input pulse with 1 ps FWHM and 200 μW pulse power in presence and without considering the CP for two different input and CP temporal positions. The *dotted line* corresponds to the case that the CP is not applied [45]

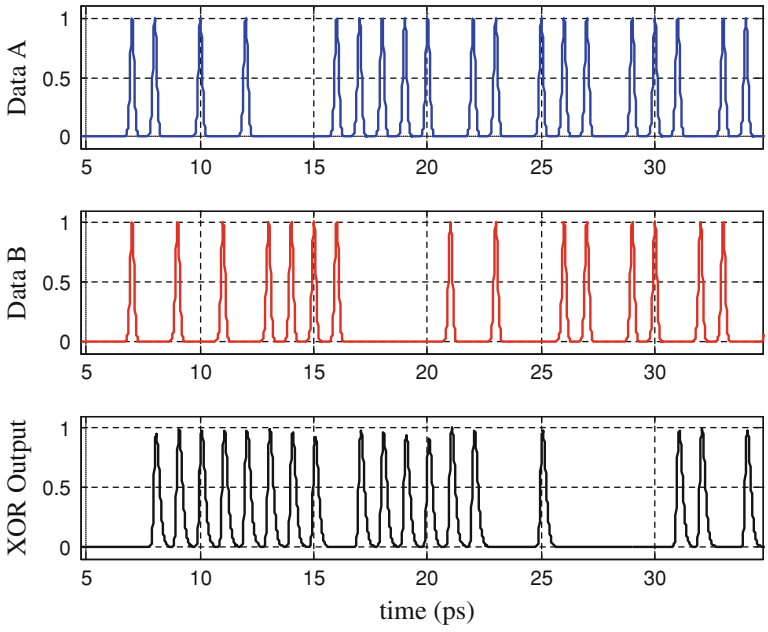

Fig. 3.32 XOR operation of QD-SOA-MZI structure for 1 Tb/s input bit Sequence and 50 mA injected current. The input signal, CP and probe signal powers are: 200 μW, 2 mW and 2 μW respectively [45]

last term in (29) (absorption of CP) on increasing the population of ES vanishes. Thus, temporal decrease of h motivates the term (1-2h) to become positive and effective absorption of CP will happened. It should be mentioned that the process of controlling the h value below 0.5 is related to XGM phenomenon. In fact, the influence of the CP on gain recovery process is similar to a fast current source which is applied when the gain dynamics reaches to its minimum value.

In Fig. 3.31 the two possible temporal positions of input signal and CP with 1 ps FWHM and also the related gain variations are illustrated. It can be concluded that applying the CP when the gain variation tends to zero (i.e. when the input pulse reaches to its maximum amplitude), will obtain the optimum gain recovery time. In this case, absorption of the CP will populate the CBES and hence the recovery process will be accelerated.

The results for the XOR logic operation with CW probe signal at 1, 2 and 2.5 Tb/s input sequences are displayed in Figs. 3.32, 3.33, and 3.34 respectively.

The results describe that the pattern effect is negligible at 1 Tb/s but in Figs. 3.33 and 3.34 it can be seen that the form of XOR signal is distorted.

In order to obtain the eye diagram, a 2^8-1 pseudo-random return to zero (RZ) sequence input has been used. The corresponding eye diagrams of the XOR gate output signal are shown in Fig. 3.35. A quantity known as Q is widely utilized to analyze and predict the signal quality for pseudo-random signals [60] and is

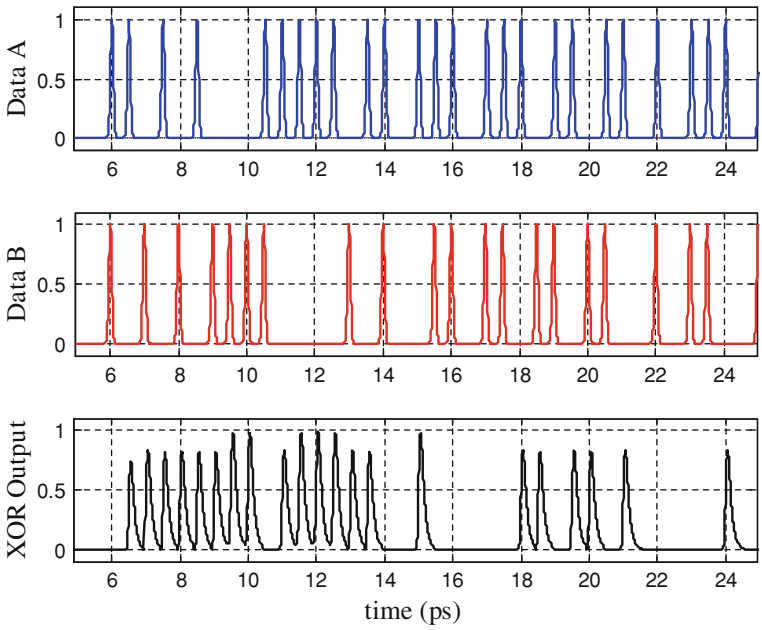

Fig. 3.33 XOR operation of QD-SOA-MZI structure for 2 Tb/s input bit Sequence and 50 mA injected current. The input signal, CP and probe signal powers are: 200 μW, 2 mW and 2 μW respectively [45]

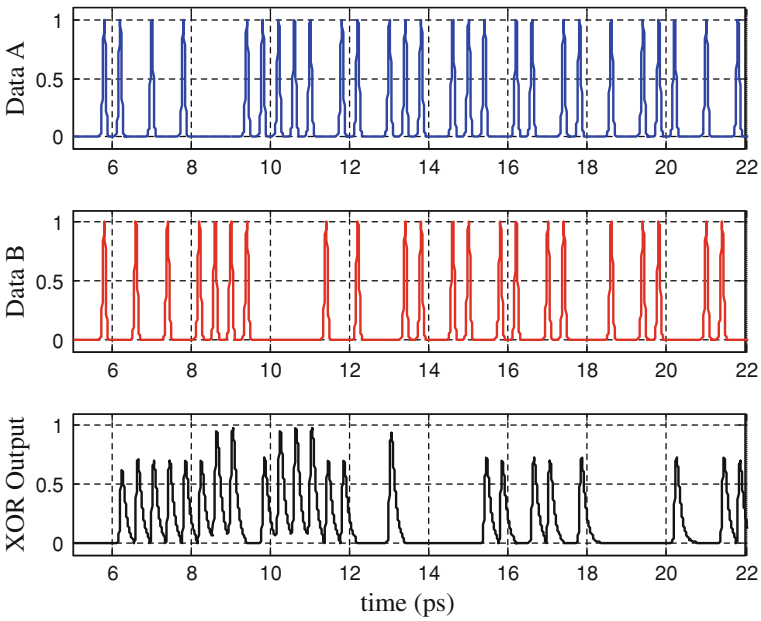

Fig. 3.34 XOR operation of QD-SOA-MZI structure for 2.5 Tb/s input bit sequence and 50 mA injected current. The input signal, CP and probe signal powers are: 200 μW, 2 mW and 2 μW respectively [45]

defined as $Q = (\bar{P}_1 - \bar{P}_0) / (\sigma_1 + \sigma_0)$ where $\bar{P}_1$and $\bar{P}_0$ are the average power of output signals "1" and "0", σ_1 and σ_0 are standard deviation of all "1" and "0" respectively.

As it described before, in a QD-SOA, bias current and electron relaxation time from WL to ES determine the SOA performance and hence high currents and faster relaxation times improve the Q factor. But beside the fact that too high current is prohibited for practical applications, the Q factor saturates above a specific bias current [52].

Also the Q value is sensitive to the input pulse width and increasing the pulse width decreases the Q factor because of overlapping of two neighboring pulses. The Q factor is also dependant on Γ parameter. Multilayer QD structures are considered as a technique to increase the modal gain due to increasing the Γ parameter and therefore reducing the threshold current. As it can be seen in Fig. 3.35, because of ultrafast gain recovery in the presence of CP, at the bit rate of 1 Tb/s, the pattern effect is almost absent and the eye pattern is clearly open with Q of 28.4. Also for the bit rate of 2 and 2.5 Tb/s the Q-factor drops to 8.8 and 4.9 respectively and the eye is gradually closing due to pattern effect.

According to the reported results for τ_{21} which are $\sim$160 fs [61–63], this parameter is not a limiting factor in conventional QD-SOA's operation at $\sim$200 Gb/s because of longer WL to ES relaxation time. However, this parameter can be important in achieving high-speed operation in the explained control-probe

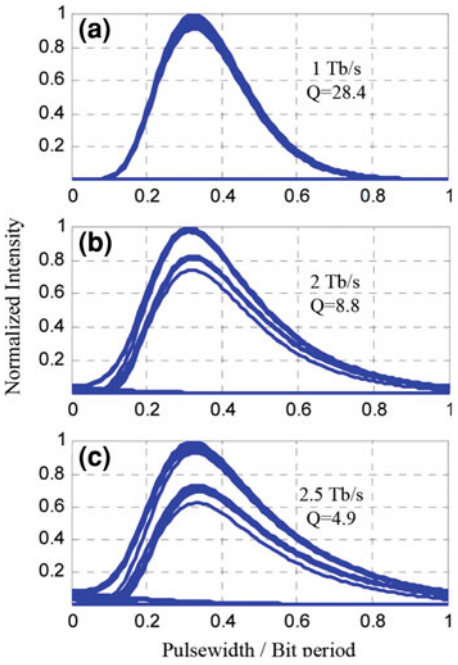

Fig. 3.35 Eye diagrams of the XOR output signals. In each case the pulse width is 1/5th of the bit period. The input bit sequences are at **a** 1 Tb/s, **b** 2 Tb/s and **c** 2.5 Tb/s [45]

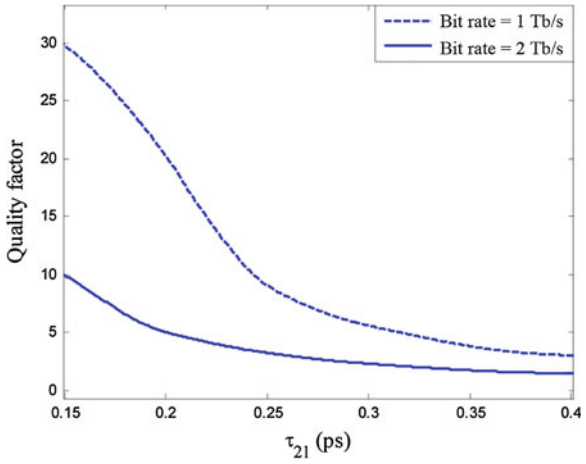

Fig. 3.36 Quality factor of XOR gate as a function of ES to GS relaxation time for input bit sequences at 1 Tb/s (*dashed*) and 2 Tb/s (*solid*) [45]

approach as a higher limit. Increasing the τ_{21} relaxation time and consequently τ_{12} ($\tau_{12} = \tau_{21} \exp[(E_2 - E_1)/K_B T]$ where K_B is the Boltzmann constant, T is the absolute temperature and $(E_2 - E_1)$ is the energy separation between the ES and GS), decreases the quality factor of XOR output, as shown in Fig. 3.36.

The potential of operation at Tb/s bit rates is quiet interesting to trade off with practical difficulties in the implementation such as generating two identically

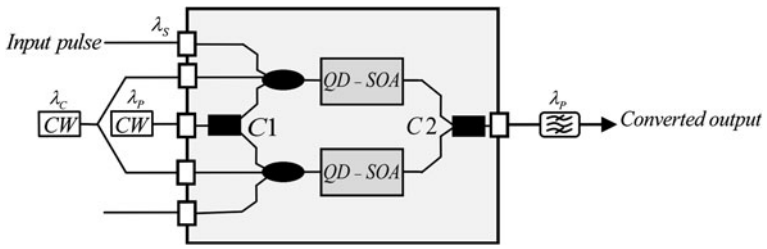

Fig. 3.37 Configuration of the control-probe-method-based all-optical wavelength converter using CW control beam

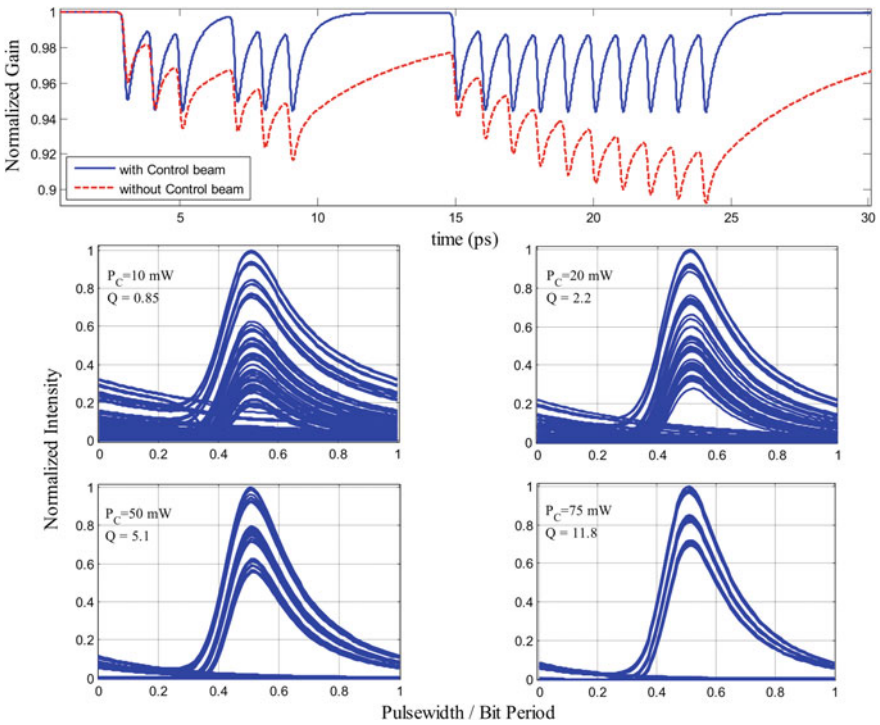

Fig. 3.38 Normalize gain dynamic of QD-SOA in the presence and without control beam (*upper figure*) and eye diagrams of the wavelength converter output signals at 1 Tb/s input bit streams (*lower figures*) for PC = 10, 20, 50 and 75 mW

patterned pulses at control and signal wavelengths. However, other possible and also easily implementable structures may introduce with the aim of reducing the technological complexities. Figure 3.37 depicts a similar structure for the control-probe method-based QD-SOA wavelength converter where the CP has replaced with a continuous beam at the previous (i.e. control) wavelength. To remove the

signal and control beams, a band pass filter (BPF) centered at λ_P is placed at the output of the structure.

The obtained gain dynamics and eye diagrams for wavelength converter performance (Fig. 3.38) at 1 Tb/s input bit stream (which depends on the control beam power) explains the operation quality. The demonstrated structure however operates at lower bit rates compared with the presented structure in Fig. 3.27 at the hands of reducing prohibitive cost and implementation equipments.

References

1. Sun, H., Wang, Q., Dong, H., Zhu, G., Dutta, N.K., Jaques, J.: Gain dynamics and saturation property of a semiconductor optical amplifier with a carrier reservoir. IEEE Photon. Technol. Lett. **18**, 196–198 (2006)
2. Sugawara, M., Akiyama, T., Hatori, N., Nakata, Y., Ebe, H., Ishikawa, H.: Quantum-dot semiconductor optical amplifiers for high-bit-rate signal processing up to 160 Gb/s and a new scheme of 3R regenerators. Meas. Sci. Technol. **13**, 1683–1691 (2002)
3. Furata, T.: High Field Minority Electron Transport in GaAs in Semiconductors and Semimetals. Academic, New York (1993)
4. Reschner, D.W., Gehrig, E., Hess, O.: Pulse amplification and spatio-spectral hole-burning in inhomogeneously broadened quantum-dot semiconductor optical amplifiers. IEEE J. Quantum Electron. **45**, 21–33 (2009)
5. Berg, T.W., Mørk, J.: Saturation and noise properties of quantum-dot optical amplifiers. IEEE J. Quantum Electron. **40**, 1527–1539 (2004)
6. Sosnowski, T.S., Norris, T.B., Jiang, H., Singh, J., Kamath, K., Bhattacharya, P.: Rapid carrier relaxation in In0.4Ga0.6As/GaAs quantum dots characterized by differential transmission spectroscopy. Phys. Rev. B **57**, R9423–R9426 (1998)
7. Agrawal, G.P., Dutta, N.K.: Semiconductor Lasers. Van Nostrand Reinhold, New York (1993)
8. Mecozzi, A., Møork, J.: Saturation effect in nondegenerate four-wave mixing between short optical pulses in semiconductor laser amplifier. IEEE J. Select. Topics Quantum Electron. **3**, 1190–1207 (1997)
9. Tang, J.M., Shore, K.A.: Characteristic of optical phase conjugation of picosecond pulses in semiconductor optical amplifiers. IEEE J. Quantum Electron. **35**, 1032–1040 (1999)
10. Sugawara, M., Ebe, H., Hatori, N., Ishida, M., Arakawa, Y., Akiyama, T., Otsubo, K., Nakata, Y.: Theory of optical signal amplification and processing by quantum-dot semiconductor optical amplifiers. Phys. Rev. B Condens. Matter **69**, 235332-1–235332-39 (2004)
11. Manning, R.J., Davies, D.A.O.: Three-wavelength device for all-optical signal processing. Opt. Lett. **19**, 889–891 (1994)
12. Inoue, K., Yoshino, M.: Gain dynamics of a saturated semiconductor laser amplifier with 1.47-μm ld pumping. IEEE Photon. Technol. Lett. **8**, 506–508 (1996)
13. Usami, M., Tsurusawa, M., Matsushima, Y.: Mechanism for reducing recovery time of optical nonlinearity in semiconductor laser amplifier. Appl. Phys. Lett. **72**, 2657–2659 (1998)
14. Dupertuis, M.A., Pleumeekers, J.L., Hessler, T.P., Selbmann, P.E., Deveaud, B., Dagens, B., Emery, J.Y.: Extremely fast high-gain and low-current soa by optical speed-up at transparency. IEEE Photon. Technol. Lett. **12**, 1453–1455 (2000)
15. Tai, C., Tzeng, S.L., Chang, H.C., Way, W.I.: Reduction of nonlinear distortion in MQW semiconductor optical amplifier using light injection and its application in multichannel m-qam signal transmission systems. IEEE Photon. Technol. Lett. **10**, 609–611 (1998)

16. Yoshino, M., Inoue, K.: Improvement of saturation output power in a semiconductor laser amplifier through pumping light injection. IEEE Photon. Technol. Lett. **8**, 58–59 (1996)
17. Yu, J., Jeppesen, P.: Improvement of cascaded semiconductor optical amplifier gates by using holding light injection. J. Lightwave Technol. **19**, 614–623 (2001)
18. Ho, K.-P., Liaw, S.-K., Lin, C.: Reduction of semiconductor laser amplifier induced distortion and crosstalk for wdm systems using light injection. Electron. Lett. **32**, 2210–2211 (1996)
19. Pleumeekers, J.L., Kauer, M., Dreyer, K., Burrus, C., Dentai, A.G., Shunk, S., Leuthold, J., Joyner, C.H.: Acceleration of gain recovery in semiconductor optical amplifiers by optical injection near transparency wavelength. IEEE Photon. Technol. Lett. **14**, 12–14 (2002)
20. Talli, G., Adams, M.J.: Gain recovery acceleration in semiconductor optical amplifiers employing a holding beam. Opt. Commun. **245**, 363–370 (2005)
21. Talli, G., Adams, M.J.: Gain dynamics of semiconductor optical amplifiers and three-wavelength devices. IEEE J. Quantum. Electron. **39**, 1305–1313 (2003)
22. Liu, Y., Tangdiongga, E., Li, Z., Zhang, S., Waardt, H., Khoe, G.D., Dorren, H.J.S.: Error-free all-optical wavelength conversion at 160 Gb/s using a semiconductor optical amplifier and an optical bandpass filter. IEEE J. Lightwave Technol. **24**, 230–236 (2006)
23. Chayett, H., Ben Ezra, S., Shachar, N., Tzadok, S., Tsadka, S., Leuthold, J.: Regenerative all-optical wavelength converter based on semiconductor optical amplifier and sharp frequency response. In: Optical Fiber Communication (OFC), Los Angeles, CA, Paper Ths2 (2004)
24. Nielsen, M.L., Lavigne, B., Dagens, B.: Polarity-preserving SOA-based wavelength conversion at 40 Gb/s using bandpass filtering. Electron. Lett. **39**, 1334–1335 (2003)
25. Leuthold, J., Marom, D.M., Cabot, S., Jaques, J.J., Ryf, R., Giles, C.R.: All-optical wavelength conversion using a pulse reformatting optical filter. J. Lightwave Technol. **22**, 186–192 (2004)
26. Liu, Y., Tangdiongga, E., Li, Z., Zhang, S., de Waardt, H., Khoe, G.D., Dorren, H.J.S.: 160 Gb/s SOA-ased wavelength converter assisted by an optical bandpass filter. In: Optical Fiber Communication/National Fiber Optic Engineers Conference (OFC/NFOEC), Anaheim, CA, PDP17 (2005)
27. Mark, J., Mørk, J.: Subpicosecond gain dynamics in InGaAsP optical amplifiers: experiment and theory. Appl. Phys. Lett. **61**, 2281–2283 (1992)
28. Liu, Y., Tangdiongga, E., Li, Z., Zhang, S., de Waardt, H., Khoe, G.D., Dorren, H.J.S.: Error-free 320Gbit/s SOA based wavelength conversion using optical filtering. In: Proceedings of OFC/NFOEC, Anaheim, CA, USA, paper PDP28 (2006)
29. Nielsen, M., Mork, J.: Increasing the modulation bandwidth of semiconductor-optical-amplifier-based switches by using optical filtering. J.Opt. Soc. Am. B **21**, 1606–1619 (2004)
30. Leuthold, J.: Trends in the field of all-optical wavelength conversion and regeneration for communication up to 160 Gbit/s. In: Proceedings of ECOC, Glasgow, paper Tu3.3.6 (2005)
31. Manning, R.J.: Cancellation of nonlinear patterning in semiconductor amplifier based switches. In: Proceedings of OAA, Whistler, Canada, paper OTuC1 (2006)
32. Giller, R.: Recovery dynamics of the Turbo-Switch. In: Proceedings of OAA, Whistler, Canada, paper OTuC2 (2006)
33. Manning, R.J., Giller, R., Yang, X., Webb, R.P., Cotter, D.: SOAs for all-optical switching-techniques for increasing the speed. IEEE ICTON **2007**, 239–242 (2007)
34. Zhang, L.: Significant reduction of recovery time in semiconductor optical amplifier using p type modulation doped MQW. In: Proceedings of ECOC, Cannes, France, paper Tu4.4.5 (2006)
35. Dagens, B.: Design optimization of all-active Mach-Zehnder wavelength converters. Photon. Technol. Lett. **11**, 424–426 (1999)
36. Miyazaki, Y.: Polarization-insensitive SOA-MZI monolithic all-optical wavelength converter for full C-band 40Gbps-NRZ operation. In: Proceedings of ECOC, Cannes, France, paper Th3.4.2 (2006)

37. Giller, R., Manning, R.J., Talli, G., Webb, R.P., Adams, M.J.: Analysis of the dimensional dependence of semiconductor optical amplifier recovery speeds. Opt. Exp. **15**, 1773–1782 (2007)
38. Sokoloff, J.P., Prucnal, P.R., Glesk, I., Kane, M.: A terahertz optical asymmetric demultiplexer (TOAD). IEEE Photon. Technol. Lett. **5**, 787–790 (1993)
39. Zhang, L., Kang, I., Bhardwaj, A., Sauer, N., Cabot, S., Jaques, J., Nielson, D.T.: Reduced recovery time semiconductor optical amplifier using p-type-doped multiple quantum wells. Photon. Technol. Lett. **18**, 2323–2325 (2006)
40. Ginovart, F., Simon, J.C.: Semiconductor optical amplifier length effects on gain dynamics. J. Phys. D Appl. Phys. **36**, 1473–1476 (2003)
41. Schares, L., Schubert, C., Schmidt, C., Weber, H.G., Occhi, L., Guekos, G.: Phase dynamics of semiconductor optical amplifiers at 10–40 GHz. J. Quantum. Electron. **39**, 1394–1408 (2003)
42. Li, X., Alexandropoulos, D., Adams, M.J., Lealman, I.F.: Wavelength dependence of gain recovery time in semiconductor optical amplifiers. In: Proceedings of SPIE, vol 5722, pp. 343–350 (2005)
43. Ito, T., Yoshimoto, N., Magari, K., Kishi, K., Kondo, Y.: Extremely low power consumption semiconductor optical amplifier gate for WDM applications. Electron. Lett. **33**, 1791–1792 (1997)
44. Ju, H., Uskov, A.V., Nötzel, R., Li, Z., V′azquez, J., Lenstra, D., Khoe, G.D., Dorren, H.J.S.: Effects of two-photon absorption on carrier dynamics in quantum-dot optical amplifiers. Appl. Phys. B **82**, 615–620 (2006)
45. Rostami, A., Baghban, H., Qartavol, R.M., Rasooli, H.: Tb/s optical logic gates based on quantum-dot semiconductor optical amplifiers. IEEE J. Quantum Electron. **46**, 354–360 (2010)
46. Uskov, A.V., Berg, T.W., Mørk, J.: Theory of pulse-train amplification without patterning effects in quantum-dot semiconductor optical amplifiers. IEEE J. Quantum Electron. **40**, 306–320 (2004)
47. Ben-Ezra, Y., Haridim, M., Lembrikov, B.I.: Theoretical analysis of gain-recovery time and chirp in QD-SOA. IEEE Photon. Technol. Lett. **17**, 1803–1805 (2005)
48. Annetts, P.J., Asghari, M., White, I.H.: The effect of carrier transport on the dynamic performance of gain-saturation wavelength conversion in MQW semiconductor optical amplifiers. IEEE J. Select. Topics Quantum Electron. **3**, 320–329 (1997)
49. Watanabe, T., Sakaida, N., Yasaka, H., Kano, F., Koga, M.: Transmission performance of chirp controlled signal by using semiconductor optical amplifier. J. Lightwave Technol. **18**, 1069–1077 (2000)
50. Uskov, A.V., McInerney, J., Adler, F., Schweizer, H., Pulkuhn, M.H.: Auger carrier capture kinetics in self-assembled quantum dot structures. Appl. Phys. Lett. **72**, 58–60 (1998)
51. Bhattacharya, P., Klotzkin, D., Qasaimeh, O., Zhou, W., Krishna, S., Zhu, D.: High speed modulation and switching characteristics of InGaAs-AlGaAs self organized quantum dot lasers. IEEE J. Select. Topics Quantum Electron. **6**, 426–438 (2000)
52. Sun, H., Wang, Q., Dong, H., Dutta, N.K.: XOR performance of a quantum dot semiconductor optical amplifier based Mach–Zender interferometer. Opt. Exp. **13**, 1892–1899 (2005)
53. Ben-Ezra, Y., Lembrikov, B.I., Haridim, M.: Ultrafast all-optical processor based on quantum-dot semiconductor optical amplifiers. IEEE J. Quantum Electron. **45**, 34–41 (2009)
54. Steiner, T. (ed.): Semiconductor Nanostructures for Optoelectronic Applications. Artech House, London (2004)
55. Asryan, L., Suris, R.: Longitudinal spatial hole burning in a quantum-dot lasers. IEEE J. Select. Topics Quantum Electron. **36**, 1151–1160 (2000)
56. Qasaimeh, O.: Characteristics of cross-gain (XG) wavelength conversion in quantum dot semiconductor optical amplifier. IEEE Photon. Technol. Lett. **16**, 542–544 (2004)
57. Qasaimeh, O.: Optical gain and saturation characteristics of quantum-dot semiconductor optical amplifiers. IEEE J. Quantum Electron. **39**, 793–798 (2003)

58. Newell, T.C., Bossert, D.J., Stinz, A., Fuchs, A., Malloy, K.J.: Gain and linewidth enhancement factor in InAs quantum-dot laser diodes. IEEE Photon. Technol. Lett. **11**, 1527–1529 (1999)
59. Dagens, B., Markus, A., Chen, J.X., Provost, J.-G., Make, D., de Gouezigou, O., Landreau, J., Fiore, A., Thedrez, B.: Giant linewidth enhancement factor and purely frequency modulated emission from quantum dot laser. Electron. Lett. **41**, 323–324 (2005)
60. Agrawal, G.P.: Fiber Optic Communication Systems. John Wiley, New York (2002)
61. Borri, P., Langbein, W., Hvam, J.M., Heinrichsdorff, F., Mao, H.M., Bimberg, D.: Spectral hole-burning and carrier-heating dynamics in quantum-dot amplifiers: comparison with bulk amplifiers. Phys. Status. Solidi. B **224**, 419–423 (2001)
62. Meuer, C., Kim, J., Laemmlin, M., Liebich, S., Capua, A., Eisenstein, G., Kovsh, A.R., Mikhrin, S.S., Krestnikov, I.L., Bimberg, D.: Static gain saturation in quantum dot semiconductor optical amplifiers. Opt. Exp. **16**, 8269–8279 (2008)
63. Schneider, S., Borri, P., Langbein, W., Woggon, U., Sellin, R.L., Ouyang, D., Bimberg, D.: Excited-state gain dynamics in InGaAs quantum-dot amplifiers. J. Lightwave Technol. **17**, 2014–2016 (2005)

Chapter 4
Applications and Functionalities

4.1 Introduction

Realization of future all-optical switching networks regardless of their exact operational specifications strongly depends on all-optical signal processing methods and elements. Advanced all-optical signal processing functions such as all-optical header recognition, buffer, switching, wavelength conversion, logic gates, flip-flop memory, etc. should be realized. In particular, wavelength conversion is very crucial in all of optical switching schemes including optical circuit switching, optical burst switching and optical packet switching. All-optical signal processing functions are usually performed using nonlinear optical effects that occur in a device under certain conditions. All-optical signal processing based on optical fibers profit several advantages such as easy coupling to the transmission link, low operation noise and ultrafast nonlinear phenomena (tens of femotoseconds) which make them attractive for high-speed all-optical signal processing beyond 1 Tb/s. However, these elements suffer from bulky nature of fiber-based devices which is demanded for observation of noticeable nonlinear effect and prevent the integration of the processing unit. Also, due to small nonlinear coefficient, the input optical power (usually more than 20 dBm) is too high for practical application in ultra-high bit rate all-optical signal processing systems.

Semiconductor optical amplifier-based devices have been proposed to suitable alternatives in all-optical signal processing due to the gain and nonlinear properties, operation at low powers and small device dimensions. One drawback of SOA-based devices relates to long carrier lifetimes (typically tens to hundreds of picoseconds) which result in significant pattern effect limiting the maximum pattern-effect-free bit rate. The advent of DQ-SOAs has promised higher pattern-free operation capabilities of SOA-based devices. Although several studies have been done to increase the operation speed and gain recovery time of QD-SOAs as discussed in previous chapters. In recent years considerable progress has been

A. Rostami et al., *Nanostructure Semiconductor Optical Amplifiers*,
Engineering Materials, DOI: 10.1007/978-3-642-14925-2_4,

made in SOA-based all-optical signal processing including demonstration of complicated logic devices which are mainly based on SOA nonlinear phenomena like cross gain modulation (XGM), cross phase modulation (XPM), four wave mixing (FWM) and cross polarization modulation (XPolM). Combination of these effects has yielded state of the art all-optical devices and functions such as high-speed all-optical wavelength conversion at 320 Gb/s, 640 Gb/s-to-40 Gb/s all-optical demultiplexing, penalty-free all-optical 3R regeneration (re-amplification, reshaping and re-timing) at 84 Gb/s, 8-state optical flip-flop memory, optical shifter register and an optical pseudo-random binary series generator, optical half adder and full adder, etc. In these complicated systems, optical logic gates play a significant role. Optical logic gates, specifically, XOR gates, are actually used to realize packet address recognition in the IST-LASAGNE project [1]. These examples clarify the importance of SOA-based devices in all-optical signal processing. In this chapter we describe the general operation of simple SOA-based logic gates and then more complicated signal processing circuits will be discussed. Since most of the experimentally demonstrated SOA-based elements up to day appertain to bulk or quantum well SOAs rather than QD-SOAs, therefore the operation principles and experimental results will be introduced based on general SOA concept. Also, the available researches for QD-SOA based elements will be presented.

4.2 SOA-MZI Gate

Practical implementation of all-optical signal processing unit requires integrated all-optical devices for ease of manufacturing, installation, and operation. The semiconductor optical amplifier Mach–Zehnder interferometer (SOA-MZI) is an integrated all-optical logic gate which can fulfill these requirements. Conceptually, SOA-MZI-based logic gate operation is straightforward, relying on optically inducing XGM, XPM or other nonlinear phenomena between the SOAs located in each of the two interferometer arms. Figure 4.1 shows the configuration of a SOA-MZI gate also known as symmetric Mach–Zehnder (SMZ) where SOAs used as nonlinear elements are placed in both arms of a MZI. The control light governs the dynamics of nonlinear optical effects and the probe light experiences the nonlinear optical effects. The control and probe beams can be either return-to-zero (RZ) pulses, as in Fig. 4.1, or non-return-to-zero (NRZ) light. The control pulse induces carrier depletion and thus modulates the gain and phase of the probe light which are called XGM and XPM, respectively. These nonlinear optical effects induced through the carrier density change in semiconductors, are generally highly efficient, which means that device operation can be realized in a compact size and with low power control beam. In addition to this, the control light, which depletes carriers, is amplified in SOA and thus, lowers the required power of input control light. Differential arrangement of SOAs on both arms of the MZI with an appropriate time delay, ΔT, resolves the low gain recovery time since the similar

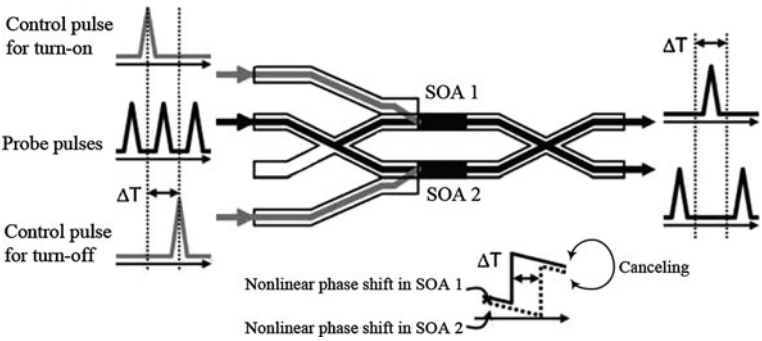

Fig. 4.1 SMZ configuration and nonlinear phase response cancel out mechanism

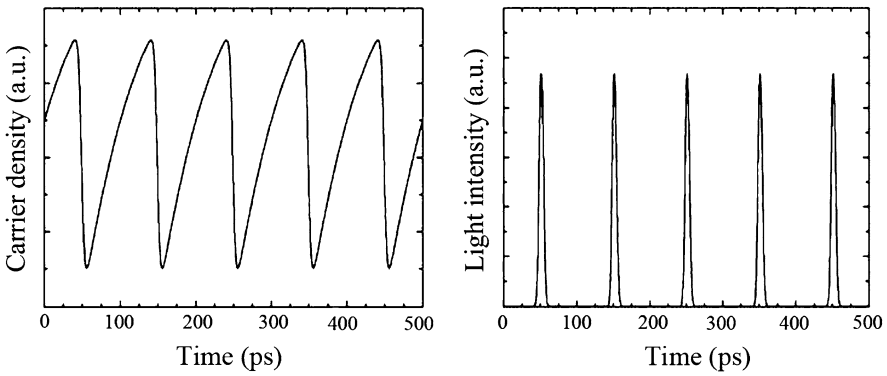

Fig. 4.2 Total carrier density of the SOAs in the presence of control pulses (*left*) and SMZ gate output (*right*)

phase responses of the SOAs cancel out each other as depicted schematically in Fig. 4.1.

The variation of total carrier density in SOAs and the gating window with the SMZ gate is presented in Fig. 4.2. Control pulses with a specified duration and repetition rate cause the change in the total carrier number or the carrier density in SOAs. Short control pulses cause depletion in the carrier density and the slow recovery in the carrier density is compensated by exciting both arms with an interval of ΔT. In this timing interval the gating window for the probe beam opens while outside this interval the destructive interference for the probe beam at the output of the Mach–Zehnder interferometer is maintained even though the carrier density in the SOAs on both arms is slowly recovered. Therefore, the rising and falling of the gate window are defined by the control pulse duration.

The technology of integrating optical circuits is an important key for developing practical MZI-based all-optical gates. SOAs incorporated into Mach–Zehnder interferometers can be used as appropriate unit call for optical

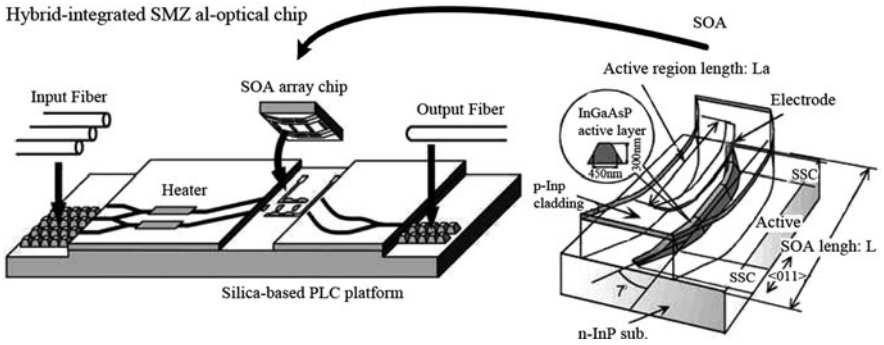

Fig. 4.3 Structure of SOA and hybrid-integrated SMZ gate [3]

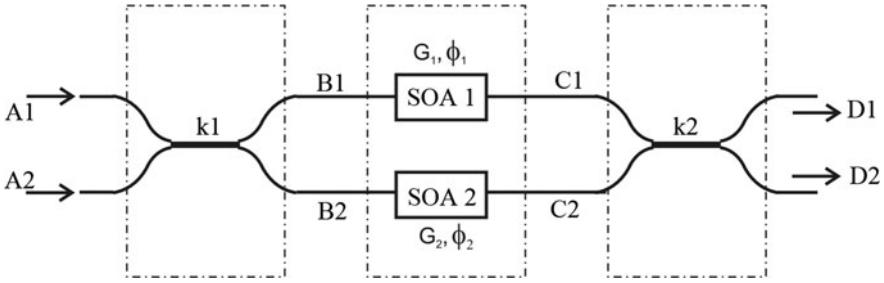

Fig. 4.4 Schematic of SOA incorporated MZI structure

logic gates. The integration of active and passive waveguides for SMZ gates has been developed both in a hybrid manner and in a monolithic manner. Figure 4.3 depicts a hybrid integrated device where SOAs are mounted on a silica-based planar lightwave circuit (PLC) [2].

Monolithic integration of SMZ gates with other active devices, such as input and output optical amplifiers and fixed or tunable diode lasers and significant reduction in the footprint of Mach–Zehnder optical circuits using photonic-crystal waveguides [4] are important technological outcomes in the way of realizing integrated all-optical signal processing devices.

4.3 SOA-MZI Transfer Function

SOAs incorporated with MZI are one of the most applicable configurations in optical logic gates. Similar to other fiber-based devices including SOAs as nonlinear element such as semiconductor laser amplifier loop optical mirror (SLALOM) and terahertz optical asymmetric demultiplexer (TOAD), SOA in MZI structure presented in Fig. 4.4 can be modeled with a nonlinear device with a gain

effect and phase shift applied on input signal. Thus, the transfer function of such a structure can be obtained through following manner.

In the above configuration (A1, A2) and (D1, D2) are input and output lightwaves, respectively, (k1, k2) are normalized coupling coefficients of the input and output couplers and (B1, B2) and (C1, C2) are input and output lightwaves to the SOAs, respectively. The gain and phase shift of each SOA is considered with (G_1, Φ_1) and (G_2, Φ_2) for upper and lower arm SOAs. Considering each pair of input and output lightwaves one can write

$$\begin{pmatrix} B_1 \\ B_2 \end{pmatrix} = \begin{pmatrix} \cos K_1 & i \sin K_1 \\ i \sin K_1 & \cos K_1 \end{pmatrix} \begin{pmatrix} A_1 \\ A_2 \end{pmatrix} \tag{1}$$

An optical signal travelling through the amplifier will experience an amplification of $\sqrt{G}$ and a phase shift of Φ. Therefore,

$$\begin{pmatrix} C_1 \\ C_2 \end{pmatrix} = \begin{pmatrix} \sqrt{G_1} e^{i\Phi_1} & 0 \\ 0 & \sqrt{G_2} e^{i\Phi_2} \end{pmatrix} \begin{pmatrix} B_1 \\ B_2 \end{pmatrix} \tag{2}$$

Then, the transfer function can be described as

$$\begin{pmatrix} D_1 \\ D_2 \end{pmatrix} = \begin{pmatrix} H_{11} & H_{12} \\ H_{21} & H_{22} \end{pmatrix} \begin{pmatrix} A_1 \\ A_2 \end{pmatrix} \tag{3}$$

where

$$\begin{aligned} H_{11} &= \cos K_1 \cos K_4 \sqrt{G_1} e^{i\Phi_1} - \sin K_1 \sin K_4 \sqrt{G_2} e^{i\Phi_2} \\ H_{12} &= i\left(\sin K_1 \cos K_4 \sqrt{G_1} e^{i\Phi_1} + \cos K_1 \sin K_4 \sqrt{G_2} e^{i\Phi_2}\right) \\ H_{21} &= i\left(\cos K_1 \sin K_4 \sqrt{G_1} e^{i\Phi_1} + \sin K_1 \cos K_4 \sqrt{G_2} e^{i\Phi_2}\right) \\ H_{22} &= -\sin K_1 \sin K_4 \sqrt{G_1} e^{i\Phi_1} + \cos K_1 \cos K_4 \sqrt{G_2} e^{i\Phi_2} \end{aligned} \tag{4}$$

Denoting the input and output signal powers with P_{A1}, P_{A2}, P_{D1} and P_{D2} and assuming an ideal 3 dB coupler ($\cos k_i = \sin k_i = \sqrt{2}/2$) the transfer function reduces to

$$H_{D_1} = \frac{P_{D_1}}{P_{A_1}} \left| \left[\frac{D_1}{A_1}\right]_{A_2=0} \right|^2 = \frac{1}{4} G_1 + \frac{1}{4} G_2 - \frac{1}{2} \sqrt{G_1 G_2} \cos \Delta\Phi \tag{5}$$

$$H_{D_2} = \frac{P_{D_2}}{P_{A_1}} \left| \left[\frac{D_2}{A_1}\right]_{A_2=0} \right|^2 = \frac{1}{4} G_1 + \frac{1}{4} G_2 + \frac{1}{2} \sqrt{G_1 G_2} \cos \Delta\Phi \tag{6}$$

$$\Delta\Phi = \Phi_1 - \Phi_2 \tag{7}$$

4.4 Michelson Interferometer

The Michelson interferometer (MI) as sketched in Fig. 4.5 (similar to the MZI configuration of Fig. 4.4) is simply a folded version of the MZI where the left input facet is reflective (~33%), and made by cleaving the SOA material along its crystal plane. A control signal (data signal) is coupled directly into the upper interferometer arm of the MI counter-directionally to the probe beam. The operation principle of such a configuration in optical logic circuits is similar to MZI structure except the reflective facet which reflects the probe beam as it reaches the left input facet. Therefore, the probe beam propagates twice through the interferometer arm before recombining at the output of the interferometer.

Although the MZI and MI basically function the same way, there are some differences in characteristics due to their different structures. Since the probe beam enters and leaves the same port of the MI, a circulator is needed to separate the two components. Also, a filter should be used to omit the control signal wavelength at the output. On the other hand, because the control signal is injected directly into the interferometer and probe beam propagates twice through the SOAs, a larger modulation bandwidth and high-speed performance is expected compared with MZI due to large photon intensity and a long interaction length. However, transient effects associated with the counter-propagation in the MI will limit the actual modulation bandwidth and the MZI is expected to exhibit better performance at higher bit rates.

4.5 Wavelength Conversion

4.5.1 XGM-Based Wavelength Conversion

Cross-gain modulation based wavelength conversion is one of simplest schemes to achieve all-optical wavelength conversion which employs gain saturation effect in active region of SOAs. The principle of this scheme for a QD-SOA based wavelength converter is illustrated in Fig. 4.6. The input data signal at the wavelength λ_{in}

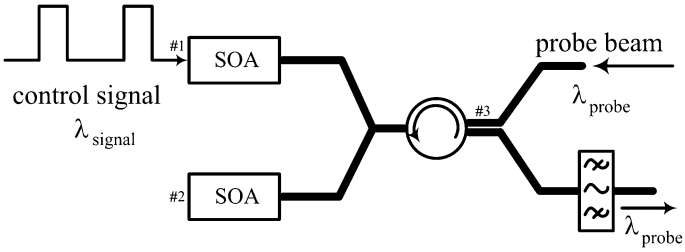

Fig. 4.5 Schematic of a typical Michelson interferometer configuration incorporated with SOAs for demonstration of optical logic gates

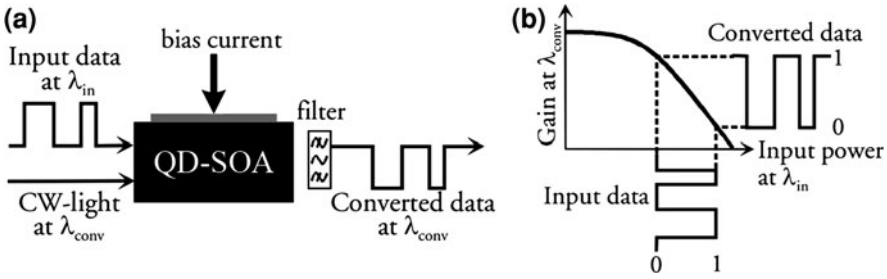

Fig. 4.6 **a** Wavelength conversion scheme based on cross-gain modulation in an SOA and **b** mechanism of XGM-based on gain saturation

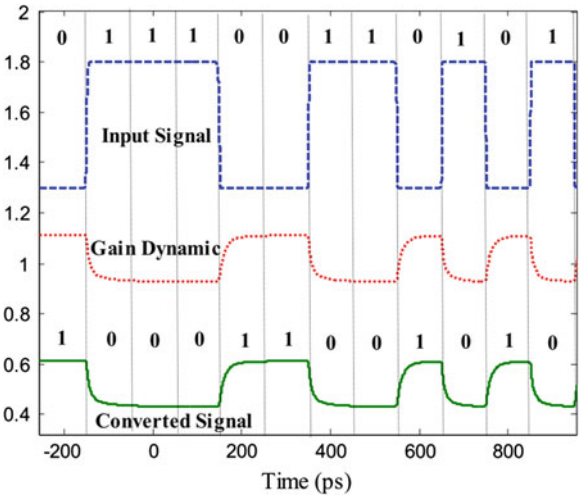

Fig. 4.7 Input data signal at 10 Gb/s, gain dynamics and converted output signal obtained from the QD-SOA XGM-based wavelength converter

and a co-propagating CW-beam at the wavelength λ_{conv} are coupled into the SOA. Due to high optical power of data signal, it causes total carrier depletion in the active region and therefore the gain saturation occurs. The CW-signal at λ_{conv} experiences this change in the gain so that CW-beam traversing the SOA with a mark (in data signal) will experience a lower gain than light traversing with a space. This scenario is sketched in Fig. 4.6b. Therefore, the SOA output contains a copy of the original data signal with inverted polarity at λ_{conv}. A filter should be placed at the output of the SOA in this technique to omit the λ_{in} and pass the λ_{conv}. This filter can be omitted if the two signals counter-propagate through the SOA.

Figure 4.7 displays the simulation results for the QD-SOA based wavelength converter of Fig. 4.6. The simplicity of this technique is the main advantage of XGM-based wavelength. High-speed operation of XGM-based wavelength converter with bulk SOA and a high-pass filter using a detuned grating at 100 Gb/s [5] is another impressive result reported for this scheme. Furthermore, XGM-based conversion is polarisation-independent if the gain of SOA is polarisation independent. The methods to obtain polarisation-independent gain in QD-SOAs were

discussed previously. However, this can be achieved in bulk or quantum well SOAs by using a device with square cross-section or by introducing strain. Beside the mentioned advantageous of this scheme, the chirped output signal caused by XGM [6], the smaller differential gain for longer wavelengths [7] and the possible polarity conversion-based problems in signal processing are main disadvantageous of this method. The first problem arises from the frequency shift at the leading and trailing edges of the converted pulses due to carrier dynamics which results in a severe penalty in polarity conversion scheme and hence limits the transmission distance in a dispersive fiber.

The second deficiency results in smaller output extinction ratio for up-conversion (conversion to longer wavelengths) than for down-conversion (conversion to shorter wavelengths).

The polarity conversion-based problem of the introduced structure becomes much important in the case of using RZ data format. Since the polarity inversion is associated with pulse inversion, devices employing this scheme should have identical RZ pulse shapes.

4.5.2 XPM-Based Wavelength Conversion

Cross-phase modulation based wavelength conversion is another technique that doesn't have the limitations of the XGM-based scheme. Figure 4.8a schematically

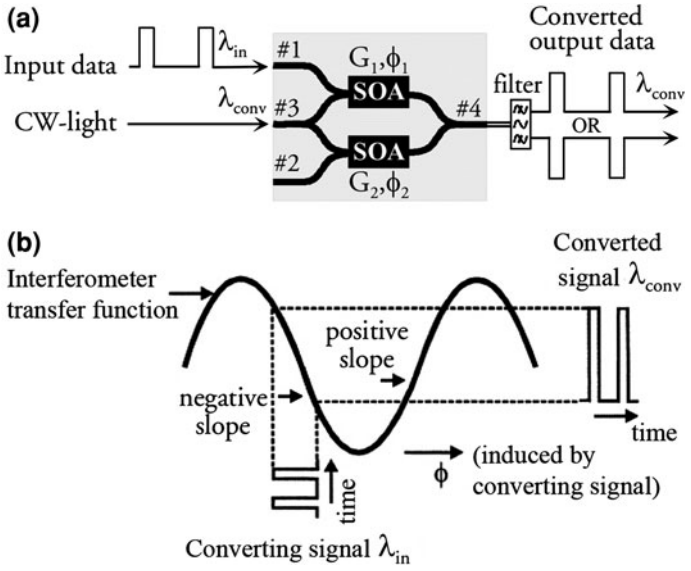

Fig. 4.8 **a** Schematic of SOA-MZI configuration for wavelength conversion based on cross-phase modulation effect and **b** transfer function of the structure

shows the structure of which consists Mach–Zehnder interferometer with two SOAs on both arms of the interferometer. Wavelength conversion in this scheme is achieved according to the different phase changes experienced by the CW beam in two interferometric arms of MZI. The data signal at the wavelength λ_{in} coupled to the port 1 modulates the carrier density and therefore the refractive index of the active region of SOA due to its high power. Meanwhile, the CW beam at the wavelength λ_{conv} is coupled to port 3 of the MZI-SOA structure and is split into two equal parts (if the coupler is 3 dB) travelling through the upper and lower interferometer arms. The CW beam in the lower arm experiences a constant phase change, φ_2, which depends on the lower SOA bias current while the phase change experienced by the CW beam in the upper arm, φ_1, depends on the bit pattern of the input data signal. Therefore, at the output of the MZI the split CW beams can combine constructively or destructively to transfer the data signal pattern to the CW beam.

The transfer function for this configuration ($P_{cw,out}/P_{cw,in}$) can be obtained through Eqs. 5 and 6 which is schematically shown in Fig. 4.8b. Depending on the phase difference term, $\cos(\Delta\Phi)$, between the two arms, the transfer function can reach to its maximum or minimum value. Therefore, the output signal can be inverted or non-inverted in comparison with the input data signal which corresponds to operation on the negative slope (out-of-phase operation) or positive slope (in-phase operation) of the transfer function depicted in Fig. 4.8b.

In the above configuration, the converting signal results in gain compression beside the phase change which can unbalance the amplitude in the interferometer arms and decrease the output extinction ratio. A passive phase-shifter on one of the interferometer arms can enhance the wavelength conversion efficiency.

4.5.3 FWM-Based Wavelength Conversion

Four wave mixing (FWM) in an SOA is another mechanism for realizing wavelength conversion. FWM is a fast process inherently compared with the XGM and XPM effects which can be utilized in WDM systems since it is possible to handle many wavelength channels simultaneously.

In a typical FWM-based wavelength converter as depicted in Fig. 4.9, a data signal at frequency of $\omega_0 - \Omega$ and a continuous wave beam at frequency ω_0 are coupled to a SOA (data signal and CW beam are considered to have same polarisations to achieve high efficiency). The nonlinear FWM process is generated by carrier density modulation and nonlinear gain effects in the presence of data signal and because of the FWM effect in the SOA, a new conjugate signal that is a spectrally inverted replica of the input data signal at frequency of $\omega_0 + \Omega$ is generated. Therefore, an optical band-pass filter is required to select the conjugate signal which is converted [8]. The output signal wavelength in this scheme depends on both the CW and the data signal wavelengths, so the CW should be tunable even for converters with fixed output wavelength. A considerable point to

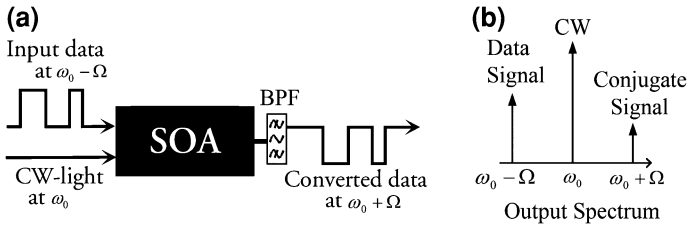

Fig. 4.9 **a** Configuration of FWM-based wavelength conversion and **b** frequency spectra of input and output signal to the SOA

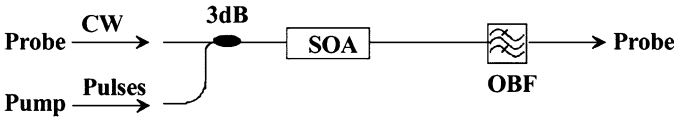

Fig. 4.10 Configuration of a wavelength converter using an optical band-pass filter (OBF) [11]

note is FWM sensitivity to polarisation which can be resolved by inserting an extra signal [9, 10].

4.5.4 Wavelength Conversion in SOA-BPF Configuration

Wavelength conversion by utilizing a single SOA followed by an optical band pass (OBP) filter also known as shifted filtering is another method that can overcome to the patterning effects associated with the SOA carrier recovery [5, 11]. Figure 4.10 exhibits a typical setup for wavelength conversion using a SOA in conjunction with a OBP.

In this method, it is possible to exploit XGM or XPM effect as primary nonlinearity for realization of wavelength conversion based on the offset of the shifted filter. Error-free wavelength conversion at 320 Gb/s based on XGM effect [11] and 80 Gb/s conversion based on XPM effect [12] and shifted filtering are of reported experimental results. The principle of shifted filtering associates to gain and phase changes in a SOA. In the case of XGM and XPM the gain and phase changes modulate the probe (CW) signal, respectively. In the presence of a pump pulse, the probe signal experiences a positive phase shift corresponding to the generation of red-chirped components as a consequence of gain depletion. This process has a time frame corresponding to the input pulse width. After the gain depletion, the SOA gain starts to recover in accordance to different recovery processes (SHB, CH and interband carrier recovery) which cause a negative phase shift and thus generates blue-chirped components. The gain and chirp dynamics of a SOA following a pump pulse are illustrated in Fig. 4.11.

According to the chirp specifications, a filter can be placed at the output of the SOA to retain only the red chirp spectral components or longer wavelength

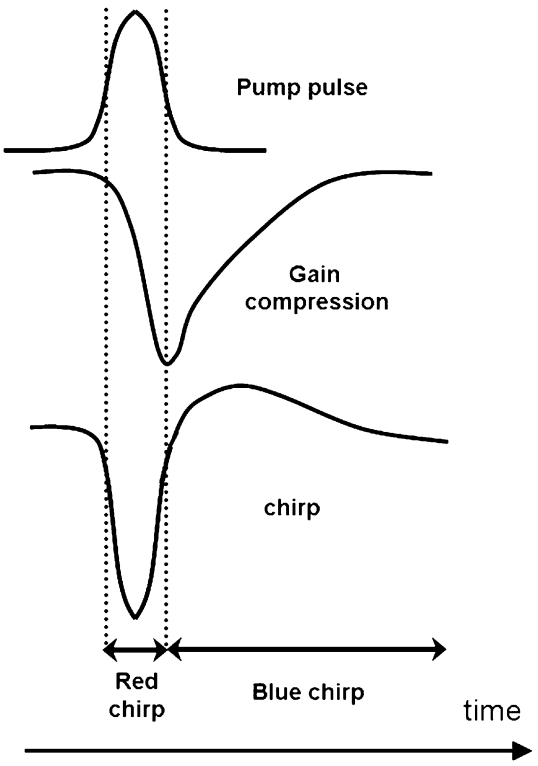

Fig. 4.11 Gain compression and chirp of a SOA following a pump pulse [12]

components of the probe signal known as red-shifted filtering (RSF). Also, the filter can be tuned to obtain the blue-shifted spectral probe components known as blue-shifted filtering (BSF). If the filter is shifted such that the original CW potion of the probe and either the red/blue shifted components are kept this process primarily exploits XGM. In this case, the output signal remains inverted in comparison to the input signal. Otherwise, if the CW component of the probe is rejected the process exploits XPM effect but the polarity of output signal is preserved in this case. These justifications are illustrated via experimental results in Fig. 4.12.

In the 320-Gb/s wavelength conversion experiment that is described in previous chapters, input pulses with duration of 1.1 ps were used. The center wavelengths of the pump signal and the CW probe beam are 1540.32 and 1553.82 nm, respectively, and an OBF with a central wavelength of 1553.82 nm and a 3-dB bandwidth of 2.7 nm is used to select the probe light and to reject the pump signal. Using an OBF with a central wavelength that is 1.6 nm blue-shifted with respect to the central wavelength of the probe beam leads to a wavelength-converter recovery time of less than 1.8 ps for a SOA with an initial full gain recovery of 56 ps.

Although the bit rates achieved through XPM and shifted filtering are limited compared with XGM scheme and shifted filtering, preserving the polarity of the wavelength converted signal and a higher ER are the main advantageous of the

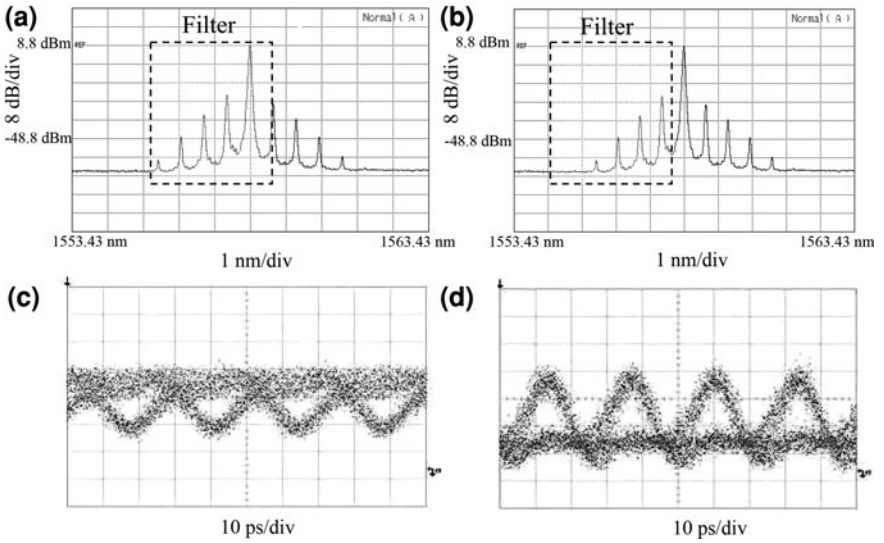

Fig. 4.12 Selection of blue shifted spectral components and original CW component which relates to XGM (**a**) and corresponding eye diagram (**c**), selection of blue shifted spectral components without CW component which relates to XPM (**b**) and corresponding eye diagram (**d**) at 40 Gb/s [13]

XPM based scheme. Placing the filter to longer or shorter wavelengths in this technique will suppress the DC probe component and the phase modulation of the probe beam converts to intensity modulation. Thus, the polarity of the input signal can be preserved [14].

This process can be justified more by considering an arrangement of '0's and '1's as an input sequence to the SOA. As it is clear, a '0' input pulse won't cause gain saturation and consequently no wavelength shift of probe spectral components is expected. However, in the case of input '1' pulse, the probe spectral components are shifted first to longer wavelengths and then to lower wavelengths (red and blue shift). Therefore, the filter can keep either the red or blue spectral components and suppress the other spectral components.

According to the mentioned process in above paragraph, larger output extinction ratio can be obtained at the hands of suppressing the DC spectral components more and more. Also, short and energetic input pulses increase the amount of induced spectral broadening (chirp) and lead to higher power efficiency in this method.

An experimental setup for XPM and shifted filtering wavelength conversion is presented in Fig. 4.13. In this structure Mode-locked pulses with a full width half maximum (FWHM) of 2.3 ps and at a wavelength of 1545 nm are generated and after amplification by an erbium-doped fiber amplifier (EDFA), pass through a Mach–Zehnder intensity modulator to obtain a return to zero pseudo-random bit sequence (RZ-PRBS) of $2^7 - 1$ [12].

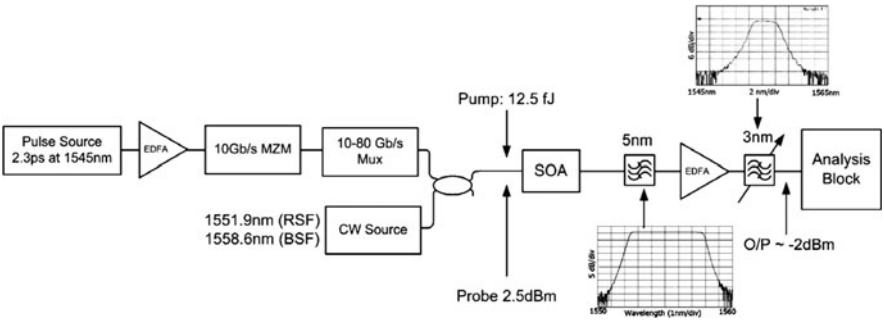

Fig. 4.13 Experimental setup for realization XPM and shifted filtering-based wavelength conversion [12]

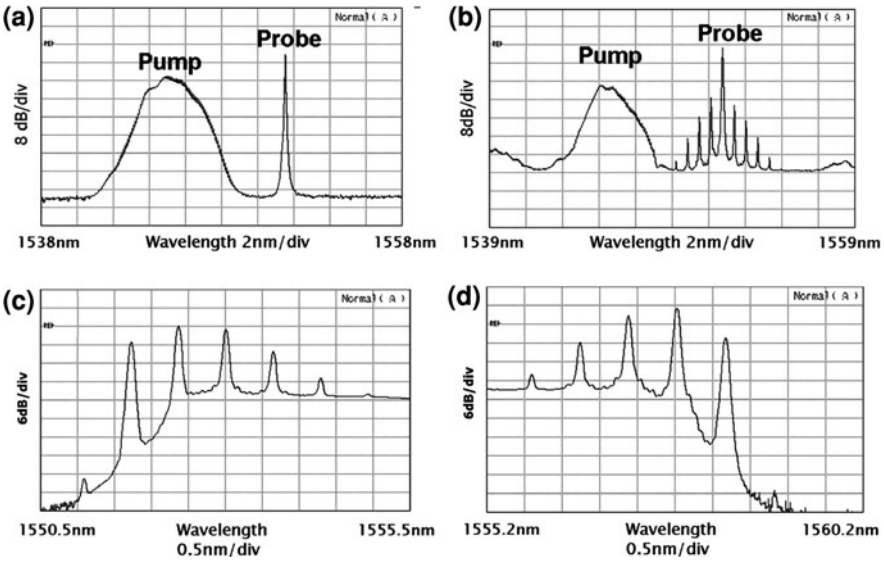

Fig. 4.14 Signal spectra: **a** at the input of the SOA, **b** at the output of the SOA, **c** after RSF, and **d** after BSF, in the wavelength conversion process at 80 Gb/s [12]

The first filter after the SOA is a fixed filter that allows selection of RSF or BSF through tuning the probe wavelength. The second filter which is a 3 nm tunable Gaussian filter is used to suppress the DC probe components completely along with the first filter. Achieving higher ER is the main reason for placing this filter. To reduce the high insertion loss due to the shifted filtering an EDFA is placed between the two filters. Since this configuration allows both RSF and BSF, it will be worthwhile to study the quality of the obtained signal after RSF and BSF. Figure 4.14 shows the signal spectra at different points during the wavelength conversion process (i.e. at the input of the wavelength converter, at the output of the SOA, after RSF and after BSF).

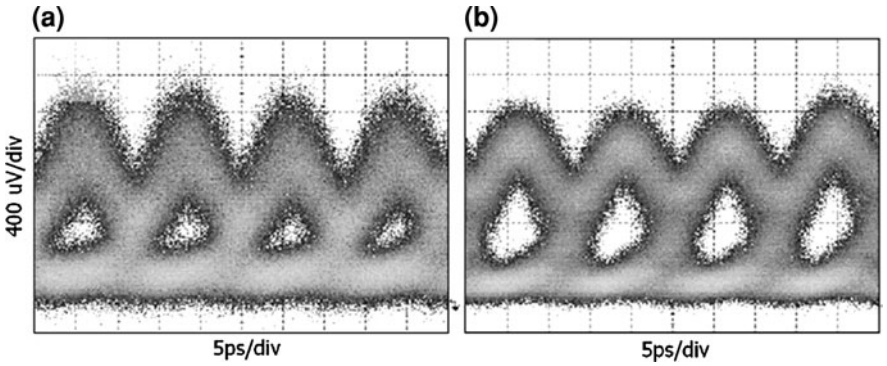

Fig. 4.15 Eye diagrams related to wavelength conversion at 80 Gb/s after **a** RSF and **b** BSF [12]

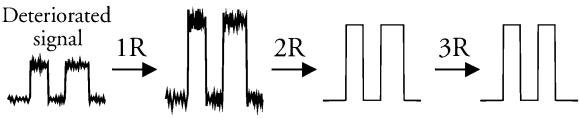

Fig. 4.16 Schematic of regenerating a deteriorated signal after three steps (1R: re-amplification, 2R: re-shaping, 3R: re-timing)

Since the magnitude of the red chirp corresponds to the gain saturation by the pulse, a large patterning effect due to the slow gain recovery time of the SOA in RSF is expected. However, for the case of BSF, the patterning effects are reduced considerably. The eye diagrams related to wavelength conversion at 80 Gb/s verify the effect of patterning in the RSF case which corresponds to small eye opening with a bit error rate (BER) of $\sim 10^{-7}$ while a large eye opening is obtained in the case of BSF with a BER of $\sim 10^{-9}$ denoting an error-free operation at this bit rate.

Figure 4.15 depicts the related eye diagrams for both RSF and BSF techniques.

4.6 All-Optical Regeneration

3R regeneration (re-amplification, re-shaping and re-timing) of data signals is one of the essential functions in optical networks. Since accumulation of detrimental effects degrade signal quality during transmission and switching, hence, all-optical regeneration should be implemented to retain the signal quality especially in large-scale networks. Optical losses in fiber couplers, noise addition in optical amplifiers such as EDFAs and SOAs and signal distortion and jitter through data transmission are examples of signal deterioration in optical networks.

Figure 4.16 schematically illustrates three steps (1R, 2R, and 3R) that a deteriorated signal undergoes to be regenerated. Re-amplification of the signal is the first step that is typically performed by an EDFA to enhance the signal to noise

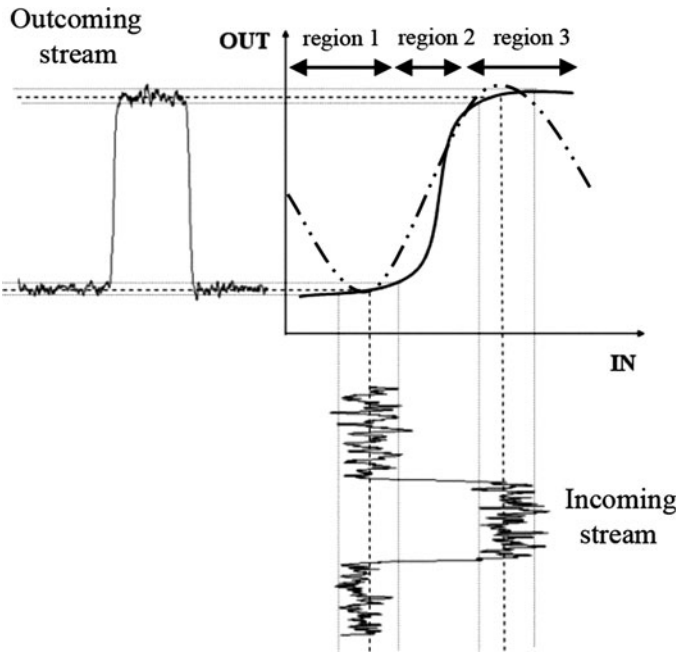

Fig. 4.17 Principle of re-shaping based on sinusoidal transfer function of a MZI

ratio (SNR). In the re-shaping step, the fluctuations of signals '0' and '1' level must be suppressed. EDFAs themselves can add noise to the signal in this level. The re-timing step includes correction of the jitter induced by the EDFAs or caused during transmission in the network. It should be noted that 2R regeneration including re-amplification and re-shaping can easily realized in an interferometric configuration such as interferometric wavelength converter due to inherent sinusoidal transfer function of MZI.

Re-shaping (suppressing the amplitude modulation) process in such a structure is schematically shown in Fig. 4.17. Although an ideal transfer function depicted by solid curve in Fig. 4.17 requires flatter characteristics in region 1 and 3 to suppress the noise and steeper characteristic in region 2 to act as a decision threshold, the sinusoidal transfer function of MZI depicted by dash-dotted curve, can effectively suppress the power fluctuations. Furthermore, cascading these interferometric structures can yield better suppression of amplitude fluctuations and decision thresholding [15]. The re-timing process, however, is to somewhat different from other stages and requires clock signal which can be recovered from the data signal. Generation of a short pulse for each transition from low to high and a subsequent bandpass filtering is one of the methods for generation of a recovered clock [16]. All-optical clock recovery of data signal through injection into a self-pulsating laser is a more efficient method which the laser generates a clock signal with the same rate as the original data signal [17]. Figure 4.18 presents a schematical configuration for 3R regeneration. For many applications,

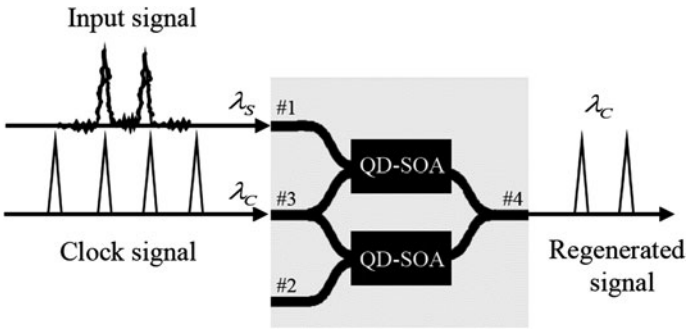

Fig. 4.18 Schematic configuration used for 3R regeneration in an MZI

Fig. 4.19 Input noisy and broadened data signal with timing jitter and regenerated output signal exploited from 3R regenerator configuration presented in Fig. 4.18

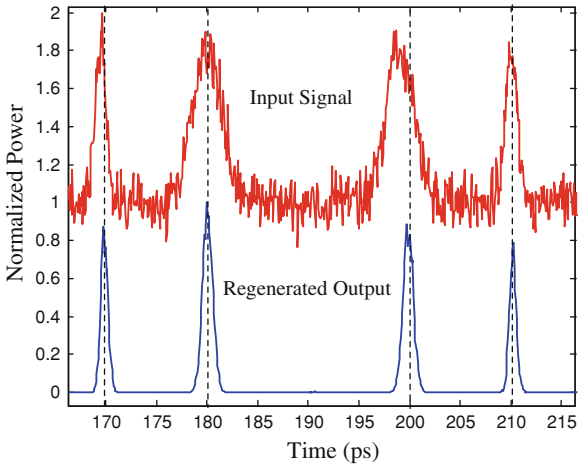

combination of wavelength conversion and 3R regeneration as done in this configuration can be beneficial.

Simulation of the QD-SOA-MZI-based 3R regenerator for a noisy input signal with timing jitter and broadening is shown in Fig. 4.19. By advent of quantum dot SOAs, these devices have been forecasted to realize high bit-rate and multi wavelength signal processing [18, 19]. The spatial isolation of quantum dots after growth process results in spectrally localized effects and therefore to crosstalk suppression between WDM channels under gain saturation conditions. For wavelength channels that have a similar energy level strong interaction via XGM can occur when channels are within the homogeneous broadening of the single-dot gain. This feature can be utilized switching applications.

These features of QD-SOAs can be utilized to operate as multi-wavelength regenerators [20] that can be a fundamental step in demonstration of all-optical transmission systems beside the capability of multi-channel amplification potentials of QD-SOAs [21]. Two cascaded QD-SOAs can serve as 2R regenerators exploiting XGM effect. Figure 4.20 schematically shows this regenerator subsystem where the

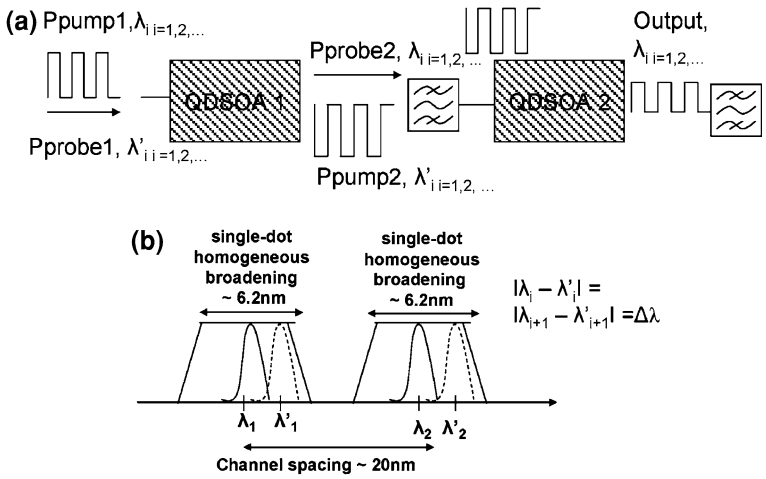

Fig. 4.20 **a** Subsystem schematic of multi-channel 2R regeneration in two cascaded QD-SOA configuration and **b** channel spacing of two adjacent channels within inhomogeneous broadening gain spectrum of QD-SOAs [20]

adjacent channels are within in-homogeneous broadening gain spectrum of QD-SOA [20]. The input channels at the wavelengths λ_i serve as pump signals carrying the data and modulate the carrier density, phase, and the gain of the QD-SOAs. Also, the CW probe signals at the wavelengths λ_i' experience the modulation effects mostly due to corresponding pump signal at the center λ_i wavelength. Therefore, the corresponding pump and probe signals within a homogeneous broadening of a dot have a close detuning denoted by $\Delta\lambda = |\lambda_i - \lambda_i'|$.

The first QD-SOA serves as a wavelength converter where the data of input channels are copied to probe signals and also inverted. A BPF omits the pump signals at the output of the first QD-SOA and therefore the probe signals at the wavelength λ_i' serve as pump signals for the second QD-SOA.

Efficient regenerative operation requires not only preservation of suitable extinction ratio but also proper suppression of the amplitude fluctuation. In multi-channel operation scheme, high power levels of probe signal injected to the first SOA (P_{probe1}) provide sufficient pump powers at the input of second SOA (i.e. QD-SOA2) since it minimizes the extinction ratio degradation at the second stage of the regenerator and improves the output quality factor. The latter associates to the power transfer function of QD-SOA which becomes steeper due to the deep gain saturation caused by the incoming pulses in XGM operation. Also, increasing the power level of probe signal at the input of second QD-SOA (P_{probe2}) will degrade extinction ratio of channel 2 severely due to gain saturation in XGM operation. A similar result is expected for channel 1 either.

The eye diagrams of the regenerator for two channels in conjunction with the quality factors at 40 and 160 Gb/s can indicate the performance of the subsystem. The eye diagrams of deteriorated signals at the input of two channels are illustrated

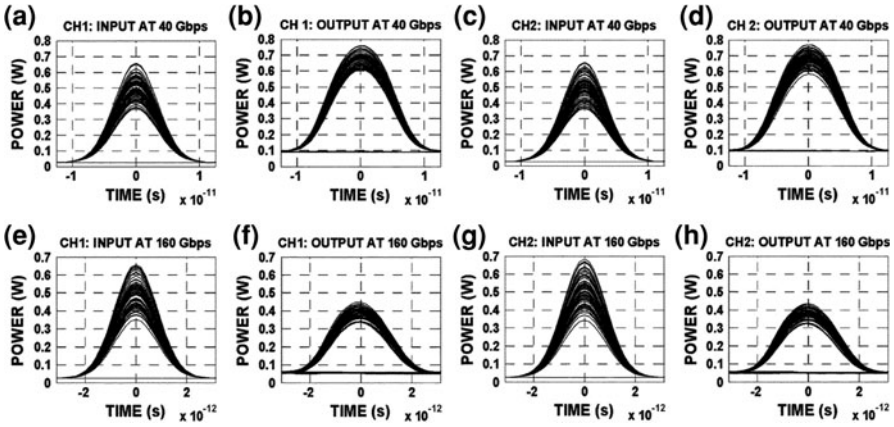

Fig. 4.21 Eye diagrams for channel 1 and channel 2 at the input and the output of the 2R regenerator at 40 Gb/s (**a**–**d**) and at 160 Gb/s (**e**–**h**) [20]

in parts (a) and (c) for 40 Gb/s and in parts (e) and (g) for 160 Gb/s bit rates. The CW signal power levels are −5 dBm for P_{probe1} and 0 dBm for P_{probe2}, at 40 Gb/s and −5 dBm for P_{probe1} and −8 dBm for P_{probe2} at 160 Gb/s, respectively. According to the eye diagrams, the amplitude fluctuation at the marks has been suppressed resulting in a Q-factor improvement of 3.2 dB for channel 1 and 3.1 dB for channel 2 at 40 Gb/s and an improvement of 2.6 dB for channel 1 and 2.8 dB for channel 2 at 160 Gb/s operation regimes Fig. 4.21.

These results for two-channel regeneration can be promising for QD-SOA based all-optical signal processing.

4.7 Logic Gates

4.7.1 XOR Gate

XOR logic gate is one of the most applicable gates in optical signal processing and is a key element to implement primary systems for binary address and header recognition, binary addition and counting, pattern matching, decision and comparison, generation of pseudorandom binary sequences, encryption and coding. This gate has been demonstrated at 40 Gb/s [22] and 80 Gb/s [23] using SOA-MZI differential schemes that have been deployed to overcome the speed limitations imposed by the bulk SOAs slow recovery time. However, it is predicted that QD-SOA based XOR gates have the potential to operate at ∼250 Gb/s bit rates [24]. Figure 4.22 shows a MZI based configuration for XOR operation where two input data streams at the wavelengths $\lambda_{in,1}$ and $\lambda_{in,2}$ along with a CW beam at the wavelength λ_{XOR} are coupled into ports #1, #2 and #3, respectively. The data

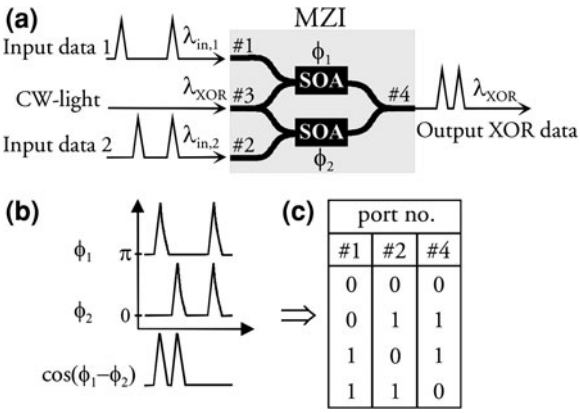

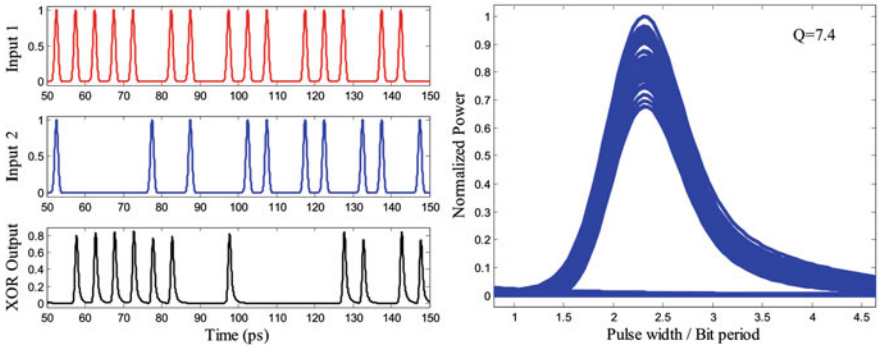

Fig. 4.23 XOR logic operation of two data streams in QD-SOA based gate (*left*), and related eye-diagram and quality factor (*right*)

streams cause carrier modulation and therefore refractive index modulation while traveling through the SOAs which leads to phase modulation of the CW beam according to the data pattern of the input signals.

Constructive or destructive combination of CW-beam at the output of the SOAs which depends on the phase difference term, $\cos(\varphi_1 - \varphi_2)$, results in logic XOR of two input streams at the converted wavelength λ_{XOR}. The principle of this operation is sketched in Fig. 4.22b and the truth table of the XOR logic operation is presented in Fig. 4.22c.

In a QD-SOA based XOR gate, as described in [24], the operation speed is limited to carrier relaxation time from the wetting layer into QD confined states. Although, increasing the bias current increase the quality factor in operation bit rate, higher bias current will lead to saturation of the quality factor.

Figure 4.23 presents the simulation results for QD-SOA based XOR gate where the structural parameters of the SOA are L = 2 cm, w = 10 μm and the input bias current is 30 mA.

4.7.2 AND Gate

Logic AND operation is another important Boolean function which corresponds to the sampling of one signal with another. The principle of logic AND employing the MZI involves coupling the two input signals into port #1 and #3 of the SOA-MZI configuration as depicted in Fig. 4.24. If operation is performed on the positive slope of the interferometer transfer function (Fig. 4.8b), the input signal 2 will sample input signal 1. Therefore, the selective switching of the data pulses at λ_{AND} occurs exclusively during the mark of signal 1 which yields the logical AND operation.

Figure 4.25 shows the simulation results for QD-SOA based AND gate configuration of Fig. 4.24. The structural parameters are similar to the parameters considered for XOR gate in Fig. 4.23.

MZI based differential scheme is another configuration for realization of AND logic [26]. In this configuration which is presented in Fig. 4.26, the incoming data signals are launched into the two SOAs where they modulate the gain of the SOAs and thereby the gain and phase of propagating signal. The data signal B at the wavelength λ_2 is coupled into the middle port of the MZI and it is split into upper and lower arms simultaneously. The data signal A at the wavelength λ_1 and a delayed

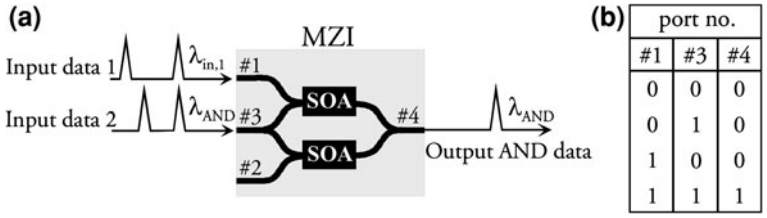

port no.		
#1	#3	#4
0	0	0
0	1	0
1	0	0
1	1	1

Fig. 4.24 Configuration of a SOA-MZI structure for AND operation, **b** logical AND truth table [25]

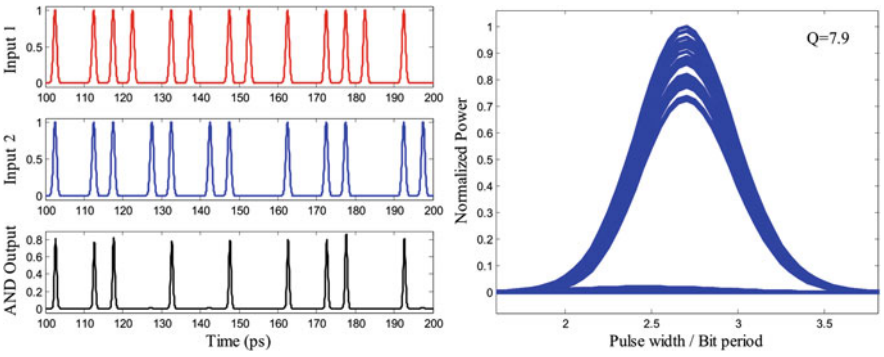

Fig. 4.25 AND logic operation of two data streams in QD-SOA based gate (*left*), and related eye-diagram and quality factor (*right*)

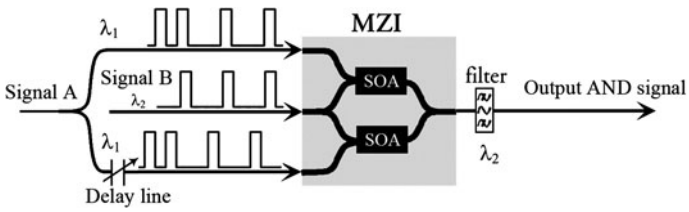

Fig. 4.26 MZI-based differential configuration for logical AND operation

version of it are injected at the upper and lower port of the SOA-MZI, respectively. The presence of A affects the phase of data signal B due to the cross phase modulation. When there is a mark, '1' in data signal A, a phase shift occurs on the data signal B in the upper arm while a delayed phase shift appears on the data B in the lower arm. This acts like a phase gate for signal B. If the data signal B is '1', the output of the MZI will become '1' and if the signal A is '0', the output will be '0'. A similar conclusion can be obtained for signal A and B in different levels.

4.7.3 OR Gate

Logic OR gate is one of the logical gates that has not been demonstrated as wide as XOR and AND gates since the later gates have found more extensive applications for simple optical signal processing. Figure 4.27a presents a schematic of a single SOA-based OR gate which operated based on gain saturation in the SOA [27]. Two input data streams at wavelengths within the gain spectrum of the SOA are combined before the SOA and are coupled into the SOA and the output signal exhibits the OR logic function. The output power, P_{out}, as a function of the total input power, P_{in}, is illustrated in Fig. 4.27b where the output power saturates for input powers larger than a certain value. Therefore, when only one the input signals is '1' the output will be saturated and operates as OR logic gate.

XGM-based OR function can be realized in MZI structure as the configuration presented in Fig. 4.28. In this configuration two input data signals at the wavelengths of the λ_A and λ_B are coupled to port #1 of the SOA-MZI structure and a CW-light at the frequency λ_{OR} couples to the middle port of the structure. In the absence of the data signals, the SOA is considered to be balanced and the output will be minimum. However, in the presence of one or both of the signals the structure becomes unbalance and OR logic operation appears at the output port. The converted output is a advantage for this configuration. The truth table for the OR logic gate is shown in Fig. 4.28b and the simulation results for QD-SOA based configuration is depicted in Fig. 4.29.

It is noteworthy that when both of the input signals are '1' the upper SOA lies in high saturation mode and the output power is higher than the situation where only one of the inputs is '1'. Therefore, it is important to select the input powers such that the SOA work in the saturation region in the presence of only of input data stream.

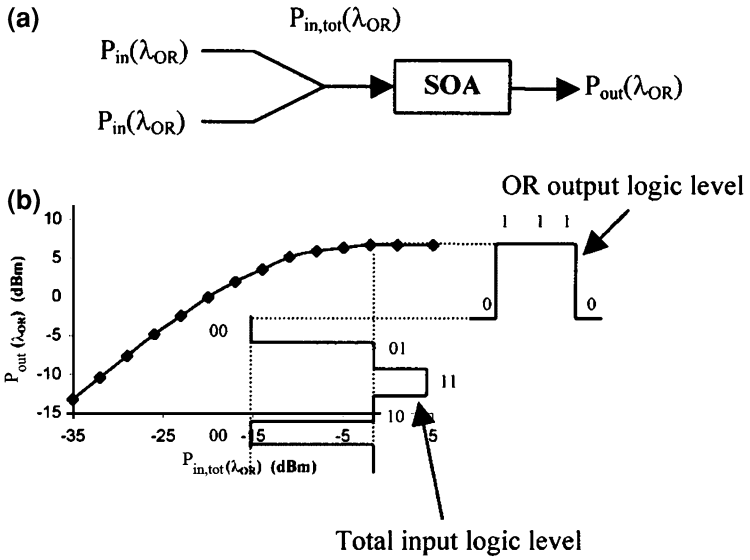

Fig. 4.27 **a** Schematic configuration of the all-optical OR logic gate and **b** OR gate operation principles according to experimental static curve of the gain saturation [27]

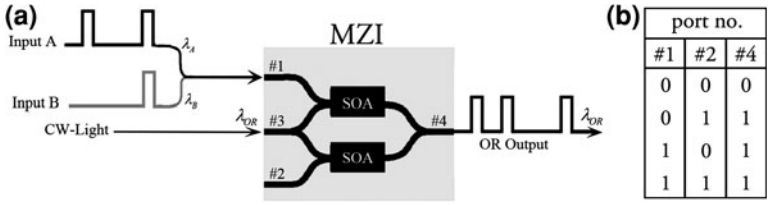

Fig. 4.28 **a** Configuration of a SOA-MZI structure for OR operation and **b** logical OR truth table

4.7.4 NOR Gate

The NOR logic gate is one of the most applicable and of course universal gates which can be realized using either XGM or XPM in a SOA. Although the operation speed of XGM-based logic gates is limited by the slow gain recovery time of the SOA, optical bandpass filters can be used in combination with XGM-based configurations in order to resolve this problem as it was previously discussed for the wavelength converters.

Combination of a blue-shifted OBF along with a single SOA can result in logic NOR or OR gates [28]. Figure 4.30 shows the configuration of the NOR and OR gates where the NOR function can be developed according to XGM effect with RZ or NRZ data formats while the OR function can be realized with RZ data format and based on XPM effect in the SOA. In the case of the OBF with large detuning,

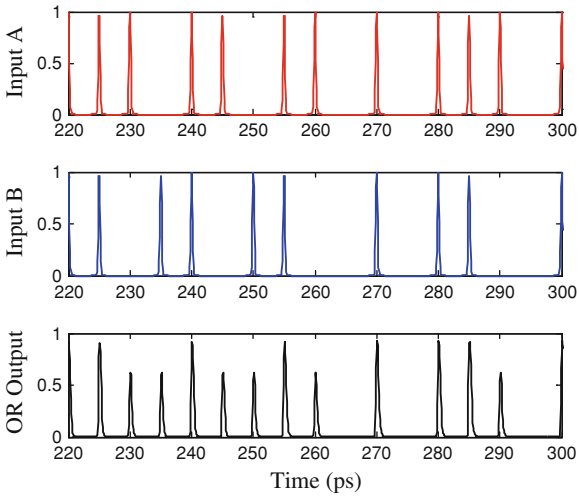

Fig. 4.29 OR logic operation of two data streams at 200 Gb/s in QD-SOA based gate

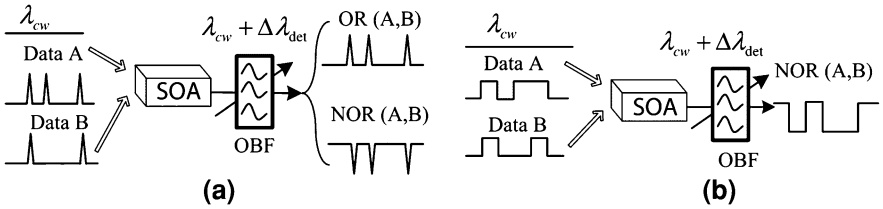

Fig. 4.30 Schematic of SOA with OBF configuration for **a** NOR/OR gate with RZ data format and **b** NOR gate with NRZ data format [28]

$\Delta\lambda_{det}$, the OBF rejects the CW probe signal and selects the blue-shifted spectrum of the input data signals A and B. Therefore, If both data signal A and data signal B are absent, the OBF will block the probe carrier without blue shifted spectrum. Otherwise, when at least one of the data signal are present, the OBF selects the blue shifted spectrum of the data and hence the OR logic is realized.

For small OBF detuning, the probe carrier is not suppressed effectively and due to the XGM effect on data signal A or B or both of them, the output will be inverted and NOR logic is demonstrated. When data signals are in NRZ format, as in Fig. 4.30b, the output NOR logic becomes NOT function of the inputs. It should be noted that in NRZ data format the OR function cannot be realized since the NRZ amplitude is constant under successive '1' bits which could not induce wavelength shifts to the probe signal.

Experimental and simulation results for NOR and OR functions with different data formats have presented in Figs. 4.31 and 4.32. As it mentioned before, the NOR output for data signal with RZ format will be inverted as depicted in Fig. 4.31(iii). However, non-inverted RZ format can be obtained if a synchronized clock replaces the CW light. The simulation result for clock pulse injection is

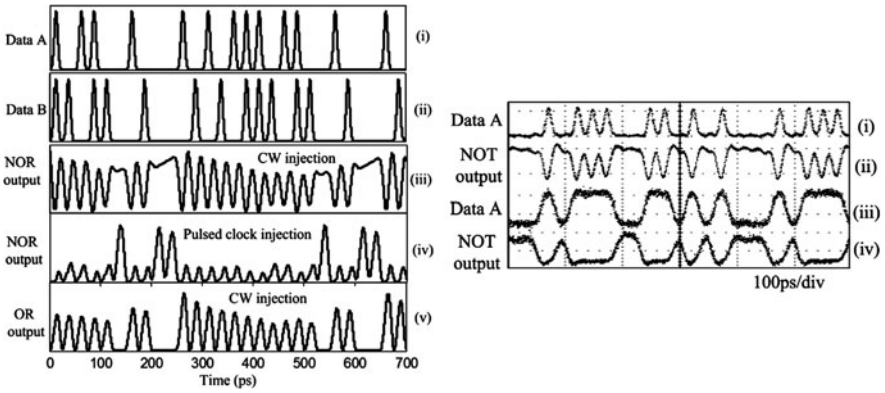

Fig. 4.31 NOR and OR logical operations with RZ format. *Left* Simulation results: *i* waveform of data signal A, *ii* waveform of data signal B, *iii* NOR output with CW probe beam, *iv* NOR output with clock pulses as probe beam, *v* OR output with CW probe beam. *Right* Experimental results: *i* waveform of data signal A, *ii* waveform of data signal B, *iii* NOR output, *iv* OR output [28]

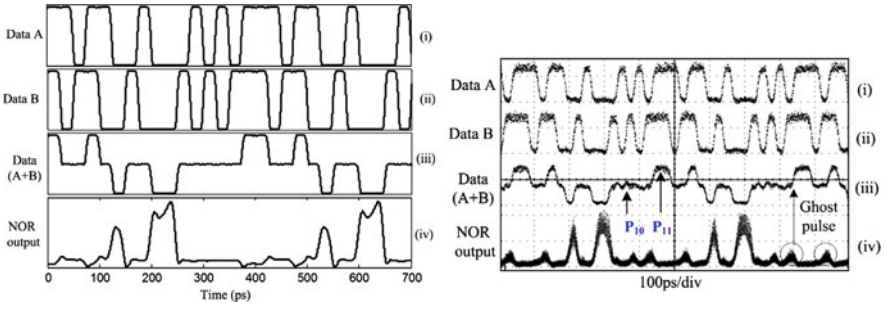

Fig. 4.32 NOR logic operation with NRZ format. *Left* Simulation results: *i* waveform of data signal A, *ii* waveform of data signal B, *iii* combined waveform of signals A and B, *iv* NOR output. *Right* Experimental results: *i* waveform of data signal A, *ii* waveform of data signal B, *iii* combined waveform of signals A and B, *iv* NOR output [28]

presented in Fig. 4.31(iv). Simulation and experimental results for NOR function with NRZ format is presented in Fig. 4.32. As it is clear some 'ghost' pulses appear at '0' level of the output, which can limit the quality factor of the gate performance. These unwanted pulses occur as a result of leading or trailing edges at the transitions like '01' to '10' or vice versa and like '01' to '11' in the input signals and lead to phase modulation of CW probe beam. The phase modulation can be partially converted to intensity modulation by the blue-shifted OBF and lead to 'ghost' pulses. Reducing the detuning of OBF is a solution for this problem which leads to increased pattern effect in turn. Thus, a tradeoff should be considered between these two undesired effects.

Another scheme for NOR gate consists of two cascaded SOAs in counter-propagating configuration as shown in Fig. 4.33a. In this configuration, the two

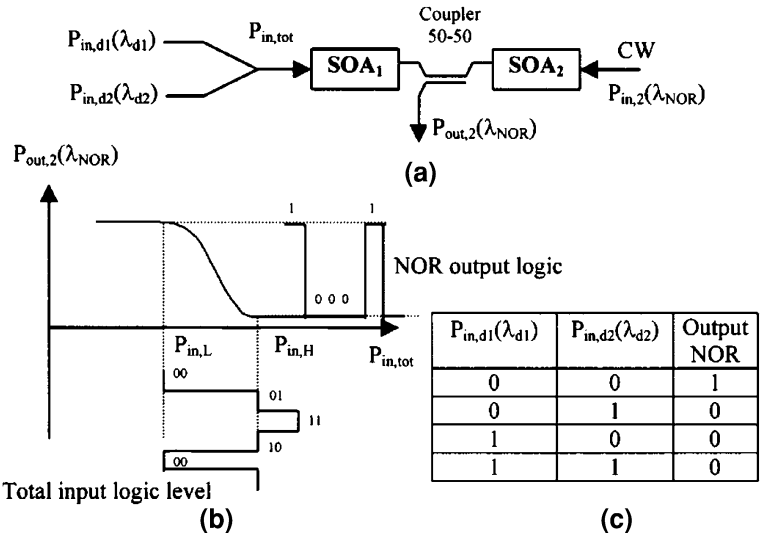

$P_{in,d1}(\lambda_{d1})$	$P_{in,d2}(\lambda_{d2})$	Output NOR
0	0	1
0	1	0
1	0	0
1	1	0

Fig. 4.33 **a** Configuration of NOR logic gate based on two cascade SOAs, **b** transfer function and operation principles of the NOR function, and **c** NOR logic truth table [29]

SOAs are coupled together through a 2 × 2 ports 50:50 coupler. In this configuration the feedback between the two SOAs enhances their gain nonlinearities.

In the other words, the modulated gain of one SOA depends on the gain of the other SOA. For low $P_{in,tot}$ input power, $P_{in,2}$ is amplified in SOA_2 and reduces the SOA_1 gain. By increasing $P_{in,tot}$ input power, the SOA_2 gain is reduced and thus its output power becomes lower. At the same time, the output power of SOA_1 increases due to the weakening of the counter-propagating signal power at λ_{NOR} due to decrease of SOA_2 gain. This behavior results in a transfer function which is suitable for NOR logic and is presented in Fig. 4.33b. The Operation principle for NOR operation is also illustrated in this part of Fig. 4.33 where $P_{in,tot}$ is combination of input data signals at the wavelengths λ_{d1} and λ_{d2} that enters SOA_1 and a CW probe light at the wavelength of λ_{NOR} enters SOA_2. The total data input modulates the output signal $P_{out,2}$ (λ_{NOR}) and NOR function is realized at this output. The truth table for NOR logic operation is presented in Figs. 4.33c and 4.34 shows the output results as a function of total input logic levels.

A good performance in terms of contrast can be seen in the output waveform of the NOR gate.

MZI-based NOR gate is another configuration where the two input signals are added together and inserted to the upper arm of the SOA-MZI structure as shown in Fig. 4.35. A clock signal at the same bit rate of the input signals is coupled to the lower MZI arm and a CW light is inserted to the middle arm. The phase of CW light is modulated by the input pattern of the data signals in the upper arm SOA and the clock signal in the lower arm SOA. Hence, the power level of each input signals should be half of the clock signal to provide the condition for logic NOR function.

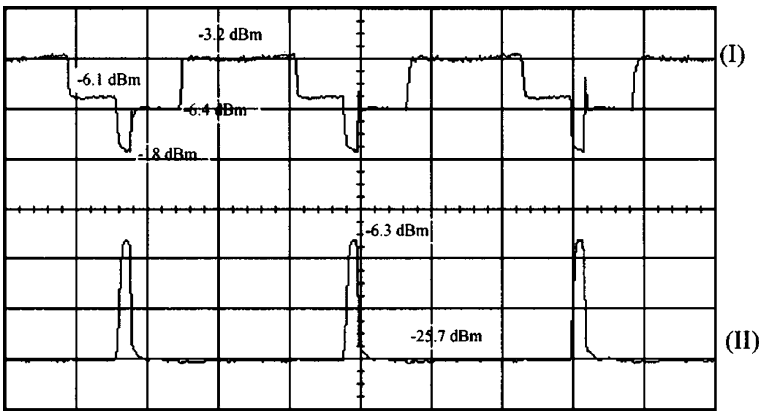

Fig. 4.34 Experimental results for NOR gate, *I* total input data power and *II* NOR logic output power [29]

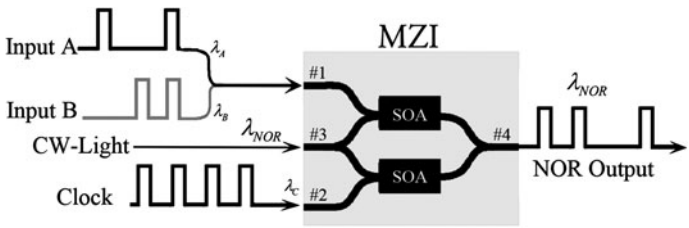

Fig. 4.35 SOA-MZI based configuration for NOR logic gate

The input and output waveforms and also the output eye diagram of the introduced configuration based on QD-SOA are presented in Figs. 4.36 and 4.37, respectively. The input RZ data streams at 200 Gb/s and power levels of $P_A = P_B = 0.5$ mW and clock signal power of $P_C = 1$ mW have considered in simulations.

The output quality factor of $Q = 17.2$ for this configuration along with the clearly open eye diagram exhibit successful operation for this structure.

4.7.5 XNOR Gate

The SOA-MZI based configuration for XNOR logic gate is completely similar to the logic NOR gate unless the input signals and clock power should be equal. In this case, the MZI structure will be balanced when only one of the input signals is '1' and the output will be minimum. The schematic configuration and truth table of the logic XNOR gate are shown in Fig. 4.38a and b, respectively.

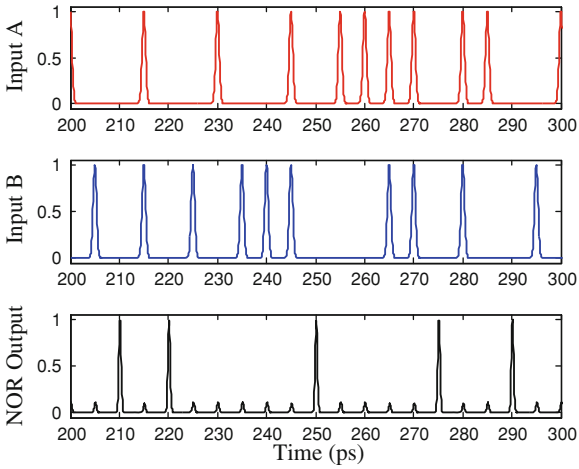

Fig. 4.36 Input streams and simulation results for NOR gate configuration of Fig. 4.35

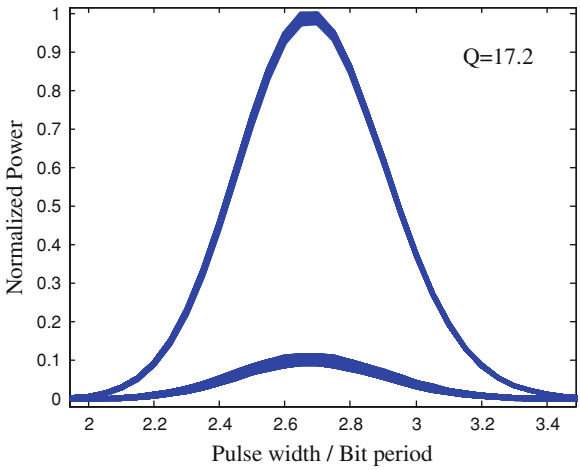

Fig. 4.37 Eye diagram of the NOR logic gate for random RZ input streams at 200 Gb/s

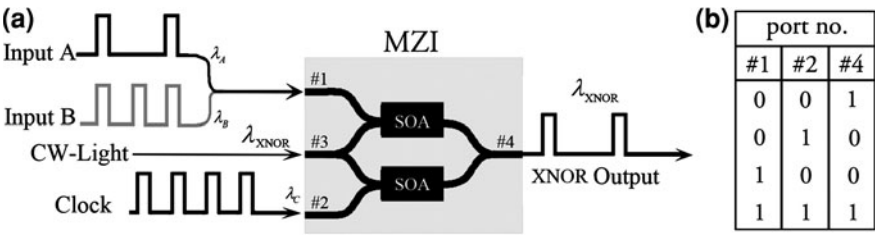

Fig. 4.38 Figure 4.35. SOA-MZI based configuration for XNOR logic gate

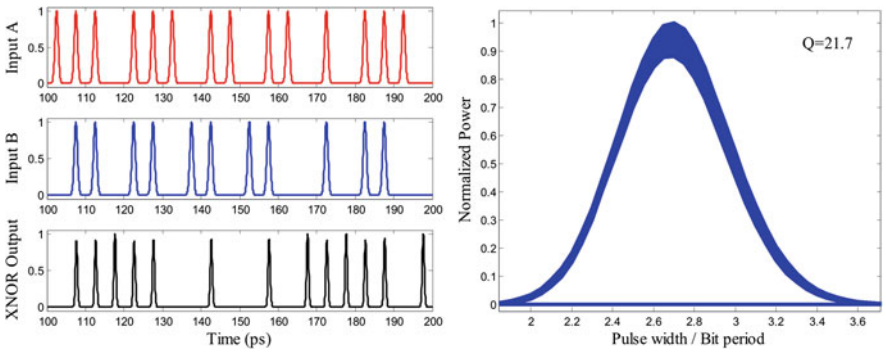

Fig. 4.39 XNOR logic operation of two data streams in QD-SOA based gate (*left*), and related eye-diagram and quality factor for random RZ input streams at 200 Gb/s (*right*)

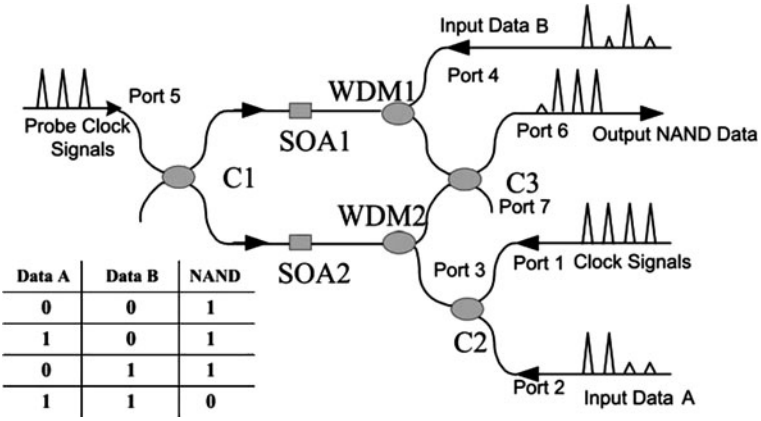

Data A	Data B	NAND
0	0	1
1	0	1
0	1	1
1	1	0

Fig. 4.40 Schematic configuration of SOA-MZI based NAND gate and truth table of NAND operation [31]

Simulation results for QD-SOA-MZI based XNOR gate including input bit streams at 299 Gb/s, output waveform and related eye diagram are presented in Fig. 4.39. The input data signals and clock powers are set to be $P_A = P_B = P_{Clock} = 1$ mW.

4.7.6 NAND Gate

Optical NAND gate is one of important and also universal logic gates that can be used in variety of applications such as all-optical signal regeneration [30]. Although several methods have been introduced for realization of this logic gate, a few techniques based on SOAs have proposed. Schematic of SOA-MZI based NAND gate along with the truth function is presented in Fig. 4.40. In this

configuration, the amplitude of the '1' pulses are the same in data A, data B and the control clock pulses and the intensity splitting ratio of all couplers is 50/50.

The operation principles of the NAND gate can be summarized as follows: Input data B and combination of clock signal and input data A modulate the carrier density and thus the refractive indexes of the upper and lower arm SOAs, respectively. Depending on the differential phase shifts that the probe clock signal experiences at the presence of the control signal and input data, the two probe components can interfere either constructively or destructively at the output of the MZI. When input data A and B are both '1', the control signals at port 3 and 4 will be identical and the differential phase shift of the probe signal will be 0 which results in '0' output. Otherwise, unbalance phase shift through two SOAs will lead to generation of a pulse at the wavelength of the probe signal. The simulation results for two 10 Gb/s PRBS input data streams with bit patterns of A = (0, 1, 0, 1, 0, 0, 1, 0, 1, 0) and B = (1, 1, 1, 1, 0, 0, 1, 0, 1, 0) are presented in Fig. 4.41 where parts c and d present the gain dynamics and differential phase shift, $\Delta\Phi(t)$, respectively. An important challenge in this configuration is the bit pattern-dependence output which rises from different differential phase shift experienced by the probe clock. In the other words, this configuration works with three different input power levels, i.e. (0.5, 1), (0.5, 0) and (1, 0) at (port3, port4) inputs. Thus, the output power level of '1' can be different according to the initial input

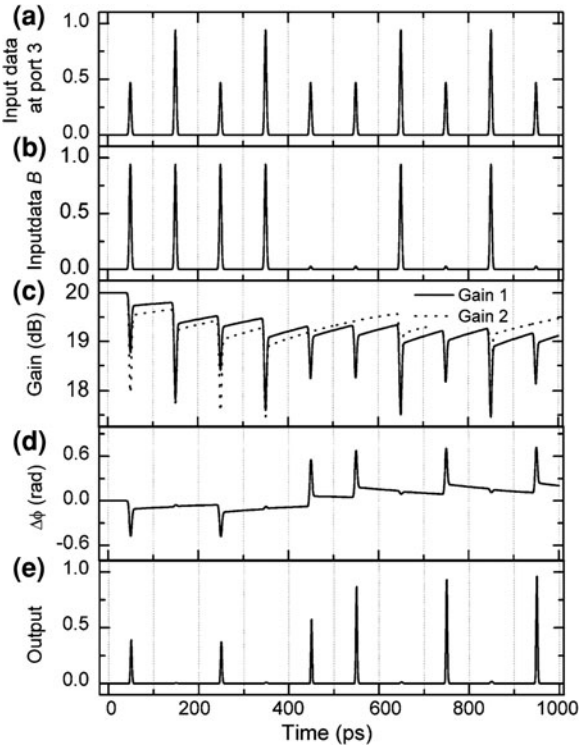

Fig. 4.41 Simulation results of the NAND gate with A = (0, 1, 0, 1, 0, 0, 1, 0, 1, 0) and B = (1, 1, 1, 1, 0, 0, 1, 0, 1, 0). **a** Input data at port 3 (clock + data A), **b** input data B, **c** gain dynamics for signals at upper (gain 1) and lower arm (gain 2) of MZI, respectively, **d** differential phase shift, and **e** NAND output [31]

patterns. The other important note to consider is the synchronization between the clock signal and the input data A and B which is crucial to achieve suitable contrast ration at the output of the structure. This synchronization between different incoming data can be obtained by using a tunable wavelength converter and a piece of highly dispersive fiber.

4.7.7 NOT Gate

Unitary NOT function is the simplest Boolean functions which performs a logical inversion of the input data. The simple schemes for this function are XGM-based wavelength conversion in SOAs. Also, by operating on the negative slope of the interferometer transfer function, as shown in Fig. 4.8b, logical inversion can be obtained. Figure 4.42 presents a SOA-MZI configuration that is similar to the structure presented in Fig. 4.22a for XOR logic function. In this configuration a clock signal is assigned to port 2 while a CW light at the wavelength of λ_{NOT} enters the port 3 and the output will contain logical inversion of the data signal at the wavelength of CW light.

The data signal pattern, clock signal and NOT logic output along with the eye diagram and quality factor of the operation are shown in Fig. 4.43 for QD-SOA based NOT gate at 200 Gb/s bit rate.

4.8 All-Optical Multiplexing and Demultiplexing

By increasing the channel bit rate in the optical networks to 40 Gb/s and more, a combination of time-division multiplexed (OTDM) and wavelength-division multiplexed (WDM) architectures offer a flexible network, where switching and add/drop functionalities can be accomplished in both the wavelength and time domains by using wavelength converters and (de)multiplexers as key elements. Time-division multiplexing consists of extracting and replacing the individual data pulses in a serial data signal. This is an important networking functionality in the context of OTDM systems. OTDM data signals are formed by bit-interleaving

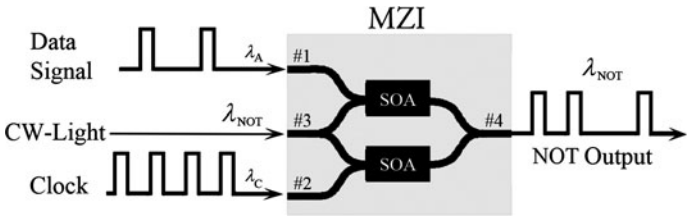

Fig. 4.42 SOA-MZI based configuration for NOT logic gate

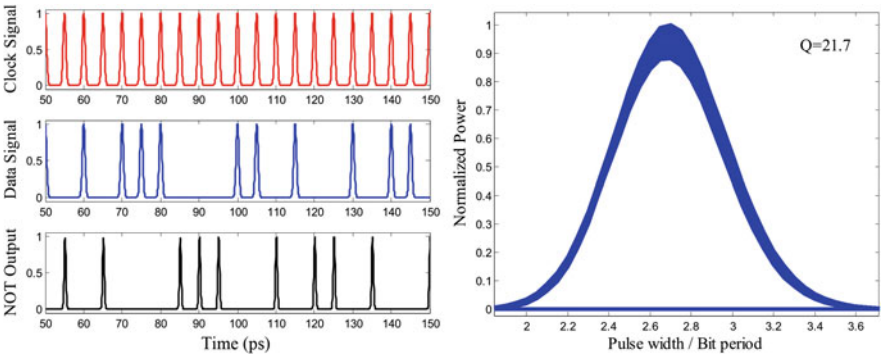

Fig. 4.43 NOT logic operation input data stream at 200 Gb/s for QD-SOA based gate (*left*) and output eye-diagram and related quality factor (*right*)

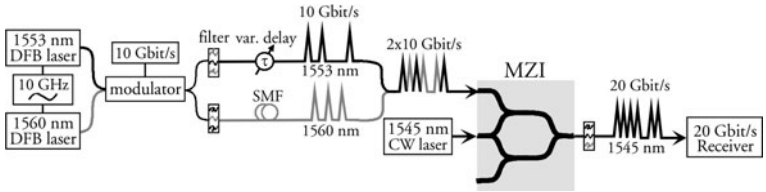

Fig. 4.44 Experimental set-up for 2 × 10 Gb/s to 20 Gb/s multiplexing [32]

narrow-pulsed, identical-wavelength data channels at a low base rate (e.g. 10 Gb/s), enabling aggregate bit rates currently up to 640 Gb/s. Optical demultiplexer, on the other hand, extract a signal channel at the base rate of a time-multiplexed high-bit-rate data stream. Optical demultiplexers with ultra-high-speed operation can be realized by utilizing fiber nonlinearities but at the expense of high optical powers and performance instability.

4.8.1 SOA-MZI-Based Multiplexing

An experimental configuration for SOA-MZI all-optical multiplexer is presented in Fig. 4.44 to describe the operation principle. 10 GHz clock pulses having a pulse width of ∼20 ps are generated at 1553 and 1560 nm using two gain-switched DFB lasers and are combined and encoded simultaneously at 10 Gb/s with a $2^{31} - 1$ PRBS sequence. These data sequences are decorrelated with respect to each other through passive splitting, filtering and delay of one data signal with respect to the other and then the two sequences are combined together with an offset of one half 10 Gb/s. The obtained data stream with an input power of 0 dBm is coupled to the input port of MZI and at the same time a CW-light at the wavelength 1545 nm and input power of −2.4 dBm is coupled to middle port of the MZI structure.

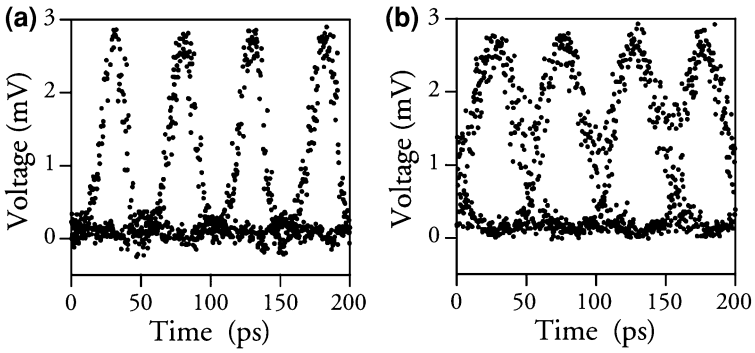

Fig. 4.45 **a** Eye-diagram of 2 × 10 Gb/s data signal at MZI input and **b** 20 Gb/s converted eye-diagram at MZI output [32]

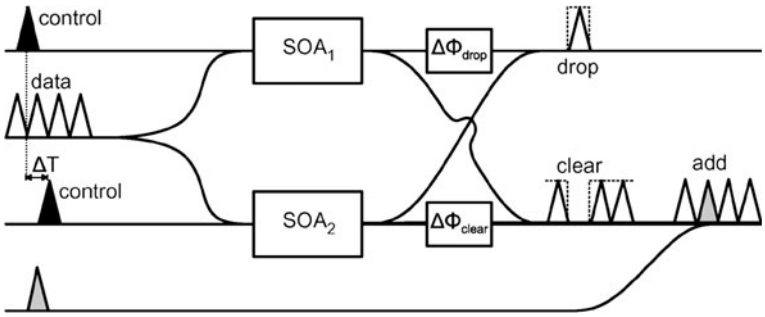

Fig. 4.46 ADM scheme based on SOA-MZI [35]

At the output of the structure, both channels are wavelength converted to the CW laser wavelength. The eye-diagram for the 2 × 10 Gb/s input signal and the output eye-diagram for the 20 Gb/s wavelength converted signal are presented in Fig. 4.45 where clear and open eyes exhibit high extinction ratio.

In recent years the concept of OTDM add-drop multiplexing (ADM) has attracted considerable attention [33, 34]. An ADM is a key functionality that enables the communication between the backbone network working at aggregate bit rates and the lower speed network branches working at base data rates. Compactness and low operation power of SOA-MZI has made this structure a suitable technology for demonstration of OTDM ADMs. Figure 4.46 schematically shows an ADM configuration that operates based on differential control scheme in SOA-MZI structure. In this scheme, phase modulation occurs in the upper and lower interferometer arms in the presence of the control signals. If the delay between the control pulses in the upper and lower arm (ΔT) is chosen properly, the corresponding phase difference will create a switching window having a short, well-defined time span.

In the configuration presented in Fig. 4.46, a copy of the electrical fields after each SOA interferes with its counterpart in an additional coupler and simultaneous optimization of phases for both output ports can be accomplished through the phase shifter placed after each SOA output coupler [35]. In this cased the transfer function of the drop and clear ports can be defined as

$$\begin{aligned} T_{\text{drop}}(t) &= \frac{1}{8}\left(G_1 + G_2 - 2\sqrt{G_1 G_2}\cos\left(\Delta\Phi + \Delta\Phi_{\text{drop}}\right)\right) \\ T_{\text{clear}}(t) &= \frac{1}{8}\left(G_1 + G_2 + 2\sqrt{G_1 G_2}\cos\left(\Delta\Phi - \Delta\Phi_{\text{drop}}\right)\right) \end{aligned} \tag{8}$$

where G_1 and G_2 are the gains of SOA_1 and SOA_2 and $\Delta\Phi = \Phi_1 - \Phi_2$ is the phase difference of the electrical fields after the SOAs. $\Delta\Phi_{\text{clear}}$ and $\Delta\Phi_{\text{drop}}$ are the phase offsets for clear and drop ports that can be adjusted independently to provide an optimization for the phase shift for both output ports simultaneously. This optimization can be especially helpful in the case of insufficient (less than π) phase shift $\Delta\Phi$ for the clear port which may be compensated by a proper adjustment of $\Delta\Phi_{\text{clear}}$.

4.8.2 SOA-MZI-Based Demultiplexing

Generally, there are two different schemes for demultiplexing in a SOA-MZI structure, i.e. demultiplexing without wavelength conversion and demultiplexing with wavelength conversion of the initial data signal. These schemes are schematically illustrated in Fig. 4.47. In the first scheme, the data signal is coupled into

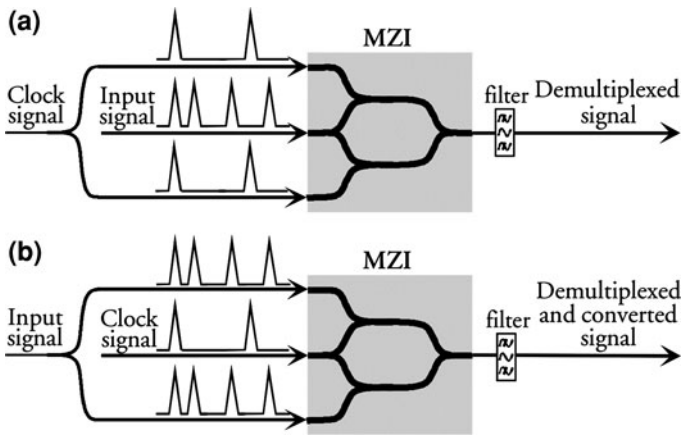

Fig. 4.47 Schematic of two different schemes for all-optical time-division demultiplexing based on SOA-MZI. **a** Demultiplexing without wavelength conversion and **b** simultaneous demultiplexing and wavelength conversion [25]

common arm of MZI while the clock signal is coupled into the upper and lower arms in differential scheme (clock signal in one of the arms is delayed and attenuated before entering the SOA in comparison with the signal in the other arm to prepare a pre-defined switching window). The clock pulses modulate the phase of the lower-rate data channel and result in constructive interference of this specific channel at the MZI output, while the remaining a suppressed.

In the second scheme, the clock signal couples to the common arm and serves as a probe signal and samples the input signal. Therefore, the data encoded on the channel synchronized to the clock signal is modulated onto the clock pulses and can be selected at the output using a filter. Figure 4.48 shows the experimental results for 40 Gb/s demultiplexing into two 10 Gb/s channels. Part (b) and (c) display the '1110' and '1011' bit sequences, respectively, that have been selected from input pulse train.

Demonstration of all-optical demultiplexing using a single SOA by employing an optical bandpass filter is another approach for SOA based demultiplexing that utilizes the chirp properties of SOA as described previously in wavelength conversion based on SOA-BPF. 160/320/640 to 40 Gb/s demultiplexing are of reported results that employ this approach [36, 37]. Figure 4.49 shows an experimental setup for all-optical demultiplexing which consists of an OTDM transmitter and an OTDM receiver in a back-to-back configuration [36]. A 10 GHz optical clock signal at the wavelength of $\lambda_S = 1545$ nm is optically quadrupled ($\times 4$) to 40 GHz. Then, this signal is modulated to form a 40 Gb/s base rate of $2^7 - 1$ RZ PRBS. By using passive pulse interleavers the 40 Gb/s data signal is

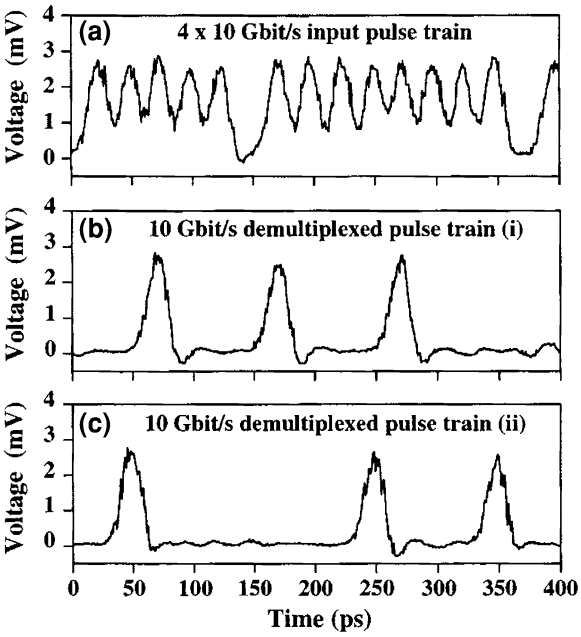

Fig. 4.48 **a** Input pulse train at 40 Gb/s and **b**, **c** two different demultiplexed 10 Gb/s channels [30]

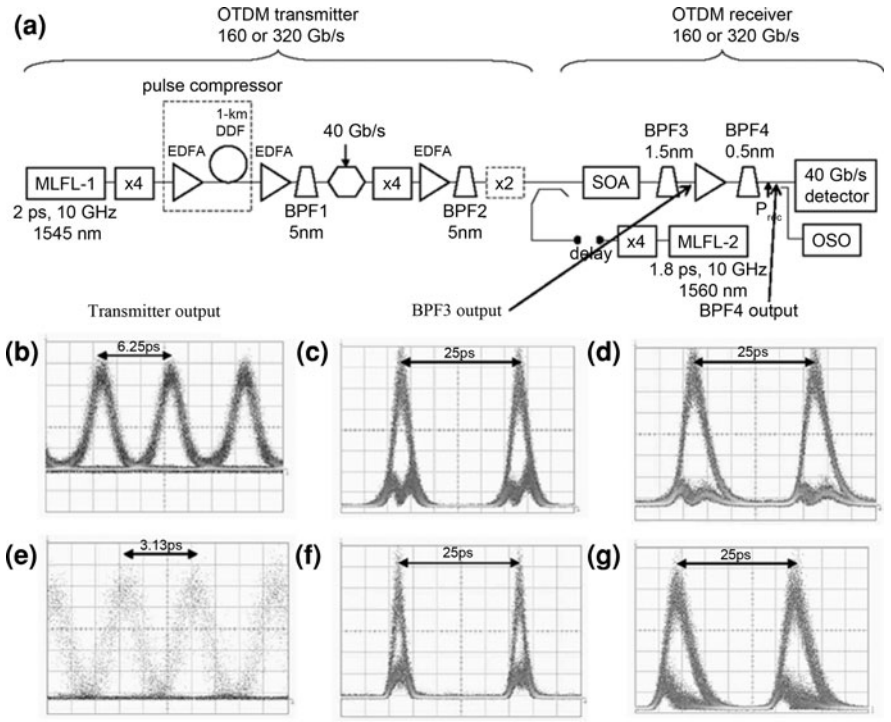

Fig. 4.49 **a** Experimental setup for 160/320 Gb/s to 40 Gb/s demultiplexing and eye-diagrams of (**b**), **e** input data signals at 160 and 320 Gb/s, **c**, **f** output multiplexed data after the BPF3, **d**, **g** output multiplexed data after the BPF4, for 160 and 320-Gb/s input signal, respectively [36]

time-multiplexed to 160 Gb/s (×2) or 320 Gb/s (×4) bit rates and then combines with a 40 GHz and 1.8-ps pulse train at $\lambda_C = 1560$ nm. In the receiver part, the demultiplexer is consisted of an SOA, a 1.5 nm optical filter (BPF3), an EDFA and a 0.5 nm optical filter (BPF4) where the last two elements are used to improve the optical signal-to-noise ratio (OSNR) of the demultiplexed signal. The utilized SOA has an initial gain recovery time of 90 ps and is capable of demultiplex error-free OTDM signals at bit rates of <40 Gb/s.

The injected data signal (λ_S) modulates the SOA gain and therefore affects the control pulse (λ_C) through XGM effect and hence the output of the SOA contains the demultiplexed data to 40 Gb/s channels at the wavelength λ_C. The blue-shifted spectral component of the chirped control pulse (due to refractive index modulation in the presence of data signal) can be selected by BPF3 to enhance the SOA recovery time as discussed previously. The central wavelength of BPF3 is located approximately 1 nm from the central wavelength of the control pulses as shown in Fig. 4.50 where the wavelength position of 160 Gb/s data signal is also depicted.

The obtained eye-diagrams for input data signals at 160 and 320 Gb/s, the output multiplexed data at 40 Gb/s after the BPF3 for 160 and 320-Gb/s input

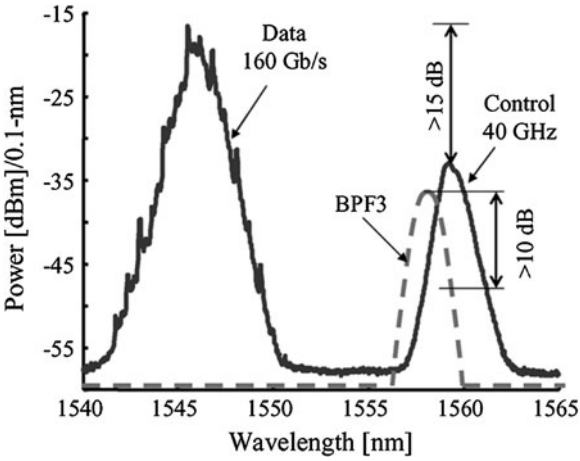

Fig. 4.50 Central wavelength of the optical filter (BPF3) relative to the data signal and control pulse [36]

signal and the output multiplexed data at 40 Gb/s after the BPF4 for 160 and 320-Gb/s input signal are depicted in Fig. 4.49b and e, c and f, d and g, respectively.

4.9 Data Format Conversion

The technology trend of developing all-optical networks is going to combine the advantageous of the WDM and the OTDM networks and exploit the benefits of both networks. In these networks, conventional RZ and NRZ data formats have been used to transmit, process, and receive the information. The RZ format is widely employed in OTDM networks as it has large tolerance to fiber nonlinearities in spite of the dispersion induced effect, and the NRZ format is especially efficient and thus is better suited for the dense wavelength division multiplexing (DWDM) system. Thus, modulation format conversion will become an important interface technology for new generation of optical networks that will include different data formats. On the other hand, in the clock recovery of NRZ format, NRZ-to-RZ conversion is unavoidable since NRZ does not contain clock components in its modulation spectra while RZ format contains clock components.

Several methods have been proposed for all-optical data format conversion. However, SOA based methods are preferable for our discussion.

4.9.1 NRZ-to-RZ Data Format Conversion

Figure 4.51a depicts the schematic SOA-MZI configuration for NRZ-to-RZ format conversion where a probe clock signal is split equally and is coupled to upper and lower arms of the MZI. The NRZ input data signal is coupled to the upper arm of

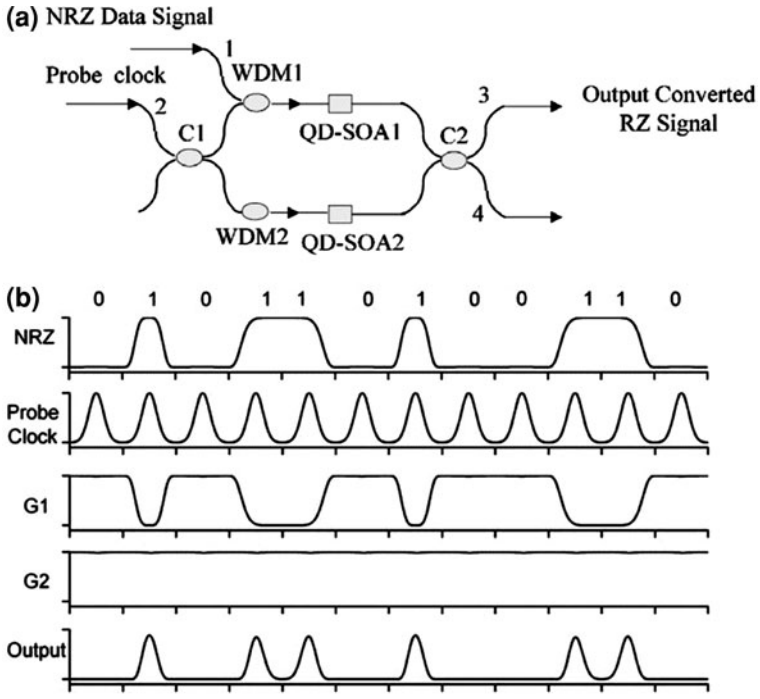

Fig. 4.51 **a** Schematic configuration for NRZ-to-RZ format conversion based on QD-SOA-MZI structure and **b** operation principle of NRZ-to-RZ format conversion [38]

the MZI as a control signal and modulates the gain and the phase of the co-propagating probe signal through XGM and XPM effects in QD-SOA. Since the two probe components propagating through upper and lower arms have differences in gain and phase, their combination at the output of the MZI result in the data format and simultaneously wavelength conversion. The principles of format conversion in terms of the input NRZ stream, the probe clock signal, and the gain dynamics of QD-SOAs is presented in Fig. 4.51b. The simulation results for data conversion is shown in Fig. 4.52 which indicates the system operation capability up to 160 Gb/s limited by QD-SOA recovery time. It is noteworthy that increasing the bias current will enhance the quality factor of the output converted probe signal. Since gain saturation induced by long series of '1's leads to the broadening of the switch window (third panel in Fig. 4.52) and results in the pulse broadening of the converted RZ signal, increasing the bias current will increase the saturation density and thus higher quality factor is expected.

It should be noted that using a CW light for probe signal will reduce the patterning-effect by increasing the probe power. This is because the CW light serves as a holding beam and accelerates the gain recovery of the QD-SOA. On the contrary, in the case of periodic clock signal as probe, as in the structure presented in Fig. 4.51, the acceleration of gain recovery induced by time-dependent clock is

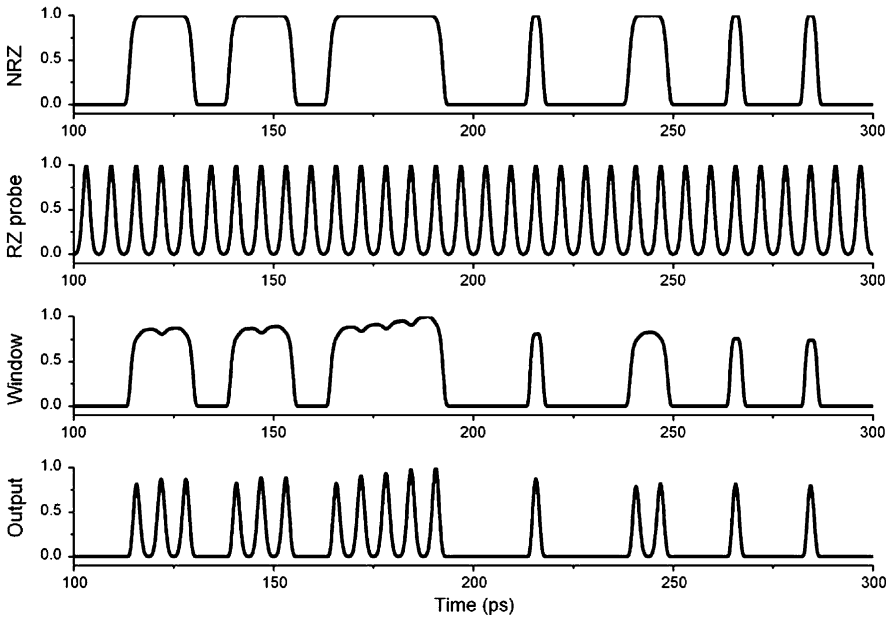

Fig. 4.52 Input NRZ data signal, RZ probe pulse, switching window and output converted RZ signal at 160 Gb/s [38]

uneven and this effect is much larger under higher probe power. Therefore, increasing the periodic probe signal power decreases the output signal quality factor.

4.9.2 NRZ-to-PRZ Data Format Conversion

SOA in conjunction with shifted filtering can be utilized for data format converting from NRZ format to pseudoreturn-to-zero (PRZ) format. Similar to RZ format, PRZ data format contains clock components in its modulation spectra and can be used for clock extraction. Figure 4.53 presents a schematic for SOA-BPF based setup where the filter can be tuned to select either red-shifted or blue-shifted spectral components of the NRZ signal to perform format conversion or waveform reshaping operation, respectively.

Two laser diodes generate optical signals at $\lambda_S = 1563.6$ nm (LD1) and $\lambda_C = 1556.3$ nm (LD2). The generated signal from LD1 modulates by the Mach–Zehnder Modulator (MZM) at 10 Gb/s and forms $2^{31} - 1$ NRZ PRBS signals which combines with CW light at λ_C and couples to SOA. As it is known, during amplification of a NRZ signal, the waveform becomes asymmetric as it is depicted in Fig. 4.54a and an overshoot appears at the leading edge which is due to gain saturation, resulting in SPM which generates large red chirp components

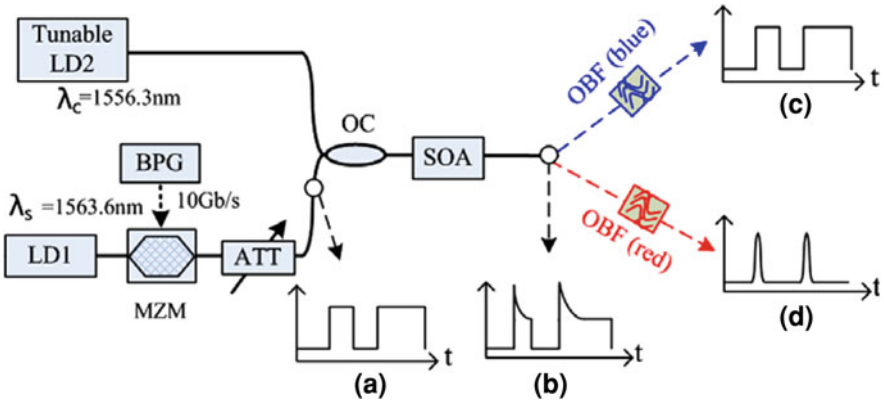

Fig. 4.53 Schematic of experimental setup and operation principle for NRZ-to-PRZ data format conversion: **a** input NRZ data signal, **b** deformed signal after SOA, **c** reshaped NRZ with blue-shifted OBF, and **d** converted PRZ with red-shifted OBF [39]

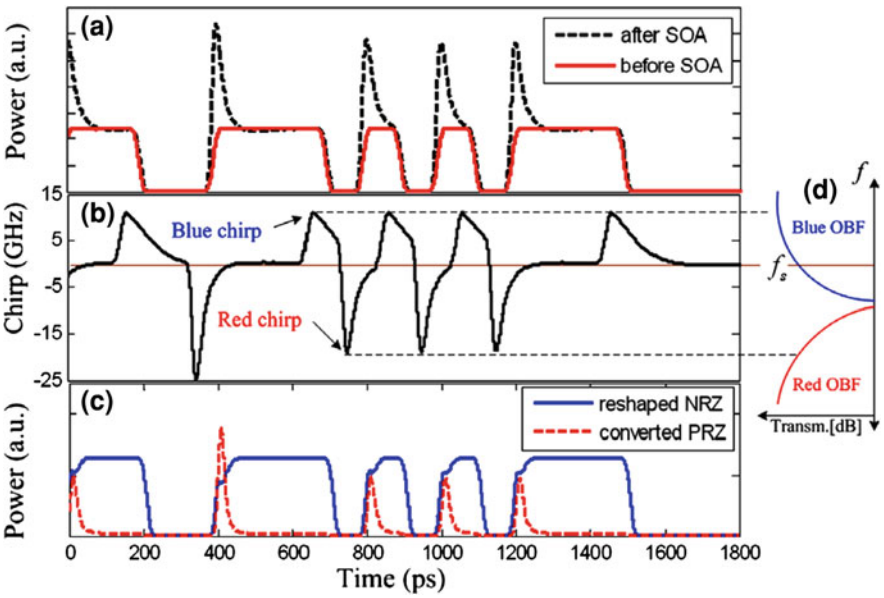

Fig. 4.54 **a** Input NRZ signal and its distortion after the SOA, **b** the frequency chirp, **c** the reshaped NRZ signal and converted PRZ signal after OBF, and **d** the transmission of the detuning OBF [39]

(Fig. 4.54b) [40]. A red shifted OBF after SOA is capable of converting the red chirp to amplitude information due to the linear slope of the transmission spectrum of the OBF and therefore converting the signal format to PRZ. Since the central carrier frequency is modulated with the NRZ format signal, a narrow-bandwidth

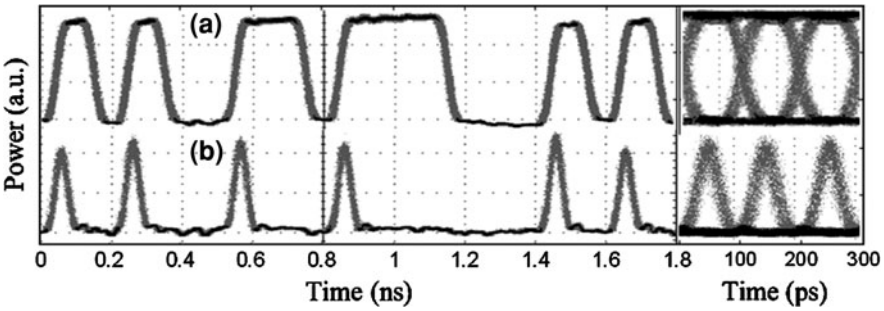

Fig. 4.55 Experimental results for *a* input NRZ data signal, *b* output converted PRZ signal (*left column*). *Right column* related eye diagrams [39]

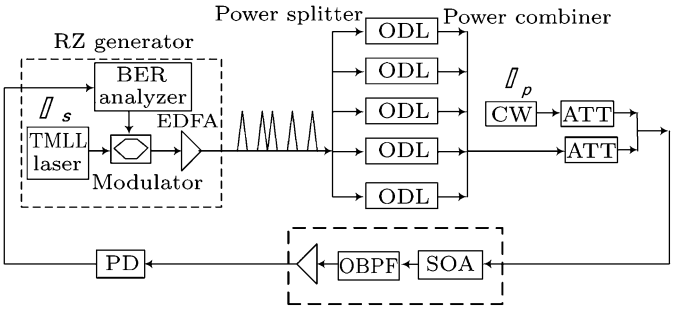

Fig. 4.56 Schematic of experimental setup for RZ-to-NRZ data format conversion [42]

filter is required to remove the carrier frequency (an OBF with 0.32 nm bandwidth and red-shifted by 0.42 nm has used). A blue-shifted OBF on the other hand removes large red shifted component and permits distortion-free amplification of the NRZ signal as depicted in Fig. 4.54c.

The continuous wave generated by the LD2 serves as a holding beam to saturate the SOA and improve the output performances [41].

The input NRZ data at a bit rate of 10 Gb/s and the obtained PRZ pulses at the leading edge of the input signal are presented in Fig. 4.55. The right column of this figure illustrates the related eye-diagrams. With a 0.42 nm red-shifted filter, the output ER of the converted PRZ is larger than 10 dB while the amplitude fluctuation is around 1.6 dB.

4.9.3 RZ-to-NRZ Data Format Conversion

RZ-to-NRZ format conversion can be performed by the SOA-OBF configuration. A schematic of experimental setup for this demand is presented in Fig. 4.56.

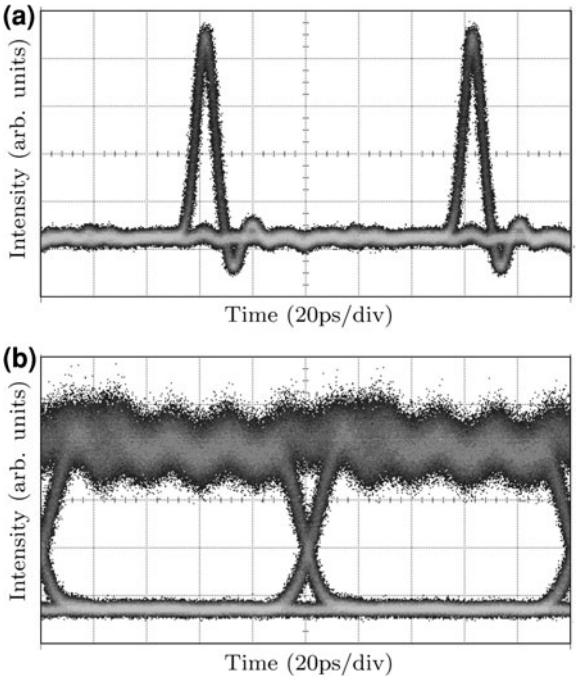

Fig. 4.57 **a** Eye diagram of input RZ signal and **b** eye diagram of converted NRZ signal [42]

The 10 Gb/s RZ data signal at the central wavelength of 1550.97 nm is generated at the generator block and forms $2^{31} - 1$ PRBS signal. A CW source generates a probe beam at the wavelength 1559.68 nm which combines with the data signal and coupled to the SOA. The OBF has a bandwidth of 0.3 nm and is blue-shifted about 0.32 nm with respect to the probe wavelength. A preprocessor system consisted of a power splitter, a power combiner and five optical delay lines (ODL) providing 20 ps delay in each arm has designed to preprocess the signal pulses and an EDFA and two attenuators (ATT) control the signal and probe powers.

Figure 4.57 shows the measured eye-diagrams for input RZ signal and converted NRZ format. The output extinction ratio (>11 dB) and bit error rate (5.5×10^{-9} when the power of NRZ is -10 dBm) demonstrate good conversion quality for this topology.

4.10 All-Optical Flip-Flop

All-optical flip-flops are technologically important elements in all-optical networks since these elements can serve as optical memories and replace the electronic RAMs in electro-optical networks. Although we are interested to introduce SOA-based configurations for optical flip-flops but there is other successful recently developed methods especially based on coupled laser diodes [43, 44].

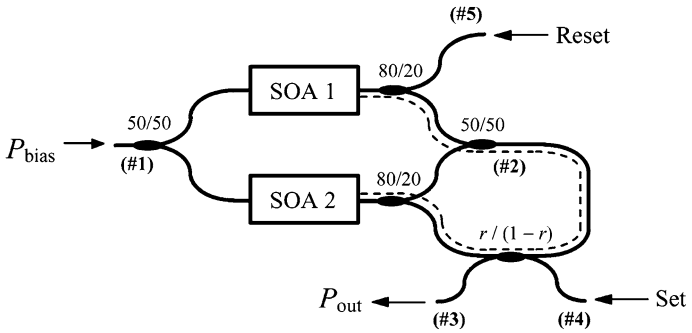

Fig. 4.58 Configuration schematic of an all-optical flip-flop based on SOA-MZI [45]

Schematic of a SOA-MZI based all-optical flip-flop which operated in counter-propagation mode is presented in Fig. 4.58 [45]. The scheme consists of a CW signal, P_{bias}, which couples to MZI port #1. The MZI output signal is extracted from port #2 and is inserted to the lower SOA (SOA 2) via an optical loop which includes a 2 × 2 coupler with a coupling factor of r and an 80/20 coupler as shown in the figure. The optical signals to set and reset the flip-flop are injected to ports #4 and #5, respectively. By applying a set (reset) pulse to the MZI port, the carrier density and consequently the optical gain of the SOA 2 (SOA 1) is reduced and therefore the CW signal undergoes a gain and phase change while propagating through the lower (upper) SOA which results in unbalanced structure and an output signal at port #2. The main difference between the operation mechanism of the set and the reset signals relies in the feedback loop which re-injects a fraction of output power to the lower SOA when the set pulse is applied. Thus, the lower SOA keeps its state ensuring the output state after passing the set pulse. A similar scenario takes place for the reset pulse unless the fact that the carrier density and optical gain of both SOAs have reduced in the presence of the reset signal (affects SOA 1) and the re-injected signal via feedback loop (affects SOA 2). Therefore, the structure will be balanced and no output signal is expected. It should be considered that the latter condition requires proper selection of the reset signal energy and the coupling factor of the 2 × 2 coupler.

The simulation results of the structure including the carrier density of the SOAs and the output power in presence of the set and the reset pulses are depicted in Fig. 4.59.

The Gaussian set and reset pulses with 1.33 pJ of energy have been applied alternatively which change the carrier densities as displayed in the middle panel of Fig. 4.59. Applying a set pulse reduces the carrier density of SOA 2 while maintains the carrier density of SOA 1 (small variation is due to counterclockwise pulse propagation through the loop) and therefore a stable output power with an extinction ratio higher than 20 dB is obtained. The output power of this configuration can be maximized by adjusting the coupling factor which

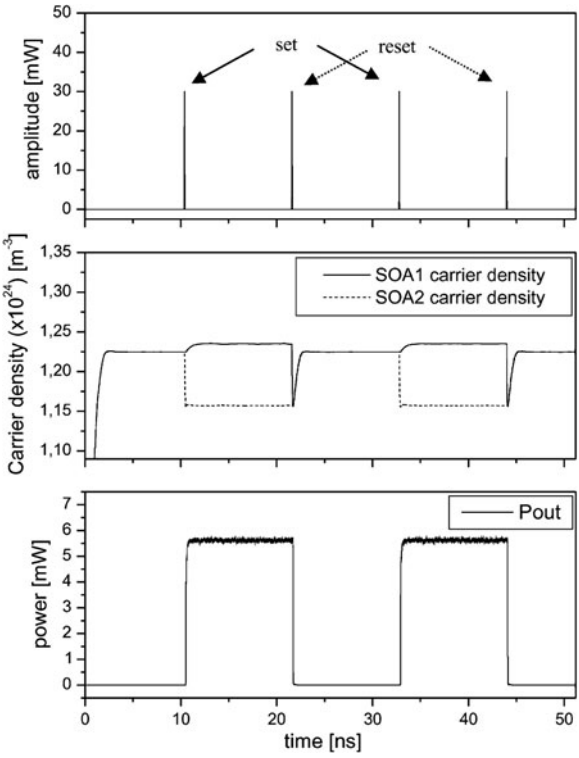

Fig. 4.59 *Upper panel* Input set and reset pulses timing and amplitude, *middle panel* carrier densities of the SOAs, and *lower panel* flip-flop output power [45]

is proportional to adjust the phase difference between the MZI branches to be near π.

Figure 4.60 illustrates another SOA-based configuration for all-optical flip-flop which utilizes two coupled MZIs containing a SOA on one arm [46]. The operation principle of this flip-flop is similar to the coupled laser diodes where the dominant wavelength inhibits the emission of the second wavelength until an external excitation change the dominant wavelength. The two coupled MZIs in the architecture presented in Fig. 4.60 have hybrid integrated on a silica on silicon passive assembly. Two CW bias signals at $\lambda_1 = 1562$ nm and $\lambda_2 = 1565$ nm are injected to the MZIs and the MZIs are phase biased by utilizing thermo-optic silica waveguide phase shifters such that the CW signals exit the interferometers at the cross ports in the absence of external set and reset pulses.

The operation principle of the flip-flop can be justified by assuming that the device is in a specific state, e.g. state 1 (λ_1). In this case the bias signal at λ_1 enters to SOA 2 causing a π phase shift in SOA 2 and consequently switches the λ_2 bias signal to the bar port of MZI 2. Hence, the output 1 will emit λ_1 signal as dominant state. By applying an external pulse to set state 2 port, SOA 1 undergoes a π phase shift which leads to λ_1 signal switching to the bar port of the MZI 1. Therefore, the gain and phase recovery of SOA 2 results in λ_2 switching to the cross port of MZI

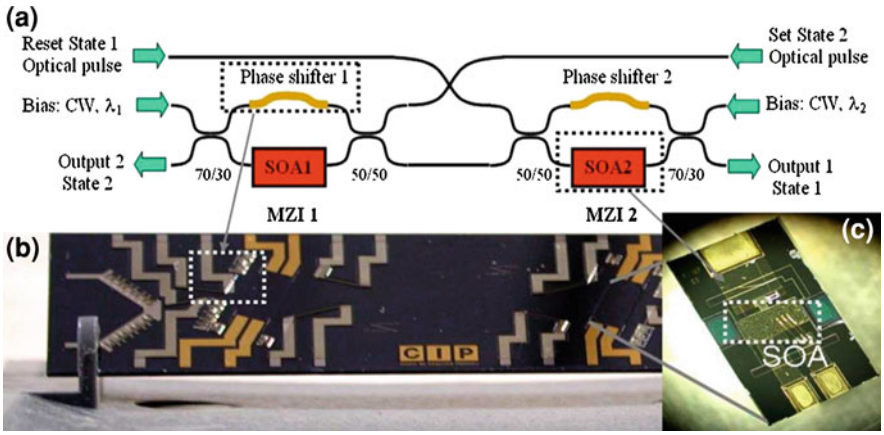

Fig. 4.60 **a** Configuration schematic of an all-optical flip-flop based on two coupled MZIs and developed using hybrid technology, **b** planar silica motherboard, and **c** daughterboard with twin SOAs flip chipped and wirebonded [47]

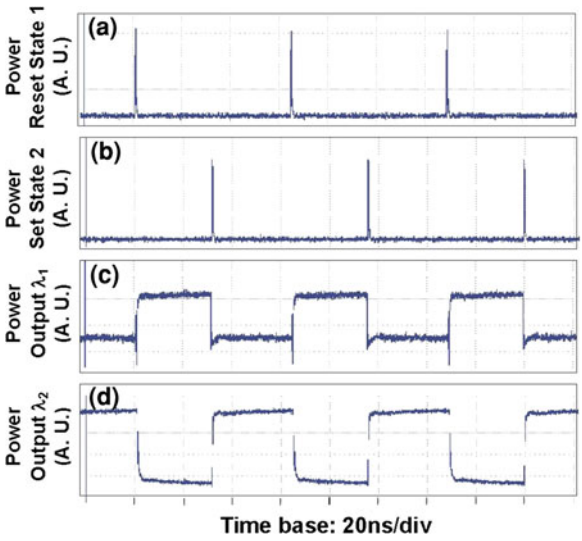

Fig. 4.61 Dynamics of optical pulses corresponding to **a** reset state 1, **b** set state 2, **c** state 1 output at λ_1, and **d** state 2 output at λ_2 [46]

2, coupling to SOA 1, appearing at the output state 2 and inhibiting the operation of the λ_1 signal. This process is illustrated via temporal dynamics of the output state 1 and output state 2 in the presence of the alternative set state pulses in Fig. 4.61. It is clear that reset state 1 pulse dominates the λ_1 signal at output 1 and vice versa. Contrast ratios of 13 and 10 dB have obtained for state 1 and state 2, respectively, and the switching time of the flip-flops (32 ns) is limited mainly due to SOAs recovery time.

4.11 All-Optical PRBS Generation

Pseudorandom bit sequences (PRBSs) have been typically used to verify the correct transmission of optical data through optical fiber networks. PRBS circuit is a basic building block for the implementation of a high-speed all-optical bit error rate tester (BERT) that is expected to possess cost and performance advantages over its electronic counterpart. The generation principles of an all-optical PRBS rely on linear feedback shift register (LFSR) element. The structure of a general feedback shift register of length m is an arrangement of m delay elements which are driven simultaneously by a clock and are shifted to the next element at every clock pulse. The PRBS is created by implementing the XOR function between the binary values at the end of the register and some tap point within the register. The XOR result is fed back into the start of the register and this process continues to generate the PRBS output. The PRBS sequence generated with a shift register of length m has a period of $2^m - 1$. The capacity of the shift register can be a few hundred bits owing to the length of the optical fiber and this can generate PRBSs with extremely long periods ($2^{500} - 1$) [48, 49]. In order to generate an all-optical PRBS one need to realize the XOR logic gate in the optical domain. Also there have been introduced several methods to do this but we are interested in generation methods based on SOAs in MZI structure.

A schematic for PRBS generation based on the QD-SOA XOR gate is depicted in Fig. 4.62 [50]. At each clock period, The XOR operation is done on the nth and mth bits and the result is reshaped and wavelength converted by using an AND gate. The result is then feed back to the front of LFSR while the output PRBS signals can be tapped from the end of the LFSR. As it is obvious from Fig. 4.62b, two data bits at the wavelength λ_1 along with a clock signal at λ_2 are injected into the XOR gate where the XOR operation is realized through XGM and XPM effects in the SOAs. In order to have an efficient XGM, the frequency detuning between the data and clock signals should be smaller than the homogeneous broadening of a QD. The converted signal at the wavelength λ_2 is then couples to the AND gate where a clock signal at λ_1 and a trigger signal (here '1' to yield AND operation) are injected to the common and the lower MZI ports, respectively. By placing a BPF at the output of the AND gate, the output of the XOR operation will be wavelength converted to λ_1 and also will be reshaped by passing through the AND gate.

Simulation result for the all-optical PRBS generator using a 7-bit LFSR at operation speed of 250 Gb/s is presented in Fig. 4.63a. Also, the related output eye-diagram for a 1 ps FWHM pulse width is plotted in Fig. 4.63b which depends on FWHM pulse width, single pulse energy, transition lifetime from QD excited to ground state and injected pump current density. The output quality of the PRBS result at 250 Gb/s for injected current density >1.8 kA/cm, single pulse energy ~0.6–1.0 pJ, and pulse width ~1.0 ps $Q > 8$. The repetition PRBS sequence period of this method ($2^m - 1$) can be further increased by increasing m and thus the generated PRBS spectrum can be more continuous just similar to a true random sequence.

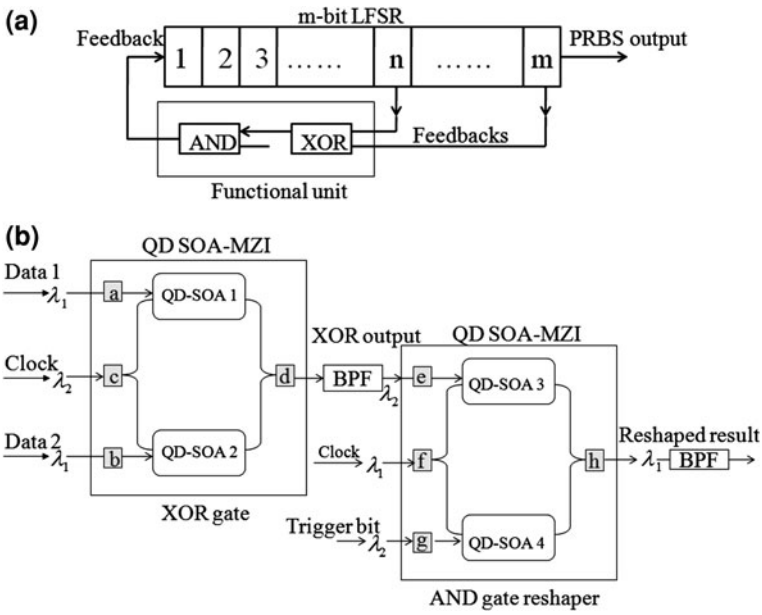

Fig. 4.62 **a** Block diagram of a LFSR-based PRBS generator and **b** schematic configuration of XOR and AND gates based on QD-SOA-MZI [50]

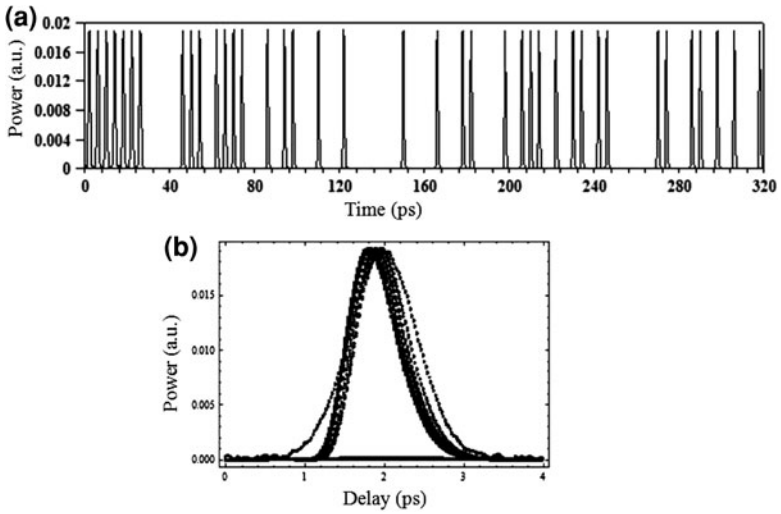

Fig. 4.63 **a** Simulation result of PRBS sequences generated using 7-bit LFSR, operating at 250 Gb/s and **b** related output eye-diagram [50]

4.12 All-Optical Clock Recovery

Synchronizing the optical gates and subsystems is an important issue in realization of optical packet switched networks. Hence, an all-optical clock recovery unit should be capable of acquiring the timing information from input data packets and retaining the synchronization signal for incoming packet duration. Recently, there has been great interest in developing clock recovery techniques without any synchronization to local oscillators. So far, clock recovery has been realized using synchronized mode-locked ring lasers [51], self-pulsating DFB lasers [52], and electrical phase-locked loops [53]. Fabry–Perot filter (FPF)-based clock recovery is one of the interesting techniques that is capable of clock extraction on a per-packet basis without requiring any synchronization to local oscillators. Exploiting the short memory effect of the filter, incoming data packets are transformed to clock-resembling packets. A schematic configuration of FPF-based clock recovery is illustrated in Fig. 4.64 which requires an optical power-limiting device such as a SOA as it is obvious.

A FPF should be utilized with free spectral range (FSR) equal to the line rate (e.g. 40 GHz) and low-finesse (the number of internal reflections in the filter is low) which leads to exponentially decaying time-domain impulse response. Thus, if a random bit sequence is fed into the filter, the '0' bit sequences will be partially filled by preceding '1's and therefore, incoming data packets are transformed to clock-resembling packets. However, since the packet stream is convolved with the exponentially decaying response function of the filter, the obtained clock packets suffer from highly modulated amplitude. The amplitude modulation at the output of the FPF can be reduced by taking advantage of the non-linear switching function of a high speed, optical gate such as SOA-based ultrafast nonlinear interferometer (UNI). Applying a strong CW signal to the SOA-based UNI will highly saturate the amplifier and thus, the SOA will be biased close to its material transparency point and will act similar to a power-limiting gate. So, the amplitude modulated clock pulses cause similar SOA gain variation which leads to amplitude equalization. Figure 4.65 shows the experimental setup configuration for achieving clock recovery. The formed $2^7 - 1$ PRBS data packets at 40 Gb/s bit rate are generated in the optical packet generator block and then is fed into the FPF with a finesse of 50.

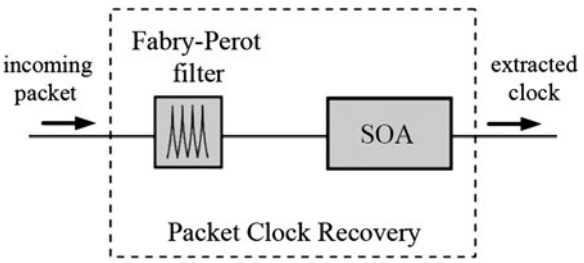

Fig. 4.64 Schematic scheme for all-optical clock recovery based on a SOA and a Fabry–Perot filter

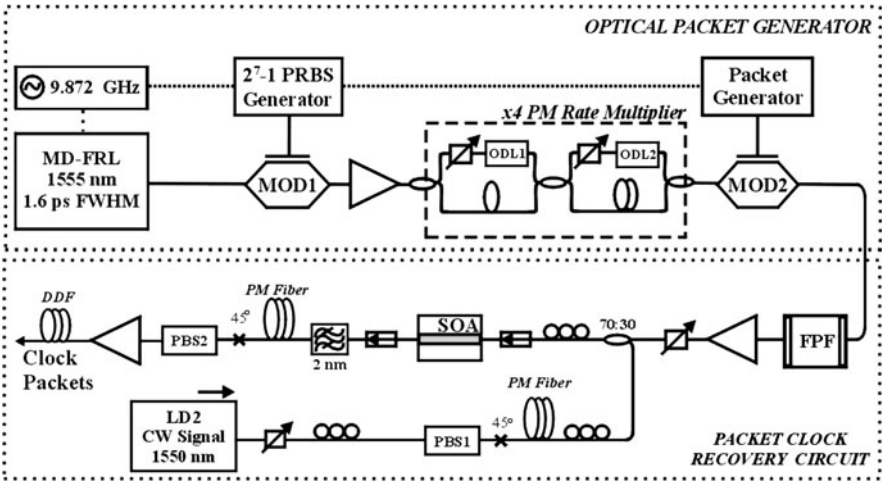

Fig. 4.65 Experimental setup for realizing all-optical clock recovery using a SOA and a FPF [54]

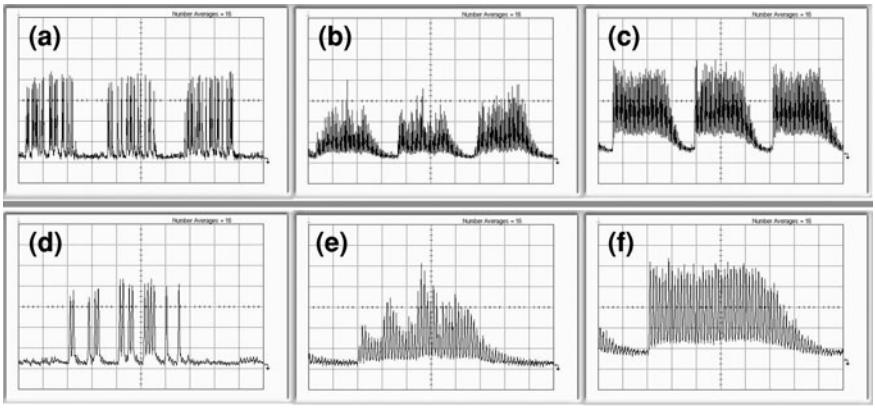

Fig. 4.66 Optical traces of **a** input data packets, **b** output of the FPF, **c** recovered clock packets, **d** single input data packet, **e** single output of the FPF, and **f** single recovered clock packet. The vertical scale is 335 μW/div and the time bases for *upper* and *lower panels* are 500 and 200 ps/div, respectively [54]

The output of the filter is coupled to the UNI gate after amplification and a CW signal at 1550 nm is used to saturate the SOA. An optical band-pass filter tuned at the initial wavelength of the input data stream is placed at the output of the interferometer. The optical traces of the input packets, the output of the FPF and the reshaped output after the SOA are depicted in Fig. 4.66. A single recovered clock packet, as displayed in panel (f), exhibits sharp rise time due to heavily saturated SOA and 16-bit fall time (400 ps) due to lifetime of the filter. It should

be noted that the rise time determines the lock acquisition time of the system while the fall time defines the minimum intra-packet guardband.

Although single wavelength clock recovery does not require complicated architectures, clock extraction of WDM signals tends to require a complicated system because the WDM signals should be demultiplex before being recovered and multiplexed again after clock extraction. Also, due to lack of clock recovery systems capable of operating on multiple channels at the same time, the same number of clock extraction units as the wavelength channels are required. Multiwavelength clock recovery can be developed by utilizing comb-like transfer function of a FPF which can be designed to cover a wide frequency range and spectrally localized nonlinear gain characteristics of a QD-SOA. This feature of QD-SOAs stems from the discrete states in QDs. Hence, carrier relaxation to another wavelength always involves carrier transfer to another dot since carriers are constrained within the homogeneous spectral width of the resonant wavelengths while in bulk and QWs, localized gain changes due to the SHB is followed by a broad gain change because of carrier thermalization [55]. Thus, it is possible to reach every wavelength channel independently. The gain spectra of a QD-SOA for four input wavelength channels are depicted in Fig. 4.67 which verify the mentioned facts. The input wavelengths (λ_1, λ_2, λ_3 and λ_4) are assumed to start with $\lambda_1 = 1232.3125$ nm with a channel spacing of $\Delta\lambda = 5.125$ nm when the homogeneous broadening is considered to be 4 meV (Fig. 4.67a) and $\lambda_1 = 1224.994$ nm with a channel spacing of $\Delta\lambda = 12.505$ nm when the homogeneous broadening is 10 meV (Fig. 4.67b) [56]. These CW input wavelengths are considered to have enough power to saturate the QD-SOA and create a spectral hole in their corresponding wavelengths although they affect the gain spectra over a wide wavelength range. This effect is much stronger for 4 meV homogeneous broadening than 10 meV case since carrier depletion occurs over wider spectral range and influences the overall gain further. Figure 4.68 shows a schematic scheme for multiwavelength clock recovery based on QD-SOA as described above

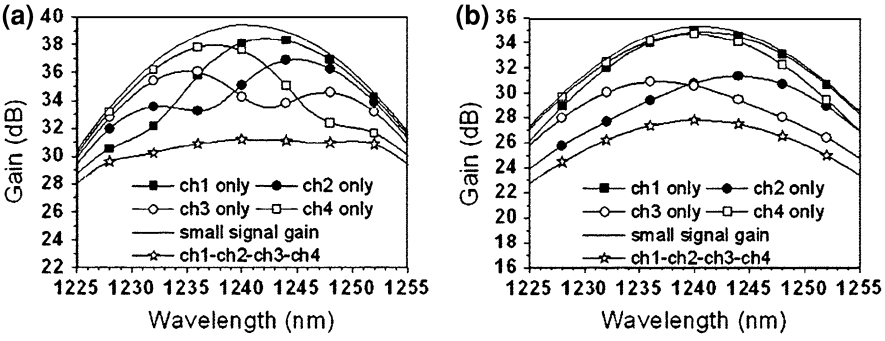

Fig. 4.67 Gain spectra of a QD-SOA for **a** 4 meV and **b** 10 meV homogeneous broadening. The gain curves have plotted for the cases when no input saturating signal is present, when a single input signal and when all four input signal channels are present [56]

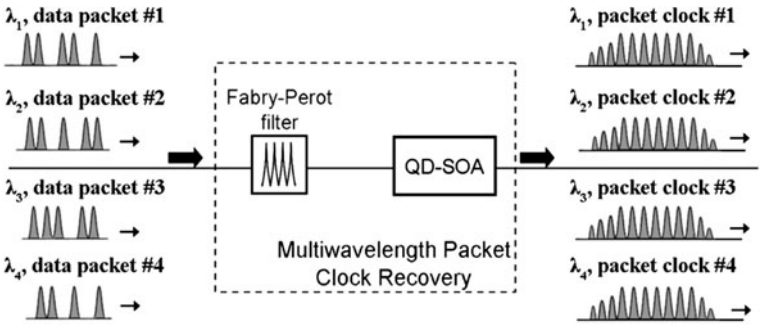

Fig. 4.68 Schematic scheme for multiwavelength clock recovery based on a QD-SOA and a Fabry–Perot filter [56]

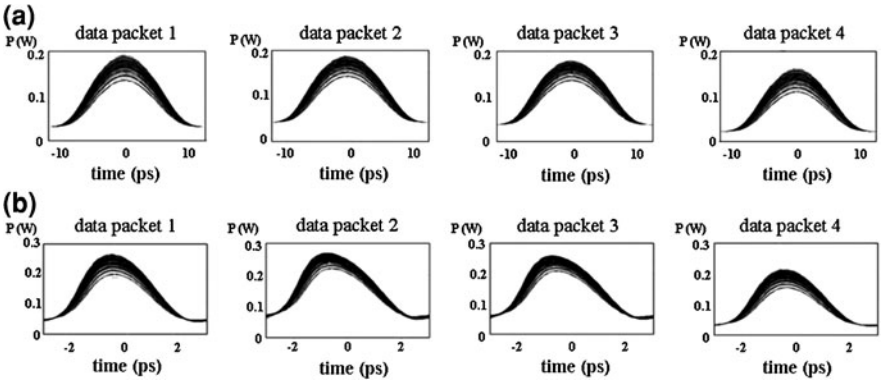

Fig. 4.69 Eye diagrams of the recovered clock signals at four different wavelengths (data packet i at λ_i) at **a** 40 Gb/s and **b** 160 Gb/s [56]

[56]. By assuring that the channel spacing is greater than spectral content of each wavelength and spectral matching of incoming wavelengths with respective resonance peaks of the FPF, this configuration can successfully perform the multiwavelength clock extraction form incoming packets.

The simulated eye-diagrams of the recovered clock signals from the input data packets (127-bit long data packets at 40 and 160 Gb/s) at four different wavelengths are presented in Fig. 4.69. Considering an extinction ratio (the ratio of the mean value of the amplitude at the higher level to the mean amplitude of the lower level) of 16 dB for the input signals, synchronization per wavelength is achieved with less than 1.8 and 1.5 dB amplitude variation for the two outer and the two inner channels at 40 Gb/s, respectively, and 1.5 and 1.1 dB at 160 Gb/s. The reason of better extinction ratio at 160 Gb/s relates to shorter time interval between two successive pulses for SOA gain recovery.

This short time interval for gain recovery results in reduced gain for zero-power level.

References

1. Ramos, F., Kehayas, E., Martinez, J.M., Clavero, R., Herrera, J., Seoane, J., Nielsen, P.V., et al.: IST-LASAGNE: towards all-optical label swapping employing optical logic gates and optical flip-flops. IEEE J. Lightwave Technol. **23**, 2993–3011 (2005)
2. Schubert, C., Berger, J., Diez, S., Ehrke, H.J., Ludwig, R., Feiste, U., Schmidt, C., Weber, H.G., Toptchiyski, G., Randel, S., Petermann, K.: Comparison of interferometric all-optical switches for demultiplexing applications in high-speed OTDM systems. J. Lightwave Technol. **20**, 618–624 (2002)
3. Ishikawa, H. (ed.): Ultrafast All-Optical Signal Processing Devices. Wiley, New York (2008)
4. Nakamura, H., Sugimoto, Y., Kanamoto, K., Ikeda, N., Tanaka, Y., Nakamura, Y., Ohkouchi, S., Watanabe, Y., Inoue, K., Ishikawa, H., Asakawa, K.: Ultra-fast photonic crystal/quantum dot all-optical switch for future photonic networks. Opt. Express **12**, 6606–6614 (2004)
5. Ellis, A.D., Kelly, A.E., Nesset, D., Pitcher, D., Moodie, D.G., Kashyap, R.: Error free 100 Gbit/s wavelength conversion using grating assisted cross-gain modulation in 2 mm long semiconductor optical amplifier. Electron. Lett. **34**, 1958–1959 (1998)
6. Perion, J.S., Wiesenfeld, J.M., Glance, B.: Fibre transmission of 10 Gbit/s sigals following wavelength conversion using a travelling-wave semiconductor optical amplifier. Electron. Lett. **30**, 256–258 (1994)
7. Durhuus, T., Mikkelsen, B., Joergensen, C., Danielsen, S.L., Stubkjaer, K.E.: All-optical wavelength conversion by semiconductor optical amplifiers. J. Lightwave Technol. **14**, 942–954 (1996)
8. Diez, S., Schmidt, C., Ludwig, R., Weber, H.G., Obermann, K., Kindt, S., Koltchanov, I., Petermann, K.: Four-wave mixing in semiconductor optical amplifiers for frequency conversion and fast optical switching. IEEE J. Sel. Top. Quantum Electron. **3**, 1131–1145 (1997)
9. Connelly, M.J.: Semiconductor Optical Amplifiers. Kluwer Academic Press, Boston (2002)
10. Lacey, J.P.R., Summerfield, M.A., Madden, S.J.: Tunability of polarisation-insensitive wavelength converters based on four-wave mixing in semiconductor optical amplifiers. J. Lightwave Technol. **16**, 2419–2427 (1998)
11. Liu, Y., Tangdiongga, E., Li, Z., de Waardt, H., Koonen, A.M.J., Khoe, G.D., Shu, X., Bennion, I., Dorren, H.J.S.: Error-free 320-Gb/s all-optical wavelength conversion using a single semiconductor optical amplifier. IEEE J. Lightwave Technol. **25**, 103–108 (2007)
12. Girault, G., Clarke, A.M., Reid, D., Guignard, C., Bramerie, L., Anandarajah, P., Barry, L.P., Simon, J.-C, Harvey, J.: Analysis of bit rate dependence up to 80 Gbit/s of a simple wavelength converter based on XPM in a SOA and a shifted filtering. Opt. Commun. **281**, 5731–5738 (2008)
13. Clarke, A.: Optical pulse processing towards Tb/s high-speed photonic systems. PhD thesis, School of Electronic Engineering, Faculty of Engineering and Computing, Dublin City University (2007)
14. Nielsen, M.L.: Polarity-preserving SOA-based wavelength conversion at 40 Gbit/s using bandpass filter. Electron. Lett. **39**, 1334–1335 (2003)
15. Poustie, A.J., Blow, K.J., Manning, R.J.: Storage threshold and amplitude restoration in an all-optical regenerative memory. Opt. Commun. **146**, 262–267 (1998)
16. DeVito, L.M.: Clock recovery and data retiming presentation by analog devices, advanced engineering course on IC design for optical communications systems, Part II. Lausanne, Switzerland (2001)
17. Bauer, S., Bornholdt, C., Brox, O., Hoffmann, D., Möhrle, M., Sahin, G., Sartorius, B., Schelhase, S., Lavigne, B., Chiaroni, D.: Ultrafast locking optical clock for IP packet switching applications. In: Tech. Dig. OFC 2000, paper TuF5 (2000)
18. Sugawara, M., Akiyama, T., et al.: Quantum-dot semiconductor optical amplifiers for high-bit-rate signal processing up to 160 Gb/s and a new scheme of 3R regenerators. Meas. Sci. Technol. **13**, 1683–1691 (2002)

19. Borri, P., Langbein, W., Hvam, J.M., Heinrichsdorff, F., Mao, M.-H., Bimberg, D.: Ultrafast gain dynamics in InAs–InGaAs quantum-dot amplifiers. IEEE Photonics Technol. Lett. **12**, 594–596 (2000)
20. Spyropoulou, M., Sygletos, S., Tomkos, I.: Simulation of multiwavelength regeneration based on QD semiconductor optical amplifiers. IEEE Photonics Technol. Lett. **19**, 1577–1579 (2007)
21. Wong, H.C., Ren, G.B., Rorison, J.M.: The constraints on quantum-dot semiconductor optical amplifiers for multichannel amplification. IEEE Photonics Technol. Lett. **18**, 2075–2077 (2006)
22. Webb, R.P., Manning, R.J., Maxwell, G.D., Poustie, A.J.: 40 Gbit/s all-optical XOR gate based on hybrid-integrated Mach-Zehnder interferometer. Electron. Lett. **39**, 79–81 (2003)
23. Sun, H., Wang, Q., Dong, H., Chen, Z., Dutta, N.K., Jaques, J., Piccirilli, A.B.: All-optical logic XOR gate at 80 Gb/s using SOA-MZI-DI. IEEE J. Quantum Electron. **42**, 747–751 (2006)
24. Sun, H., Wang, Q., Dong, H., Dutta, N.K.: XOR performance of a quantum dot semiconductor optical amplifier based Mach-Zehnder interferometer. Opt. Express **13**, 1892–1899 (2005)
25. Fjelde, T.: Traffic analysis and signal processing in optical packet switched networks. PhD thesis, Research center COM, Technical University of Denmark, Kgs. Lyngby, Denmark (2001)
26. Dong, H.,Sun, H., Wang, Q., Dutta, N.K., Jaques, J.: 80 Gb/s all-optical logic and operation using Mach-Zehnder interferometer with differential scheme. Opt. Commun. **265**, 79–83 (2006)
27. Hamie, A., Sharaiha, A., Guegan, M.I.: Demondtration of an all-optical logic OR gate using gain saturation in an SOA. Microw. Opt. Technol. Lett. **39**, 39–42 (2003)
28. Dong, J., Zhang, X., Xu, J., Huang, D.: 40 Gb/s all-optical logic NOR and OR gates using a semiconductor optical amplifier: experimental demonstration and theoretical analysis. Opt. Commun. **281**, 1710–1715 (2008)
29. Hamié, A., Sharaiha, A., Guégan, M., Pucel, B.: All-optical logic NOR gate using two-cascaded semiconductor optical amplifiers. IEEE Photonics Technol. Lett. **14**, 1439–1441 (2002)
30. Wolfson, D., Kloch, A., Fjelde, T., Janz, C., Dagens, B., Renaud, M.: 40-Gb/s all-optical wavelength conversion, regeneration, and demultiplexing in an SOA-based all-active Mach-Zehnder interferometer. IEEE Photonics Technol. Lett. **12**, 332–334 (2000)
31. Ye, X., Ye, P., Zhang, M.: All-optical NAND gate using integrated SOA-based Mach-Zehnder interferometer. Opt. Fiber Technol. **12**, 312–316 (2006)
32. Fjelde, T., Kloch, A., Wolfson, D., Dagens, B., Brenot, R., Labrousse, A., Roux, E., Gaborit, F., Poingt, F., Renaud, M.: Simultaneous 2 $\times$ 10 to 20 Gbit/s time-division multiplexing and wavelength conversion using an integrated SOA-based Mach-Zehnder interferometer. In: Proceedings of OECC/IOOC2001, paper TueL.4, Sydney, Australia (2001)
33. Schubert, C., Schmidt, C., Ferber, S., Ludwig, R., Weber, H.: Error-free all-optical add-drop multiplexing at 160 Gb/s. Electron. Lett. **39**, 1074–1076 (2003)
34. Tangdiongga, E., Turkiewicz, J.P., Rohde, H., Schairer, W., Lehmann, G., Sikora, E.S.R., Zhou, Y.R., Lord, A., Payne, D., Khoe, G.D., de Waardt, H.: 160 Gb/s OTDM add/drop networking using 275 km installed fibres. Electron. Lett. **40**, 552–554 (2004)
35. de Melo, A.M., Randel, S., Petermann, K.: Mach-Zehnder interferometer-based high-speed OTDM add-drop multiplexing. IEEE J. Lightwave Technol. **25**, 1017–1026 (2007)
36. Tangdiongga, E., Liu, Y., de Waardt, H., Khoe, G., Dorren, H.J.S.: 320-to-40-Gb/s demultiplexing using a single SOA assisted by an optical filter. IEEE Photonics Technol. Lett. **18**, 908–910 (2006)
37. Tangdiongga, E., Liu, Y., de Waardt, H., Khoe, G.D., Koonen, A.M.J., Dorren, H.J.S., Shu, X., Bennion, I.: All-optical demultiplexing of 640 to 40 Gbits/s using filtered chirp of a semiconductor optical amplifier. Opt. Lett. **32**, 835–837 (2007)
38. Yang, W., Zhang, M., Ye, P.: Analysis of 160 Gb/s all-optical NRZ-to-RZ data format conversion using quantum-dot semiconductor optical amplifiers assisted Mach-Zehnder interferometer. Opt. Commun. **282**, 1744–1750 (2009)

39. Dong, J., Zhang, X., Wang, F., Hong, W., Huang, D.: Experimental study of SOA-based NRZ-to-PRZ conversion and distortion elimination of amplified NRZ signal using spectral filtering. Opt. Commun. **281**, 5618–5624 (2008)
40. Agrawal, G.P., Olsson, N.A.: Self-phase modulation and spectral broadening of optical pulses in semiconductor laser amplifiers. IEEE J. Quantum Electron. **25**, 2297–2306 (1989)
41. Crottini, A., Salleras, F., Moreno, P., Dupertuis, M.A., Deveaud, B., Brenot, R.: Noise figure improvement in semiconductor optical amplifiers by holding beam at transparency scheme. Photonics Technol. Lett. **17**, 977–979 (2005)
42. Yuan, X., Guo, Z., Qiang, W., Yi, Y., Ping, X.: All-optical RZ to NRZ format conversion using single SOA assisted by optical band-pass filter. Chin. Phys. Lett. **25**, 2051–2054 (2008)
43. Hill, M.T., de Waardt, H., Khoe, G.D., Dorren, H.J.S.: All-optical flip-flop based on coupled laser diodes. IEEE J. Quantum Electron. **37**, 405–413 (2001)
44. Takenaka, M., Nakano, Y.: Realization of all-optical flip-flop using directionally coupled bistable laser diode. IEEE Photonics Technol. Lett. **16**, 45–47 (2004)
45. Clavero, R., Ramos, F., Martinez, J.M., Marti, J.: All-optical flip-flop based on a single SOA-MZI. IEEE Photonics Technol. Lett. **17**, 843–845 (2005)
46. McDougall, R., Liu, Y., Maxwell, G., Hill, M.T., Harmon, R., Zhang, S., Rivers, L., Huijskens, F.M., Poustie, A., Dorren, H.J.S.: Hybrid integrated, all-optical flip-flop memory element for optical packet networks. In: Proceeding of ECOC, Cannes, France, Paper th.1.4.5. (2006)
47. Kehayas, E., Seoane, J., Liu, Y., Martinez, J.M., Herrera, J., Holm-Nielsen, P.V., Zhang, S., McDougall, R., Maxwell, G., Ramos, F., Marti, J., Dorren, H.J.S., Jeppesen, P., Avramopoulos, H.: All-optical network subsystems using integrated SOA-based optical gates and flip-flops for label-swapped networks. IEEE Photonics Technol. Lett. **16**, 1750–1752 (2006)
48. Poustie, A.J., Blow, K.J., Manning, R.J., Kelly, A.E.: All-optical digital processing using semiconductor optical amplifiers. In: IEE Colloquium on New Developments in Optical Amplifiers, London, UK (1998)
49. Zoiros, K.E., Houbavlis, T., Kalyvas, M.: Ultra-high speed all-optical shift registers and their applications in OTDM networks. Opt. Quantum Electron. **36**, 1005–1053 (2004)
50. Ma, S., Sun, H., Chen, Z., Dutta, N.K.: High speed all-optical PRBS generation based on quantum-dot semiconductor optical amplifiers. Opt. Express **17**, 18469–18477 (2009)
51. Tangdiongga, E., Turkiewicz, J.P., Khoe, G.D., de Waardt, H.: Clock recovery by a fiber ring laser employing a linear optical amplifier. IEEE Photonics Technol. Lett. **16**, 611–613 (2004)
52. Slovak, J., Bornholdt, C., Sartorius, B.: All-optical 3R regenerator for asynchronous data packets at 40 Gb/s. In: Proceedings of European Conference on Optical Communication, pp. 388–389. Stockholm, Sweden (2004)
53. Phillips, I.D., Gloag, A., Moodie, D.G., Doran, N.J., Bennion, I., Ellis, A.D.: Drop and insert multiplexing with simultaneous clock recovery using an electroabsorption modulator. IEEE Photonics Technol. Lett. **10**, 291–293 (1998)
54. Kehayas, E., Stampoulidis, L., Avramopoulos, H., Liu, Y., Tangdiongga, E., Dorren, H.J.S.: 40 Gb/s all-optical packet clock recovery with ultrafast lock-in time and low inter-packet guardbands. Opt. Express **13**, 475–480 (2005)
55. Akiyama, T., Kuwatsuka, H., Simoyama, T., Nakata, Y., Mukai, K., Sugawara, M., Wada, O., Ishikawa, H.: Nonlinear gain dynamics in quantum-dot optical amplifiers and its application to optical communication devices. IEEE J. Quantum Electron. **37**, 1059–1065 (2001)
56. Spyropoulou, M., Pleros, N., Papadimitriou, G., Tomkos, I.: A high-speed multiwavelength clock recovery scheme for optical packets. IEEE Photonics Technol. Lett. **20**, 2147–2149 (2008)

Chapter 5
Application of SOA-Based Circuits in All-Optical Signal Processing and Switching

5.1 Introduction

Towards the effort for all-optical implementation of the important signal processing subsystems required in a packet switched node, emphasis have been given on exploiting the advantages provided by SOA-based switching technology. Realization of optical packet switched networks is certainly a demanding technological challenge since key network node functionalities have to be performed directly in the optical domain and the optical subsystems should process the inherently packet-formatted traffic on a packet-by-packet basis on-the-fly. In this way, unique specifications of SOA-based optical gates and systems including their ultra-fast operation speed and strong nonlinear characteristics, especially when operating in the deeply saturated regime, are promising for SOA-based demonstration of all-optical switching nodes as well as realization of all-optical processing techniques.

In this chapter, a number of recent improvements in demonstration of all-optical signal processing systems and all-optical switching architecture which utilize SOA-based logic gates and circuits as their basis foundation will be introduced. Although the proposed subjects only cover a small contribution of SOA-based systems capabilities in future all-optical switching and processing scenarios, it has been tried to represent a variety of different techniques to give a bright point of view for numerous applications of SOA-based architectures.

5.2 All-Optical Header/Payload Separation

In order to transmit packets from source to destination in all-optical packet switching networks, it is usually required to separate the header information and payload embedded in the data packets. In an effort toward all-optical routing,

A. Rostami et al., *Nanostructure Semiconductor Optical Amplifiers*, Engineering Materials, DOI: 10.1007/978-3-642-14925-2_5,

several techniques have been proposed for the all-optical header/payload separation such as utilizing terahertz optical asynchronous demultiplexers (TOAD) [1] and time-to-wavelength mapping technique [2].

A SOA-MZI based all-optical packet header separation system is presented in Fig. 5.1 which is consisted of an all-optical packet clock recovery circuit that generates an optical clock signal persisting for the duration of the incoming data packet and a SOA-MZI based optical AND gate to separate header and payload. The extracted clock serves as a control signal and is coupled to the MZI2 where a delayed version of the input packet enters to the other MZI port. The amount of temporal delay between the input packet and the extracted clock should be equal to the packet header length. Therefore, the recovered clock opens a switching window for the packet payload as schematically illustrated in Fig. 5.1a and the separated header and payloads are appeared at the output of the AND gate. The packet payloads consist of $2^7 - 1$ PRBS with 1.5 ns duration, two preamble bits, two label bits and a stuffed bit have placed in the header structure to contribute to successful clock extraction as depicted in Fig. 5.1b.

The simulation results of the 40 Gb/s header/payload separation circuit have depicted in Fig. 5.2 illustrating the incoming data packet in panel (a) with a header "11010100", the extracted clock packet with 12 bit 1/e fall time and instantaneous lock time in panel (b) and separated header and payload in panels (c) and (d) respectively. The obtained extinction ratio of 13 dB for the extracted label and 11 dB for the extracted payload describe the successful operation of the circuit.

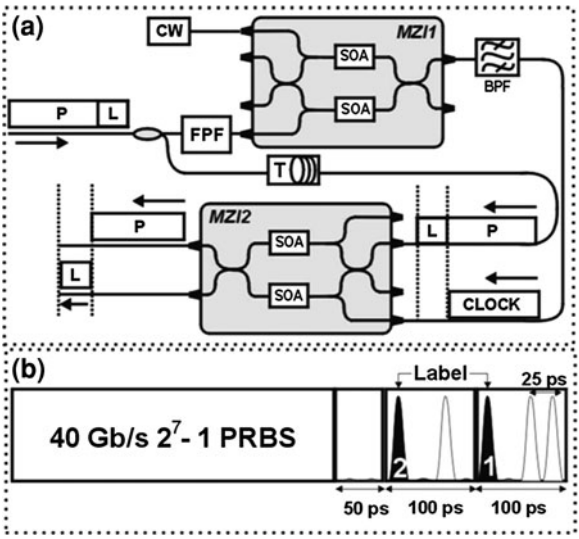

Fig. 5.1 **a** SOA-MZI-based all-optical header/payload separation circuit, and **b** data packet format designed for proper clock recovery [3]

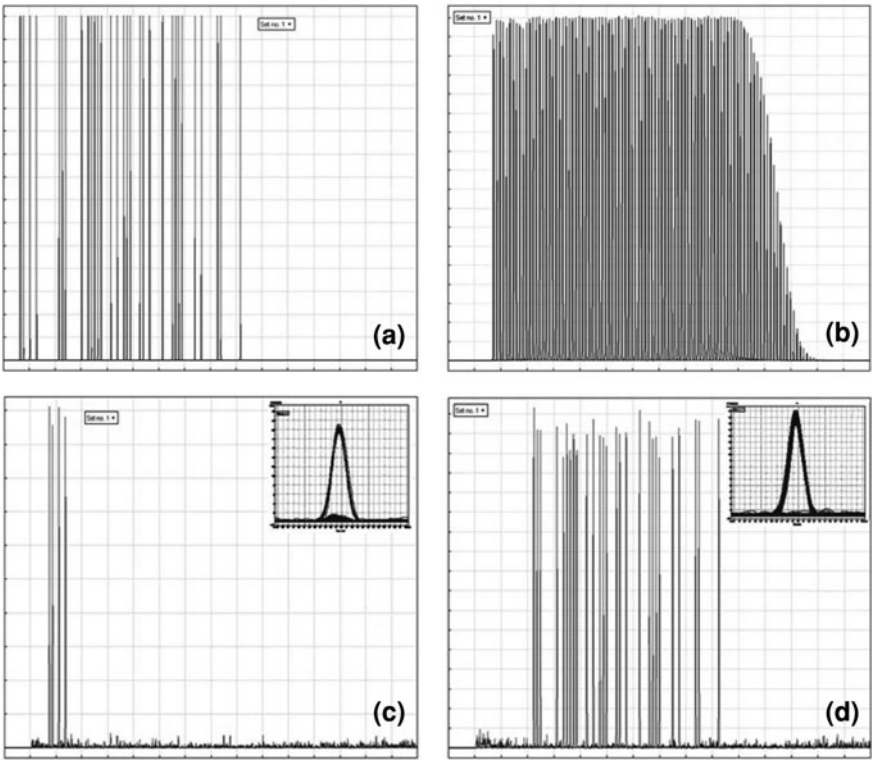

Fig. 5.2 Simulation results of label/payload separation circuit at 40 Gb/s. **a** Incoming data packet, **b** recovered clock packet, **c** extracted header, and **d** extracted payload. Insets depict eye diagrams of four packets containing all possible 2-bit label combinations and time base is 200 ps/div [3]

5.3 All-Optical Correlator

Recognizing optical packet headers or labels as a part of data packets which contains routing information by comparing the header bits with a reference address is the first step in developing an all-optical switching architecture. In current optical networks, header processing takes place electronically in each network node and therefore optical labels undergo optoelectronic (OE) conversion and are required to have lower bit rates compared with high bit rate packet payload which remains in optical domain. Also, packet header processing is done electronically [4] or takes the switching decisions employing electronic control systems [5]. Increasing the data traffic in the optical networks demand for higher payload bit rates and consequently header bit rate. From optical signal processing point of view, packet header recognition can be realized by comparing the optical header with a reference address. SOA-based logics especially XOR gate have been considered for this

purpose due to their specific properties and several architectures have been demonstrated for all-optical header comparison [6]. An all-optical header processor or correlator compares two sequences and provides an optical pulse at the output when address matching occurs. Therefore, such a system is an important block in all-optical packet routers. An all-optical correlator can be obtained by cascading SOA-MZI based XOR gate as presented in Fig. 5.3 [7]. In this structure, the two input data streams and a CW probe light are coupled into ports #1, #2 and #4 and the output stream which is XOR function of the two input data couples to the port #4 of the second stage after proper attenuation and delay. The number of the XOR stages depends on the number of the header bits in arrived optical packet. Also, the configuration utilizes counter-propagating XOR scheme to avoid optical filtering between stages.

The cascade scheme can be described by a logic function defined by

$$\begin{aligned} S_i^{(j)} &= S_{i-1}^{(j-1)}\, C_i \\ \text{and,} \quad C_i &= A_i \oplus B_i \end{aligned} \tag{1}$$

where $S_i^{(j)}$is the i-th bit of the signal at the output of the j-th stage, A_i and B_i are the i-th bits of the input data signals. Hence, C_i is the XOR output corresponding to two i-th input data signals and $S_i^{(0)} = 1$ denotes the CW signal coupled to the first stage. Considering N stages for the structure (N-bit data streams), the final output of the structure can be defined by

$$\begin{aligned} S_i^{(N)} &= 0, \quad i < N; \\ S_N^{(N)} &= \begin{cases} 0, & \text{if A} \neq \bar{\text{B}} \\ 1, & \text{if A} = \bar{\text{B}} \end{cases} \end{aligned} \tag{2}$$

The simulation results for all-optical address recognition at 10 Gb/s (limited by bulk SOA recovery time) are shown in Fig. 5.4 where the input data streams are considered to be A = [1000, 0011, 1110, 0100, 1011] and B = [0011, 1101, 1001, 1011, 0010]. As it is obvious, an address matching pulse is obtained for the forth word, '1011', which is common in both of the streams. It is important to note that the number of stages in the scheme presented in Fig. 5.3 is limited by the ASE noise level of the SOA. Although the optical correlator structure can perform address matching for any N-bit header and matching streams theoretically, but the

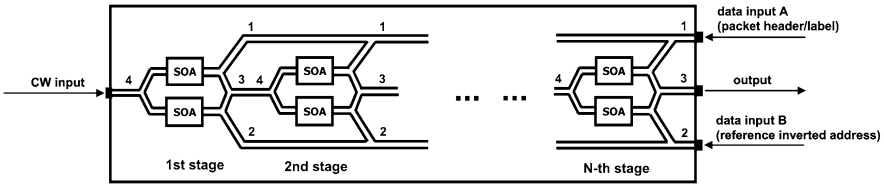

Fig. 5.3 SOA-MZI based all-optical header processor [7]

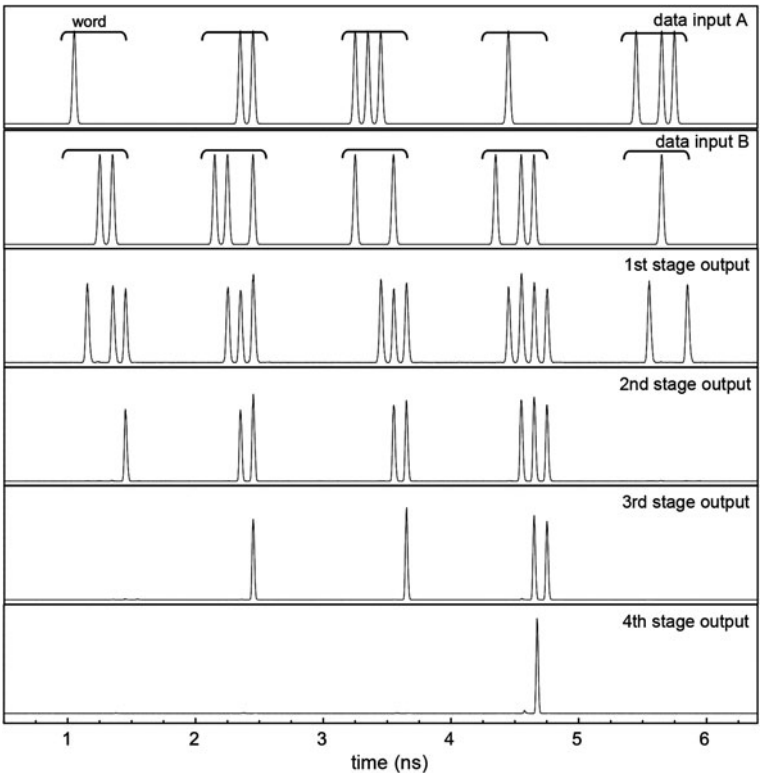

Fig. 5.4 Simulation results for address recognition scheme [7]

synchronization of the control (probe) signal and the data signals will be very important in a practical case.

To achieve a better understand of the synchronization between the SOA-MZI stages it might be worthwhile to study a practical 2-bit all-optical correlator which operates based on the cascaded SOA-MZI XOR gates [8].

The proposed setup in Fig. 5.5 consists of two signal generation blocks where a CW laser is modulated with 1 GHz repetition-rate pulses to form the optical control signal and input data signals are generated at 10 Gb/s bit rate using a pulsed fiber laser Mach–Zehnder modulator. At the output of the data signal generation block an optical coupler and fiber patch-cords and ODLs have placed to obtain different data patterns. The output signal of the first XOR gate (port #4) contains the XOR information of the first bits from Data A and Data B. This output pulse synchronizes with the second bits of the data streams and couples to the second SOA-MZI stage and serves as an enabling pulse for second XOR operation as it is clear in Eq. 1, i.e. if the first bits of the two streams mismatched, a '1' signal enables the second bits comparison at the second stage. A '1' pulse at the output of the second stage

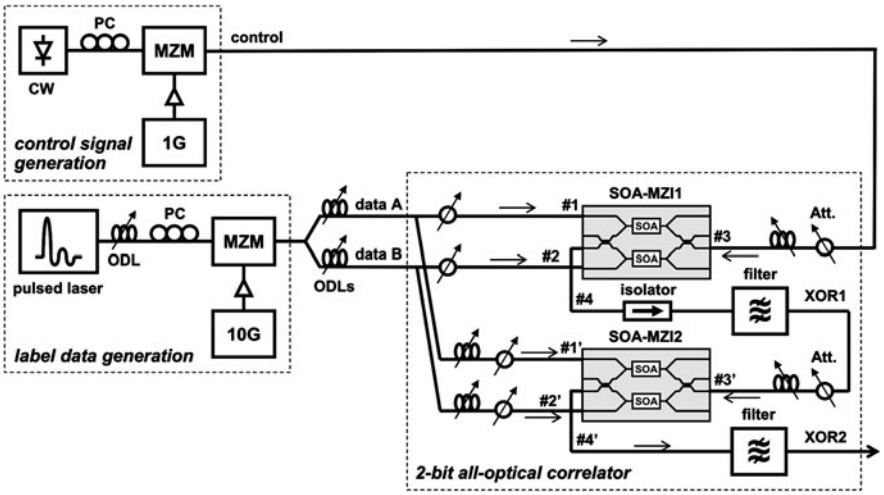

Fig. 5.5 Experimental setup for the 2-bit all-optical correlator [8]

corresponds to data pattern matching or $A = \bar{B}$. The outputs of each stage pass through an optical filter to lower the cascaded ASE noise effect. Operation results of 4 different input data streams (A = '00', B = '01'), (A = '11', B = '01'), (A = '11', B = '00'), and (A = '10', B = '01'), are illustrated in Fig. 5.6 from left to right boxes respectively. The XOR operations of first bits have yielded '1' pulse except for the first data streams as presented in the third row of the figure whereas only the two latter streams meet the $A = \bar{B}$ condition. Thus, the '1' pulses at the part (d) describe the patter matching validation.

To avoid the structure complexity and increasing the number of cascaded SOA-MZI structures at larger headers the N-bit all-optical XOR gate with feedback has proposed [9]. In this scheme which is schematically illustrated in Fig. 5.7 the control signal which consists of a train of pulses enables the bit-by-bit comparison for the first bit of each header word. This means that the control pulses are synchronized to the first bit of input signals while the comparison result of the first bit plays as a pulse which enables or disables the comparison process of the following bits through coupling to port 3 of SOA-MZI structure (via feedback loop).

As it is obvious in Fig. 5.7, the output pulse of the SOA-MZI is attenuated and delayed to avoid SOA saturation in multiple amplification stages and to become synchronized to the following bit.

The simulation results for two input data streams including 3 words with 5-bit sequences at each data signal are depicted in Fig. 5.8. The data pattern of 10 Gb/s input signals are: Data 1 = ('10010 10101 00001') and Data 2 = ('00011 01010 10100'). The output of the 5-bit comparison is emphasized by dotted boxes in Fig. 5.8d where only the second input words meet the matching condition.

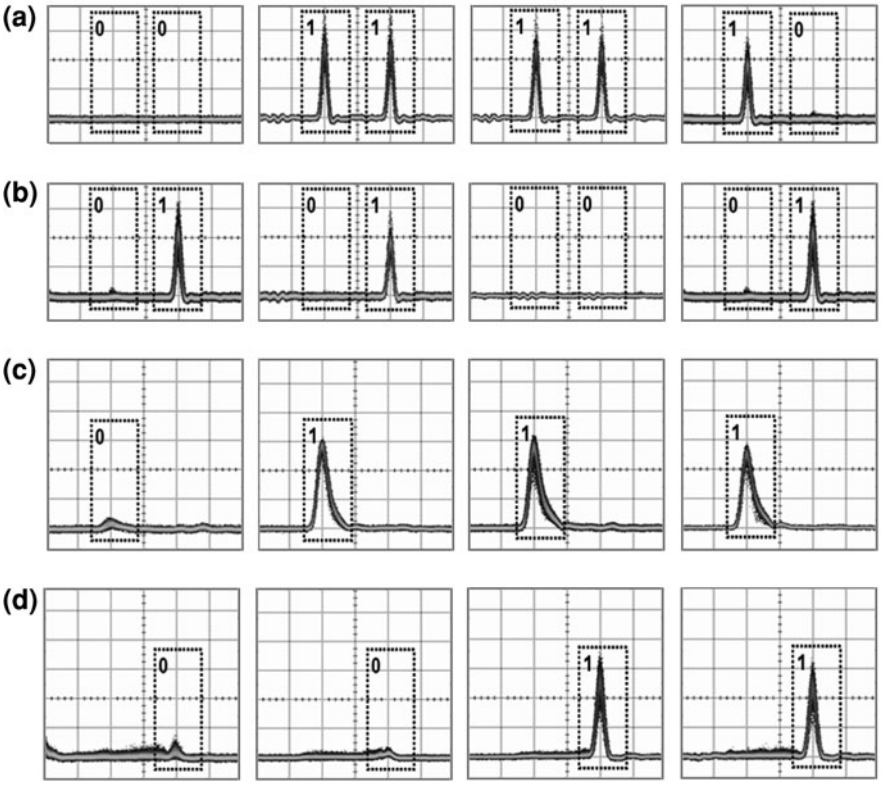

Fig. 5.6 Measured results of 2-bit correlator: **a** data stream A, **b** data stream B, **c** output of the first XOR stage, and **d** output of the second XOR stage [8]

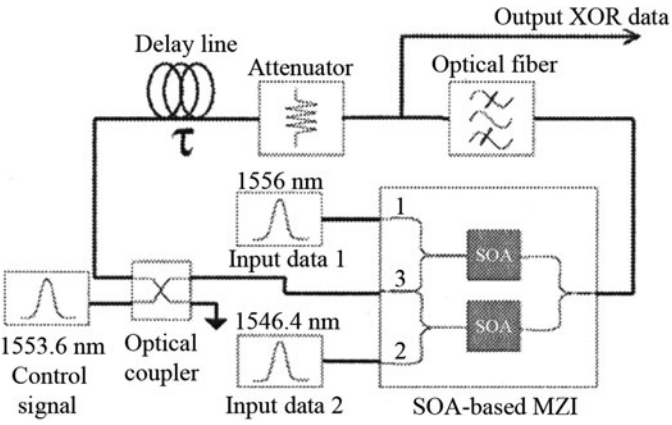

Fig. 5.7 N-bit all-optical XOR gate with feedback proposed to perform all-optical header processing [9]

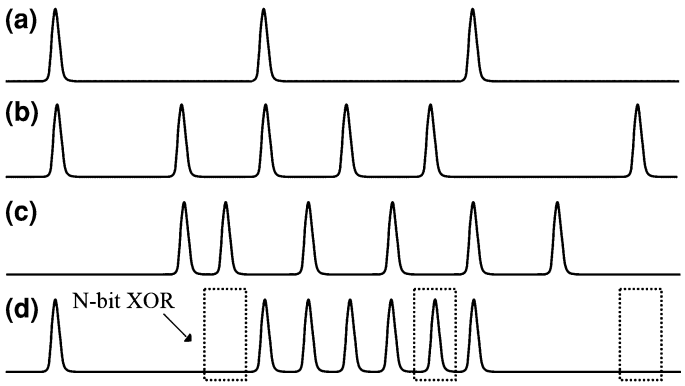

Fig. 5.8 N-bit all-optical XOR gate with feedback proposed to perform all-optical header processing [9]

Error-free operation on 8-bit-word streams with quality factor larger than 8.8, can be an impressive outcome for this configuration. However, the bit number limitation of the N-bit XOR gate relies on the fact that the quality of the control pulses degrade after multiple passing through the feedback loop due to SOA jitter.

5.4 All-Optical Packet Routing

All-optical packet routing is the next step toward developing an all-optical processing unit. This stage takes place after the header or address recognition of the received packets and the packet is switched to the proper node according to routing algorithms.

Schematic of an all-optical packet routing system based on SOA-MZI structure is depicted in Fig. 5.9. Upon arrival of a data packet, the header and payload separation takes place and the separated labels are forwarded to an array of all-optical correlators to address matching. These correlators serve as lookup table in electronically-switched optical networks that operate based on electronic RAMs. The all-optical flip-flops introduced previously are set to have high output level at the wavelength λ_i and receive the output pulse of the optical correlators as an input to their reset port.

The output pulse of each correlator will reset the corresponding flip-flop if the received address doesn't match the reference address and no signal appears at the output of the flip-flop. Otherwise, no pulse appears at the output of the correlators and the flip-flops keep emitting at λ_i. The output pulse of the optical flip-flops are combined together and are injected to a wavelength conversion block consisted of the SOA-MZI architecture as displayed in Fig. 5.10. Also, the extracted and separated labels from the incoming data packets are swapped by new labels in a label generation and insertion block and data packets with new headers are

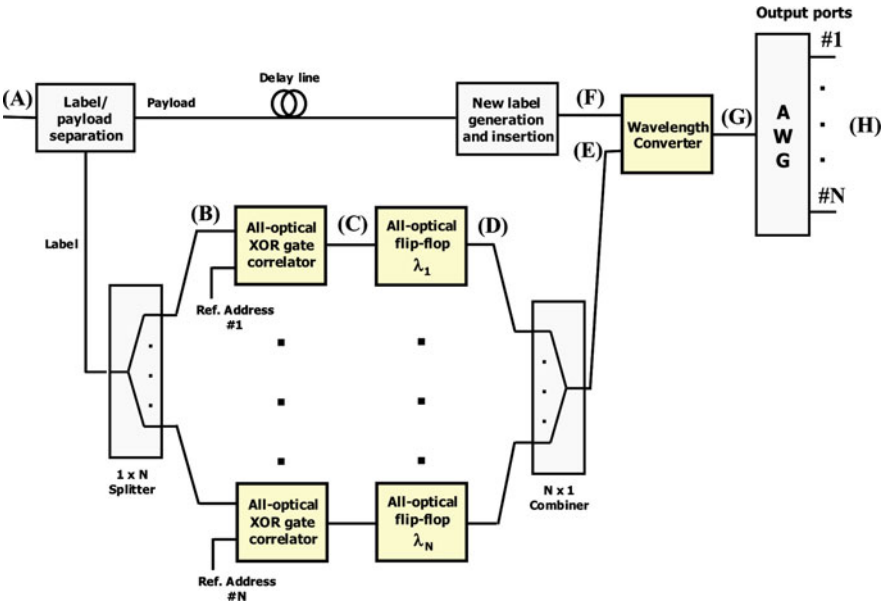

Fig. 5.9 All-optical packet routing architecture [10]

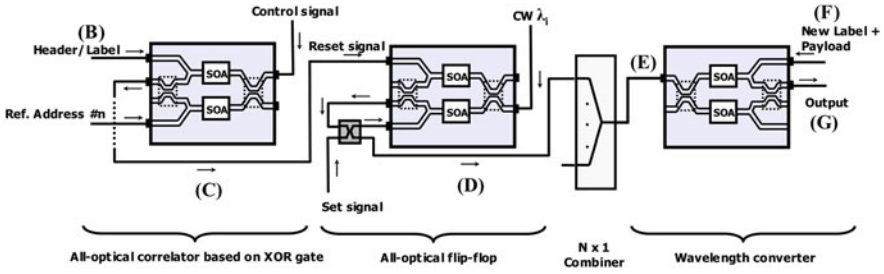

Fig. 5.10 Internal connections of the main units of the all-optical routing architecture [10]

inserted to the wavelength converter too. The injected wavelength to the converter block from the optical flip-flop array converts the wavelength of the incoming packets making it possible to route the data packets by means of array waveguides (AWG) or other available methods [11].

The simulation results for a 1×4 packet routing based on the discussed architecture of Fig. 5.9 and for 10 Gb/s data packets with RZ data format at 1553.6 nm are shown in Fig. 5.11. Each packet includes a 4-bit length header and a 128-bit length payload. The label separation and new label generations blocks have considered ideal although some methods for demonstration of these blocks have been proposed previously [12, 13].

The incoming data packets have depicted in Fig. 5.11a and the outputs of the 4th correlator at point C (see Fig. 5.10) have illustrated in Fig. 5.11b. Since the second packet label matches the fourth reference address, so, no reset pulses appear for the second packet. Absence of the reset pulses at the input of the corresponding flip-flop leads to generation of a CW signal during the time span of the second package as illustrated in Fig. 5.11c. This CW signal enables the wavelength conversion of the data packet to the specific wavelength of the flip-flop. Therefore, the wavelengths of the whole incoming packets are converted to λ_2, λ_4, λ_1, and λ_3 corresponding to the first, the second, the third, and the fourth input packets respectively. The insets of Fig. 5.11d–g also display the optical spectra of each packet.

5.5 All-Optical Header Processing

Figure 5.12 shows schematic setup of an experimental demonstration of a 4 × 4 all-optical label swapper (AOLS) and router subsystem based on SOA-MZI blocks. The label recognition subsystem which is consisted of two interconnected XOR correlators is capable of recognizing 2-bit header addresses at 10 Gb/s and wavelength switching at 40 Gb/s through an optically controlled wavelength converter driven by all-optical flip-flops [14]. The operational block diagrams of the 4 × 4 AOLS node is sketched in Fig. 5.13 describing that the experimentally developed 2-bit label processor with the interconnected flip-flop demonstrate a branch of the whole architecture. Each flip-flop emits at two wavelengths; a common λ_0 wavelength and one of the uncommon $\lambda_1 \ldots \lambda_4$ wavelengths depending on whether the address matching has failed or not. The common wavelength λ_0 will be filtered out finally.

The experimental setup of the header processor presented in Fig. 5.14a includes a transmitter for generating label patterns, a clock signal as input, two cascaded XOR correlators, optical delay lines to synchronize interacting signals within the optical gates, and variable optical attenuators (VOA) to tune the signal powers before injection to the SOAs. If the address matching occurs in the label processor subsystem, a matching pulse will be provided at the output which will be forwarded to the flip-flops. The optical flip-flops have been developed by using hybrid integration technology as previously described.

Two CW sources provide the two output states of each flip-flop and a modulated CW signal at the bit rate of 2.5 Gb/s and at the wavelength of 1565 nm serves as the set and reset pulses for the flip-flop with pulse period of 13 ns. The output state (signal) of the flip-flops is forwarded to the wavelength converter as illustrated in Fig. 5.12b. Also, a 40-Gb/s pattern generator modulates the data on short pulses and generates 1.6-ns packets separated by 2.7 ns. In a dynamic operation, an adaption stage is used to connect the 2-bit all-optical correlator and the flip-flop as displayed in Fig. 5.14. This stage consists of an optical delay line with a timing delay of 100 ps, 5 km length single-mode fiber (SMF), an EDFA, and an optical bandpass

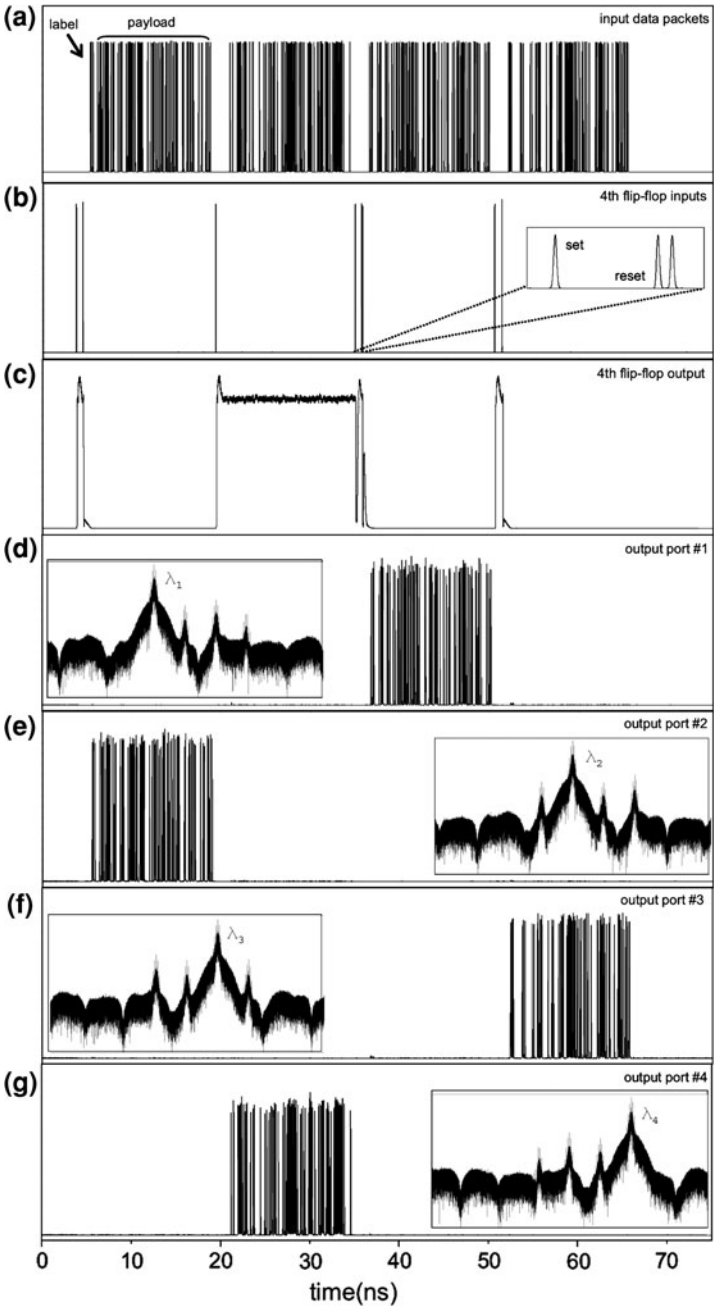

Fig. 5.11 Simulation results of 1 × 4 all-optical packet routing architecture. **a** Input data packets, **b** outputs from the 4th correlator, **c** output from the 4th flip-flop, **d** AWG output port #1, **e** AWG output port #2, **f** AWG output port #3, and **g** AWG output port #4 [10]

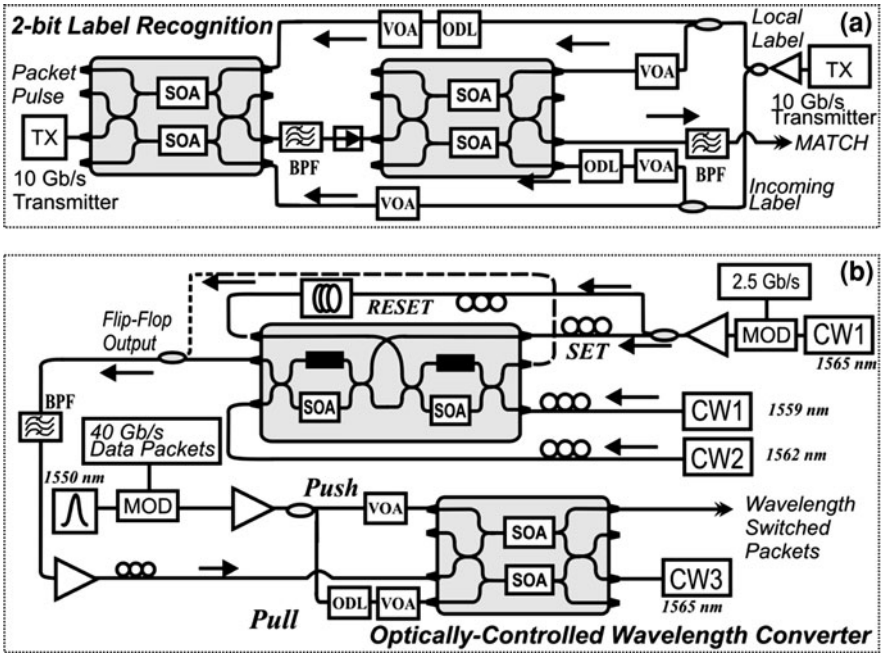

Fig. 5.12 Experimental setups of the all-optical network subsystems: **a** all-optical label processor, and **b** optically controlled wavelength converter [14]

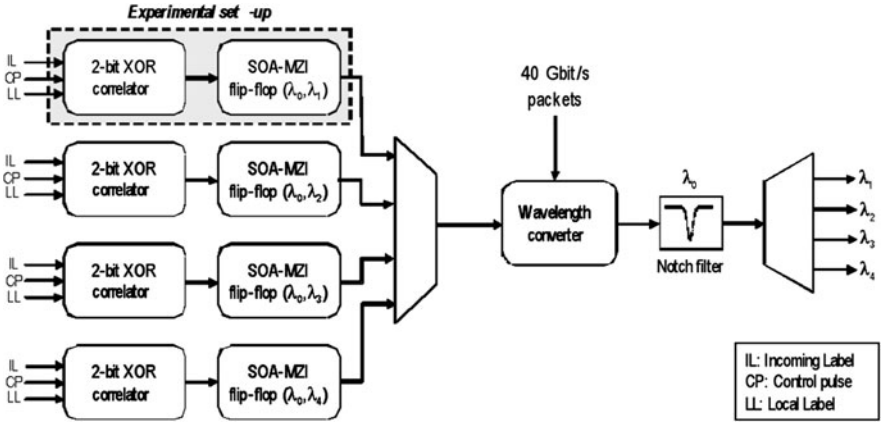

Fig. 5.13 Block diagrams of the all-optical label swapping and routing system [15]

filter with 1 nm 3 dB-bandwidth and provides a wide pulse with appropriate power level needed for the flip-flop from weak and short pulse obtained from the correlator (converts an input pulse with 3 mW peak power and an FWHM of $\sim$12 ps into an output pulse with 15 mW peak power and an FWHM of $\sim$200 ps). The correlator

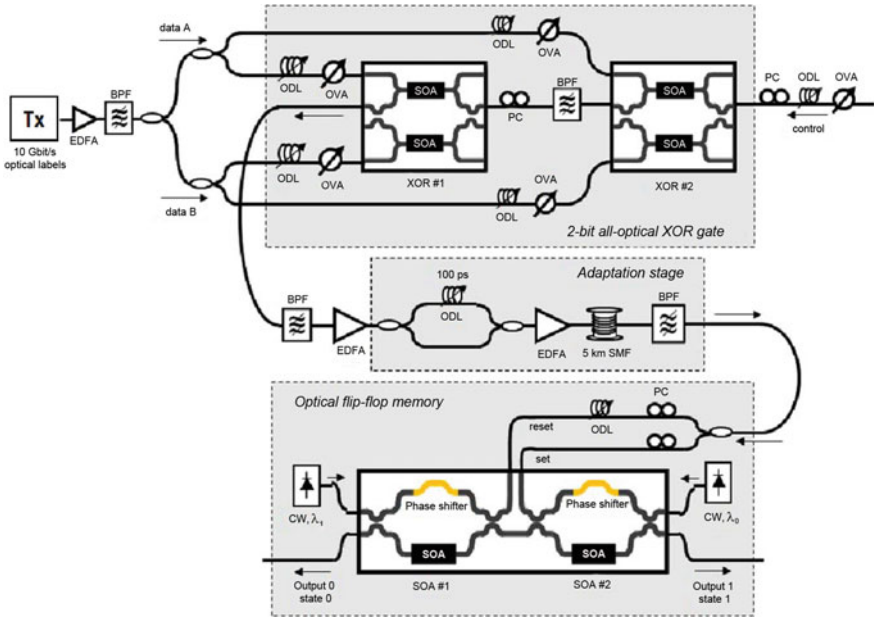

Fig. 5.14 Schematic of experimental setup of the 2-bit all-optical correlator, adaption stage and the optical flip-flop [15]

output signal is coupled to the flip-flop set and reset ports after the adaption stage. This signal is time delayed about 2.5 ns before injection to the reset port which is determined by the packet length. In this time interval the flip-flop keeps its output state. The obtained results for the routing operations are depicted in Fig. 5.15. The incoming packets along with the CW light appeared at the output of the flip-flop are shown in Fig. 5.15a and b respectively.

The wavelength obtained from the flip-flop determines the conversion wavelength of the incoming packets which is presented in Fig. 5.15c. The visible crosstalk from the remaining packets is due to the extinction ratio of the flip-flop (8.5 dB) that can be further enhanced by utilizing a regenerator circuit or optimization of the flip-flop operation.

5.6 All-Optical Packet Switching Based on In-Band Filtering

In the previously discussed adaption stage in AOLS architecture, a 5 km SMF had utilized to broaden the input pulse which induces a considerable latency to the processing unit. Using chirp fiber grating with a typical length of a few centimeters is another alternative approach to reduce the node latency [16]. Filter-based label processing is another scheme that utilizes an optical bandpass filter to extract the

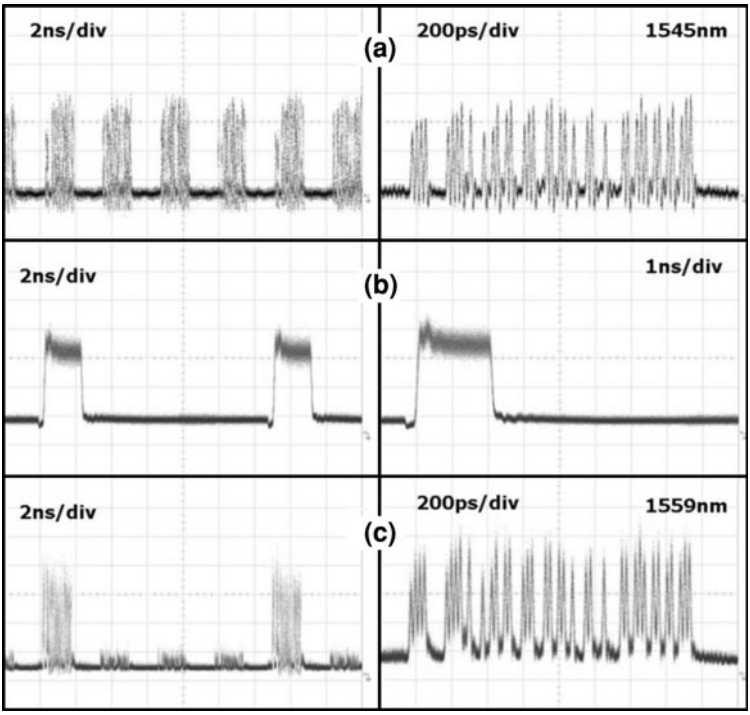

Fig. 5.15 Eye patterns showing all-optical routing. **a** Incoming packets, **b** flip-flop output, and **c** wavelength-switched packets [14]

label on-the-fly and shortens the delay required for the time alignment between the packet and the flip-flop output. Hence, reduces the header processing latency [17]. In the experimental setup of this scheme presented in Fig. 5.16 the in-band labeling method [18] is utilized in which the optical labels have enough energy to set and reset the flip-flop before arriving the high-bit rate payload. The wavelengths of the labels are selected such that they lay in-band within the payload bandwidth. Therefore, increasing the payload bit-rate which results in wider spectrum increases the number of available labels.

Since the payload spectrum is wide enough, the in-band labels can be selected using a narrowband optical filter. The packet transmitter unit generates 10 Gb/s payloads including predefined 768 bit sequence modulated over 2 ps RZ pulses at $\lambda_P = 1546$ nm which are time-multiplexed to 160 Gb/s ($\times 16$). Also, optical labels are generated at two alternating wavelengths $\lambda_{L1} = 1547.4$ nm and $\lambda_{L2} = 1544.6$ nm which are within the 20-dB bandwidth of the data payload. The generated packets consist of 9 ns labels and 56.8 ns data payloads separated with 4.6 and 6.4 ns guard times. The power of the transmitted packet is then split equally toward the tunable bandpass filter as the header processor and the wavelength converter. The wavelength conversion is realized using another BPF and

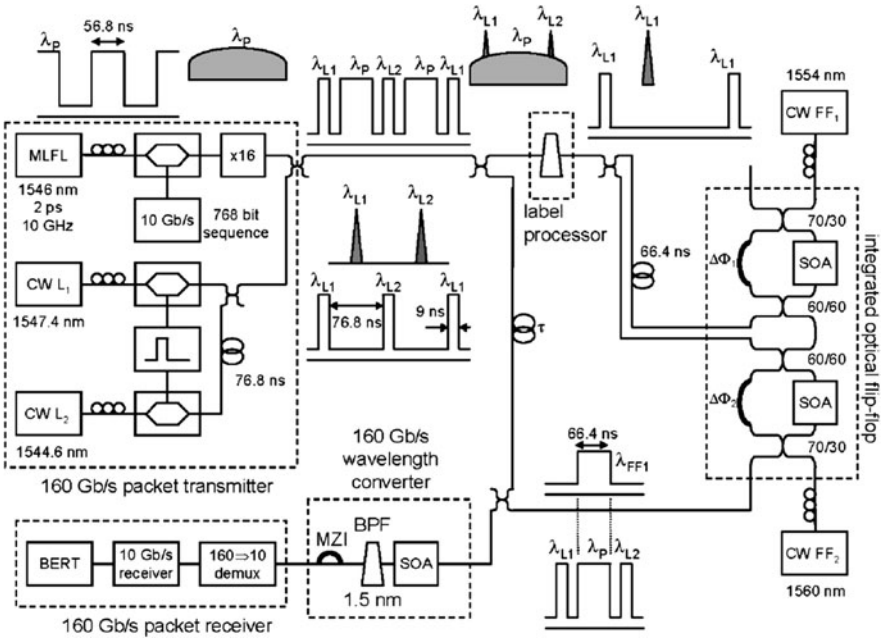

Fig. 5.16 Experimental setup for all-optical packet switching based on in-band filtering scheme [17]

using chirp characteristics of the pulses passing through the SOA (shifted filtering). Finally, at the packet receiver block, payloads are demultiplexed to 10 Gb/s and are analysis by a BER tester. Figure 5.17 shows the optical pulse shapes and related eye-diagram in different positions of the packet switching system. The output of the header extractor is depicted in Fig. 5.17c when the filter is tuned at λ_{L1} and the corresponding flip-flop output at λ_{FF1} with the timing duration proper to the payload duration is depicted in panel (d). The wavelength-converted packet payloads along with the related eye-diagram are displayed in panels (e) and (f) respectively. It is noteworthy that in the in-band filtering scheme described above, up to 25 different labels can be placed within the 5-nm-wide bandwidth at 20 dB of a 160-Gb/s payload using commercially available AWGs ($BW_{-3\ dB} = 0.1$ nm and $BW_{-30\ dB} = 0.2$ nm).

5.7 All-Optical Self-Routing Node and Network Architecture

The lack of optical random access memories capable of storing data has caused some limitations in routing plane of all-optical networks. Despite of development of optical flip-flops as optical memories, optical RAMs are still far from the

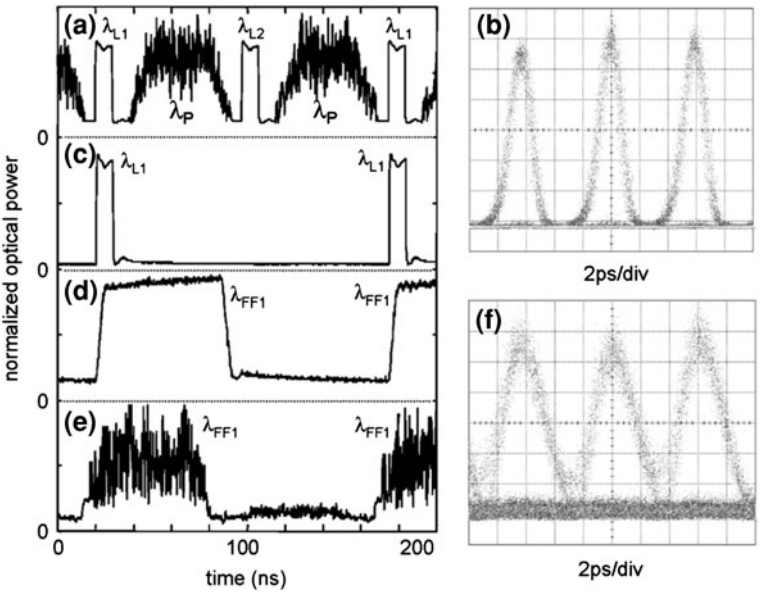

Fig. 5.17 **a** Optical trace of input packets, **b** eye-diagram of input packet payload, **c** output of header extractor with filter tuned at λ_{L1}, **d** output of optical flip-flop, **e** wavelength converter output, and **f** eye-diagram of wavelength converted payload [17]

capability of being used in all-optical processing and routing scenarios. Specially, dealing with fiber delay lines as optical memories, increasing the number of packet header bits imposes some constraints on local-address-generation procedure in the node architectures which perform header recognition by comparing with a local address. Therefore, implementation of bufferless self-routing nodes and switches can be a solution to resolve the mentioned problems. In a self-routing-network, the intermediate nodes forward the incoming packets to the appropriate output ports according to routing information embedded at the source node. Schematic of a self-routing-network architecture without need for optical header recognition is displayed in Fig. 5.18 [19].

In this network architecture transmission of optical packets through the network nodes is realized using optical headers that contain stacked optical tags. Each packet tag corresponds to a specific node and contains bit-level information for optically controlling the switching matrix of the node and thus routing the data packet to the appropriate outgoing link. According to the computed path and the transmission commences between two nodes, an optical header is embedded in each packet in all of the nodes which contains the tags of computed nodes in the path. For example, considering a packet travelling way from node A to node E in Fig. 5.18, when the packet arrives to the next node, the first tag ("B") is all-optically removed and the packet is forwarded to the appropriate outgoing link of the node by the control signals embedded within the specific tag "B".

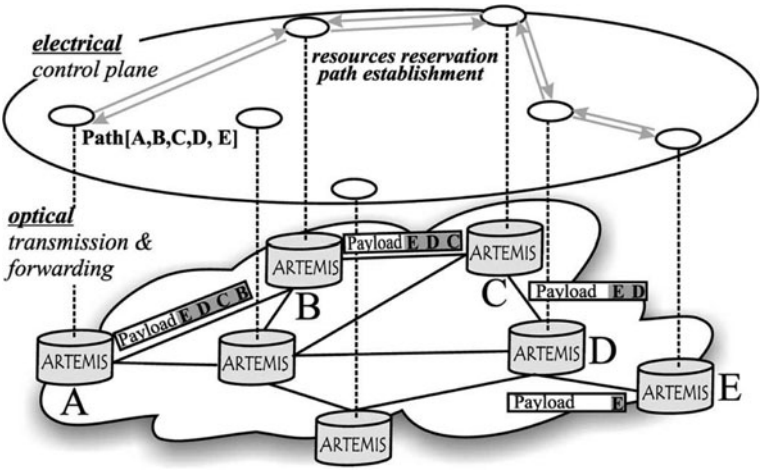

Fig. 5.18 Schematic of self-routing network architecture based on all-optical packet forwarding [19]

The physical-layer node implementation of the network contains three main subsystems: the self-synchronization stage, the all-optical header-processing, and the switching matrix. Figure 5.19 depicts these subsystems along with the packet format designed for self-routing operation. The header and payload are at 40 Gb/s RZ format where the optical header consists of several stacked tags for routing in each node. Each tag contains two preamble bits (50 ps) to assist clock extraction at each node and one guardband bit (25 ps) between the payload and the routing bits to account for the clock acquisition time of the self-synchronization stage.

The self-synchronization stage extracts the clock and a single pulse from the incoming data packets at the line and packet rates respectively as illustrated in Fig. 5.20. The packet clock recovery is fulfilled by utilizing a passive comb-generating filter for retiming and a saturated nonlinear gate for reshaping at 40-Gb/s in each node. Clock extraction on a per-packet basis without requiring any synchronization to local oscillators, is the main advantage of this scheme that can lead to packet-format transparency. Also, a single optical pulse is generated for each incoming pulse according to XGM effect in a single SOA. The incoming packets and the recovered packet clock in the header processing and forwarding subsystem are utilized to extract the node tags by passing through a SOA-MZI based AND logic gate. Figure 5.21 depicts the architecture of the header processing and forwarding unit where the recovered packet clocks serve as switching windows.

By proper synchronization of the clock and the incoming packet, the first tag remains outside the switching windows while the packet payload and the other tags are forwarded toward the switching matrix. The separated tag #1 enters into the processing unit which consists of an array of SOA-MZI AND gates to extract

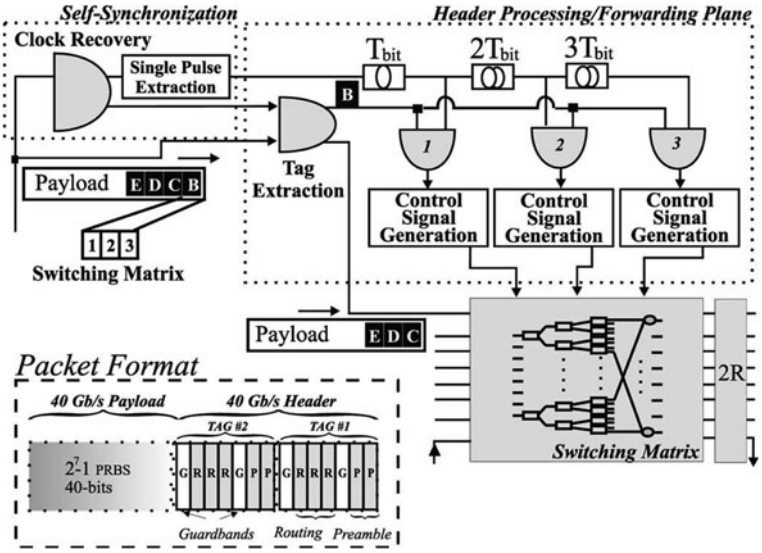

Fig. 5.19 Node architecture of the self-routing all-optical network including self-synchronization, header processing and forwarding, and switching matrix subsystems. The packet format comprising 40 Gb/s payload, routing bits, preamble bits and guardband bit is also displayed [19]

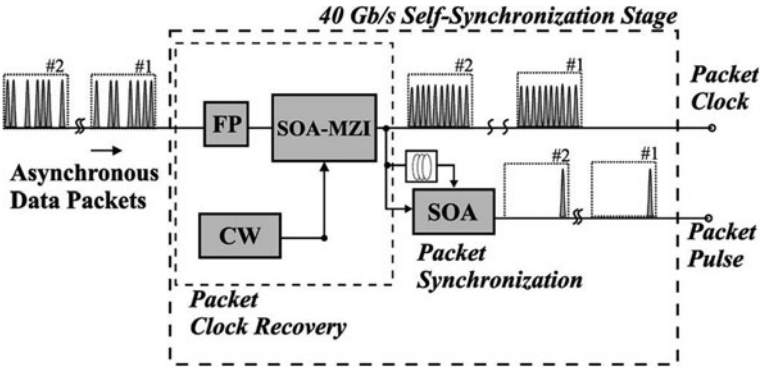

Fig. 5.20 Self-synchronization stage consisting of a 40-Gb/s packet clock recovery and a packet synchronization subsystem [19]

the tag bits via introducing bit-length delay at the input of the AND gates. Thus, a single routing bit is obtained at the output of each gate which leads to generation of a proper control signal at the control signal generation unit. The control signal should be a pulsed CW signal with duration equal to the total packet length which is forwarded to the switching matrix to perform the packet routing to defined link. The simulation results of different functions in the header processing subsystem including tag and routing bit extraction and CW control pulse generation are displayed in Fig. 5.22.

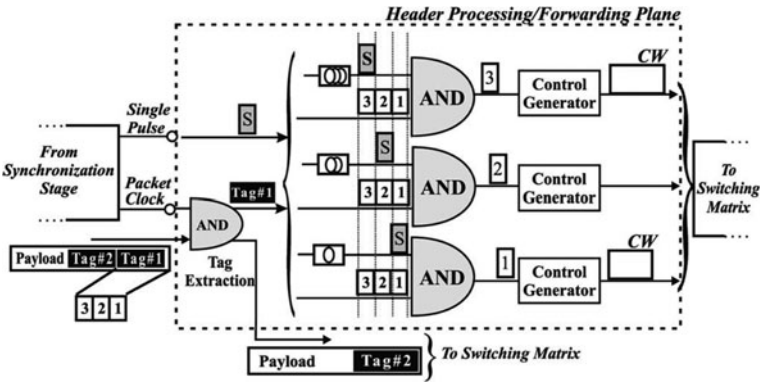

Fig. 5.21 Schematic architecture of the header processing and forwarding unit [19]

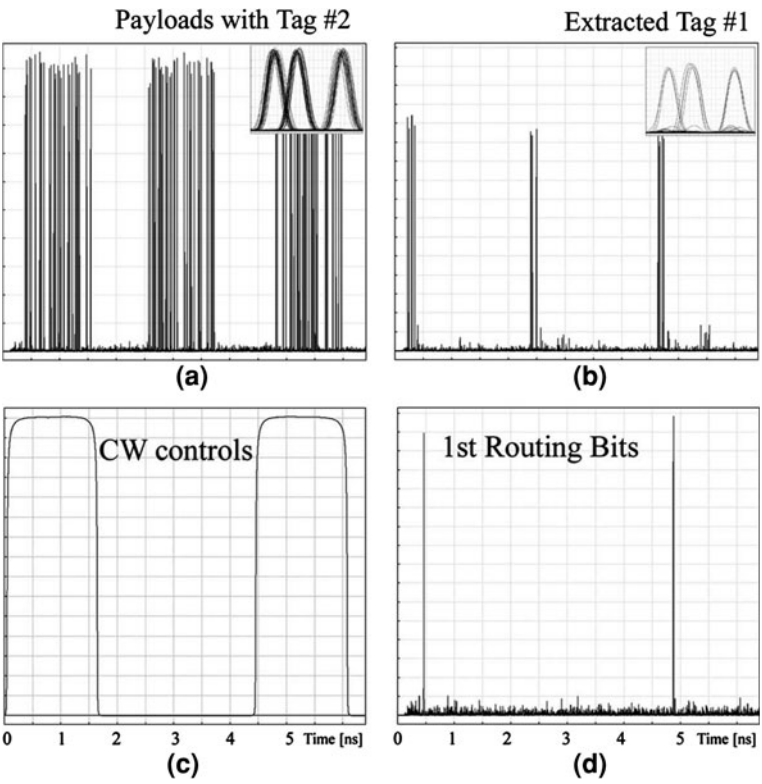

Fig. 5.22 Simulation results of the header processing unit at 40 Gb/s **a** extracted payload and remaining tag, **b** extracted tag #1, **c** generated CW control signal, and **d** extracted routing bit of each packet [19]

References

1. Ji, W., Zhang, M., Ye, P.: All-optical-packet header and payload separation for unslotted optical-packet-switched networks. J. Lightwave Technol. **25**, 703–709 (2007)
2. Cardakli, M.C., Lee, S., Willner, A.E., Grubsky, V., Starodubov, D., Feinberg, J.: Reconfigurable optical packet header recognition and routing using time-to-wavelength mapping and tunable fiber Bragg gratings for correlation decoding. IEEE Photon. Technol. Lett. **12**, 552–554 (2000)
3. Ramos, F., Kehayas, E., Martinez, J.M., Clavero, R., Marti, J., Stampoulidis, L., et al.: IST-LASAGNE: towards all-optical label swapping employing optical logic gates and optical flip-flops. J. Lightwave Technol. **23**, 2993–3011 (2005)
4. Koonen, T., Sulur, Tafur, I., Jennen, J., de Waardt, H.: Optical labeling of packets in IP-over-WDM networks. In: Proc. 28th European Conference on Optical Communications, Copenhagen, Denmark, paper 5.5.2 (2002)
5. Takahashi, R., Nakahara, T., Takenouchi, H., Suzuki, H.: 40-Gbit/s label recognition and 1×4 self-routing using self-serial-to-parallel conversion. IEEE Photon. Technol. Lett. **16**, 692–694 (2004)
6. Fjelde, T., Kloch, A., Wolfson, D., Dagens, B., Coquelin, A., Guillemot, I., Gaborit, F., Poingt, F., Renaud, M.: Novel scheme for simple label-swapping employing XOR logic in an integrated interferometric wavelength converter. IEEE Photon. Technol. Lett. **13**, 750–751 (2001)
7. Martinez, J.M., Ramos, F., Marti, J.: All-optical packet header processor based on cascaded SOA-MZIs. Electron. Lett. **40**, 894–895 (2004)
8. Martinez, J.M., Herrera, J., Ramos, F., Marti, J.: All-optical address recognition scheme for label-swapping networks. IEEE Photon. Technol. Lett. **18**, 151–153 (2006)
9. Martinez, J.M., Ramos, F., Marti, J., Herrera, J., Llorente, R.: All-optical N-bit XOR gate with feedback for optical packet header processing. In: Proc. European Conf. on Optical Communication (ECOC'2002), Copenhagen, Denmark, paper P4–8 (2002)
10. Clavero, R., Martinez, J.M., Ramos, F., Marti, J.: All-optical packet routing scheme for optical label-swapping networks. Opt. Express **12**, 4326–4332 (2004)
11. Hill, M.T., Srivatsa, A., Calabretta, N., Liu, Y., de Waardt, H., Khoe, G.D., Dorren, H.J.S.: 1×2 optical packet switch using all-optical header processing. Electron. Lett. **37**, 774–775 (2001)
12. Tsiokos, D., Kehayas, E., Kanellos, G.T., Stampoulidis, L., Guekos, G., Avramopoulos, H.: All-optical 10 Gb/s header replacement for variable-length data packets. In: Proc. European Conference on Optical Communication (ECOC'2003), paper We4.P.83 (2003)
13. Olsson, B.-E., Öhlén, P., Rau, L., Rossi, G., Jerphagnon, O., Doshi, R., Humphries, D.S., Blumenthal, D.J., Kaman, V., Bowers, J.E.: Wavelength routing of 40 Gbit/s packets with 2.5 Gbit/s header erasure/rewriting using all-fibre wavelength converter. Electron. Lett. **36**, 345–346 (2000)
14. Kehayas, E., Seoane, J., Liu, Y., Martinez, J.M., Herrera, J., Holm-Nielsen, P.V., Zhang, S., McDougall, R., Maxwell, G., Ramos, F., Marti, J., Dorren, H.J.S., Jeppesen, P., Avramopoulos, H.: All-optical network subsystems using integrated SOA-based optical gates and flip-flops for label-swapped networks. IEEE Photon. Technol. Lett. **18**, 1750–1752 (2006)
15. Martinez, J.M., Liu, Y., Clavero, R., Koonen, A.M.J., Herrera, J., Ramos, F., Dorren, H.J.S., Marti, J.: All-optical processing based on a logic XOR gate and a flip-flop memory for packet-switched networks. IEEE Photon. Technol. Lett. **19**, 1316–1318 (2007)
16. Litchinitser, N.M., Patterson, D.B.: Analysis of fiber bragg gratings for dispersion compensation in reflective and transmissive geometries. J. Lightwave Technol. **15**, 1323–1328 (1997)
17. Herrera, J., Tangdiongga, E., Liu, Y., Hill, M.T., McDougall, R., Poustie, A., Maxwell, G., Ramos, F., Marti, J., de Waardt, H., Khoe, G.D., Koonen, A.M.J., Dorren, H.J.S.: 160-Gb/s

all-optical packet-switching with in-band filter-based label extraction and a hybrid-integrated optical flip-flop. IEEE Photon. Technol. Lett. **19**, 990–992 (2007)
18. Herrera, J., Tangdiongga, E., Liu, Y., Hill, M. T., McDougall, R., Poustie, A., Maxwell, G., Ramos, F., Marti, J., de Waardt, H., Khoe, G.D., Koonen, A.M.J., Dorren, H.J.S.: 160 Gb/s all-optical packet switching employing in-band wavelength labelling and a hybrid integrated optical flip-flop. In: Proc. ECOC, Cannes, France, paper th.4.1.5 (2006)
19. Kehayas, E., Vyrsokinos, K., Stampoulidis, L., Christodoulopoulos, K., Vlachos, K., Avramopoulos, H.: ARTEMIS: 40-Gb/s all-optical self-routing node and network architecture employing asynchronous bit and packet-level optical signal processing. J. Lightwave Technol. **24**, 2967–2977 (2006)